Lecture Notes in Mechanical Engineering

Kanishka Jha
Piyush Gulati
Uma Kant Tripathi *Editors*

# Recent Advances in Sustainable Technologies

## Select Proceedings of ICAST 2020

Springer

# Lecture Notes in Mechanical Engineering

**Lecture Notes in Mechanical Engineering (LNME)** publishes the latest developments in Mechanical Engineering—quickly, informally and with high quality. Original research reported in proceedings and post-proceedings represents the core of LNME. Volumes published in LNME embrace all aspects, subfields and new challenges of mechanical engineering. Topics in the series include:

- Engineering Design
- Machinery and Machine Elements
- Mechanical Structures and Stress Analysis
- Automotive Engineering
- Engine Technology
- Aerospace Technology and Astronautics
- Nanotechnology and Microengineering
- Control, Robotics, Mechatronics
- MEMS
- Theoretical and Applied Mechanics
- Dynamical Systems, Control
- Fluid Mechanics
- Engineering Thermodynamics, Heat and Mass Transfer
- Manufacturing
- Precision Engineering, Instrumentation, Measurement
- Materials Engineering
- Tribology and Surface Technology

To submit a proposal or request further information, please contact the Springer Editor of your location:

**China:** Ms. Ella Zhang at ella.zhang@springer.com
**India:** Priya Vyas at priya.vyas@springer.com
**Rest of Asia, Australia, New Zealand:** Swati Meherishi at swati.meherishi@springer.com
**All other countries:** Dr. Leontina Di Cecco at Leontina.dicecco@springer.com

To submit a proposal for a monograph, please check our Springer Tracts in Mechanical Engineering at http://www.springer.com/series/11693 or contact Leontina.dicecco@springer.com

**Indexed by SCOPUS. All books published in the series are submitted for consideration in Web of Science.**

More information about this series at http://www.springer.com/series/11236

Kanishka Jha · Piyush Gulati · Uma Kant Tripathi
Editors

# Recent Advances in Sustainable Technologies

## Select Proceedings of ICAST 2020

Springer

*Editors*
Kanishka Jha
School of Mechanical Engineering
Lovely Professional University
Phagwara, Punjab, India

Piyush Gulati
School of Mechanical Engineering
Lovely Professional University
Phagwara, Punjab, India

Uma Kant Tripathi
Mechnox Pvt. Ltd.
Ghaziabad
Uttar Pradesh, India

ISSN 2195-4356 ISSN 2195-4364 (electronic)
Lecture Notes in Mechanical Engineering
ISBN 978-981-16-0975-6 ISBN 978-981-16-0976-3 (eBook)
https://doi.org/10.1007/978-981-16-0976-3



This Springer imprint is published by the registered company Springer Nature Singapore Pte Ltd.
The registered company address is: 152 Beach Road, #21-01/04 Gateway East, Singapore 189721, Singapore

# Contents

# About the Editors

**Kanishka Jha** is currently working as an Associate Professor in the School of Mechanical Engineering, Lovely Professional University, Phagwara, Punjab. He obtained his doctorate degree in the field of bio-degradable composites. His major areas of research interests include machining, green composites, biodegradable material and nanomaterials and also use of bio-waste materials in composite engineering applications. He has published 12 papers in respected international journals. Dr. Kanishka Jha is a reviewer in many reputed journals like *Journal of the Brazilian Society of Mechanical Sciences and Engineering* (BMSE), *World Journal of Engineering* and many more. Currently, he is a board member of the Savvy Science Publisher. He has guided five master's thesis and currently he is guiding three Ph.D. thesis.

**Piyush Gulati** is presently working as an Associate Professor in the School of Mechanical Engineering, Lovely Professional University, Phagwara, Punjab. He completed his Ph.D. from Dr. B. R. Ambedkar National Institute of Technology Jalandhar, India, in 2019 and M. Tech. from PEC University of Technology Chandigarh, India, in 2010. His research interests include friction stir welding, green composites, and material characterization. He has published various research papers in different national/international journals and conferences of repute and has published 30+ patents. He has supervised and guided various dissertations and projects at PG and UG level. He has been a part of international conference as organizing committee member at Lovely Professional University. He has 12 years of teaching experience to his credit.

**Uma Kant Tripathi** is a Six Sigma Green Belt and Supply Chain Certified professional with over 23 years of extensive experience with focus on material sourcing, vendor development, new product development re-verifying design specification, purchase of capital equipment & indirect material, supplier quality development and assurance, formulation and implementation of sourcing strategies. He holds proficiency in procuring raw material, CNC machining, press components plastic injection & hand moulded components, pressure die casting of Al and Zn alloy, investment castings, sintered material, rubber material, SS pipes, heat treatments,

anodizing, plating, welding, new tool development, etc. He has a proven track record of leading the organization to increase revenues and profitability, streamline workflow and create a team environment to increase productivity. He is skilled in managing multiple operations i.e. resourcing planning, material planning, in process inspection, vendor development, supplier audit, team building & coordination with internal customer. He has experience on ERP system like BaaN, SAP, MFG-Pro.

# An Exploratory Study on Various Properties of Graphite–Aluminium Metal Matrix Composites Fabricated Through Powder Metallurgy Route


**Rajib Gupta, Sourav Debnath, and Akshay Kumar Pramanick**

## 1 Introduction

With the improvement of modern technologies, various lightweight materials have widely demanded in different sectors for sophisticated designing [1, 2]. In aerospace and aeronautics, industries have required low-density, high-strength materials for designing various parts. Automobile industries [2] also required lightweight materials for designing the structure to reduce fuel consumption. Not only outer structure, suitable light metals are preferred for designing engine parts also [1, 2]. Powder metallurgy is an economic technique by which lightweight, exact dimension porous metal can be fabricated which will be widely required for designing engine parts, especially gear arrangements [1–9].

Aluminium is a well-known easily available metal and is being used in various mechanical, electrical and electronics industries. Aluminium has low-density, lightweight, good corrosion resistant, moreover easy machinability [1–10] promote it from other metal and alloys. Low strength [3–8] and low melting point [8, 9] restrict the applications of pure aluminium from large-scale use. These problems can be shorted out with incorporating suitable second phase as reinforcement into pure aluminium [9–20].

The present study focuses on the fabrication and various evaluations of graphite–aluminium metal matrix composites. In the previous studies, researchers have taken several attempts towards fabricating aluminium matrix composites with incorporating TiC, $Al_2O_3$, fused silica, Ti-Aluminide and so on through different methods [1–20], but the fabrication of graphite–aluminium composites followed by powder metallurgy route is completely rare.

R. Gupta · S. Debnath (✉) · A. K. Pramanick
Jadavpur University, Kolkata, West Bengal 700032, India



K. Jha et al. (eds.), *Recent Advances in Sustainable Technologies*,
Lecture Notes in Mechanical Engineering,
https://doi.org/10.1007/978-981-16-0976-3_1

## 2 Experimental Procedure

### *2.1 Fabrication of Graphite–Aluminium Composites*

For fabricating graphite–aluminium metal matrix composites, constituent materials have mixed into a hand-driven motor parcel. In this mixing, graphite powder has varied from 1.5 to 9.0 wt%, and the rest is aluminium. Different compositions of graphite–aluminium powders (mesh size ~200 μm) have considered separately for pressing and sintering simultaneously into hot press unit considering 500 °C temperatures for 2 h. Samples are permitted to cool slowly into the same furnace. The stepwise fabrication methodology has elaborated in our previous studies [8, 9, 20]. However, after removing from furnace, fabricated metal matrix composites have polished and considered for measurement of various properties, finally corrosion study [6–8] with employing "Potentiostat Galvanostat, Super-PG1000".

## 3 Results and Discussions

### *3.1 XRD*

XRD analysis after sintering of graphite–aluminium metal matrix composite is plotted in Fig. 1. In this diffraction pattern, aluminium has identified at $2\theta$ angle of

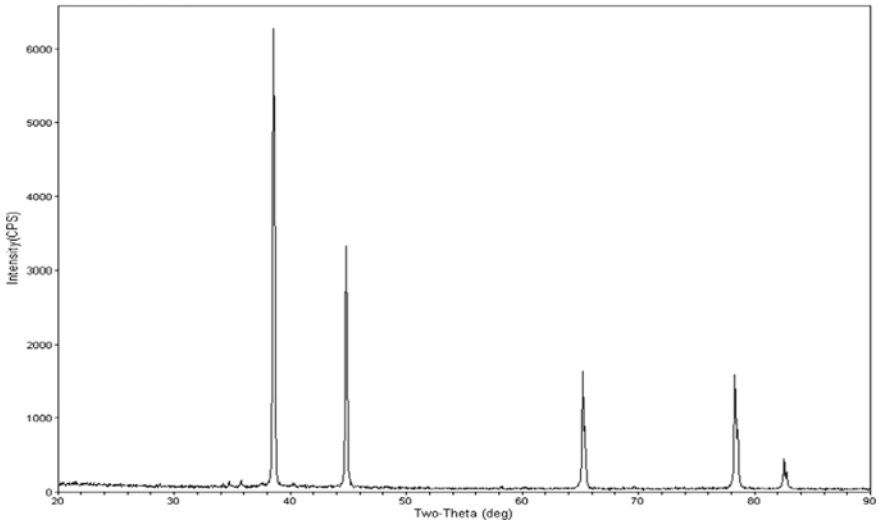


**Fig. 1** XRD pattern for 4% (based on wt%) graphite–aluminium metal matrix composite

~38.494°, 44.74°, 65.012°, 78.019°, 82.07°, and graphite is diffracted with low abundance peak at $2\theta$ angle of ~26.7°. The presence of individual phases after sintering implies that no reaction occurred between the matrix and reinforcement for these fabricating environments. However, in this study, XRD has carried out from $2\theta$ of ~20° to 80° with continuous scanning 5°/min using "RigakuUltima III analytical diffractometer".

### *3.2 SEM*

Surface morphology for the fabricated composites after sintering is shown in Fig. 2. Systematic distribution of graphite has seen into aluminium matrix. Tendency of formation of pores has increased significantly beyond addition of graphite by 2.5 wt% as seen in Fig. 2.

### *3.3 Density Measurement*

Density has decreased gradually with graphite reinforcements shown in Fig. 3. This is quite natural as graphite has less density than aluminium and consequent improvement of void spaces with reinforcements.

### *3.4 Hardness Survey*

Table 1 has demonstrated the obtained micro-hardness based on the hardness survey carried out with model no. "LM248SAT". Hardness has improved gradually up to 2.5 wt% addition of graphite and then tends to deteriorate with further reinforcement of graphite. Beyond 2.5 wt% addition of graphite, bonding between metal matrix and reinforcement hampers with consequent improvement of pores as observed in SEM morphology shown in Fig. 2.

### *3.5 Apparent Porosity*

Improvement of porosity has observed with the addition of graphite as shown in Fig. 4. Porosity has varied from 0.15% to maximum 0.54% which can be considered as tolerable limit.

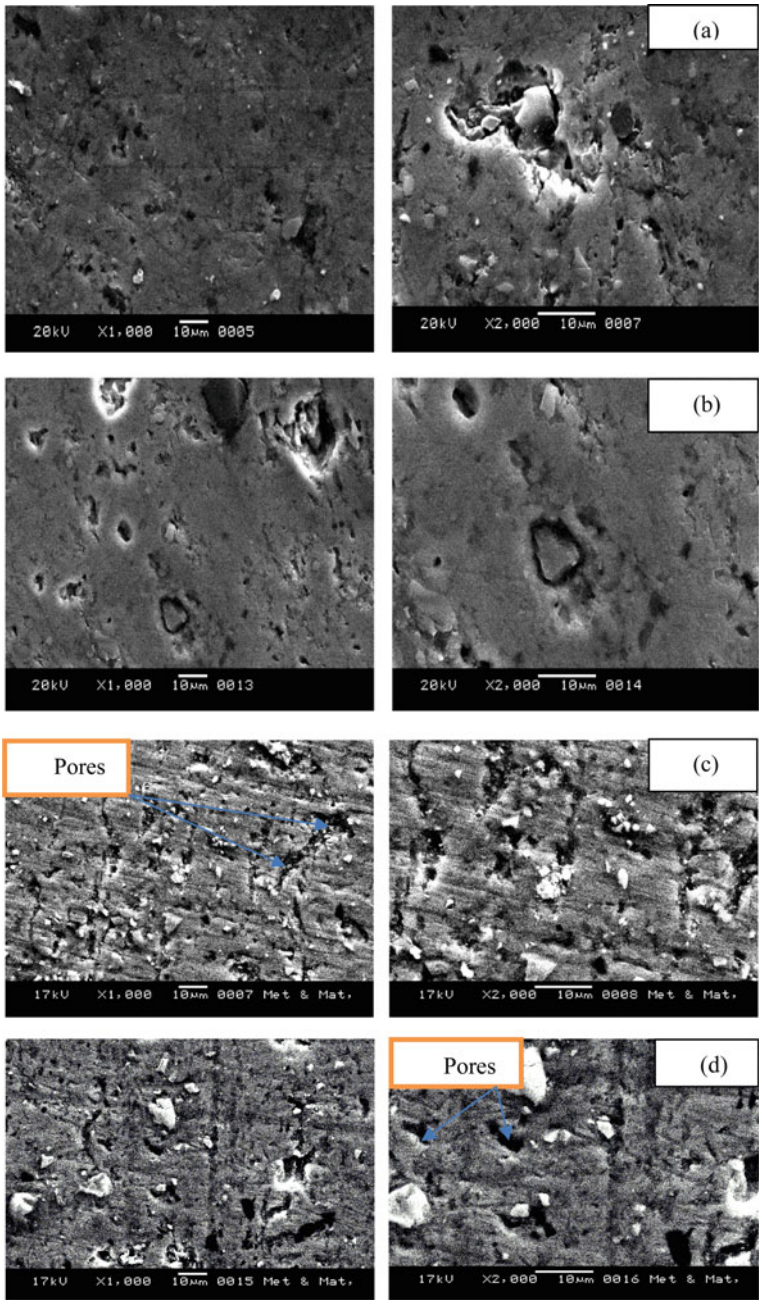


**Fig. 2** SEM (Model: "JSM 6360") image of **a** 1.5%, **b** 3.0%, **c** 5.0%, **d** 9.0% (based on wt%) graphite–aluminium metal matrix composites

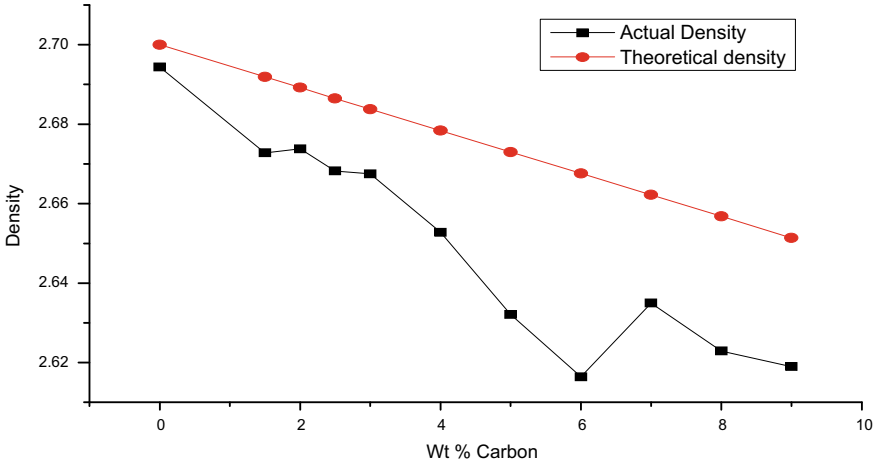


**Fig. 3** Variation of sintered density due to addition of graphite into aluminium matrix

**Table 1** Variation of micro-hardness

| Sample | Hardness in MPa |
|---|---|
| 1.5 wt% graphite–aluminium composite | 331.50 |
| 2.0 wt% graphite–aluminium composite | 337.10 |
| 2.5 wt% graphite–aluminium composite | 345.00 |
| 3.0 wt% graphite–aluminium composite | 335.40 |
| 4.0 wt% graphite–aluminium composite | 331.90 |
| 5.0 wt% graphite–aluminium composite | 328.60 |
| 6.0 wt% graphite–aluminium composite | 322.00 |
| 7.0 wt% graphite–aluminium composite | 312.90 |
| 8.0 wt% graphite–aluminium composite | 303.79 |
| 9.0 wt% graphite–aluminium composite | 301.60 |

## *3.6 Corrosion Evaluation*

All the fabricated materials are considered for chemical property evaluation at seawater environment, and corresponding $E_{corr}$ versus $I_{corr}$ graphs are plotted in Fig. 5. It has seen that the corrosion rate is decreased up to 2.5 wt.% addition of graphite and then tends to make increase as a consequence of interacting with seawater as plotted in Fig. 6. Variation of corrosion rate with graphite reinforcements is shown in Fig. 6.

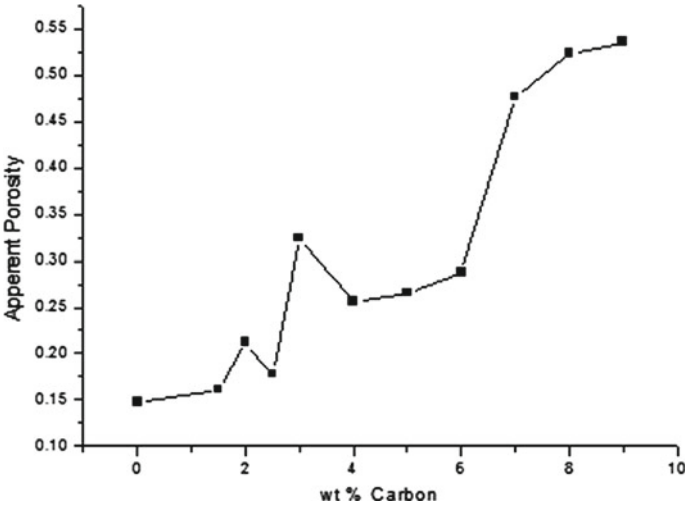


**Fig. 4** Apparent porosity for graphite–aluminium metal matrix composites

## 4 Conclusion

Aluminium matrix composites reinforced with graphite have fabricated successfully adopting "powder metallurgy route". Prepared graphite–aluminium composites have less weight compared with pure sintered aluminium. Improvement of both hardness and corrosion properties has observed up to 2.5 wt% incorporating graphite into aluminium matrix. Beyond the addition of graphite by 2.5% (by wt%), void spaces increase and realized that materials suffer from lack of stability. Naturally, porosity tends to improve after 2.5% graphite reinforcement.

Finally, it can be concluded from this study that improvement of physical, mechanical and chemical properties has observed up to 2.5 wt% addition of graphite and hence, 2.5 wt% graphite–aluminium composite holds all improved properties compared to the others.

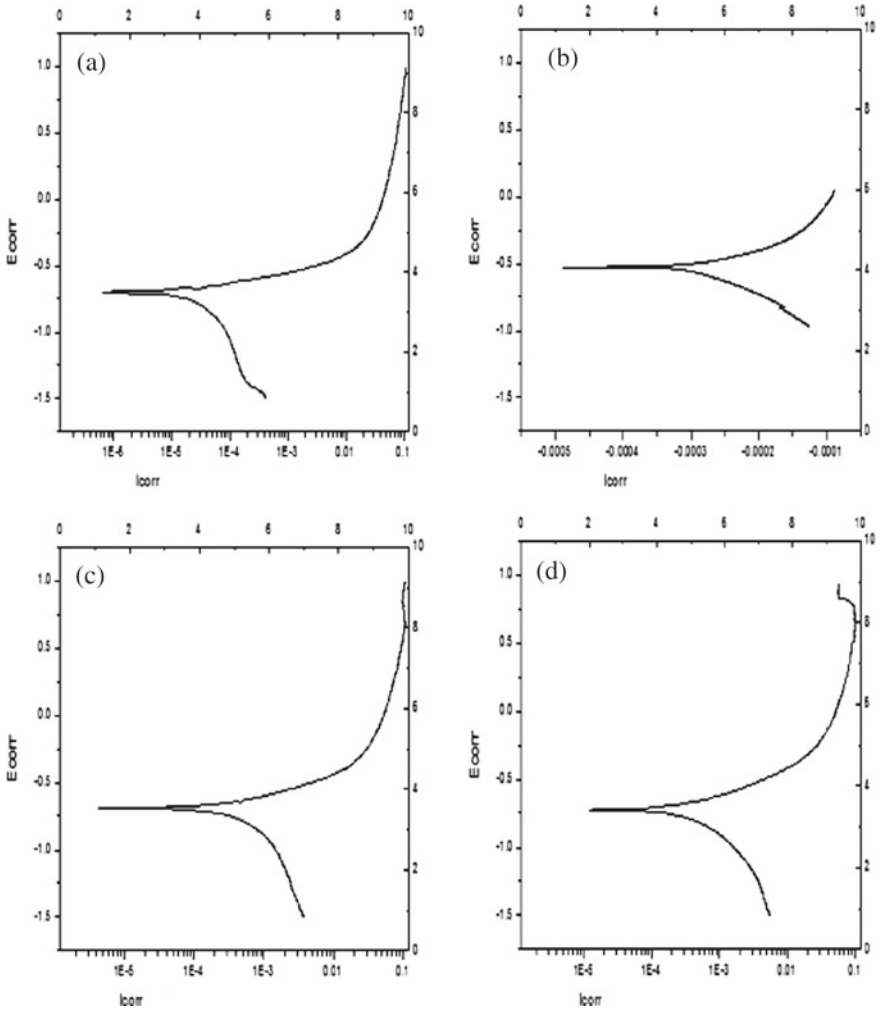


**Fig. 5** Corrosion behaviour of **a** pure sintered aluminium, **b** 2.5%, **c** 6.0%, **d** 9.0% (based on wt%) graphite–aluminium composites into seawater environment

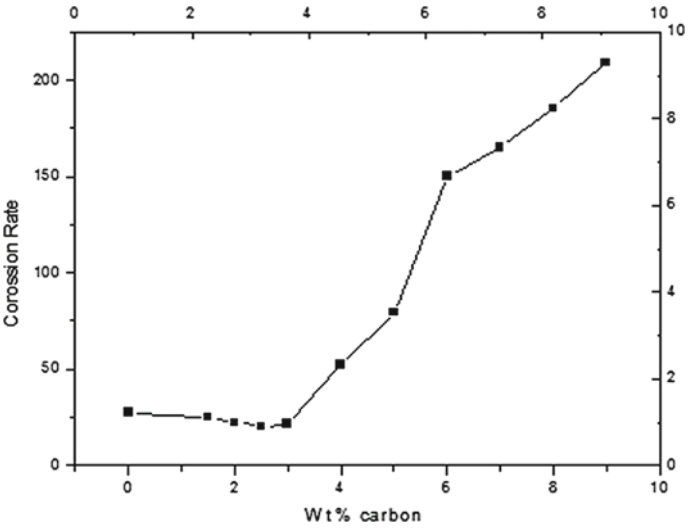


**Fig. 6** Variation of corrosion rate due to addition of graphite into aluminium matrix

## References


1. Bodunrin MO, Alaneme KK, Chown LH (2015) Aluminium matrix hybrid composites: a review of reinforcement philosophies; mechanical, corrosion and tribological characteristics. JMR&T 4(4):434–445
2. Prasad SV, Asthana R (2004) Aluminium metal matrix composites for automotive applications; tribological considerations. Tribol Lett 17(3)
3. Singh G, Bharti H (2017) Fabrication of the aluminium graphite composite material: a review. SSRG-IJME 4(7):1–6
4. Chawla N, Chawla KK (2006) Metal matrix composites in ground transportation. Springer, New York, p 401
5. Patnaik SC, Swain PK, Mallik PK, Sahoo SK (2014) Wear characteristics of aluminium-graphite composites produced by stair casting technique. J Mater Metall Eng 4(3):13–20
6. Kulkarni SJ (2015) A review on studies and research on corrosion and its prevention. Int J Res Rev 2(9):574–578
7. Rani BEA, Bai B, Basu J (2012) Green inhibitors for corrosion protection of metals and alloys: an overview. Int J Corros 2012(Article Id 380217):1–15
8. Debnath S, Pramanick AK (2016) Development and evaluation of various properties of crystalline silica-aluminium metal based composites. IJERGS 4(2):236–245
9. Debnath S, Pramanick AK (2016) Development and study on different properties of aluminium-crystalline silica ceramic matrix composites at different sintering temperatures. Int J Eng Res Gen Sci 4(3):415–423
10. Usman AM, Raji A, Waziri NH, Hassan MA (2014) Production and characterization of aluminium alloy-bagasse ash composites. IOSR J Mech Civ Eng (IOSR-JMCE) 11(4):38–44. Ver. III (2014)
11. Tong XC, Ghosh AK (2001) Fabrication of in situ TiC reinforced aluminum matrix composites. J Mater Sci 36:4059–4069
12. Hesabi ZR, Simchi A, Raihani SMS (2006) Structural evolution during mechanical milling of nanometric and micrometric $Al_2O_3$ reinforced Al matrix composites. Mater Sci Eng A428

13. Magesh M, Baruch LJ, Oliver DG (2014) Microstructure and hardness of aluminium alloy-fused silica particulate composite. Int J Innovative Res Adv Eng (IJIRAE) 1(5)
14. Hamouda AMS, Sulaiman S, Vijayaram TR, Sayuti M, Ahmad MHM (2007) Processing and characterization of particulate reinforced aluminium silicon matrix composite. J Achievements Mater Manuf Eng 25(2)
15. Bharath V, Auradi MV (2012) Preparation of 6061Al-$Al_2O_3$ metal matrix composite by stir casting and evaluation of mechanical properties. Int J Metall Mater Sci Eng 2(3):22–31
16. Kleme SA, Reponen PK, Liimatainen J, Hellman J, Hannula SP (2006) Abrasive wear properties of metal matrix composites produced by hot isostatic pressing. Proc Estonian Acad Sci Eng 12(4):445–454
17. Wakeel S (2017) Fabrication and mechanical properties of aluminium composites. Scholar-Press, Omniscriptum Publication Group, Germany. ISBN 978-3-639-71638-2
18. Roy D, Ghosh S, Basumallick A, Basu B (2006) Preparation of Ti-aluminide reinforced in situ aluminium matrix composites by reactive hot pressing. J Alloy Compd 436(1–2):107–111. https://doi.org/10.1016/j.jallcom.2006.07.017
19. Huo H, Woo KD (2006) In situ synthesis of $Al_2O_3$ particulate reinforced Al matrix composite by low temperature sintering. J Mater Sci 41:3249–3253
20. Debnath S, Roy S, Pramanick AK (2020) An exploratory comparative study of fabricated silica–aluminium metal matrix composites with casted aluminium-silicon alloys. JPCS 1579(012014):1–6

# Cost Optimization for Transportation Using Linear Programming


**A. Vamsikrishna, Vigneshwar Raj, and S. G. Divya Sharma**

## 1 Introduction

A company's transportation services and methods are really important in building a larger customer group and if an effective logistics or transportation model is designed then it can make a really good turnover for the company. Jonsson [1] (a logistics and supply chain expert) claim that 10–30% of turnover or profit can be made by optimizing the direct cost section of the logistics department. In this present situation where the population is increasing drastically and where the world is becoming a global village, it is really important for a company to have a cost-efficient and time-efficient transportation system which strives to produce its services to each and every corner of the world.

Since transportation is a very important key factor which plays a major role in the growth of a company, many logistics and supply chain experts have researched various aspects of the transportation system. Ronald et al. [2] have generated a genetic algorithm that considers the geographic information system (GIS) which solves problems regarding the transportation routes. Dorer and Calisti [3] have worked on the concept of adaptive transportation network which automatically optimizes the existing transportation system accordingly. Authors of [4] have discussed various methods and aspects of linear programming and its applications. In [5], Chandrakantha has provided a solution for optimization problems using the EXCEL solver option. Jonsson [1] have discussed logistics and supply chain management and the part which deals with direct costing in logistics was really helpful in optimizing the transportation system and reducing its cost. Caris et al. [6] have researched intermodal freight transport systems and have provided solutions considering routes,

A. Vamsikrishna · V. Raj · S. G. Divya Sharma (✉)
Department of Mechanical Engineering, Amrita School of Engineering, Amrita Vishwa Vidyapeetham, Bengaluru, India
e-mail: sg_divya@blr.amrita.edu



K. Jha et al. (eds.), *Recent Advances in Sustainable Technologies*,
Lecture Notes in Mechanical Engineering,
https://doi.org/10.1007/978-981-16-0976-3_2

climate, and the traffic parameters. Authors of [7] have mainly concentrated on increasing the profits of a company by working on their transportation model using linear programming method. Authors of [8] have worked on a transportation model where mosquito coils have to be transported from warehouse to distributors and they provided a cost-efficient transportation model using EXCEL solver function. Tatavarthy and Sampangi [9] have worked on reverse supply chain and provided a better transportation model by incorporating genetic algorithms on reverse supply chain. Authors of [10] have worked on public transport fare and they have provided a solution for this by using a simulation which increased the operator profit and also benefited public transport commuters. Authors of [11] have focused on solving problems regarding fuzzy transportations where the need for a number of products is uncertain and they provided a solution for fuzzy transportations problems by generating an algorithm. Martínez-López et al. [12] focused on providing a motorways system of transportation for shipping companies considering the environmental conditions. Mathur et al. [13] have worked on providing a solution for fuzzy transportation problems by generating algorithms. Authors of [14] have worked on public transport networks and made a transportation model or design that used the ideology of integrated optimization that improved urban mobility. Sharma and Tatavarthy [15] have focused on working on a disaster management problem regarding how to optimize the supply chain of necessary needs during a disaster and they achieved this by surveying various papers. Mangala et al. [16] have discussed about operational excellence for a sustainable supply chain. Also, they have mentioned that integration of various technologies like blockchain, big data, etc., could help create a more efficient supply chain system.

In this paper, the cost of transportation was tried to be reduced to the cheapest transportation model while taking all the constraints into consideration during the process of designing the model. A model of a flavors and fragrance company had to be optimized which consisted of three plants, three warehouses, and nine markets, and the optimization of the transportation model was done using the EXCEL solver function.

## 2 Problem

The network consisted of three manufacturing units or the plants, three warehouses, and nine markets. The product flow was such that it was manufactured in the plants and sent to the warehouses and then from the warehouses it was sent to the market. Cost of transportation did not remain the same for every transport situation. The existing model in company approximately costed about Rs. 3,800,000 and was seeking for an improved model. Hence, out of all possible combinations, it was necessary to find the cheapest transporting route with the optimal quantities to be transported as it will benefit the company.

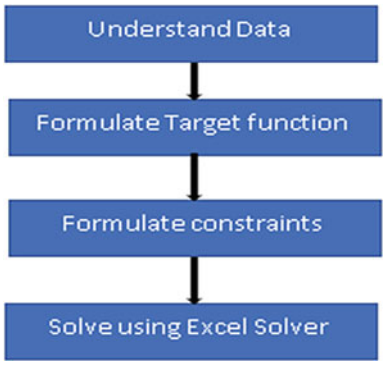


**Fig. 1** Methodology flowchart

## 3 Methodology

Initially, the transportation costs for each of the cases were collected and tabulated. Then the cost function or the target function was formulated for the given case. All the existing constraints were listed out and then the target function was minimized using EXCEL solver. Figure 1 shows a simple flowchart of the methodology adopted in solving the problem.

## 4 Results and Discussions

Since it is necessary to understand actual product flow, a network diagram was drawn as shown in Fig. 2.

In Table 1, the cost of distribution for various cases can be seen. $P1$, $P2$, and $P3$ stand for the three plants, $W1$, $W2$, and $W3$ stand for the three warehouses, and $M1$ to $M9$ stand for the nine markets. The cell corresponding to a plant and a warehouse denotes the transportation cost per unit from the plant to the warehouse while the cell corresponding to a market and a warehouse denotes the transportation cost per unit from the warehouse to the market. As mentioned above, this data was collected from a flavors and fragrance manufacturing industry.

In Table 2, the variables to be determined can be viewed, i.e., number of units to be transported. For example, $x(P1, W1)$ represents the no. of units to be transported from the plant 1 to the warehouse 1 while $x(W3, M8)$ represents no. of units to be transported from warehouse 3 to the market 8.

Further, the cost function was formulated. Cost function or the target function signifies the total transportation cost. In this case, it is nothing but the summation of the product of the corresponding cells of Tables 1 and 2, i.e.,

$$\{6 \times x(P1, W1) + 5 \times x(P2, W1) + \cdots + 3 \times x(W1, M8) + 2 \times x(W1, M9) + 3 \times x(P1, W2) + 4 \times x(P2, W2) + \cdots + 4 \times x(W2, M8) + 5 \times x(W2, M9)$$

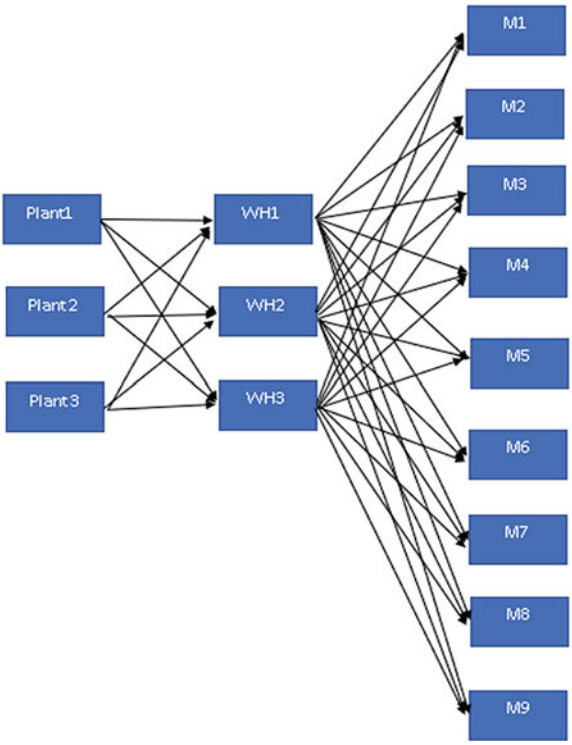


**Fig. 2** Network diagram of the product

**Table 1** Distribution cost of the product (per unit) in Rs

| Distribution costs per unit (Rs) | | | | | | | | | | | | |
|---|---|---|---|---|---|---|---|---|---|---|---|---|
| | $P1$ | $P2$ | $P3$ | $M1$ | $M2$ | $M3$ | $M4$ | $M5$ | $M6$ | $M7$ | $M8$ | $M9$ |
| $W1$ | 6 | 5 | 1 | 3 | 8 | 4 | 7 | 9 | 4 | 3 | 3 | 2 |
| $W2$ | 3 | 4 | 5 | 6 | 6 | 5 | 7 | 9 | 4 | 3 | 4 | 5 |
| $W3$ | 4 | 3 | 2 | 5 | 8 | 2 | 4 | 4 | 6 | 4 | 4 | 6 |

$$+ 4 \times x(P1, W3) + 3 \times x(P2, W3) + \cdots + 4 \times x(W3, M8)$$
$$+ 6 \times x(W3, M9)\} = F(x)$$

The Min $(F(x))$, i.e., minimum of the function $F(x)$ is to be determined. The values of $x(P1, W1)$, $x(P2, W1)$, …, $x(W3, M8)$, $x(W3, M9)$ for which the minimum value of $F(x)$ can be obtained will be the required solution. But for finding the minimum of $F(x)$, it is necessary to formulate all the constraints. Hence, the company gave the expected quantities from each market after performing the demand forecast. It can be seen in Table 3.

It is also necessary to note that every plant has a manufacturing capacity. Plants 2 and 3 can manufacture maximum 100,000 and 150,000 units per annum while the

**Table 2** No. of units to be transported

| No of units to be transported | | | | | | | | | | | | |
|---|---|---|---|---|---|---|---|---|---|---|---|---|
| | $P1$ | $P2$ | $P3$ | $M1$ | $M2$ | $M3$ | $M4$ | $M5$ | $M6$ | $M7$ | $M8$ | $M9$ |
| $W1$ | $x(P1, W1)$ | $x(P2, W1)$ | $x(P3, W1)$ | $x(W1, M1)$ | $x(W1, M2)$ | $x(W1, M3)$ | $x(W1, M4)$ | $x(W1, M5)$ | $x(W1, M6)$ | $x(W1, M7)$ | $x(W1, M8)$ | $x(W1, M9)$ |
| $W2$ | $x(P1, W2)$ | $x(P2, W2)$ | $x(P3, W2)$ | $x(W2, M1)$ | $x(W2, M2)$ | $x(W2, M3)$ | $x(W2, M4)$ | $x(W2, M5)$ | $x(W2, M6)$ | $x(W2, M7)$ | $x(W2, M8)$ | $x(W2, M9)$ |
| $W3$ | $x(P1, W3)$ | $x(P2, W3)$ | $x(P3, W3)$ | $x(W3, M1)$ | $x(W3, M2)$ | $x(W3, M3)$ | $x(W3, M4)$ | $x(W3, M5)$ | $x(W3, M6)$ | $x(W3, M7)$ | $x(W3, M8)$ | $x(W3, M9)$ |

**Table 3** Demand forecast values for the markets per annum

| Forecast values | |
|---|---|
| $M1$ | 50,000 |
| $M2$ | 40,000 |
| $M3$ | 100,000 |
| $M4$ | 80,000 |
| $M5$ | 30,000 |
| $M6$ | 35,000 |
| $M7$ | 45,000 |
| $M8$ | 70,000 |
| $M9$ | 65,000 |

plant 1 can manufacture up to 800,000 units per annum as it is a very big plant. It is also assumed that the number of units reaching the warehouse will leave the warehouse and go to the market for the simplicity of calculation.

Considering the plants, it is known that the sum of all the quantities from the plant must be less than or equal to its capacity. Hence, the formulation can be seen as follows in Eqs. (1a)–(1c).

$$x(P1, W1) + x(P1, W2) + x(P1, W3) \leq 800{,}000 \tag{1a}$$

$$x(P2, W1) + x(P2, W2) + x(P2, W3) \leq 100{,}000 \tag{1b}$$

$$x(P3, W1) + x(P3, W2) + x(P3, W3) \leq 150{,}000 \tag{1c}$$

With respect to the markets, the sum of all the quantities reaching the market must be equal to the forecast values of Table 3. So, in total, nine equations are obtained, one for each market as follows in Eqs. (2a)–(2i).

$$x(W1, M1) + x(W2, M1) + x(W3, M1) = 50{,}000 \tag{2a}$$

$$x(W1, M2) + x(W2, M2) + x(W3, M2) = 40{,}000 \tag{2b}$$

$$x(W1, M3) + x(W2, M3) + x(W3, M3) = 100{,}000 \tag{2c}$$

$$x(W1, M4) + x(W2, M4) + x(W2, M4) = 80{,}000 \tag{2d}$$

$$x(W1, M5) + x(W2, M5) + x(W3, M5) = 30{,}000 \tag{2e}$$

$$x(W1, M6) + x(W2, M6) + x(W3, M5) = 35{,}000 \tag{2f}$$

$$x(W1, M7) + x(W2, M7) + x(W2, M7) = 45{,}000 \tag{2g}$$

$$x(W1, M8) + x(W2, M8) + x(W3, M8) = 70{,}000 \tag{2h}$$

$$x(W1, M9) + x(W2, M9) + x(W3, M9) = 65{,}000 \tag{2i}$$

It should be noted that the number of quantities entering the warehouse equals the number of quantities leaving the warehouse. There are three warehouses and hence three equations are formulated for the same as follows in Eqs. (3a)–(3c).

$$\begin{aligned} x(P1, W1) + x(P2, W1) + x(P3, W1) = \{&x(W1, M1) + x(W1, M2) \\ &+ x(W1, M3) + x(W1, M4) \\ &+ x(W1, M5) + x(W1, M6) \\ &+ x(W1, M7) + x(W1, M8) \\ &+ x(W1, M9)\} \end{aligned} \tag{3a}$$

$$\begin{aligned} x(P1, W2) + x(P2, W2) + x(P3, W2) = \{&x(W2, M1) + x(W2, M2) \\ &+ x(W2, M3) + x(W2, M4) \\ &+ x(W2, M5) + x(W2, M6) \\ &+ x(W2, M7) + x(W2, M8) \\ &+ x(W2, M9)\} \end{aligned} \tag{3b}$$

$$\begin{aligned} x(P1, W3) + x(P2, W3) + x(P3, W3) = \{&x(W3, M1) + x(W3, M2) \\ &+ x(W3, M3) + x(W3, M4) \\ &+ x(W3, M5) + x(W3, M6) \\ &+ x(W3, M7) + x(W3, M8) \\ &+ x(W3, M9)\} \end{aligned} \tag{3c}$$

After defining all the constraints and the target functions, these were calculated in the EXCEL spreadsheet using existing functions like SUM, AVERAGE, etc. Further, these equations were solved using EXCEL solver by defining all the necessary inputs. Figure 3 shows the dialog box for EXCEL solver.

The cell that corresponds to the target function should be set as the objective. Since this is a cost function and is to be minimized, the radio button that says 'Min' was selected. As defined earlier, the LPP has a lot of constraints. These constraints need to be added in the 'Subject to the Constraints' box. Solving method should be chosen as 'Simplex LP'. After setting all these, the solve button was clicked.

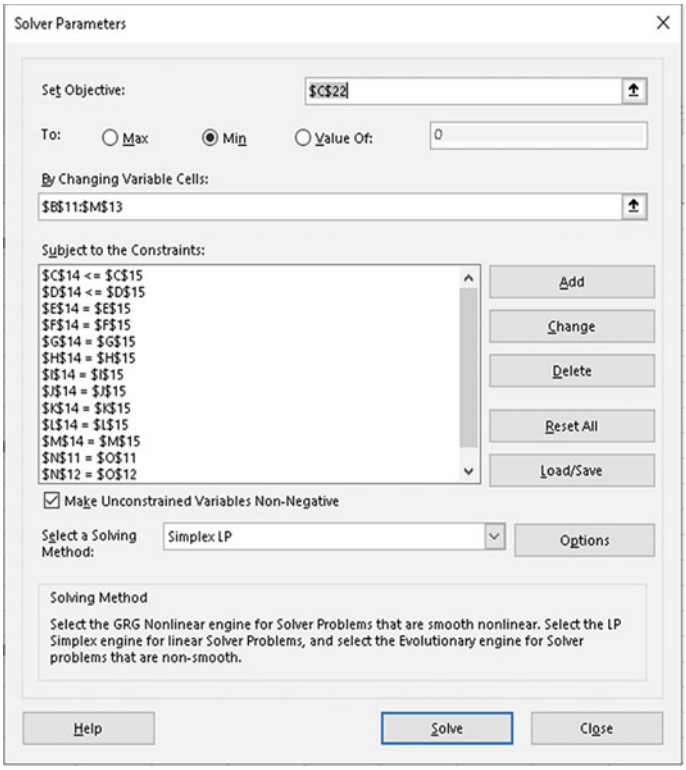


**Fig. 3** Solver parameter dialog box for solving the LPP

After the solutions are fount to converge, the values for optimal distribution quantity is obtained for the transportation from each plant to each warehouse and from each warehouse to each market as shown in Table 4.

For the above condition, the transportation cost estimation was Rs. 3,035,000. Previously as stated by the company, the cost was approximately Rs. 3,800,000. Therefore, savings of about Rs. 765,000 per annum was calculated if the new transportation model was adopted.

## 5 Conclusion

A transportation optimization model was developed. It consisted of three plants, three warehouses, and nine markets and was optimized using the EXCEL solver function to design the transportation model. The transportation cost was reduced in the best possible way by using linear programming. The cost obtained was Rs. 3,035,000. A savings of about Rs. 765,000 per annum was estimated comparing the cost of new

**Table 4** Optimal distribution strategy

| Optimal distribution strategy (No. of units) | | | | | | | | | | | | |
|---|---|---|---|---|---|---|---|---|---|---|---|---|
| | $P1$ | $P2$ | $P3$ | $M1$ | $M2$ | $M3$ | $M4$ | $M5$ | $M6$ | $M7$ | $M8$ | $M9$ |
| $W1$ | 0 | 0 | 150,000 | 50,000 | 0 | 0 | 0 | 0 | 0 | 0 | 35,000 | 65,000 |
| $W2$ | 155,000 | 0 | 0 | 0 | 40,000 | 0 | 0 | 0 | 35,000 | 45,000 | 35,000 | 0 |
| $W3$ | 110,000 | 100,000 | 0 | 0 | 0 | 100,000 | 80,000 | 30,000 | 0 | 0 | 0 | 0 |

transportation model to that of the previous one. This paper further creates scope for research on designing transportation models and solving them with the help of linear programming method which simplifies the cost optimization technique. However, the scope of the work extends to consider multivariable problems and use EXCEL solver to consider different optimization techniques to solve multiple problems related to transportation.

## References

1. Jonsson P (2008) Logistics and supply chain management. McGraw-Hill, New York
2. Ronald S, Kirkby S, Eklund P (1997) Multi-chromosome mixed encodings for heterogeneous problems. In: Proceedings of 1997 IEEE international conference on evolutionary computation (ICEC' 97). IEEE, pp 37–42
3. Dorer K, Calisti M (2005) An adaptive solution to dynamic transport optimization. In: Proceedings of the fourth international joint conference on autonomous agents and multiagent systems, pp 45–51
4. Eiselt HA, Sandblom CL (2007) Linear programming and its applications. Springer Science & Business Media, Berlin
5. Chandrakantha L (2008) Using EXCEL solver in optimization problems. Mathematics and Computer Science Department, New York
6. Caris A, Macharis C, Janssens GK (2008) Planning problems in intermodal freight transport: accomplishments and prospects. Transp Plan Technol 31(3):277–302
7. Fagoyinbo IS, Akinbo RY, Ajibode IA, Olaniran YOA (2011) Maximization of profit in manufacturing industries using linear programming techniques: Geepee Nigeria Limited. Mediterr J Soc Sci 2(6):97–97
8. Khan MA (2014) Using linear programming transportation cost optimization. In: International conference on mechanical, industrial and energy engineering, pp 2241–2245
9. Tatavarthy SR, Sampangi G (2015) Solving a reverse supply chain TSP by genetic algorithm. In: Applied mechanics and materials, vol 813. Trans Tech Publications Ltd., Switzerland, pp 1203–1207
10. Kaddoura I, Kickhöfer B, Neumann A, Tirachini A (2015) Agent-based optimisation of public transport supply and pricing: impacts of activity scheduling decisions and simulation randomness. Transportation 42(6):1039–1061
11. Chandran S, Kandaswamy G (2016) A fuzzy approach to transport optimization problem. Optim Eng 17(4):965–980
12. Martínez-López A, Sobrino PC, González MM (2016) Influence of external costs on the optimisation of container fleets by operating under motorways of the sea conditions. Int J Shipping Transp Logistics 8(6):653–686
13. Mathur N, Srivastava PK, Paul A (2018) Algorithms for solving fuzzy transportation problem. Int J Math Oper Res 12(2):190–219
14. Fuchs F, Corman F (2019) An open toolbox for integrated optimization of public transport. In: 2019 6th international conference on models and technologies for intelligent transportation systems (MT-ITS). IEEE, pp 1–7
15. Sharma SD, Tatavarthy SR (2019) Development of optimized solution for a generic disaster management problem through construction of responsive supply chain a review. In: AIP conference proceedings, vol 2148, no 1. AIP Publishing LLC, USA, p 030049
16. Mangla SK, Kusi-Sarpong S, Luthra S, Bai C, Jakhar SK, Khan SA (2020) Operational excellence for improving sustainable supply chain performance. Resour Conserv Recycl 162:105025

# Experimental Investigation of Semi-elliptical Arc Groves on Piston Crown of Direct Injection Diesel Engine Using Apricot Oil

**Sk. Mohammad Shareef, A. L. N. Arun Kumar, and T. Venkatesh**

## 1 Introduction

In this project, experimental work is executed on single cylinder 4-stroke DI diesel engine with semi-hemispherical bowl in the piston to study the effect of groves on incidental fluid flow and their by the engine performance. It is proposed to provide ellipsoidal arc grooves are provided at the periphery of the piston crown also the result of increasing the quantity of grooves on piston with using the apricot seed oil as biodiesel.

Vijaya Kumar et al. [1] have conducted experiment on direct injection diesel engine at constant speed with 20:1 as the compression ratio and 300 bar as injection pressure at different injection timings. Performance characteristics like mechanical efficiency break thermal efficiency and emissions like HC, NO*x* are calculated and shown in results.

Mamilla [2] have conducted experiment on direct injection diesel engine by changing the combustion chamber design by using different blends of Jathropa methyl ester as alternative fuel and results are shown.

Swarna Kumari et al. [3] have done research on direct injection diesel engine for calculating the performance and emissions characteristics by using sunflower oil as biodiesel and the results are shown.

Subba Reddy et al. [4] have conducted experiment on direct injection diesel engine using cotton seed oil as biodiesel by changing injection pressures and concluded that at 200 bar injection pressure with 20% of biodiesel engine have better performance and less emissions which are shown in results.

Nurun Nabi and Najmulhoque [5] have conducted experiment on direct injection diesel engine by using linseed oil as biodiesel and also done production biodiesel from

Sk. Mohammad Shareef (✉) · A. L. N. Arun Kumar · T. Venkatesh
CVR College of Engineering, Hyderabad, Telangana 501510, India



K. Jha et al. (eds.), *Recent Advances in Sustainable Technologies*,
Lecture Notes in Mechanical Engineering,
https://doi.org/10.1007/978-981-16-0976-3_3

**Table 1** Engine specifications

| Particulates | Specifications |
|---|---|
| Model | AV1 |
| Make | KIRLOSKAR |
| Engine type | Single cylinder, four strokes, water cooled Compression ignition engine |
| Bore | 80 mm |
| Stroke | 110 mm |

linseed crude oil and concluded that with 20% of biodiesel having high performance and less emissions.

## *1.1 Experimental Setup*

The experiment is carried out on single cylinder diesel engine with hemispherical bowl. The specifications of the engine are given in Table 1.

For analyzing the emissions parameters, five gas analyzer is used.

## *1.2 Piston Modification*

Piston is the main part of the engine. The combustion parameters are depending on the combustion chamber design which will increase the turbulence leads to increase the efficiency. In this work, the normal piston is modified as elliptical arc groves piston by adding the semi-elliptical shapes on the crown of the hemispheric bowl of the piston. In this work, three ellipsoidal arc groves at 180°, 120°, and 72° on the piston with different widths 10 mm, 8 mm, and 6 mm are created on three pistons of 80 mm diameter and continuing the depth of 3 mm prepared by CNC machine.

Three pistons of elliptical arc grooves at 180°, 120°, and 72° are shown in Fig. 1.

## *1.3 Alternative Fuels*

Apricot seed kernel oil was from apricot, which has been available in world. The main combination of Apricot seed kernel oil like some edible oil is acyl glycerol, which is the ester of three fatty acids and one glycerol. The fatty acid composition of apricot seed kernel oil is given. Apricot seed kernel oil methyl ester has been turned as an alternative fuel by transesterification process. B10 represents the 10% apricot oil and 90% diesel.

Table 2 shows that different properties of apricot seed oil which is used as

(a) (b) (c)

**Fig. 1** Two, three, and five groove elliptical pistons

**Table 2** Properties of apricot seed oil

| Pproperties | Diesel | Apricot | B10 |
|---|---|---|---|
| Density (kg/m$^3$) | 831 | 884.3 | 848.78 |
| kinematic viscosity | 2.4 | 4.92 | 2.81 |
| Calorific values (kJ/kg) | 4200 | 39,952 | 41,528 |
| Fire point (°C) | 68 | 120 | 76 |
| Flash point (°C) | 51 | 111 | 67 |

alternative fuel.

### *1.4 Nomenclature*

- Normal: Normal piston with apricot oil (10% Apricot oil + 90% diesel).
- 2EGPA: Two semi-ellipsoidal arc groove piston with apricot oil (10% Apricot oil + 90% diesel).
- 3EGPA: Three semi-ellipsoidal arc groove pistonwith apricot oil (10% Apricot oil + 90% diesel).
- 5EGPA: Five semi-ellipsoidal arc groove piston with apricot oil (10% Apricot oil + 90% diesel).

## 2 Results and Discussions

The performance parameters are measure in the form of brake specific fuel consumption, brake thermal efficiency, exhaust gas temperature. The emissions of the engine

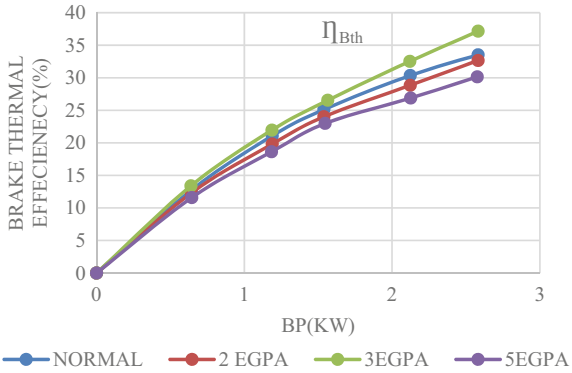


**Fig. 2** Brake power versus brake thermal efficiency with biodiesel

are measured in percentage of HC and NO*x*. The results acquired by the elliptical arc grooves pistons with apricot biodiesel are compared with results of the normal piston.

## *2.1 Brake Thermal Efficiency*

Figure 2 represents the comparison of brake thermal efficiency of different pistons with biodiesel. It is clear from the graph that 3EGPA high brake thermal efficiency as compared to other pistons. The brake thermal efficiency is found to increase by 11.11% for different pistons with pure biodiesel of engine.

## *2.2 Brake Specific Fuel Consumption*

Figure 3 represents the comparison of BSFC of conventional engine with biodiesel for different pistons. It is observed from graph that 3EGPA has lower BSFC compared to other pistons. The BSFC is reduced about 9.49% compared to other pistons with biodiesel.

## *2.3 Mechanical Efficiency*

Figure 4 represents the variation of mechanical efficiency with load of different pistons. There is increase in mechanical efficiency for 3EGP with biodiesel compared to other pistons with biodiesel.

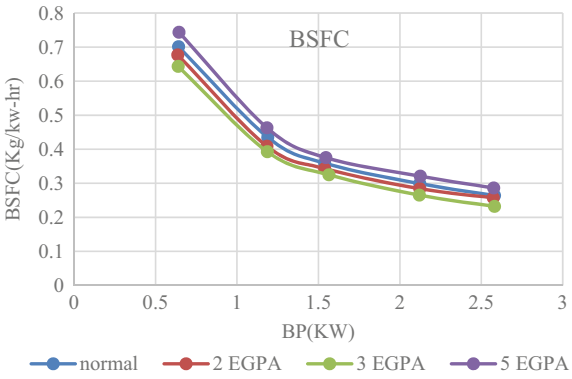


**Fig. 3** Brake power versus brake specific fuel consumption with biodiesel

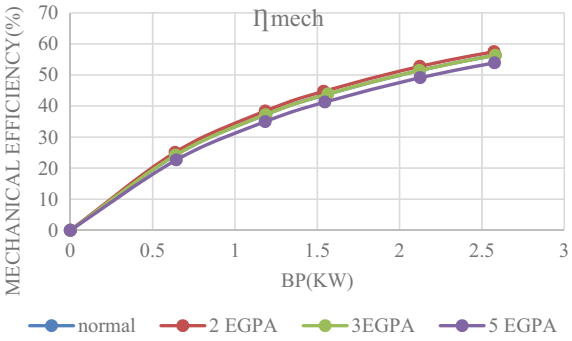


**Fig. 4** Brake power versus mechanical efficiency with biodiesel

## *2.4 HC Emissions*

Figure 5 shows the HC emissions of diesel engine by using apricot seed oil as alternative fuel for different pistons. By using 3 elliptical grooves on piston turbulence is created and proper combustion is done, due to that HC emissions are less. The

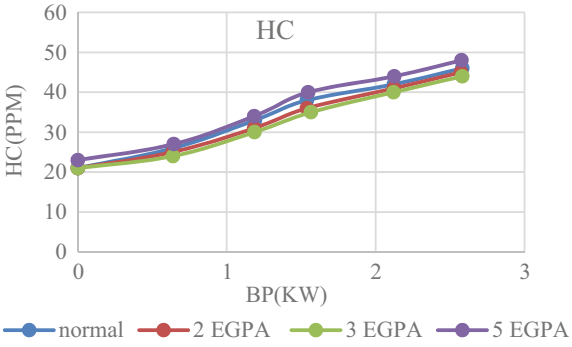


**Fig. 5** Brake power versus HC emissions with biodiesel

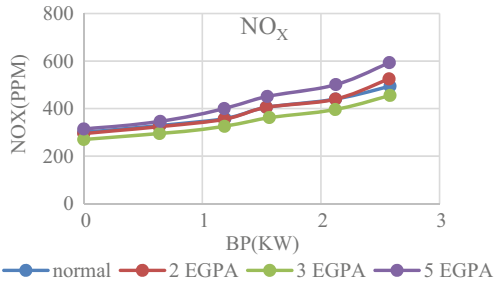


**Fig. 6** Brake power versus $NO_x$ emissions with biodiesel

graph shows that HC emission for 3EGP with alternative fuel has less compared to other pistons.

### *2.5 NOx Emissions*

Figure 6 shows the variation of $NO_x$ emissions with load for different pistons by using alternative fuel. It is clear from the graph that 3 EGP has low $NO_x$ emissions compared to other pistons, and this is happened due to low temperatures produced inside the combustion chamber.

## 3 Conclusions

The experiment is carried out on single cylinder direct injection diesel engine with 2, 3, and 5 elliptical grooves on piston crown by using apricot seed oil at load of 1.5 kW. The results may be summarized as follows.

1. Break thermal efficiency is increased by 11.11% by changing the normal piston with three semi-elliptical arc groves piston with biodiesel (3EGPA).
2. Break specific fuel consumption is decreased by 9.49% for 3EGPA piston compared to normal piston.
3. HC emissions reduction is considerably a lot below normal piston, but it is reduced by 7.89% for changed pistons (3EGPA) by adding biodiesel.
4. The spiral grooves on changed piston slightly reduced the compression ratio that control the high temperature of combustion and proper mixture facilitate to reducing the $NO_x$ throughout the combustion. It is determined that the Nox emissions are reduced 10.61% by using 3EGPA piston instead of normal piston.
5. Mechanical efficiency of the normal piston by 3EGPA piston has increased slightly.

By considering all parameters, three ellipsoidal grooves piston with biodiesel (3EGPA) is better than normal, two and five ellipsoidal grooves piston with biodiesel (normal, 2EGPA, 5EGPA).

## References

1. Vijaya Kumar K, Babitha D, Srinivasa Raghavan K, Shailesh P (2018) Investigation of diesel engine performance with design modifications in piston.: inducing turbulence by swirl. Int J Mech Eng Rob Res 7(5):495–499
2. Mamilla VR (2013) Effect of combustion chamber design on a DI diesel engine fueled with jatropha methyl esters blends with diesel. J Procedia Eng 64:479–490
3. Swarna Kumari A, Penchalayya CH, Sita Rama Raju AV (2013) Performance evaluation of diesel engine with safflower oil. J Eng Stud Res 19(2):63–69
4. Subba Reddy CV, Eswara Reddy C, Hema Chandra Reddy K (2012) Effect of fuel injection pressures on the performance and emission characteristics of D. I. diesel engine with biodiesel blends cotton seed oil methyl ester. Int J Res Rev Appl Sci 13(1):139–149
5. Nurun Nabi Md, Najmulhoque SM (2008) Biodiesel production from linseed oil and performance study of a diesel engine with diesel biodiesel. J Mech Eng 39(1):40–44

# Hydrogen Storage Techniques for Stationary and Mobile Applications: A Review


**Aasim Akif Dafedar, Shivam Sudarshan Verma, and Aman Yadav**

## 1 Introduction

The global emission level is reaching record-high levels with no sign of peaks that have forced the climate action summit to make concrete and enhanced contributions to curb emissions of about 40% by the decade end net-zero carbon foot print by 2050 [1]. The research carried on by the University of Michigan portrays that the annual cost of running a gasoline-based vehicle is twice the cost of an electrically powered vehicle. Hydrogen though being the most abundant element in nature is present in forms of compounds and forms of hydrocarbons. Hydrogen has almost thrice the heating value compared to diesel, and have no emission. Hydrogen-based fuel cells are the most efficient solutions for the clean delivery of electricity for automobiles with a by-product of water. However, it needs a reliable source of transport and storage for both on-board and stationary applications [2]. The average consumption by humans is about 2 kW/person. The production of hydrogen by various methods cost almost three times as mining of fossil fuels. The modern world is keenly interested to produce hydrogen using methane and algae. The critical point of storage remains a barrier for society to accept hydrogen as a primary fuel for automobiles and industrial applications [3]. The generation of electricity required to convert all automobiles on-road as of today in a country like India where electricity is majorly generated using thermal power plants will increase passive pollution than the primary emission from gasoline-based vehicle itself [4]. This review paper gives insight on some cutting edge methods of hydrogen storage for both vehicles and stationary applications.

A. A. Dafedar (✉) · S. S. Verma · A. Yadav
School of Mechanical Engineering, Lovely Professional University, Phagwara, Punjab, India

S. S. Verma
e-mail: shivam.19473@lpu.co.in



K. Jha et al. (eds.), *Recent Advances in Sustainable Technologies*,
Lecture Notes in Mechanical Engineering,
https://doi.org/10.1007/978-981-16-0976-3_4

## 2 High-Pressure Cylinder

The work [Wt.] required theoretically for isothermal compression of hydrogen ($H_2$) is given by

$$G = RT.\ln(P_2/P_1) \tag{1}$$

$R$—Gas constant (8.314 J $mol^{-1}$ $k^{-1}$), $T$—Absolute temp, $P_2$—End pressure, $P_1$—Starting pressure.

The types of tanks used for hydrogen storage depend on the material combination incorporated in their design and fabrication. There are four types of tanks having varying pressure ranges for various applications based on materials. Type 1 tank is one of the oldest pressure vessels to contain compressed gas [5]. It is made up of all metal and metallic alloys such a steel and aluminum alloys [6]. These tanks have a pressure capacity of about 300 bar and are used for CNG, LPG, and other liquefied fuels for various applications [7]. Type 2 tank has metal construction over the most surface with hoop wound composite wrap over hoop direction. It has a pressure capacity of about 200 bars. Metallic alloys and composites such as carbon fiber were used for the constructional purpose [8]. Type 3 tanks have metallic liners in innermost layers and complete composite wrap over the entire surface. It has a pressure capacity of about 700 bars. These tanks are being currently used to store hydrogen at hydrogen fuel plants and stationary industrial applications. Type 4 tank having an inner liner and outer cover both made of high-density composite fibers is a cutting edge storage device with the highest weight to fuel storage efficiency is being used in mobile applications such as Mirai by TOYOTA [9] (Fig. 1).

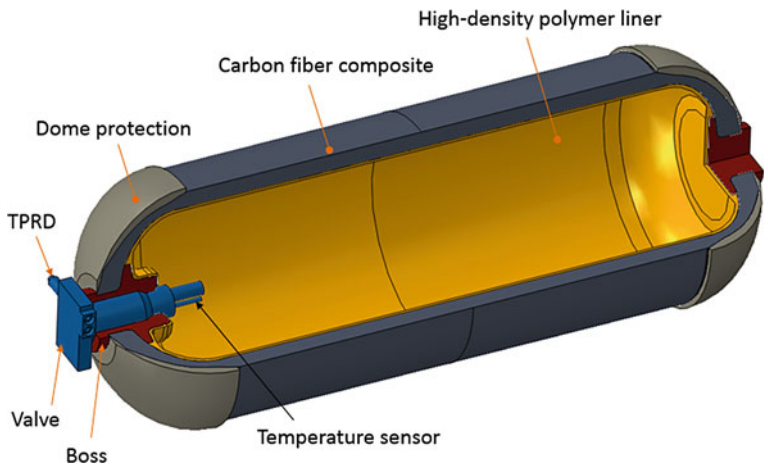


**Fig. 1** Hydrogen storage device. Copyright—Process Modeling Group, Nuclear Energy Division. Argonne National laboratory [ANL] [10]

At 800 bar, the gravimetric density of a high-pressure gas cylinder made up of using a lightweight composite cylinder is 13%; hence, the volumetric density of 36 kg $m^3$. Among various designs of pressure tanks using hoop wound geometry for industrial applications, the technical efficiency of such a cylinder is 0.25 $m^3$/kg using a composite cylinder. This has 55% increased efficiency then monolithic conventional cylinder-like steel and aluminum alloy. Hoop wound design is easy to fabricate and cost efficient; it is preferred more over other designs for storage applications [9]. Wrapping made up of composite materials is applied along the parallel section, i.e., the vertical walls of the cylinder. In fully wound design composite, lightweight material covers the entire external surface of the cylinder using Fiber-reinforced plastic (CRFP) lamination method [6]. The structure of the tank in Toyota Mirai helped to improve the weight effectiveness of the entire system by approximately 15% compared to Toyota FCHV-adv.

Plastic liners at the innermost layer to seal in hydrogen gas covered by stay composite fiber-reinforced plastic layer are capable to withstand the required pressure. This system is further covered by GFRP, layer providing impact resistance and protection. Aluminum bosses are present at both ends of the plastic liner with a valve fitting at the top end. The weight of newly developed tanks was reduced by improving the CFRP layer and reduction of the amount of material used. Conventionally laminated CFRP tanks used three types of winding hoop, low angle helical, and high angle helical central helical winding wrapped over the centric part of tanks at an angle of 70. Hence, reinforcement efficiency is reduced leading to reduced FOS. However, using modification in a new structure, 25% of total laminated structure—high cycle helical winding was eliminated. Hoop winding was used to strengthen the central region of the tank conventionally in the innermost layer of the tank having high-stress generation. It helped to have 20% of weight reduction than the conventional laminated method. The Mirai tank with internal volume of about 122.4 L having volumetric energy density to be as high as 4.90 MJ/L. The hydrogen tanks require a high-pressure capacity of around 700 bars to 800 bars hence needs extremely robust and hence the design of tanks and its size remain critical points of discussion in mobile applications. High pressure is always at risk especially in mobile applications such as a trailer or commercial 4 wheeler due to the possibility of a crash and other concerns, even though the composite fibers like carbon fiber and other composites may not be toxic in nature.

## 3 Metal–Organic Frameworks [MOFS]

Storage of hydrogen using effective and highly efficient technology requires high storage capacity and fast kinetics. Hydrogen can be stored in solid and materials using various methods such as 1. Chemical reactions between host metal and hydrogen forming chemical compounds. 2. Adsorption of hydrogen in host materials 3. Cage occupancy where hydrogen is trapped in cages. Sorption and desorption rely on a critical feature of the total surface area of MOF and its interaction with hydrogen

[11]. MOFs have been synthesized with metal and organic building blocks from solvothermal reactions in an organic solvent having boiling points near about 90 to 130 degrees [12]. The solubility restrictions for the results can be eliminated using high temp reactions condition of solvothermal synthesis [13]. Using various appropriate combinations of metal ions and ligands, a new MOF containing two kinds of metal ions is obtained using two different metal ions and ligands. The framework structure of MOF is depended on the type of solvent, reaction temperature, rate of crystal growth, and most importantly on organic building blocks [14]. Various metallic ions used for the synthesis of MOFs are zinc Cu, Mn, Cr, and Al. Carboxylic acids and hetero-cyclic compounds can be used as organic building blocks for MOFs [15].

## *3.1 Carboxylate-Based MOFs (Also Known as Low Temp (77 K) MOFs)*

MOFs are synthesized by ions of metals and carboxylic acids having a solvothermal reaction. Various metal sources are used for the synthesis of metal–organic frameworks such as Zn, Cu, Mn, CR, Co, Al, alkali metals, and lanthanide metals. Pore volumes and the surface area play a vital part in the hydrogen adsorption capacity, the type of metal ions also has an influence on it. MOFs are known for high surface area and large pore volumes possessing exclusive hydrogen uptake capacity was constructed using $Zn_4O$ and tricarboxylate ligands. Isoretricular MOFs having high surface area and large pore volumes as well were prepared with dicarboxylic acids. At a low temp of 77 K hydrogen, adsorption depends upon high pressure and the surface area incorporated with MOFs [16].

## *3.2 Zn-Based MOFs*

MOF 5 has a crystal structure of inorganic [Zn4O] 6 groups which are joined to the octahedral array of benzene-1,4-dicarboxylate (BDC) groups to form the frameworks [17]. 4.5% weight hydrogen adsorption have been obtained at 77 K and 0.7 bar. Later on, after numerous investigations at 77 K and 50 bar hydrogen adsorption at 4.5–5.2 wt% as revised by independent groups. MOFs 177 [18] has the highest hydrogen uptake amount 7.2–7.5% at recorded 77 K and 70 bar. The chemical formula of MOF 5 is $C_{24}H_{12}O_{13}Zn_{4.}$

### 3.3 Cu-Based MOFs

The very first Cu-based MOFs, HKUST1 also called CuBTC was invented by Williams et al. however MOF 5 had a higher $H_2$ adsorption amount than HKUST1. This happened due to the adsorption hydrogen amount at low passage is dependent on the binding stay of the MOFs and surface area determines the amount of the adsorbed in high pressure [19]. The thermal conductivity ($K$) of copper is 400 W/(m K) or 0.99 (cal/s)/(cm2C/cm), this low conductivity adds challenges for the thermodynamics management in the MOFs storage system. Structural impacts on which the hydrogen storage capacity are depended on various factors include surface area, hydrogen adsorption enthalpy, sensitivity to airborne moisture, pore size, and structural defects (Fig. 2) [20].

## 4 Metal Hydrides

Metal hydrides are being one of the promising ways to store hydrogen with increased density compared to compression and liquefaction. It is packed with H–H distance of as minute as 2.1 Angstroms, concluding the hydrogen density of 170 g $H_2$/L which is significantly higher than the density of liquid hydrogen by approximately twice. Metal hydrides can be broadly classified based on the nature of the sorption mechanism and the identity of the material. Conventional metal hydrides, complex hydrides, chemical hydrides, and sorbents round off to be distinguished classification of Hydrides used for hydrogen storage.

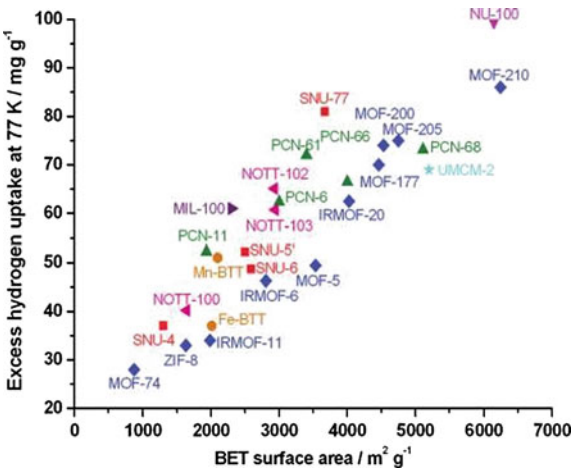


**Fig. 2** Graph representing excess HP hydrogen uptake versus BET surface area. Reprinted from Ref. [15]. Copyright—2011. https://doi.org/10.1021/cr200274s [pubs.acs.org/CR]

### 4.1 Conventional (Simple Metal Hydrides)

$$M + (x/2)H_2 = MHx \tag{2}$$

M—Metal alloy, i.e., hosts metallic alloy for hydrogen storage MHx—Metal hydride.

One of the most referred conventional metal hydrides $LnNih_6$ possesses the volumetric capacity, reversibility, thermodynamic property, kinetics, and efficiency to be satisfactory [21]. However, gravimetric capacity has significant challenges toward achieving DOE targets. Hence, gravimetric density of these metal hydrides is comparatively low, whereas H bounding is either too weak or too strong for addition or reduction of hydrogen [22].

### 4.2 Metal Borohydride

The gravimetric capacity of metal borohydride is about 14.9–18.5 wt%. The volumetric capacity reported is about 9.8–17.6 MJ/L [23]. These reported values indicate them having the potential for storing hydrogen. According to recorded data at 105 bar and –143c, a member of the borohydride family, Nanoporous hybride contains 17.4 wt% of hydrogen [24].

### 4.3 Complex Hydrides

Complex hydrides are considered as the chemisorptive hydrogen ($H_2$) stage mechanism. They liberate hydrogen endothermatically. Lithium borohydride, i.e., [$LiBH_4$], sodium alante, i.e., ($NaAlH_4$) and lithium amide ($LiNH_2$) even known as lithium azanide are examples of complex hydrides. However, complex hydrides initially were not considered for irreversible hydrogen storage due to the inability of both reduction and adsorption of hydrogen over cycles because of the thermodynamics involving unfavorable hydrogen reaction and kinetic associated with it which was slow than required/expected [25]. Novel approaches that emerged in the last few years to improve thermodynamic and kinetic properties have spiked interest in complex hydrides for both mobile and stationary storage applications. Schlesinger and Brown in 1940 reported of first pure alkali metal tetrahydroboride, synthesizing lithiumetrahydroboride ($LiBH_4$) [26] by the reaction of ethilithium and diborane ($B_2H_6$).

$$2MH + B_2H_6 - 2MBH_4[M - Li, Na, K,etc.] \tag{3}$$

## 4.4 Sorbents

Hydrogen can be stored using physiorptive attraction in porous lightweight materials (sorbents) involving molecular hydrogen having hydrogen stored equivalents proportional to the material's surface areas. Carbon-based materials and metal organics frameworks are engaged as two different types of sorbents to store hydrogen [27].

## 4.5 Chemical Hydrides

They are almost similar to complex hydrides and possess characteristics to store large quantities of hydrogen in terms of both mass and volume; they are intended for a single-use or one-time use and later, the by-product must be removed for off-board regeneration in mobile applications [28]. Promising examples of chemical hydrides are the thermal decomposition of ammonia borane also named as amminetrihydridoboron ($NH_3BH_3$) and the hydrolysis of sodium borohydride also named as sodium tetrahydroborate ($NaBH_4$). The major disadvantage of chemical hydrides is irreversible and energy efficiency compared to other storage processes although some combination may possess reasonable rate of kinetics and being thermoneutral but majorly are exothermic in nature and tends to require heat management systems [29].

## 4.6 Hydrogen Storage in Graphene

Using the physisorption method or forming chemical bonds with the c atoms, i.e., chemisorption method, the hydrogen can be stored on single graphene layers [30]. For physisorption, hydrogen is in molecular form, and the binding energy evaluated for $H_2$ was around in a range of 0.01–0.06 eV. Although the binding of molecular hydrogen being weak requiring low temperature and high pressures, the London dispersion forces are had to represent. $H_2$ forms a mono-layer uniformly over the graphene sheet with a GD of 3.3% [31]. The VD is however dependent on compacting graphene sheets which are conductive in nature in complex structures. Chemisorption of atomic hydrogen is favorable than molecular hydrogen ($H_2$) on graphene as it requires dissociative adsorption [32]. Experimental work shows one-sided hydrogenation of graphene sheets forming graphane and reversibility using annealing. Nanostructure-based graphene or 3D assemblies as multilayers of graphene are considered over the quasi-2D layer since its VD is not well defined after ultrasonic exfoliation of liquid, at 25 bar and ambient temp the reported value of GD was 2.7% chemical functionalization is one of the proposed theoretical ways to increase hydrogen adsorption in ambient temp and conditions using alkali atoms like each

Li adsorbed on graphene and nanostructured graphene can absorb 4 $H_2$ molecules, whereas GD amounted for about 10 wt% [33].

## 5 Conclusion

The amount of hydrogen stored is depended on the process and its nature such as high pressure compressed gas in an HP cylinder, or physiosorption and chemisorption on Graphene sheets, or in terms of compounds and chemical combinations using elements like k, Na, Cr, Cu, or aluminum. The storage capacity of metal hydrides ranges on factors such as type of metal, pore volumes, and total surface area. The recent adaptation in the HP cylinder using the hoop wound cylinder promises the weight reduction and satisfies the weight-to-mass storage capacity needed for automobile applications. However safety is always a major concern while dealing with such highly volatile elements; hence, the HP cylinder is still least favored among scientists, and chemical methods like metal hydrides and MOFs are gaining popularity due to high weight percent storage. Graphene has also become a potential hydrogen storage along with MOFs giving chemical storage method an edge over conventional cylinder methods. The $H_2$ capacities of various MOFs decrease as temperature increases to ambient conditions. A synthetic method needs to be developed for the construction of metal–organic frameworks having a high interactive surface with large-sized pore volumes, generating surface area of large size with low dead volumes. Just having large surface area incorporated MOFs cant be classified for $H_2$ storage, they need to chemically stable under a slight variation in pressure and temperature many MOFs possess good adsorption capacities at a low temp of 77 K or 85 K. MOFs need to have high isosteric heat at ambient temperature for high storage of $H_2$ along with high pore volumes and larger surface areas. Some MOFs have positive values regarding the isosteric heat values but had pore volumes and surface areas to be too low to store a large amount of $H_2$. With a comparison based on safety, Gravimetric capacity, and volumetric capacity of the different mentioned and discussed methods its clear that interest leans toward formulating promising chemical storage methods over physical. We expect highly stable MOFs and high storage capacity tanks of lightweight composites and other promising methods to store hydrogen in the upcoming years which will revolutionize the energy industries of both the private and commercial sectors. An economy can be envisioned with paced research and advancements for storage of hydrogen as an alternate fuel.

## References

1. Stocker TF, Qin D, Plattner G-K, Tignor M, Allen SK, Boschung J, Nauels A, Xia Y, Bex V, Midgley PM, IPCC (2013) Summary for policymakers. In: Climate change 2013. Cambridge University Press, Cambridge

2. Argonne National Laboratory (2009) Technical assessment of cryo-compressed hydrogen storage tank systems for automotive applications. U.S. Department of Energy, Oak Ridge
3. Singer S, Denruyter J-P, Yener D (2017) The energy report: 100% renewable energy by 2050. In: Towards 100% renewable energy. Springer, Cham
4. Saito S (2010) Role of nuclear energy to a future society of shortage of energy resources and global warming. J Nucl Mater 398:1–9
5. SAE International (2015) SAE J2600 compressed hydrogen surface vehicle fueling connection devices
6. Hua T, Ahluwalia R, Peng J-K, Kromer M, Lasher S, McKenney K, Law K, Sinha J (2010) Technical assessment of compressed hydrogen storage tank systems for automotive applications. Office of Scientific and Technical Information (OSTI), Oak Ridge
7. Mazloomi K, Gomes C (2012) Hydrogen as an energy carrier: prospects and challenges. Renew Sustain Energy Rev 16:3024–3033
8. Mizuno M, Ogami N, Negishi Y, Katahira N (2005) High pressure hydrogen tank for FCHV. JSAE Paper No. 84-05, pp 13–16
9. Yamashita A, Kondo M, Goto S, Ogami N (2015) Development of high-pressure hydrogen storage system for the Toyota "Mirai". SAE technical paper 2015-01-1169. https://doi.org/10.4271/2015-01-1169
10. Office of Energy Efficiency & Renewable Energy. https://www.energy.gov/eere/fuelcells/physical-hydrogen-storage
11. Millange F, Serre C, Guillou N, Ferey G, Walton RI (2008) Structural effects of solvents on the breathing of metal–organic frameworks: an in situ diffraction study. Angew Chem Int Ed 47:4100
12. He Y, Chen F, Li B, Qian G, Zhou W, Chen B (2018) Porous metal-organic frameworks for fuel storage. Coord Chem Rev 373:167–198
13. Yan Y, Yang S, Blake AJ, Lewis W, Poirier E, Barnett SA, Champness NR, Schröder M (2011) A mesoporous metal-organic framework constructed from a nanosized C 3-symmetric linker and [Cu 24 (isophthalate) 24] cuboctahedra. Chem Commun 47:9995
14. Yuan D, Zhao D, Sun D, Zhou H-C (2010) An isoreticular series of metal-organic frameworks with dendritic hexacarboxylate ligands and exceptionally high gas-uptake capacity. Angew Chem Int Ed 49:5357
15. Suh MP, Park HJ, Prasad TK, Lim D-W (2012) Hydrogen storage in metal–organic frameworks. Chem Rev 112:782–835
16. Chen B, Eddaoudi M, Hyde ST, O'Keeffe M, Yaghi OM (2001) Interwoven metal-organic framework on a periodic minimal surface with extra-large pores. Science 291:1021
17. Züttel A, Borgschulte A, Schlapbach L (2011) Hydrogen as a future energy carrier. Wiley, Hoboken, p 441
18. Saha D, Wei Z, Deng S (2008) Equilibrium, kinetics and enthalpy of hydrogen adsorption in MOF-177. Int J Hydrogen Energy 33:7479–7488
19. Choi J-S, Son W-J, Kim J, Ahn W-S (2008) Metal-organic framework MOF-5 prepared by microwave heating: factors to be considered. Microporous Mesoporous Mater 116:727–731
20. Mehtab T, Yasin G, Arif M, Shakeel M, Korai RM, Nadeem M, Muhammad N, Lu X (2019) Metal-organic frameworks for energy storage devices: batteries and supercapacitors. J Energy Storage 21:632–646
21. Sakintuna B, Lamari-Darkrimb F, Hirscher M (2007) Metal hydride materials for solid hydrogen storage: a review. Int J Hydrogen Energy 32:1121
22. Vitillo JG, Regli L, Chavan S, Ricchiardi G, Spoto G, Dietzel PDC, Bordiga S, Zecchina A (2008) Role of exposed metal sites in hydrogen storage in MOFs. J Am Chem Soc 130:8386–8396
23. Li ZP, Liu BH, Arai K, Suda S (2003) A fuel cell development for using borohydrides as the fuel. J Electrochem Soc 150:A868–A872
24. Zhou L (2005) Progress and problems in hydrogen storage methods. Renew Sustain Energy Rev 9:395–408

25. Schlapbach L, Züttel A (2002) Hydrogen-storage materials for mobile applications. Nature 414:353
26. Züttel A, Wenger P, Rensch S, Sudan P, Mauron P, Emmenegger C (2003) LiBH4 hydrogen storage and distribution systems. J Power Sources 5194:1–7
27. Kapelewski MT, Runčevski T, Tarver JD, Jiang HZH, Hurst KE, Parilla PA, Ayala A, Gennett T, FitzGerald SA, Brown CM, Long JR (2018) Chemistry of materials. Chem Mater 30:8179−8189
28. Klaus Y (1998) Complex transition metal hydrides. CHIMIA Int J Chem 52:613–619
29. Zttel A (2004) Hydrogen storage methods. Naturwissenschaften 91:157–172. https://doi.org/10.1007/s00114-004-0516-x
30. Züttel A, Sudan P, Mauron P, Kyiobaiashi T, Emmenegger C, Schlapbach L (2002) Hydrogen storage in carbon nanostructures. Int J Hydrogen Energy 27:203–212
31. Sljivancanin Z, Rauls E, Hornekaer L, Xu W, Besenbacher F, Hammer B (2009) Extended atomic hydrogen dimer configurations on the graphite(0001) surface. J Chem Phys 131:084706
32. Ataca C, Aktürk E, Ciraci S, Ustunel H (2008) High-capacity hydrogen storage by metallized graphene. Appl Phys Lett 93:043123
33. Tozzini V, Pellegrini V (2013) Prospects for hydrogen storage in graphene. Phys Chem Chem Phys 15:80
34. Fakioğlu E, Yürüm Y, Nejat Veziroğlu T (2004) A review of hydrogen storage systems based on boron and its compounds. Int J Hydrogen Energy 29:1371–1376
35. Durbin D, Malardier-Jugroot C (2013) Review of hydrogen storage techniques for on board vehicle applications. Int J Hydrogen Energy 38:14595–14617
36. Thomas C (2009) Fuel cell and battery electric vehicles compared. Int J Hydrogen Energy 34:6005–6020
37. Momen G, Hermosilla G, Michau A, Pons M, Firdaous M, Marty P, Hassouni K (2009) Experimental and numerical investigation of the thermal effects during hydrogen charging in packed bed storage tank. Int J Heat Mass Transf 52:1495–1503
38. Amos WA (1998) Costs of storing and transporting hydrogen. National Technical Information Service (NTIS), Springfield
39. Ahluwalia R, Peng J, Roh H, Hua T, Houchins C, James B (2018) Supercritical cryo-compressed hydrogen storage for fuel cell electric buses. Int J Hydrogen Energy 43:10215–10231
40. Rivard E, Trudeau M, Zaghib K (2019) Hydrogen storage for mobility: a review. Materials 12:1973. https://doi.org/10.3390/ma12121973
41. Ma Y, Xia Y, Zhao M, Wang R, Mei L (2001) Effective hydrogen storage in single-wall carbon nanotubes. Phys Rev B 63:115422/1–115422/6
42. Teichmann D, Arlt W, Wasserscheid P, Freymann R (2011) A future energy supply based on liquid organic hydrogen carriers (LOHC). Energy Environ Sci 4:2767–2773
43. Sun T, Xiao F, Tang R, Wang Y, Dong H, Li Z, Wang H, Liuzhang O, Zhu M (2014) Hydrogen storageperformance of nano Ni decorated LiBH4 on activated carbon prepared through the organic solvent. J Alloy Compd 612:287–292
44. Ming Y, Purewal J, Yang J, Xu C, Veenstra M, Gaab M, Müller U, Siegel DJ (2016) Stability of MOF-5 in a hydrogen gas environment containing fueling station impurities. Int J Hydrogen Energy 41:9374–9382
45. Meng Z, Lu R, Rao D, Kan E, Xiao C, Deng K (2013) Catenated metal-organic frameworks: promising hydrogen purification materials and high hydrogen storage medium with further lithium doping. Int J Hydrogen Energy 38:9811–9818
46. Gadzikwa T, Farha OK, Mulfort KL, Hupp JT, Nguyen ST (2009) A Zn-based, pillared paddle-wheel MOF containing free carboxylic acids via covalent post-synthesis elaboration. Chem Commun 45:3720
47. Chen B, Ockwig NW, Millward AR, Contreras DS, Yaghi OM (2005) High $H_2$ adsorption in a microporous metal–organic framework with open metal sites. Angew Chem Int Ed 44:4745
48. Arellano JA, Molina LM, Rubio A, López MJ, Alonso JA (2002) Interaction of molecular and atomic hydrogen with (5,5) and (6,6) single-wall carbon nanotubes. J Chem Phys 117:2281

49. Yang SH, Lin X, Dailly A, Blake AJ, Hubberstey P, Champness NR, Schröder M (2009) Enhancement of $H_2$ adsorption in coordination framework materials by use of ligand curvature. Chem Eur J 15:4829
50. Sumida K, Brown CM, Herm ZR, Chavan S, Bordiga S, Long JR (2011) Hydrogen storage properties and neutron scattering studies of Mg 2 (dobdc)—a metal–organic framework with open Mg 2+ adsorption sites. Chem Commun 47:1157

51. Kim TK, Suh MP (2011) Selective $CO_2$ adsorption in a flexible non-interpenetrated metal–organic framework. Chem Commun 47:4258
52. Mavrandonakis A, Klopper WJ (2008) First-principles study of single and multiple dihydrogen interaction with lithium containing benzene molecules. Phys Chem C 112:11580

# Design and Development of High Pressure Hydrogen Storage Tank Using Glass Fiber as the Stress Bearing Component


**Aman Yadav, Shivam Sudarshan Verma, and Aasim Akif Dafedar**

## 1 Introduction

Hydrogen has one of the highest energy densities compared to most of the regularly used fuels [1, 2]. It is around 120 MJ/kg; and that for gasoline is 44 MJ/kg [2]. However, the volumetric density of hydrogen is not so attractive, which is 0.01 MJ/L, whereas the volumetric density of gasoline is 32 MJ/L [2]. Along with this issue, there are other reasons to answer why hydrogen has not overtaken the energy market yet [1]. There are numerous cases where hydrogen energy is extensively compared to battery. And a comprehensive review did present advantage of hydrogen energy over battery in cost-effectiveness and practicality [3–5].

Therefore, it is necessary that new experiments and critical thinking is put into place to tackle the challenges pertaining to the growth hydrogen energy in the world. The common hydrogen storage methods present in the industry are compressed hydrogen storage, cryogenic/liquefied hydrogen storage and the use of metal hydrides for it [1, 3]. Cryogenic storage has its demerits in efficiency and the difficulty in the development of fully insulated storage tank which could store hydrogen at its critical temperature of 22 K [6–9]. Whereas the chemical processes haven't been much of a go to one [3].

Compressed hydrogen storage has been a method of choice in vehicular application and stationary application also. And to attain the storage targets as set by US DOE (Department of Energy) for vehicular applications there has been a rapid development and race among corporations and institutions [2]. The ultimate (2020) targets are 6.5 wt% gravimetric density and 6.1 MJ/L volumetric density [2, 3]. The latest design for vehicular application along with the most promising results was witnessed in the storage tanks of Toyota Mirai automobile which provided 5.7 wt% gravimetric density and 4.90 MJ/L volumetric density [3].

A. Yadav · S. S. Verma · A. A. Dafedar (✉)
School of Mechanical Engineering, Lovely Professional University, Phagwara, Punjab, India



K. Jha et al. (eds.), *Recent Advances in Sustainable Technologies*,
Lecture Notes in Mechanical Engineering,
https://doi.org/10.1007/978-981-16-0976-3_5

It is due to the usage of a multilayer tank design consisting of three layers:

1. an inner polymer/metallic layer depending upon the tank type,
2. an stress bearing carbon fiber reinforced composite layer, and
3. an outer layer which can withhold mechanical and corrosion damage [1, 10].

A prototyping experimental tank was designed in 2011 to replicate the in use multilayer carbon fiber-reinforced plastic (CFRP) tank which had inner lining of 12.1 mm, a CFRP layer of 25.9 mm, an overwrap of 1 mm glass fiber and protective end caps of 10 mm foam [11, 12]. These kinds of various tanks which can sustain a pressure of 700 bar were designed and tested during the time. And one of the best CFRP materials which was selected from the market possessed tensile strength of the range from 2000 to 2550 MPa [1, 11–15].

In this development process, S-glass and silicon carbide were selected as the main stress bearing component of our design. As S-glass has one of the highest tensile strengths of the range from 4028 to 4650 MPa it is an excellent choice for high pressure storage applications [16]. Also, the silicon carbide has high tensile strength and modulus of elasticity [17]. The design was modeled in PTC Creo CAD software, and the analysis test was performed under an internal pressure of 700 bar. A 700 bar pressure is a standard followed by all the tanks available in the market as it tends to meet the ultimate targets of DOE [6, 7]. Also, to completely define the constraints an external pressure of 0.101325 MPa was applied on outer surfaces which took in account the atmospheric pressure around the tank.

The main aim of the design was a quest for design optimization. As for example the world's first 77 MPa stationary hydrogen storage tank placed in People's Republic of China can store 2.5 $m^3$ of the gas and has an internal diameter of 700 mm. But its wall thickness is about 200 mm [10]. These all call for a design optimization technique. And this research is a march toward it. Thus, a method was followed and a deep study into the properties of each of these selected materials was done.

## 2 Methodology

An identical tank model was created in PTC Creo Parametric CAD (computer-aided designing) software. The model consisted of various layers, and thus the modeling as well as assembly module of the software was used to finish the complete model of the tank. And after that it was put under pressure for the analysis.

The desired analysis was performed using Ansys Workbench software version 16.0. And static structural module of the software was selected to do the final analysis. The detailed methodology which was followed can be demonstrated using the flowchart below (Fig. 1).

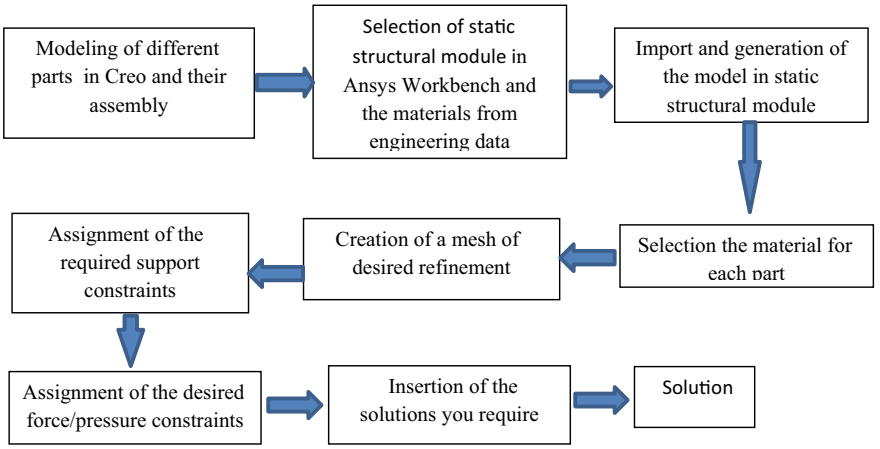


**Fig. 1** Flowchart showing the steps of modeling and analysis which were followed

## 3 Design and Material

Two types of design were tested. One of them contained a net like structure for the central S-glass layer and another one was a smooth layer. It revealed that simpler design, i.e., the later one was more reliable and easy to manufacture.

The design consisted of three layers:

1. Innermost liner
2. Central stress bearing component
3. External stress bearer (Fig. 2).

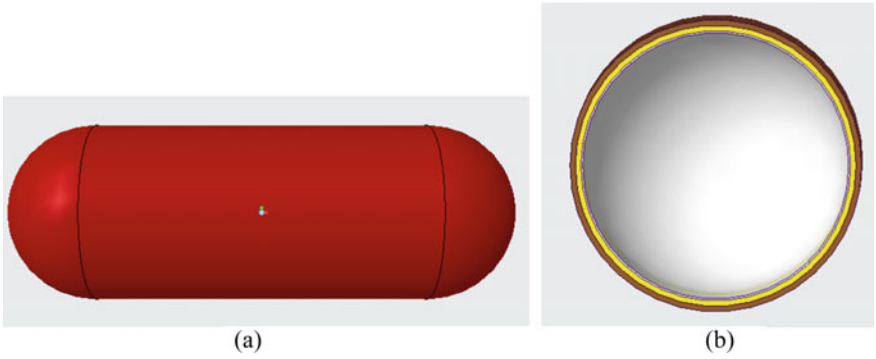


**Fig. 2** **a** Transverse placement of the complete assembly of the tank, **b** sectional CAD design representing gray inner liner, yellow glass fiber layer, and an external red SiC layer

**Table 1** Arrangement of showing respective properties of different materials in use [2, 16, 17]

| Material | Properties | | |
|---|---|---|---|
| | Density (kg/m$^3$) | Young's Modulus (MPa) | Tensile yield strength (MPa) |
| Al 7075 T6 | 2804 | 71,700 | 503 |
| S-glass | 2475 | 86,000 | 4650 |
| SiC | 3215 | 700,000 | 21,000 |

This combination of three layers with individual properties had specific functions to perform and resulted in a total mass of 34.261 kg. The liner prevented contamination of hydrogen with any other layer or chemical. The central and outer layer provided a combination of rigidity and flexibility to our design in an order that it made the complete design sustainable.

The dimensions for the tank were taken into account by studying currently available high pressure hydrogen storage tanks [18–21]. Such as the ones provided by hexagon composites ASA based on Norway. The final internal diameter was 291 mm, and internal usable length was 891 mm. Also, the external diameter was 319 mm and external length was 919 mm.

The material and their respective layers were: AL7075 T6 liner (innermost), S-glass (central), and silicon carbide (outermost). The design was put under a pressure of 700 bar from inside and an external atmospheric pressure of 1 bar. The simulation was performed in static structural module of Ansys workbench module, and the materials were selected and had the following basic properties (Table 1):

Import of the designed geometry/assembly was done in STEP file format which exports the structure in the combination of solids, volumes, and surfaces. The proper assignment of the required material was done, and necessary constraints such as pressure constraints were applied on the inner surface and outer surface (Fig. 3).

The three-layer design did not take into account the various attachments required for refilling as the main aim was the assessment of sustainability of the tank.

## 4 Results and Discussions

The analysis was done, and the results were derived in desired format. The two main aspects that were examined and which determined the reliability and sustainability of the design were the amount of maximum deformation and factor of safety. Thus, these are the two parameters have been discussed as follows:

The solution revealed promising results in the form of deformation.

The deformation solution displayed the result as shown in Fig. 4. As mentioned on the left side of the figure, the maximum deformation was 0.41015 mm and had occurred in the regions colored in red. Gradually after that the orange, yellow and the lists up to blue color show decreasing deformation, respectively. The minimum

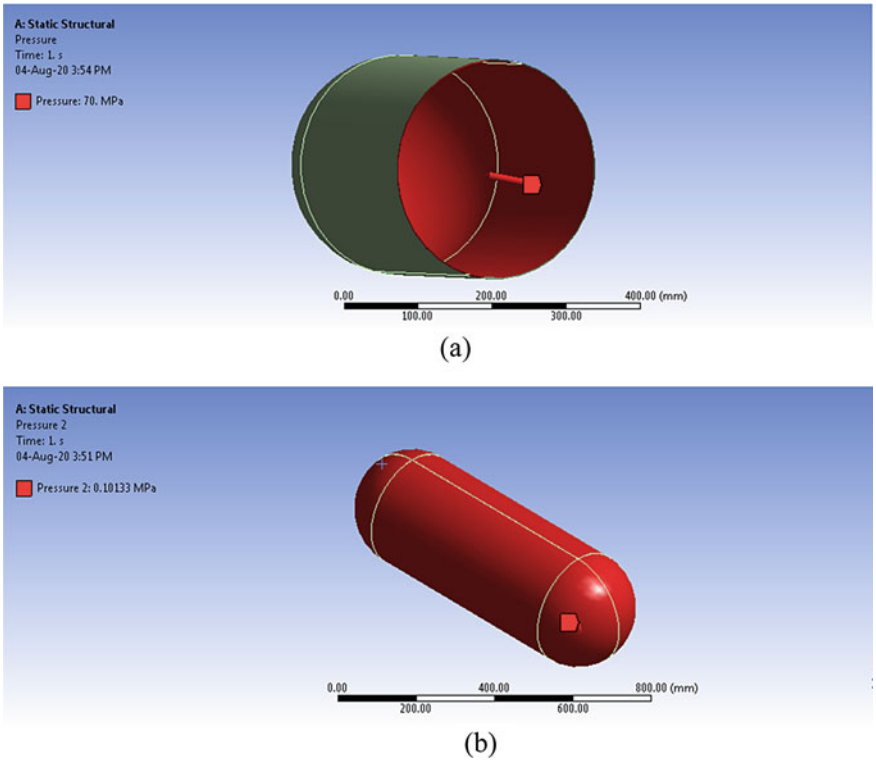


**Fig. 3** **a** Workbench screenshot displaying the application of 70 MPa internal pressure; **b** Workbench screenshot displaying the application of 0.101325 external atmospheric pressure

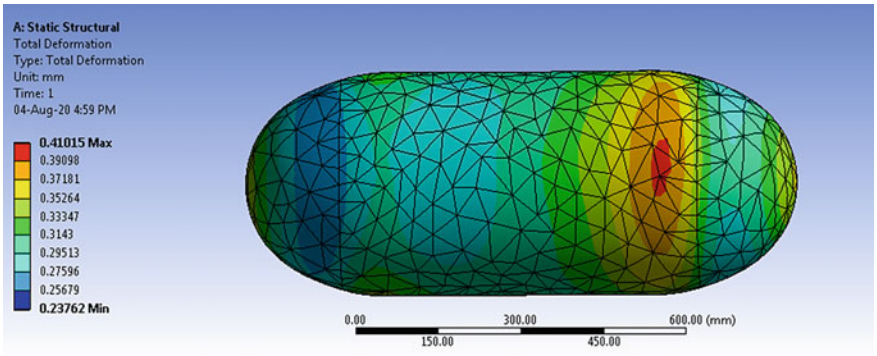


**Fig. 4** Picture depicting deformation in the tank assembly after solution

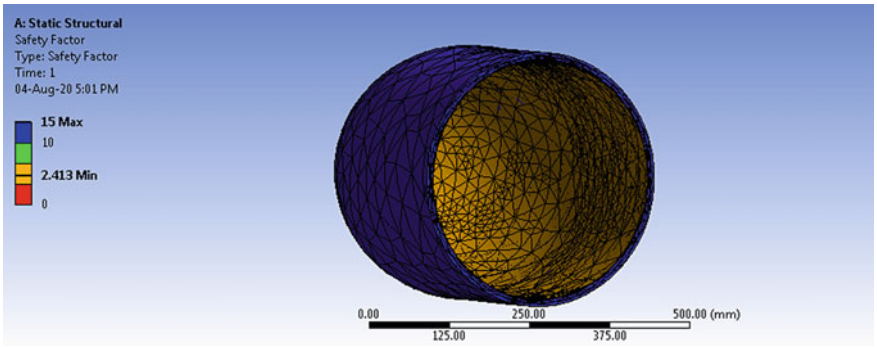


**Fig. 5** Sectional view of the factor of safety result form for the test tank

**Table 2** Desired value of properties versus acquired values

| Properties (Down) | Desired value | Acquired value |
|---|---|---|
| Deformation (mm) | <1 | 0.041015 |
| Factor of safety | 2.25 | 2.413 |

deformation which has been noted was 0.23762 mm. Both of these values were less than 1 mm. Thus, the design was accepted as negligible deformation occurred.

The result in the form of factor of safety is as follows:

The factor of safety for the final tank that was put under test came out to be a value of 2.413 as shown in Fig. 5. The tank performed well and did meet the criterion of acceptable high pressure design tank's factor of safety range which lies around 2.25 [15]. The desired and maximum acquired values from the design have been given below (Table 2).

Also, the gravimetric ratio for the tank was 5.9 wt% as compared to the gravimetric ratio of the Toyota Mirai which is 5.7 wt% [2].

## 5 Conclusion

Therefore, after the analysis various facts were learned and have been discussed below:

- The design under pressure displayed results that motivate its broader use in possible markets after a few more research work.
- Hydrogen seems to be the energy of future and it has to be employed in to our societies as scientists come close to tackling the obstructions that stall its spread.
- The design has been tested under static environmental conditions so it makes a suitable consideration for all of the three broader classifications of applications. For more, essential conditions can be simulated and studied.

There have been questions about embrittlement which can be tackled easily by employing nickel plating or any other one considering the design [22]. Also, the materials which have rarely been used for this application turned out to be a good choice and can also be employed in other high strength applications in future. Thus, it indicates the design is feasible and would help expand the hydrogen energy usage eventually [23–25].

## References


1. Züttel A (2004) Hydrogen storage methods. Naturwissenschaften 91:157–172. https://doi.org/10.1007/s00114-004-0516-x
2. Rivard E, Trudeau M, Zaghib K (2019) Hydrogen storage for mobility: a review. Materials 12:1973. https://doi.org/10.3390/ma12121973
3. Thomas CE (2009) Fuel cell and battery electric vehicles compared. Int J Hydrogen Energy 34:6005–6020. https://doi.org/10.1016/j.ijhydene.2009.06.003
4. Xu W, Li Q, Huang M (2015) Design and analysis of liquid hydrogen storage tank for high-altitude long-endurance remotely-operated aircraft. Int J Hydrogen Energy 40:16578–16586
5. Zheng J et al (2012) Development of high pressure gaseous hydrogen storage technology. Int J of Hydrogen Energy 37:1048–1057. https://doi.org/10.1016/j.ijhydene.2011.02.125
6. Sirosh N et al (2003) Hydrogen composite tank project. Progress report Department of Energy. US government
7. Nafchi et al (2018) Performance assessment of a solar hydrogen and electricity production plant using high temperature PEM electrolyzer and energy storage. Int J Hydrogen Energy 43:5820–5831
8. Cumalioglu I, Ma Y, Ertas A, Maxwell T (2007) High pressure hydrogen storage tank: a parametric design study. J Pressure Vessel Technol 129:216. https://doi.org/10.1115/1.2389036
9. Abdalla AM, Hossain S, Nisfindy OB, Azad AT, Dawood M, Azad AK (2018) Hydrogen production, storage, transportation and key challenges with applications: a review. Energy Convers Manag 165:602–627
10. Esayed A Y (2001) Metal Hydrides. Energy Sources 23:257–265. https://doi.org/10.1080/00908310151133960
11. Jorgensen S (2011) Hydrogen storage tanks for vehicles: recent progress and current status. Curr Opin Solid State Mater Sci 15:39–43. https://doi.org/10.1016/j.cossms.2010.09.004
12. Barreto L, Makihira A, Riahi K (2003) The hydrogen economy in the 21st century: a sustainable development scenario. Int J Hydrogen Energy 28:267–284
13. Yang J, Sudik A, Wolverton C, Siegel D (2010) High capacity hydrogen storage materials: attributes for automotive applications and techniques for materials discovery. Chem Soc Rev 39:656–675. https://doi.org/10.1039/b802882f
14. Aceves SM, Petitpas G, Espinosa-Loza F, Matthews MJ, Ledesma-Orozco E (2013) Safe, long range, inexpensive and rapidly refuelable hydrogen vehicles with cryogenic pressure vessels. Int J Hydrogen Energy 38:2480–2489
15. Winter C J, Nitsch J (1988) Hydrogen as an energy carrier. Springer-Verlag ISBN: 978-3-642-61561-0. https://doi.org/10.1007/978-3-642-61561-0
16. Khan I, Sravanthi M, Prasanna L (2018) An experimental study of the mechanical properties of s glass fiber reinforced high strength concrete partially replacing cement with nano silica. Int J Civ Eng Technol 9:1398–1409
17. Petersen KE (1982) Silicon as mechanical material. Proc IEEE 70(5)
18. Durbin D, Malardier-Jugroot C (2013) Review of hydrogen storage techniques for on board vehicle applications. Int J Hydrogen Energy 38:14595–14617

19. Jain I, Jain P, Jain A (2010) Novel hydrogen storage materials: a review of lightweight complex hydrides. J Alloy Compd 503:303–339
20. Fakioğlu E, Yürüm Y, Nejat Veziroğlu T (2004) A review of hydrogen storage systems based on boron and its compounds. Int J Hydrogen Energy 29:1371–1376
21. Muradov N, Vezirolu T (2005) From hydrocarbon to hydrogen? Carbon to hydrogen economy. Int J Hydrogen Energy 30:225–237
22. Dwivedi S, Vishwakarma M (2018) Hydrogen embrittlement in different materials: a review. Int J Hydrogen Energy 43. https://doi.org/10.1016/j.ijhydene.2018.09.201
23. Bossel U (2006) Does a hydrogen economy make sense? Proc IEEE 94:1826–1837
24. Aardahl C, Rassat S (2009) Overview of systems considerations for on-board chemical hydrogen storage. Int J Hydrogen Energy 34:6676–6683
25. Gye H-R, Seo S-K, Bach Q-V, Ha D, Lee C-J (2019) Quantitative risk assessment of an urban hydrogen refueling station. Int J Hydrogen Energy 44:1288–1298

# Numerical Simulation of Turbulent Flow Through a Sudden Expansion Channel: Comparison Between Three Models


**Sandip Saha**

## 1 Introduction

Turbulent water flow through sudden expansion channel has many important applications on engineering sciences and many industrial applications, namely heat exchangers, combustors, diffusers, nuclear reactors, electronic cooling equipment's, mixing vessels, and so on. Over the past few decades, the change in flow from symmetry to asymmetry through sudden expansion channels has become very interesting to researchers [1–6].

In a two-dimensional sudden expansion channel, Abbot and Kline [7] numerically studied the subsonic turbulent flow with the variation of semi-angle. They concluded that, one or more vortices appear in a three-dimensional downstream region and classical stall pattern of flow occur in a two-dimensional downstream zone. When Ar (area ratio) >1.5, they investigated that three different corner vortices appear for double step configuration. Macagno and Hung [8] investigated the viscous flow through an axi-symmetric conduit for the $\mathrm{Re} \in [36 - 4500]$. On the lower and upper walls, they studied the dynamic interaction between fluid flow and captive eddy. They noted that the major aspect of eddies is to form the flow transition with significantly small exchange of energy. In a two-dimensional sudden expansion channel with the variation of semi-angle, Shapira et al. [9] analytically perform the linear stability analysis. By energy-based method, they stated that asymmetric solution exist when $\mathrm{Re} > \mathrm{Re}_{cr}$.

Foumeny et al. [10] numerically studied the incompressible Newtonian fluid flow by considering two channels, such as a channel along with no-slip boundary conditions and another one is cascade model along with cyclic boundary conditions. For both the models, they stated that when $\mathrm{Re} > \mathrm{Re}_{cr}$(critical Reynolds number),

S. Saha (✉)
Department of Mathematics, NIT Silchar, Silchar 788010, India
e-mail: sandip_rs@math.nits.ac.in



K. Jha et al. (eds.), *Recent Advances in Sustainable Technologies*,
Lecture Notes in Mechanical Engineering,
https://doi.org/10.1007/978-981-16-0976-3_6

flow changes symmetric to asymmetric. Laminar Newtonian fluid flow in an axi-symmetric expansion channel has been investigated numerically by Oliveira and Pinho [11]. By finite volume method, they calculated the separation and reattachment vortex length and compared with the experimental results which show a good agreement between the results of experimental and numerical works. In an expansion ratio 2, Durst et al. [12] studied the flow bifurcation phenomena for low values of Re using finite volume method. They experimentally and numerically investigated that flow bifurcation breaks the symmetry for Re $>$ 125.

The motivation of this study is to investigate the performance of three turbulence models to predict the flow phenomena, velocity profile, and normalized vortex lengths in case of turbulent water flow through a sudden expansion channel. Fluent software has been employed to model the computational geometry and numerical simulations. Current study has been validated with the results of Ternik et al. [13]. Moreover, the simulated results such as normalized vortex length, and velocity profile have been compared between three turbulent models. Furthermore, $Re_{cr}$ has been calculated for each of the three models to find out the bifurcation point where the flow symmetry breaks. The paper has been formalized as follows: flow geometry prescribed in Sect. 2, governing equations are prescribed in Sect. 3, and the results and discussions have been performed in Sect. 4.

## 2 Computational Flow Geometry

Two-dimensional computational flow geometry is depicted in Fig. 1, which is divided into three sections such as inlet, outlet, lower and upper walls.

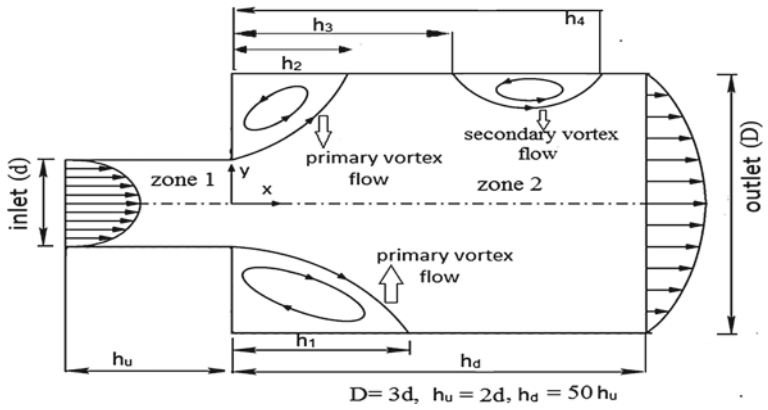


**Fig. 1** Flow geometry

## 3 Mathematical Formulation

To study the turbulent flow characteristics, various authors [14–17] have been used the following governing equations:

Continuity equation:

$$\frac{\partial u_i}{\partial x_i} = 0 \tag{1}$$

Momentum equation:

$$\frac{\partial u_i}{\partial x_j} u_j = -\frac{1}{\rho}\frac{\partial p}{\partial x_i} + \frac{\partial}{\partial x_j}\left(\frac{\mu}{\rho}\left(\frac{\partial u_i}{\partial x_j} + \frac{\partial u_j}{\partial x_i}\right) - \overline{u_i' u_j'}\right) \tag{2}$$

where $\rho = 1000\,\text{kg/m}^3$, $\mu = 0.00089$ Pa s and $p$ denoted as fluid density, dynamic viscosity, static pressure, respectively. By Kolmogorov formulation [14, 16, 18], Reynolds stress ($\overline{u_i' u_j'}$) can be written as follows:

$$-\rho\overline{u_i' u_j'} = \mu_t\left(\frac{\partial u_i}{\partial x_j} + \frac{\partial u_j}{\partial x_i}\right) - \frac{2}{3}\rho\delta_{ij}k \tag{3}$$

Here, $\mu_t$, $\delta_{ij}$ be noted as eddy viscosity, Kroenecker delta and kinetic energy ($k$) $= \overline{u_i' u_j'}/2$, respectively. Re is defined as Reynolds number, $\text{Re} = \rho u d/\mu$.

### *3.1 Boundary Conditions*

- Inlet boundary condition: $k = 0.005u_0^2$, $\varepsilon = 0.1k^2$, here $\varepsilon$ noted as inlet dissipation, $\omega = \varepsilon/k\beta^*$.
- Outlet boundary condition: $\partial u/\partial x = 0$, $\partial v/\partial x = 0$, $\partial k/\partial x = 0$, and $\partial\varepsilon/\partial x = 0$. Atmospheric pressure considered at the outside of the channel.
- Wall boundary conditions: $\partial k/\partial n = 0$, $\partial\varepsilon/\partial n = 0$.

### *3.2 Turbulence Modeling*

#### 3.2.1 Standard *k-ε* Model

The model equations are as below which are proposed by Launder and Spalding [18]. This model consists of two transport equations such as turbulent kinetic energy (Eq. 4) and dissipation of turbulent kinetic energy (Eq. 5).

$$\frac{\partial(\rho k)}{\partial t} + \frac{\partial(\rho k u_i)}{\partial x_i} = \frac{\partial}{\partial x_j}\left(\frac{\mu_t}{\sigma_k}\frac{\partial k}{\partial x_j}\right) + 2\mu_t e_{ij} e_{ij} - \rho\varepsilon_t \tag{4}$$

$$\frac{\partial(\rho\varepsilon_t)}{\partial t} + \frac{\partial(\rho\varepsilon_t u_i)}{\partial x_i} = \frac{\partial}{\partial x_j}\left(\frac{\mu_t}{\sigma_{\varepsilon_t}}\frac{\partial \varepsilon_t}{\partial x_j}\right) + C_{1\varepsilon_t}\frac{\varepsilon_t}{k}2\mu_t e_{ij} e_{ij} - C_{2\varepsilon_t}\rho\frac{\varepsilon_t^2}{k} \tag{5}$$

Here, $u_i$, $e_{ij}$, and $\mu_t$ are noted as velocity component, deformation rate, and turbulent eddy viscosity. Whereas $\mu_t = \rho C_{\mu_t}\frac{k^2}{\varepsilon_t}$ and $y^+ = \frac{\rho C_{\mu_t} k^{\frac{1}{2}} y}{\mu_t}$. Normalize distance of the walls are denoted by $y^+$. The constant parameters [18] of this model are $C_{\mu_t} = 0.09$, $C_1 = C_3 = 1.44$, $C_2 = 1.92$, $C_{\mu_t} = 1$, and $\sigma_k = 1.3$.

### 3.2.2 Realizable *k-ε* Model

$$\frac{\partial(\rho\varepsilon_t u_i)}{\partial x_i} = \left(\mu + \frac{\mu_t}{\sigma_\varepsilon}\right)\nabla^2\varepsilon_t + C_1 S_{\rho\varepsilon_t} - C_2 S_{\rho\varepsilon_t}\frac{\varepsilon_t^2}{\sigma_k + \sqrt{v\varepsilon_t}} \tag{6}$$

where $C_1 = \max[0.43, n/(n+5)]$, $C_2 = 1$, $\sigma_k = 1$, $\sigma_{\varepsilon_t} = 1.2$, $n = S_k/\varepsilon_t$ in accordance with [19].

### 3.2.3 SST *k-ω* Model

$$\frac{\partial k}{\partial x_i}u_i = \frac{1}{\rho}\left[\mu_t\frac{\partial u_i}{\partial x_i}\left(\frac{\partial u_i}{\partial x_J} + \frac{\partial u_J}{\partial x_i}\right)\right] - k\omega\beta^* + \frac{1}{\rho}\frac{\partial}{\partial x_i}(\mu + \mu_t\sigma_k)\frac{\partial k}{\partial x_i} \tag{7}$$

Dissipation rate:

$$\frac{\partial \omega}{\partial x_i}u_i = \alpha S^2 - \omega^2\beta + \frac{1}{\rho}\frac{\partial}{\partial x_i}\left[(\mu + \sigma_{\omega_1}\mu_t)\frac{\partial\omega}{\partial x_i}\right] + 2(1 - F_1)\sigma_{\omega_2}\frac{1}{\omega}\frac{\partial k}{\partial x_i}\frac{\partial\omega}{\partial x_i} \tag{8}$$

Here $F_1$ is taken in accordance with Wilcox [20]. When *k-ε* model is applicable then $F_1$ be zero from the walls and turbulent eddy viscosity is formulized in Eq. 9.

$$\breve{\upsilon}_t = \frac{a_1 k}{\max(a_1\omega,\ S\left[\tanh\left|\max\left(2\frac{\sqrt{k}}{y\omega\beta^*},\ \frac{5009}{y^2\omega}\right)^2\right|\right]} \tag{9}$$

The constant parameters of this model [20] are $\beta^* = 0.09$, $\alpha_1 = 5/9$, $\beta_1 = 3/40$, $\sigma_{K_1} = 0.85$, $\sigma_{\omega_1} = 0.5$, $\alpha_2 = 0.44$, $\beta_2 = 0.0828$, $\sigma_{K_2} = 1$, and $\sigma_{\omega_2} = 0.856$.

# 4 Results and Discussions

## *4.1 Grid Test and Model Validation*

Grid test has been studied for low computational cost and to study the effect of mesh size. From Fig. 2a, it has been clear that total number of elements be 60,820 which are sufficient for future analysis. Grid test has been done by Standard $k$-$\varepsilon$ model at Re = 5000 by considering the average pressure coefficients along the $y$-axis and at the $x$-axis total number of elements has been prescribed. For two values of Reynolds number (Re = 50, 100), the current work has been validated with the results of Ternik et al. [13] by comparing the normalize velocity profile along the centerline. Figure 2b, c states a good relationship between the present study and Ternik et al. [13] which gave an enough confidence for doing future analysis. Pressure drop states a linear indication which represents the fully developed flow condition. It shows that at the downstream section pressure increases due to the flow deceleration.

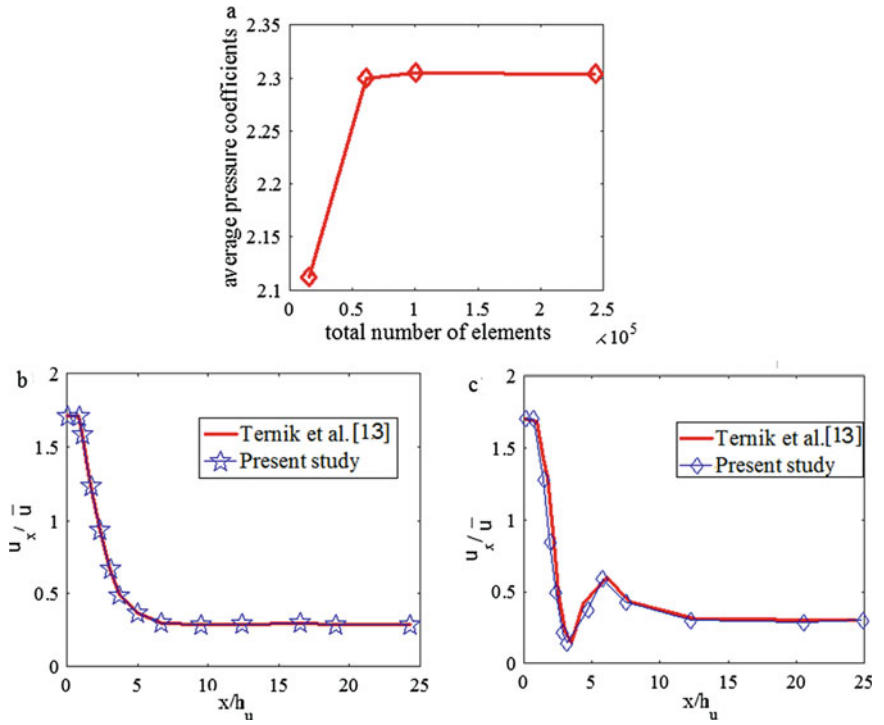


**Fig. 2** Avergae pressure coefficients versus total number of elements (**a**), normalized velocity profile at $\mathrm{Re}_N = 50$ (**b**), and $\mathrm{Re}_N = 100$ (**c**)

## 5 Flow Phenomena

By three different models, velocity streamlines have been shown in Fig. 3a–c at Re = 10, 000. From Fig. 3a–c, it is clearly observed that, due to friction and wall shear stress, low velocity and the maximum velocity exist near the walls and away from the walls. It is seen that velocity streamlines becomes more pronounced when SST $k$-$\omega$ model is adopted rather than Standard $k$-$\varepsilon$ model and Realizable $k$-$\varepsilon$ model due to high sensitivity of adverse pressure gradients. In addition, due to the presence of cross-diffusion term and blending function, SST $k$-$\omega$ model is more suitable to analyze the flow phenomena near the wall and far away from the walls. Moreover, for higher values of Reynolds number, SST $k$-$\omega$ model is more comfortable to transform the inner region of boundary layer to $k$-$\omega$ model. For Standard $k$-$\varepsilon$ model, it is observed that maximum velocity reaches 1.15 times of inlet velocity, but in Realizable $k$-$\varepsilon$ model maximum velocity becomes 1.17 times. Furthermore, it is also explored that maximum velocity becomes 1.185 times of inlet velocity when the SST $k$-$\omega$ model has been employed. Moreover, it has also been observed that recirculation region length becomes more complex in case of SST $k$-$\omega$ model. For three different models, centerline velocity profiles have been depicted in Fig. 4a at Re = 10,000. It is investigated that the SST $k$-$\omega$ model becomes more influenced in terms of velocity profile rather than other two models. It is also noted that with the increase of axial distance, velocity profile becomes more stagnant which is clearly shown in Fig. 4a. For different values of Reynolds number, normalized vortex length (Hi) has been prescribed in Fig. 4b to reveal the critical values of Reynolds number in each turbulence model. It is studied that an increase of Reynolds number causes the increase of vortex length as shown in Fig. 4b.

From Fig. 4b, it is clearly seen that in Standard $k$-$\varepsilon$ model $Re_{cr}$ becomes 2370 but in case of Realizable $k$-$\varepsilon$ model, $Re_{cr}$ becomes 2315. Moreover, it is revealed that $Re_{cr} = 2302$ when SST $k$-$\omega$ model is implemented. Furthermore, it is noted that

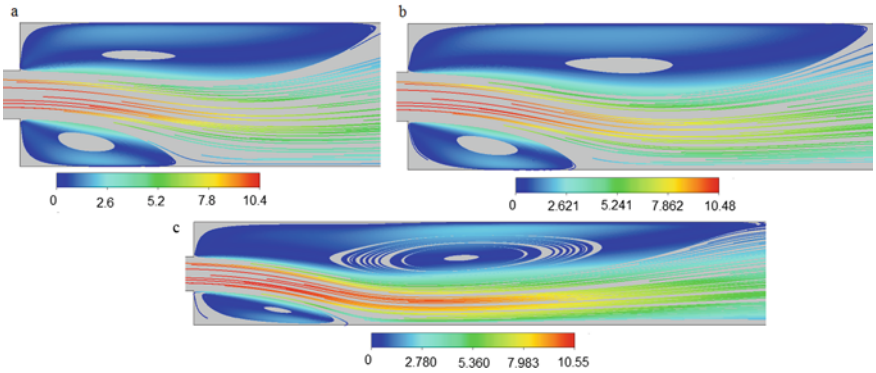


**Fig. 3** Velocity streamlines by three different models, **a** standard $k$-$\varepsilon$ model, reliazable $k$-$\varepsilon$ model (**b**), SST $k$-$\omega$ model (**c**)

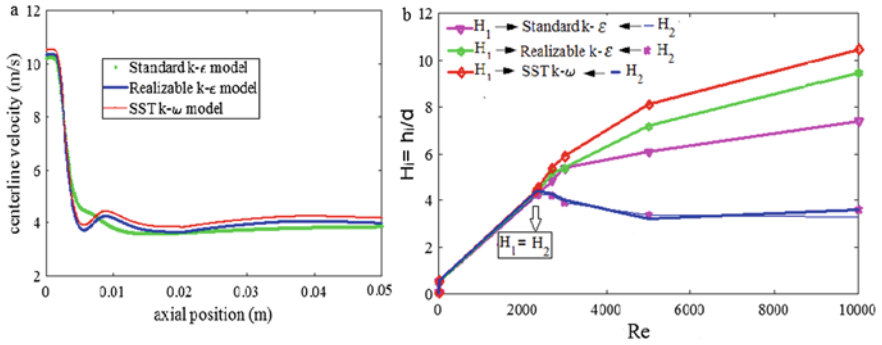


**Fig. 4** Velocity profile (**a**), and normalized vortex lengths (**b**) for various Re

when $Re < Re_{cr}$ flow becomes symmetric, which indicates that two equal lengths of vortices exist on the walls. But when $Re > Re_{cr}$ flow breaks the symmetry and two different lengths of vortices exist. Therefore, it is concluded that $Re_{cr}$ decreases in case of SST *k-ω* model rather than other models.

## 6 Conclusion

Turbulent water flow through sudden expansion channels have many important applications in engineering sciences and many industrial applications such as heat exchangers, combustors, diffusers, and so on. Three turbulence models have been employed to reveal the flow patterns and normalized vortex lengths for different values of Reynolds number. The concluding remarks have been described as follows:

- It is observed that due to friction and wall shear stress low velocity approaches near the wall but the maximum velocity reaches when the flow far away from the lower and upper walls. Moreover, it is also studied that with the increase of axial distance, velocity profile becomes more stagnant.
- In Standard *k-ε* model, it is found that maximum velocity reaches 1.15 times of inlet velocity, but in Realizable *k-ε* model maximum velocity becomes 1.17 times of inlet velocity. Furthermore, in the SST *k-ω* model, it is also revealed that maximum velocity becomes 1.185 times of inlet velocity. Moreover, it is studied that an increase of Reynolds number causes the increase of vortex lengths. It is noted that when $Re < Re_{cr}$, flow becomes symmetric but when $Re > Re_{cr}$ flow breaks the symmetry and two different lengths of vortices alternately exist on the walls.
- Furthermore, it is revealed that in Standard *k-ε* model, $Re_{cr} = 2370$ but in case of Realizable *k-ε* model $Re_{cr} = 2315$. Moreover, it is studied that critical value of Reynolds number become 2302 when SST *k-ω* model is implemented. Therefore, it is concluded $Re_{cr}$ decreases in case of SST *k-ω* model rather than other models.

Therefore, from the whole study it is concluded that SST $k$-$\omega$ turbulence model show the best prediction outcomes in terms of normalized vortex length, velocity streamlines, velocity profile and to find out the critical value of Reynolds number.

## References


1. Saha S, Biswas P, Nath S (2020) Bifurcation phenomena for incompressible laminar flow in expansion channel to study Coanda effect. J Interdisc Math 23(2):493–502
2. Saha S, Biswas P, Nath S (2019) Numerical modeling of bifurcation and leakage of blood flow in mitral valve to predict heart malfunctioning. In: Springer LAIS book series 12, pp 2662–3447
3. Poole RJ, Ridley BS (2007) Development length requirements for fully developed laminar pipe flow of inelastic non-Newtonian liquids. ASME J Fluid Eng 129:1281–1287
4. Sano M, Suzuki I, Sakuraba K (2009) Control of turbulent channel flow over a backward-facing step by suction. J Fluid Sci Technol 4:188–199
5. So RMC, Ahmed SA (1989) Characteristics of dump combustor flows. Int J Heat Fluid Flow 10:66–74
6. Koopaee KM, Rezaee M (2017) Investigation of turbulent flow through microchannels consisting of different micropost arrangements. Eng Comput 34(2):1367–1392
7. Abbot DE, Kline SJ (1962) Experimental investigation of subsonic turbulent flow over single and double backward facing steps. J Basic Eng 84:317–325
8. Macagno EO, Hung TK (1967) Computational and experimental study of a captive annular eddy. J Fluid Mech 28:43–64
9. Sahpira M, Degani D, Weihs D (1990) Stability and existence of multiple solutions for viscous flow in suddenly enlarged channels. Comput Fluids 18:239–258
10. Foumeny EA, Ingham DB, Walker AJ (1996) Bifurcations of incompressible flow through plane symmetric channel expansions. Comput Fluid 25:335–351
11. Oliveira PJ, Pinho FT (1997) Pressure drop coefficient of laminar Newtonian flow in axisymmetric sudden expansions. Int J Heat Fluid Flow 18:518–529
12. Durst F, Pereira JCF, Tropea C (1993) The plane symmetric sudden expansion flow at low Reynolds number. J Fluid Mech 248:567–581
13. Ternik P, Marn J, Zunic Z (2006) Non-Newtonian fluid flow through a planar symmetric expansion: shear-thickening fluids. J Non-Newton Fluid Mech 13:136–148
14. Demartini CL, Vielmo AH, Möller VS (2004) Numeric and experimental analysis of the turbulent flow through a channel with baffle plates. J Braz Soc Mech Sci Eng 26(2):153–159
15. Singh KS, Debnath K (2017) Turbulent flow characteristics in a rectangular channel under the influence of cube-mounted rough bed. ISH J Hydraul Eng 23(2):167–176
16. Saha S, Biswas P, Nath S, Singh L (2020) Numerical simulations of Newtonian fluid flow through a suddenly contracted rectangular channel with two different types of baffle plates. Soft Comput. https://doi.org/10.1007/s00500-020-05326-4
17. Menter RF (1994) Two-equation eddy-viscosity turbulence models for engineering applications. AIAA J 32(8):1598–1605
18. Launder EB, Spalding BD (1974) The numerical computation of turbulent flow. Comput Methods Appl Mech Eng 3:269–279
19. Rohdin P, Moshfegh B (2007) Numerical predictions of indoor climate in large industrial premises: a comparison between different k-ε models supported by field measurements. Build Environ 42:3872–3882
20. Wilcox CD (1993) Comparison of two-equation turbulence models for boundary layers, with pressure gradient. AIAA J 31:1414–1421

# Tractor-Trailer Gap Optimization of a Truck for Reduction of Aerodynamic Drag


**Merga Deraro, Ramesh Babu Nallamothu, Seshu Kishan Nallamothu, Anantha Kamal Nallamothu, and Sewagegn Zewudie**

## 1 Introduction

In the present century, the goods carrying trucks like Sino trucks are being designed for higher speeds. Due to higher speeds at which they are driven, trucks are subjected to aerodynamic drag and lift forces. Unwanted aerodynamic forces are affecting the fuel consumption of the vehicle and lift forces affect the vehicle handling and road holding capacity of the vehicle. The major target of the aerodynamic design of a vehicle is to determine the aerodynamic efficient vehicle shapes to improve the vehicle aerodynamic performance for saving the fuel. It is necessary to improve the outer shape of the vehicle for reducing the drag, without compromising other requirements of the vehicle. When a body moves through a fluid medium, it experiences resistance to forwarding motion called aerodynamic drag. Aerodynamic drag is insignificant at lower speeds. But as the speed increases, the drag increases in a parabolic fashion. In crosswinds with non-zero yaw angle, the influence of the drag takes another shape. Stability of the vehicle is affected considerably. With tractor-trailer combination for heavy-duty trucks, the drag coefficient increases considerably with increase in yaw angle [1–4]. Trailer side skirts, boat tails, cab side extensions, roof deflector are some of the addons which are used for reducing the drag. Some of

M. Deraro
Department of Mechanical Engineering, School of Engineering and Technology, Wolkite University, Wolkite, Ethiopia

R. B. Nallamothu (✉) · S. Zewudie
Mechanical Systems and Vehicle Engineering Department, SoMCME, Adama Science and Technology University, Adama, Ethiopia
e-mail: ramesh.babu@astu.edu.et

S. K. Nallamothu · A. K. Nallamothu
Politecnico di Milano, Bovisa, Milano, Italy



K. Jha et al. (eds.), *Recent Advances in Sustainable Technologies*,
Lecture Notes in Mechanical Engineering,
https://doi.org/10.1007/978-981-16-0976-3_7

them are like roof deflectors, cab side extensions, trailer "boat tails" and trailer side skirts [5, 6].

There are many other conceptual body shapes and addons which are not well studied so far. The aerodynamic analysis of body shape of Sino truck is very important for reducing fuel consumption and improving the stability and handling for the sake of safety. In particular, in the presence of crosswinds, drag and handling problems are even severe [7, 8]. The trailer and tractor gap allow the passage of air through it, which creates more turbulence and increases the flow separation on the hiding side of the trailer causing eddy formation leading higher drag. In general, in trucks, major modifications of outer shape are not possible, except very little modifications like truck front face leading-edge rounding. The drag developed on heavy trucks is mostly pressure drag [9, 10]. It is mostly focused at the front surface, wheels, trailer and tractor gap trailer and rear face of the trailer. In general, the loading of the trailer takes place through the rear surface; the rear surface modification becomes difficult for the reduction of the drag [11, 12]. In general, the truck drivers are very negligent about the usage of drag reduction devices which may interfere with their routine activities like loading, unloading, etc. [13, 14]. Drag reduction on freight-trucks could lead to both environmental and economic benefits as the energy consumption is lowered [15, 16]. At the same time, the emissions of heavy trucks and concomitant fuel combustion can be significantly reduced [17, 18]. All in all, an improvement of a truck's configuration could decrease the drag coefficient ($C_d$), leading to better fuel efficiency and a cleaner environment [19].

## 2 Modelling

### *2.1 Model Geometry Specifications*

The specifications considered for modelling are given in Table 1.

**Table 1** Aerodynamic general specifications

| No | Aerodynamic specifications | |
|---|---|---|
| 1 | Minimum tractor-trailer gap | 1700 mm |
| 2 | Minimum frontal corner | 110 mm |
| 3 | side trailer edge | 95 mm |
| 4 | Rear trailer edge | 95 mm |

**Table 2** Specifications and detail dimension of Sino truck model 321

| Specification | Detail |
|---|---|
| Length | 16.72 mm |
| Width | 3.88 mm |
| Height | 2.80 mm |

**Table 3** Experimental range

| | Range |
|---|---|
| Truck speeds | 64, 80, 96 kmph |
| Inclined angle | 0° |
| Model no | Sino truck (model 321) |

## *2.2 Specifications of Existing Sino Truck*

The specifications of the selected truck are given in Table 2, and the selected experimental ranges are given in Table 3.

## *2.3 Original Model 321 (Existing)*

The prepared models of the existing vehicle are shown in Figs. 1 and 2.

## *2.4 Reducing Drag with Aerodynamic Device*

The stream lines of the flow over the model, without the device and with the device are shown in Fig. 3.

**Fig. 1** Model 1

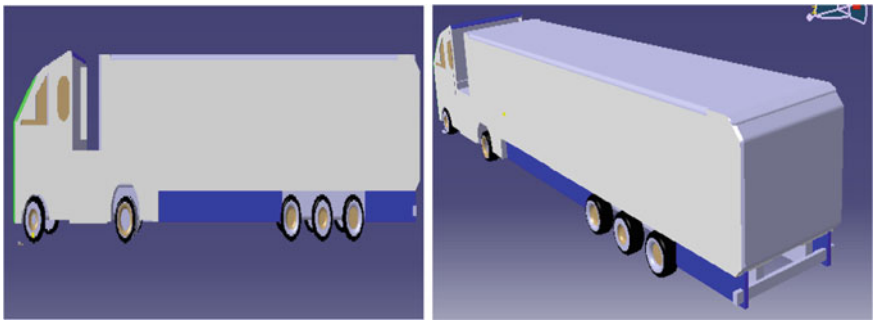

**Fig. 2** Model 2

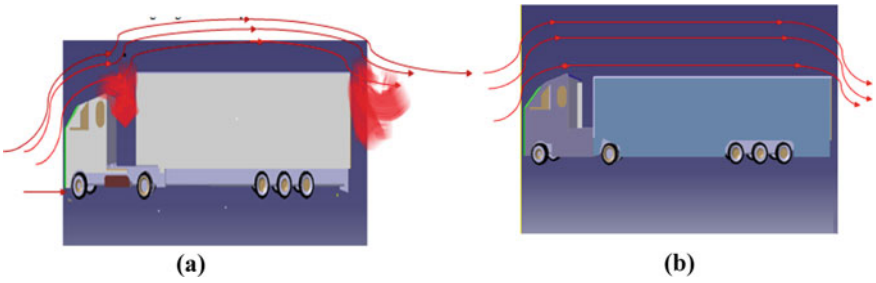


**Fig. 3** **a** A tractor-trailer without device **b** tractor-trailer with device

**Table 4** Different model modification

| | Model existing 1 | Model 2 | Model 3 |
|---|---|---|---|
| Overall length | 16.72 m | 16.72 m | 16.72 |
| Number of trailers | 1 | 1 | 1 |
| Cab | No | Yes | Yes |
| Gap length | 1.700 m | 1.300 m | 1.00 |

## *2.5 Modified Sino Truck 321 Model Testing with Varying Velocity*

Aerodynamic-related aspects and parameters are considered in the models designed. Frontal area is modified, and the pressure acting on the trailer was reduced by optimizing the gap and improving the flow through the gap. Hence, it has more influence on the drag force (Table 4).

**Step: Experiment**

The domain is $X = 80$ m, $Y = 20$ m, $Z = 12$ m. Ground plate, outlet, and inlet boundary conditions are set. The dimensions are $L(X) = 16.72$ m, $W(Y) = 3.88$ m, $H(Z) = 2.80$ m. Initial wind velocity is $V = 26.667$/s. Sensor position in the domain

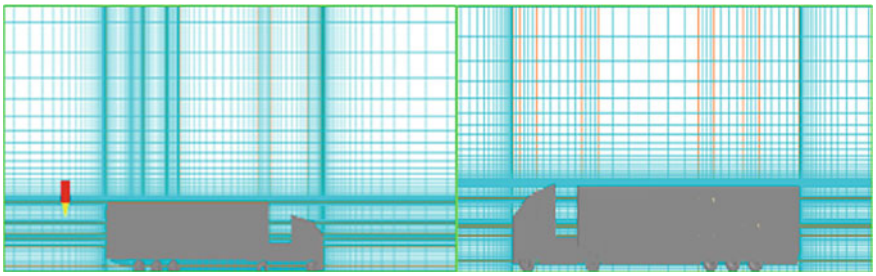

**Fig. 4** Modification of truck at v 96 km/h

at $X = 40$ m, $Y = 10$ m, $Z = 1.4$ m, is as shown. Total force momentum at $X_{\text{pos}} = 24.9975$, $Y_{\text{pos}} = 10$, and $Z_{\text{pos}} = 1.4$. Reference density of 1.189 kg/m$^3$ was used for calculating drag coefficient from total forces, reference area in $x$, $y$, and $z$ is $3.88 \times 2.80 = 10.864$ m$^2$.The air in the domain is at 20 °C, 1 atm. KECHEN standard turbulent model is selected for the solution of the velocity. Velocity and pressure are used to optimize at the selected position of the probe at a speed of 96 kmph (Fig. 4).

## 3 Meshing

Grid optimization test was done to reduce the computational difference between the two models. The truck has symmetry about its longitudinal axis. At more number of regions, the results were good. Constant velocity was considered at the inlet and zero-gauge pressure was considered at the outlet. Atmospheric pressure is operating pressure. The blue face is for velocity inlet and red face is for pressure outlet.

### *3.1 Total Drag Force*

When air flows over the surface of the vehicle, body develops drag force resisting the forward motion of the vehicle. The total drag comprises of form drag and skin friction drag. Skin friction drag develops due to the viscous effect developed in a boundary layer formation. The form drag develops due to shape variations, flow separation, and due to the pressure difference existing between the surfaces. Because the shape of the outer body of the vehicle is very much varying, integrating the pressure distribution over the surface is a very complex task. The CFD software helps in this task of estimating the pressure variations over the exposed surface of the vehicle. But it is to be adequately validated. After conducting CFD analysis, comparing two types of models for their drag and lift found that the difference is less. Sino truck may

generate less or more drag depending on test force acting on the surface, speed, the density of the air, and projected frontal area. The drag coefficient in non-dimensional form is defined as:

$$F_{\mathrm{D}} = \frac{1}{2}\rho A C_{\mathrm{D}} V 2[10] \tag{1}$$

$$C_{\mathrm{D}} = F_{\mathrm{D}}\left(\frac{1}{2\rho V 2A}\right) \tag{2}$$

where

$C_{\mathrm{D}}$ Drag coefficient
$A$ Frontal area of the Sino truck (10.86m$^2$)
$P$ Air density (1.189 kg/m$^3$)
$V$ Total wind velocity
$F_{\mathrm{D}}$ Drag force of Sino truck.

## 3.2 *Drag Coefficient ($C_d$) Calculation Performance Analysis of Sino Truck Model 321*

$$\left((C_{\mathrm{d}}\mathrm{model}\,1 - C_{\mathrm{d}}\mathrm{model}\,2)\frac{1}{C_{\mathrm{D}}1}\mathrm{model}\,1 \times 100\right) \tag{3}$$

Total resistance force is:

$$\begin{aligned} F_{\mathrm{t}} &= F_{\mathrm{d}} + F_{\mathrm{r}} + F_{\mathrm{g}} \\ F_{\mathrm{r}} &= (0.015 + 0.00016V)W \end{aligned} \tag{4}$$

where

$F_{\mathrm{r}}$ is rolling resistance
$F_{\mathrm{g}}$ is resistance due to gravitational force
$F_{\mathrm{d}}$ is resistance due to drag
$V$ is cruising speed of truck km/h
$W$ is Sino truck curb weight.

Since $F_{\mathrm{g}} = 0$ because of at 0° while $= W \times \sin 0°$. The flow is divided into two areas on the Sino truck: one inside, the boundary layer and the one outside, the boundary layer.

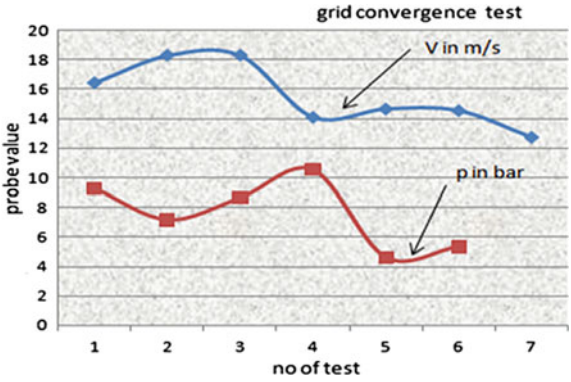


**Fig. 5** Grid convergence test

## 4 Results and Discussion

For both models, the CFD analysis was done for the flow over the surface varying the speed from 64 to 96 kmph. The grid convergence test result is given in Fig. 5. At three different velocities, the results were obtained for both models. The shape of the body is majorly influencing the drag. In this work, the shape of the standard model of Sino truck 321 was modified by redesigning the front cab surface, rounding the corners and providing the diffuser angle. Pressure and velocity distribution are shown in Fig. 6, over two models.

### *4.1 Optimum Gridtest Use Velocity and Pressure*

In any problem, to obtain the right solution, optimization is necessary. Optimization is to be performed on the design variable for getting an effective solution.

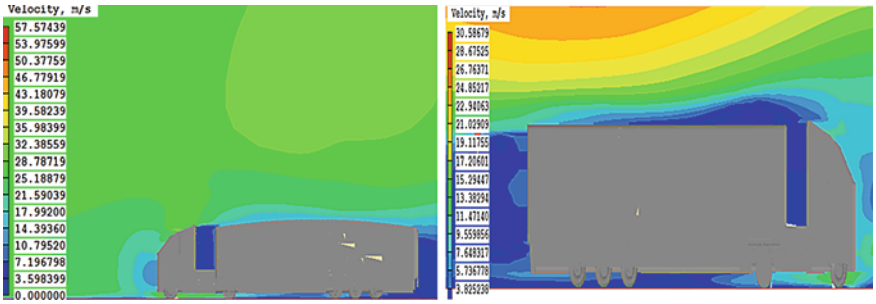


**Fig. 6** Modified model velocity distribution

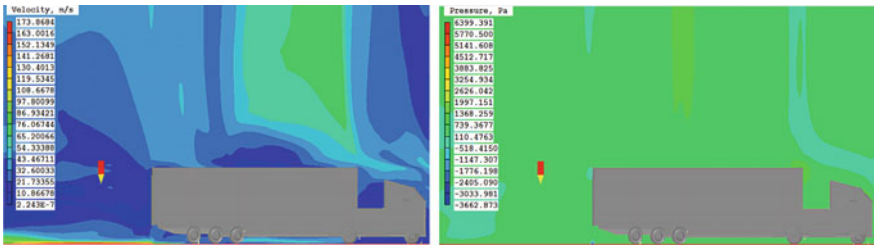


**Fig. 7** Model 1 velocity and pressure distribution (64 km/h)

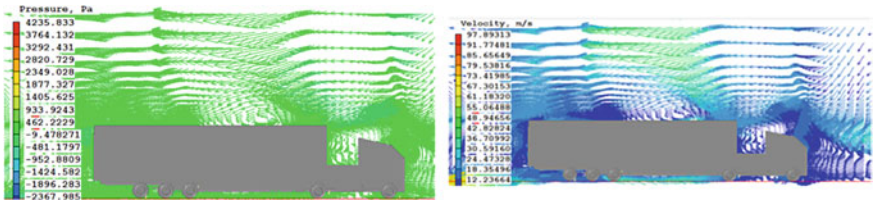


**Fig. 8** Velocity and pressure distribution 96 km/h

## *4.2 With and Without Cab*

An aerodynamic device like cab roof deflector will help in reducing the trailer front surface area over which airstrikes. Due to which the drag reduces. Due to a reduction in the drag, the amount of fuel consumed by the vehicle gets reduced. When cab roof deflector is not present, the front surface of the trailer is exposed and more air strikes the trailer surface and more drag is produced leading to higher fuel consumption. The velocity and pressure distribution of the models with and without cabs are shown in Figs. 7 and 8.

## *4.3 Drag Coefficient at Different Speeds*

Table 5 and Fig. 9 show that for all models, increase in speed causes an increase in

**Table 5** Drag coefficient at different speeds

| Drag coefficient at different speeds ($C_d$) | | | |
|---|---|---|---|
| Sino truck speed kmph | Model 1 | Model 2 | Model 3 |
| 64 | 0.4643 | 0.4123 | 0.3300 |
| 80 | 0.5492 | 0.512 | 0.4240 |
| 96 | 0.8943 | 0.8212 | 0.7480 |

**Fig. 9** Drag coefficient

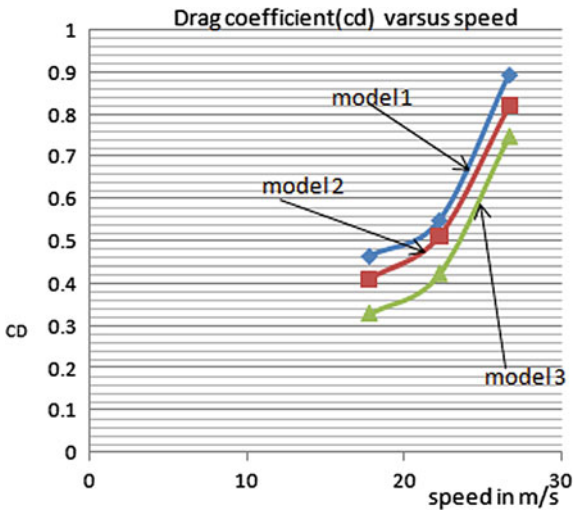


**Table 6** Drag force versus speed

| Speed km/h | Model 1 | Model 2 | Model 3 | Reduction of driving resistance |
|---|---|---|---|---|
| 64 | 947.9923 | 841.818 | 673.783 | 274.2093 |
| 80 | 1750.65 | 1632.678 | 1351.566 | 281.112 |
| 96 | 339,815.57 | 3655.226 | 3330.218 | 336.48 |

the drag coefficient. The percentage of $C_d$ reduction in each model which is *d*/*f* from each other due to shape and flow speed.

## *4.4 Total Drag Force* (N)

The variation of the drag force with speed is given in Table 6.

## *4.5 Total Resistance Force*

The variation of the total force is given in Table 7 and Fig. 10.

**Table 7** Total resistance

| Speed km/h | Model 1 | Model 2 | Model 3 |
|---|---|---|---|
| 64 | 1618.331 | 1514.1215 | 1412.457 |
| 80 | 2536.254 | 2192.654 | 1923.456 |
| 96 | 3107.783 | 2611.355 | 2412.452 |

**Fig. 10** Total resistance

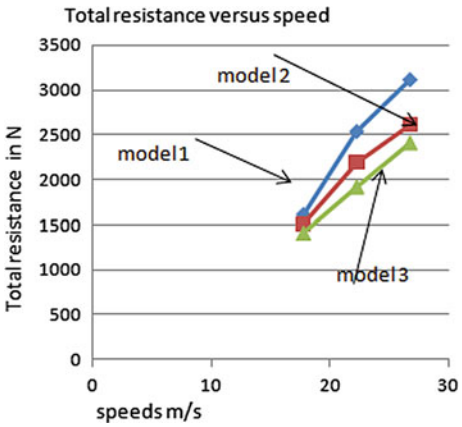


### *4.6 Power Requirement*

The power requirement applied by model 1 is greater than both model 2 and model 3; the power required in model 3 is more less than model Two. Meaning that model 1 consumes more fuel than model 2. Similarly, model 2 consumes more power than model 3.

### *4.7 Fuel Consumption*

The percentage of fuel reduction is given in Table 8. The amount of fuel saved is given in Table 9.

## 5 Conclusions

A 3D model of Sino truck model321 was drawn by using the dimensions measured from the actual truck. The model was prepared using CATIA-V5. The addons on Sino truck are investigated for their effectiveness in reducing the drag. The aerodynamic drag coefficient reduction is observed at 64 km/h, increasing the fuel economy

**Table 8** Fuel reduction

| Sino truck model 321 | Sino truck speed km/h | Aerodynamic drag reduction | % fuel reduction |
|---|---|---|---|
| Model 1 | 64 | – | – |
| | 80 | – | – |
| | 96 | – | – |
| Model 2 | 64 | 28.92 | 17.35 |
| | 80 | 22.79 | 13.67 |
| | 96 | 16.35 | 9.81 |
| Model 3 | 64 | 11.23 | 7.04 |
| | 80 | 6.73 | 4.28 |
| | 96 | 8.17 | 5.26 |

Amount of fuel save L/80 km = fuel consumption × percentages of fuel reduction/100 = 14 L/80 km × 3/5(fuel reduction/100)

**Table 9** Fuel saved in L/80 km

| Sino truck model | Speed km/h | Drag coefficient | Aerodynamic drag reduction to ($C_d$) | % fuel reduction | Fuel save L/80 km |
|---|---|---|---|---|---|
| Model1 | 64 | 0.4643 | – | – | |
| | 80 | 0.5492 | – | – | |
| | 96 | 0.8943 | – | – | |
| Model 2 | 64 | 0.4123 | 28.92 | 17.35 | 3.03 |
| | 80 | 0.512 | 22.79 | 13.67 | 0.23 |
| | 96 | 0.8212 | 16.35 | 9.81 | 0.171 |
| Model 3 | 64 | 0.3300 | 11.23 | 7.04 | 0.123 |
| | 80 | 0.4240 | 6.73 | 4.28 | 0.75 |
| | 96 | 0.7480 | 8.17 | 5.26 | 0.9 |

by 28.9%. At a speed of 96 km/h, the aerodynamic drag reduced increasing the fuel economy by 11.89%. The variation of drag coefficient ($C_d$) was also analyzed concerning body geometrical shape like advanced aerodynamic shaping, tractor-trailer gap, trailer underbody, trailer sideplate, frame extension, etc. Side plates device reduced drag on Sino truck model 1 at a speed of 64 km/h, which lead to the power saving of 2.0587 kW. And the power saving for model 3 at the same conditions is 6.953 kW. It is observed that as the speed is increasing, power saving is increasing. It is observed that drag is reduced in all the cases.

## References


1. Anderson JD (2001) Fundamentals of aerodynamics, 3rd edn. McGraw-Hill Editions, New York
2. Finnemore EJ (2005) Computational simulation of truck reducing aerodynamic devices. SAE International, 2005-01-3625
3. Cooper KR (1985) The effect of front-edge rounding and rear-edge shaping on the aerodynamic drag of bluff vehicles in ground proximity. SAE Paper No. 850288
4. Kourta A, Gilliéron P (2009) Impact of the automotive aerodynamic control on the economic issues. J Appl Fluid Mech 2(2):69–75
5. Hucho WH, Sovran G (1993) Aerodynamics of road vehicles. Ann Rev Fluid Mech 25(1):485–537 (1993)
6. Wood RM (2004) Impact of advanced aerodynamic technology on transportation energy consumption. SAE Technical Paper 2004-01-1306, Washington, DC
7. CheZakem R (2008) Aerodynamics of aftermarket rear spoiler. Bachelor thesis, University Malaysia Pahang
8. Marklund J, Lofdahl L, Danielsson H, Olsson G (2018) Performance of an automotive underbody diffuser applied to a sedan and a wagon vehicle. SAE Int J Passeng Cars Mech Syst 6(1):293–307
9. Cooper KR (1985) The effect of front-edge rounding and rear-edge shaping on the aerodynamic drag of bluff vehicles in ground proximity. SAE Paper 850288, SAE International, Warrendale, PA
10. Hucho W-H, Sovran G (1993) Aerodynamics of road vehicles. Annu Rev Inc. Fluid Mech 25:485–537
11. Hucho W-H (1998) Aerodynamics of road vehicles. SAE International, Warrendale, PA
12. Urban Bus Specifications—IIMinistry of Urban Development, Government of India
13. Kim C-H (2011) A streamlined design of a high-speed coach for fuel saving and reduction of carbon dioxide
14. Feliche E, Nallamothu RB (2017) A study on cause of rollover of sugar cane haulage semitrailer truck in Ethiopia Sugar Estate: case of Wonji Sugar Factory. Int J Eng Trends Technol (IJETT) V43(4):205–211
15. Yesfalgn Damissie H, Ramesh Babu N (2017) Aerodynamics drag reduction on locally built bus body using computational fluid dynamics (CFD): a case study at Bishoftu automotive industry. Int J Eng Res Technol (IJERT) 6(11). ISSN: 2278-0181
16. Ashagrie G, Nallamothu RB, Nallamothu AK, Nallamothu SK (2017) A study on driving stability of bus using computational fluid dynamics (CFD). Int J Res Appl Sci Eng Technol 5(XI)
17. Molla KY, Chul-Ho K, Ramesh Babu N (2017) Aerodynamic design of the Ethiopian train for energy economy under crosswind conditions. 년도한국철도학회추계계학술대회논문집, KSR 2017, South Korea
18. Siraj A, Ramesh Babu N, Srinivasa Reddy K (2019) Static analysis of dump truck chassis frame made of composite materials. Int J Eng Sci Technol 11(2):21–32
19. Alemayehu G, Nallamothu RB (2017) Programmable logic controller (PLC) application for hybrid electric vehicle (HEV) simulator. IJMET 8(9):281–292

# Design Improvement of MacPherson Strut Suspension System for Lighter Vehicle


**Yonas Hailemariam Alemayohu, Ramesh Babu Nallamothu, Anantha Kamal Nallamothu, and Seshu Kishan Nallamothu**

## 1 Introduction

The tyres are connected to the frame of a vehicle through a combination of mechanical components called suspension system. In addition to passenger comfort and safety, vehicle handling and ride, very much dependent on the vehicle suspension system. Due to this, engineers and scientists are exerting great effort in improving the suspension system. The suspension system isolates the passengers from the road shocks and maintains the comfort and safety of them. Also, the suspension should help in maintaining the contact between the wheels and road to maintain vehicle handling and steering stability. A good suspension system is very much necessary when a vehicle is being driven on real roads with potholes, bumps and imperfections. Vehicles move up and down when it is driven on the bumpy road [1].

In 1949, Earl MacPherson developed a MacPherson strut suspension system for the Ford Company. Different types of vehicles used this suspension system widely due to its less weight and compatibility in size (Fig. 1). This kind of suspension system is very popular in the front suspension of the vehicles. It is also used in rear suspension [2].

A suspension system is made up of a combination of linkages, springs and shock absorbers. Suspension allows the relative motion between wheels and the vehicle body. Also, it isolates the driver and passengers from road bumps and vibrations

Y. H. Alemayohu
Automotive Engineering Department, Mekelle University, Mekelle, Ethiopia

R. B. Nallamothu (✉)
Mechanical Systems and Vehicle Engineering Department, SoMCME, Adama Science and Technology University, Adama, Ethiopia
e-mail: ramesh.babu@astu.edu.et

A. K. Nallamothu · S. K. Nallamothu
Politecnico di Milano, Bovisa, Milano, Italy



K. Jha et al. (eds.), *Recent Advances in Sustainable Technologies*,
Lecture Notes in Mechanical Engineering,
https://doi.org/10.1007/978-981-16-0976-3_8

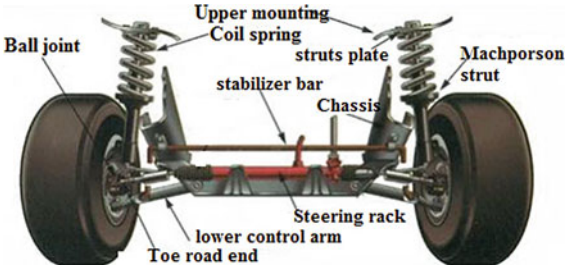


**Fig. 1** MacPherson strut suspension system

associated with the rough road. It helps in keeping the wheels always in contact with the road. Given below is the major role of the suspension system:

To give better handling and ride performance:

- Handling—ability of the vehicle to corner, brake and accelerate safely
- Ride—vehicle's ability to run smoothly on bumpy roads
  - To maintain steering control during manoeuvring
  - To support the weight of the vehicle
  - To support the control force produced due to
- Longitudinal acceleration and braking forces
- Lateral (cornering) forces
- Braking and acceleration torques [3].

## 2 Literature Review

Different works of the literature were reviewed related to MacPherson suspension system. The coil spring for MacPherson strut suspension system was designed, and it analysed the modified model for fatigue and static loading conditions. Among the existing materials, better fatigue strength material was selected for the analysis, by checking their mechanical properties. CATIA V5 was used for modelling, Hypermesh software is used for meshing, and ANSYS was used for the analysis [1].

Conceptual class A vehicle was developed. Optimum location of the roll centre of the MacPherson strut suspension was determined for class A vehicle by studying the influence of roll centre height on the dynamic behaviour of the MacPherson strut suspension. Dynamic behaviour of vehicle with different roll centre positions was analysed using ADAMS/car software. From the results, it is seen that steering response, body roll angle and body roll rate are very much influenced by the location of the roll centre. Also, it is observed that steering response and body roll are contradicting [2].

MacPherson strut suspension system which is used in a passenger car was appraised and optimized kinematically employing multi-body system approach using ADAMS/View software. The kinematic characteristics of the vehicle were studied

in this work. The required results of the camber angle change were not obtained in this research work. The increased camber angle value affected vehicle performance and ride stability [4].

For ride control application, a nonlinear model of a MacPherson strut suspension was proposed. In this model, suspension linkage kinematics was incorporated along with sprung mass vertical acceleration. The performances of the linearized and nonlinearized models were analysed and compared with conventional models. It is seen that the semi-active force has a greater influence in improving the ride quality better than the active force, whereas their effectiveness in improving the performance of the kinematic parameters is quite opposite. Using ADAMS software, the variations in kinematic parameters observed based on the linear model subjected to road disturbances are compared with that of results obtained with a virtual prototype of MacPherson suspension. It is observed that the results obtained in both analytical approaches agreeing with each other [5–8].

The causes of the premature failures of the upper strut mounts of MacPherson suspension are investigated. The service life of the components of the MacPherson strut suspension system was estimated by both numerical analysis and experimental tests [9–11]. Defect-tolerant analysis was used to assess the fatigue life of the components. It is observed from the investigation that the failure of the upper strut mount was not justified by the dynamic and static loads generated because of the irregularities of the road and vehicle manoeuvring during normal working conditions. It was concluded from the results obtained in the work, impulsive load caused failure of the upper strut mount that cannot be justified by the normal working condition for which they were designed [12–14].

The design of the suspension system was improved while discussing the features of the existing system. The modelling of suspension was done using UG, and dynamic analysis was carried out by the automatic dynamic of mechanical systems. In this work, the parameters changed are like track width, mounting head and other parameters. It is concluded that by modifying the parameters the performance of the suspension system was improved [15–17].

A comprehensive and systematic two-dimensional model of a MacPherson strut-type suspension was developed. The model was implemented using MATLAB and Simulink. The dynamics of this model was validated using a realistic two-dimensional model developed using ANSYS software. The vibrational characteristics of automobile system sprung mass were studied with the model developed by dynamic equations with the inclusion of the characteristics like a moment of inertia, mass, damping, stiffness, etc. The mathematical model was implemented on Simulink, and the obtained results were compared with results obtained from ANSYS model. It is seen that the values obtained with the mathematical model are very close to the values of acceleration and displacement of chassis of the automobile using ANSYS [18].

Vehicle designers' economical choice is MacPherson strut suspension. For the analysis of vehicle suspension and vehicle static characteristics, the leading arm has been checked previously. In this work, working of the leading arm was simulated and got the results, considering the dynamic analysis of the suspension in ADAMS

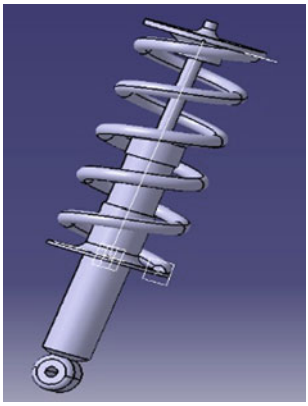

**Fig. 2** Assembly of shock absorber

software, load transfer and failure condition of the system. It is concluded from this work that design and analysis of leading arm were done for the sake of reduction of the weight and the system with leading arm suspension working well with the whole system. Modifications are done in the suspension system, and leading arm leads to the development of an effective suspension system [19].

## 3 Design and Modelling Using CATIA V5 Software

CATIA V5 is modelling software which allows 3D modelling and 2D drafting of elements. For performing the analysis of the suspension system in ANSYS, modelling of the system is to be done in any of the modelling software like SolidWorks, Pro-Engineers, or CATIA. CATIA V5 modelling software is preferred for the modelling in this thesis (Figs. 2, 3, 4, 5, 6 and 7).

**3D Models of the Existing Suspension**

## 4 Finite Element Analysis

Modelled mechanical components which are under load are generally analysed by FEA for specific results. This method is useful in the facelift of the existing product or in developing a new design for a product. It is also useful for a company to verify the proposed design as per the specifications given by the client before going for manufacturing. For improving the service condition or to improve the working

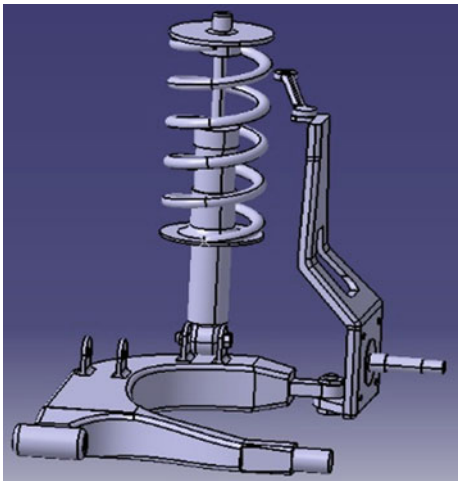

**Fig. 3** Assembly of the conventional front suspension

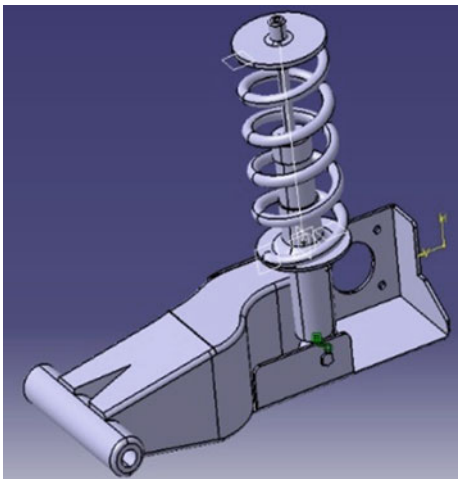

**Fig. 4** Assembly of conventional rear suspension

performance of a product, modification in the design of the existing product is necessary. FEA is very much helpful in determining the design modifications in the case of structural or product failure, to meet the new working conditions [20].

**Existing Front Suspension System**

**Boundary conditions**:

**Meshing**:

Shock absorber was meshed using tetrahedral elements. For the sake of obtaining better results, fine mesh is to be generated locally where higher stresses are expected under loading. Meshing is done with 761,949 number of elements and 1,113,869 number of nodes (Figs. 8 and 9).

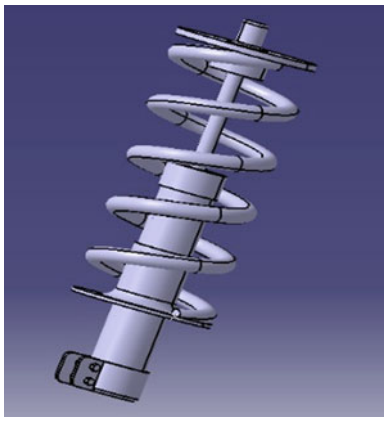

**Fig. 5** Assembly of new shock absorber

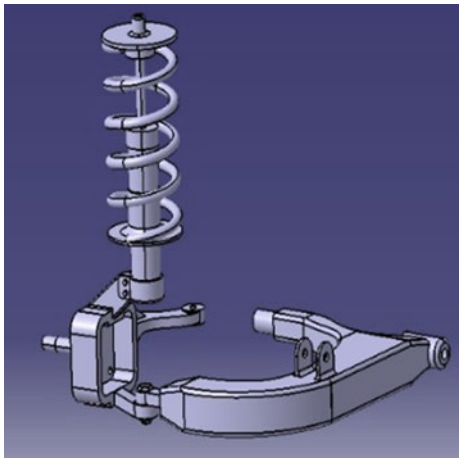

**Fig. 6** Assembly of the new front suspension

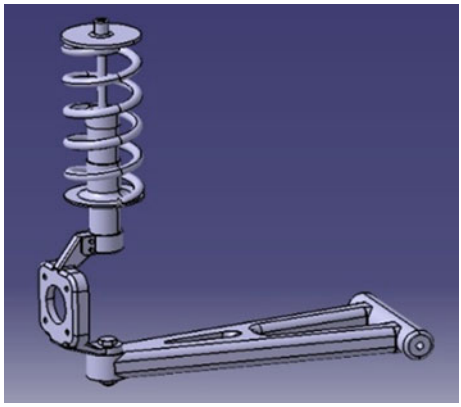

**Fig. 7** Assembly of the rear suspension

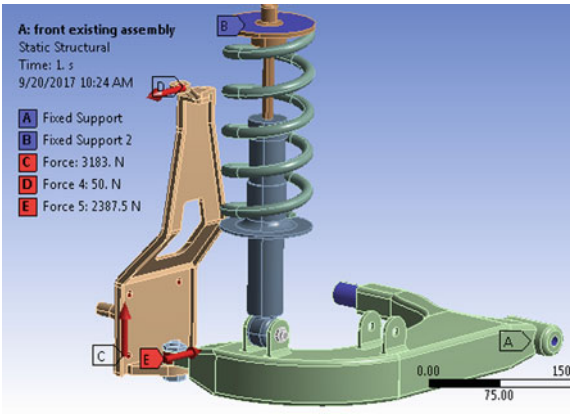


**Fig. 8** Loads and boundary conditions of the new front assembled system

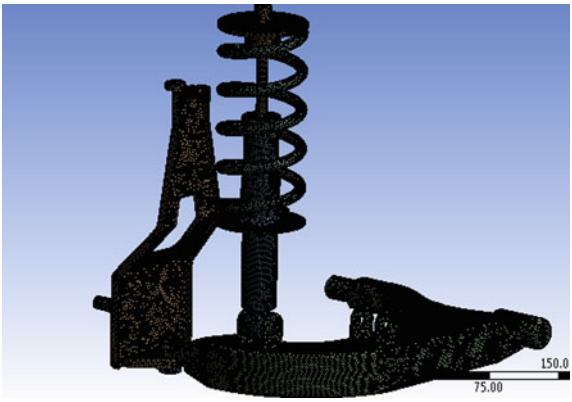


**Fig. 9** Meshing of the existing front system

**Stress analysis result**:
See Table 1.

## Existing Rear Suspension System

**Boundary conditions**:

**Meshing**:

**Table 1** Summarized results of existing front suspension system (Fig. 10)

| Analysis | Existing front suspension system results |
|---|---|
| Total deformation | 2.774 mm |
| Maximum shear stress | 247.68 MPa |
| Equivalent (von Mises) stress | 491.69 MPa |
| Equivalent elastic strain | 0.0024784 |
| Safety factor | 0.50845 |

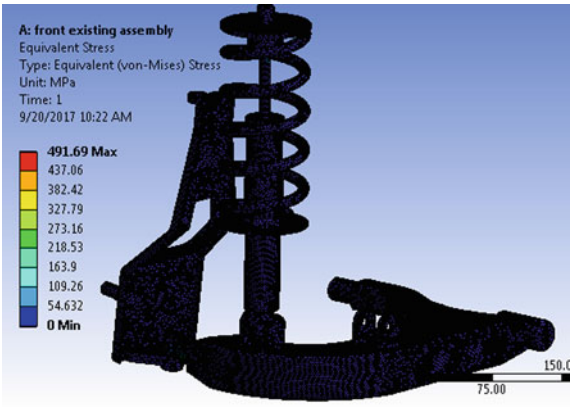


**Fig. 10** Equivalent (von Mises) stress

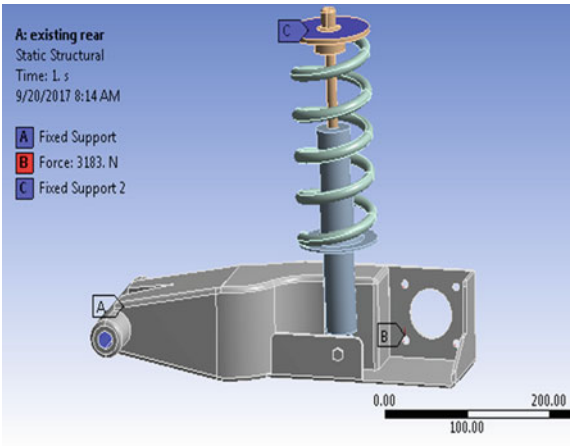


**Fig. 11** Loads and boundary conditions of new rear assembled system

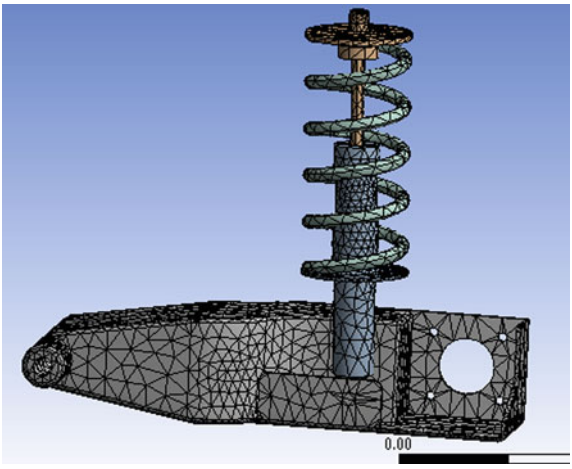


**Fig. 12** Meshing of new rear assembled system

**Table 2** Summarized results of existing rear suspension system (Fig. 13)

| Analysis | Existing rear suspension system results |
|---|---|
| Total deformation | 0.27627 mm |
| Maximum shear stress | 132.47 MPa |
| Equivalent (von Mises) stress | 245.78 MPa |
| Equivalent elastic strain | 0.001295 |
| Safety factor | 1.0172 |

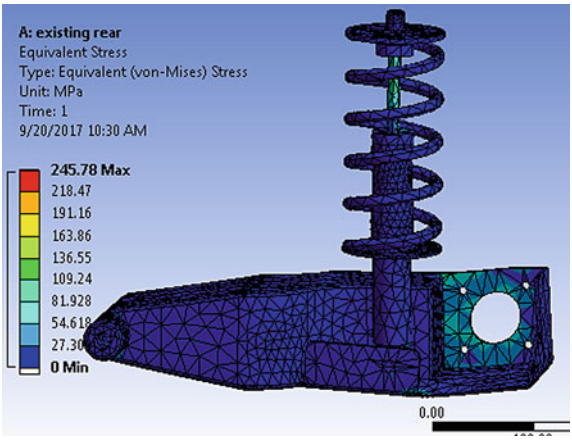


**Fig. 13** Equivalent (von Mises) stress

For the sake of obtaining better results, fine mesh is to be generated locally where higher stresses are expected under loading. Finally, the meshing was done with 27,484 number of nodes and 13,904 number of elements (Figs. 11 and 12).

**Stress analysis result**:

See Table 2.

**FEA of the Assembled New Suspension System**

**New Front MacPherson Suspension System**

**Boundary conditions**:

**Meshing**:

For the sake of obtaining better results, fine mesh is to be generated locally where higher stresses are expected under loading. Finally, 34,707 number of nodes and 7748 number of elements were found in the mesh (Figs. 14 and 15).

**Stress analysis result**:

See Table 3.

**New Rear MacPherson Suspension System**

**Boundary conditions**:

**Meshing**:

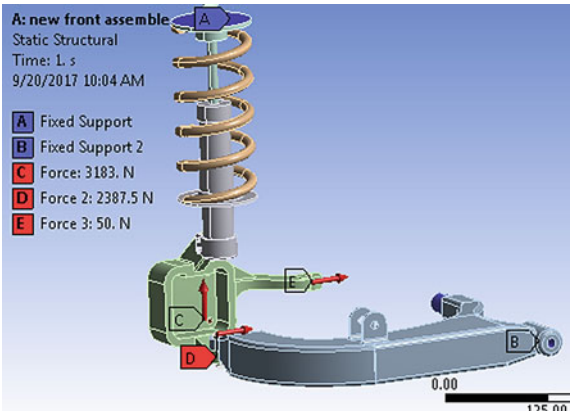


**Fig. 14** Loads and boundary conditions of new assembled system

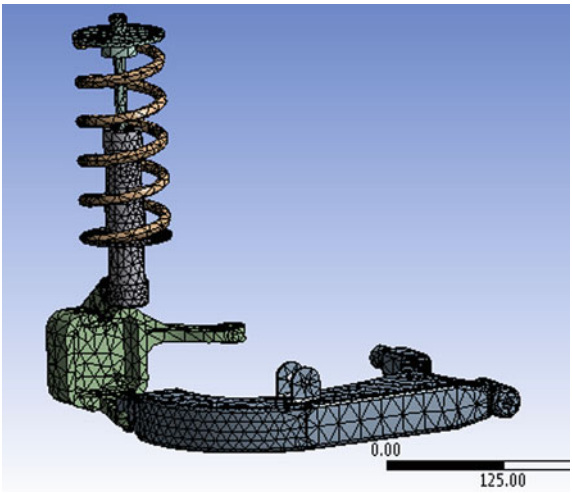


**Fig. 15** Meshing of the newly assembled system

**Table 3** Summarized results (Fig. 16)

| Analysis | New front MacPherson suspension system results |
|---|---|
| Total deformation | 0.427N29 mm |
| Maximum shear stress | 106.08 MPa |
| Equivalent (von Mises) stress | 192.13 MPa |
| Equivalent elastic strain | 0.0010421 |
| Safety factor | 1.0301 |

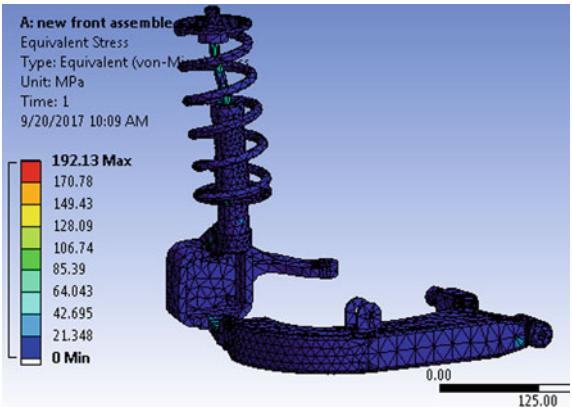


**Fig. 16** Equivalent (von Mises) stress

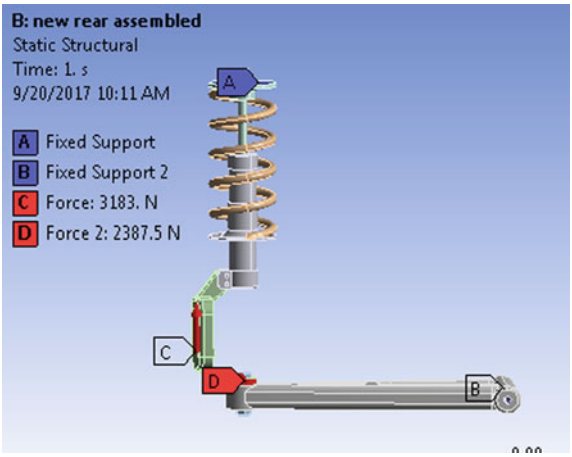


**Fig. 17** Loads and boundary conditions of new rear assembled system

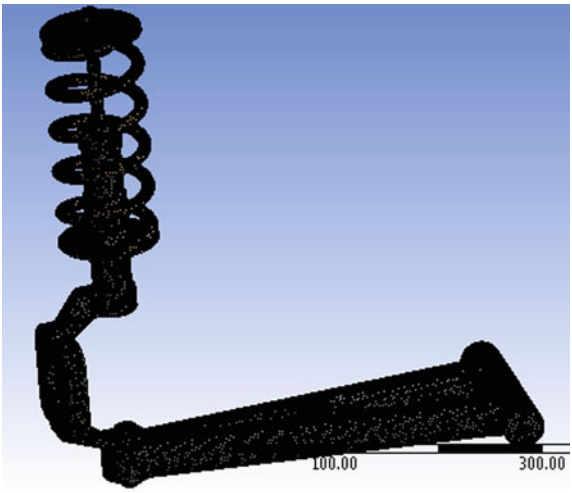


**Fig. 18** Meshing of the new rear assembled system

**Table 4** Summarized results of new rear MacPherson suspension system (Fig. 19)

| Analysis | New rear MacPherson suspension system results |
|---|---|
| Total deformation | 0.1564 mm |
| Maximum shear stress | 109.51 MPa |
| Equivalent (von Mises) stress | 191.98 MPa |
| Equivalent elastic strain | 0.0010141 |
| Safety factor | 1.3022 |

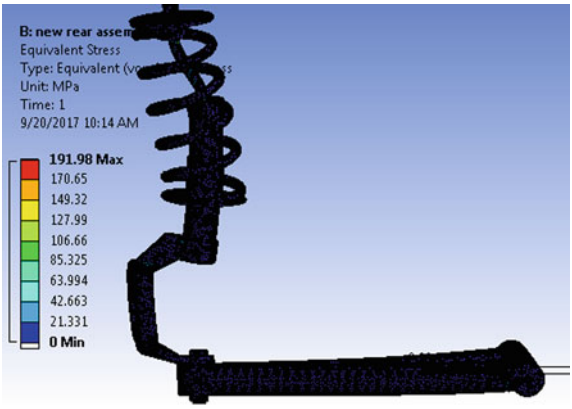


**Fig. 19** Equivalent (von Mises) stress

Meshing was done using tetrahedral elements. For the sake of obtaining better results, fine mesh is to be generated locally where higher stresses are expected under loading. Finally, 34,707 number of nodes and 774 number of elements were obtained in the mesh (Figs. 17 and 18).

**Stress analysis result**:

See Table 4.

## 5 Result and Discussion

**Assembled Existing Suspension System**

For the existing model, the maximum magnitude of von Mises stress obtained at the front and rear suspension system is 491.69 MPa and 245.78 MPa, respectively, and the maximum shear stress magnitude is 247.68 MPa and 132.47 MPa, respectively. But the factor of safety is 0.50845 and 1.0172, respectively. So, it is not safe for stiffness and thickness of the structure is not at a reliable stress level. Therefore, it indicates that it is necessary to change the suspension system of the vehicle.

**Assembled New Suspension System**

For the new model, the maximum von Mises stress obtained at the front and rear suspension system is 192.13 and 191.98 MPa and the maximum shear stress magnitude is 106.8 and 109.51 MPa. But the factor of safety is 1.3012 and 1.3022, respectively. So, it is safe for stiffness and thickness of the structure is at a reliable stress level. Therefore, it indicates that the newly designed model is acceptable for the suspension system of the vehicle.

## 6 Conclusion

All the components of new and existing suspension systems are modelled using CATIA V5 modelling software and imported into ANSYS workbench 16.0 to analyse different parameters, and the results were compared.

The new models observed to be safe than the existing in all aspects. So, the problem in the lateral direction which is flexible camber curve is solved, because the MacPherson suspension system has good camber curve not as flexible as other suspension system and also the stress in the existing system leads the system to have flexible camber; this is corrected in the new model. Also, the steering arm position is corrected to the middle of the knuckle to balance the steering force distribution.

## References

1. Dodamani SS, Suresh C, Nagaraj D (2016) Design and fatigue analysis of McPherson strut assembly coil spring. IJIRSET 5(7)
2. Meshkatifar J, Esfahanian M (2015) Optimal roll center height of front McPherson suspension system for a conceptual class A vehicle. J Appl Comput Mech 1(1)
3. Vivekanandan N, Gunaki A, Acharya C (2014) Design, analysis and simulation of double wishbone suspension system. IIJME 2(09)
4. Vadodaria D, Jain SC, Sharma P (2015) Analysis of quarter model of Macpherson and modified suspension system. Int J Adv Res Sci Eng IJARSE 3(8)
5. Fallah MS, Bhatt R (2008) New non-linear model of Macpherson suspension system for ride control application. In: American control conference, June 2008
6. Colombo D, Gobbi M, Mastinu G, Pennati M (2009) Analysis of an unusual McPherson suspension failure. Eng Fail Anal 16
7. Pathmasharma S, Suresh JK, Viswanathan P, Subramanian R (2013) Analysis of passenger car suspension system using Adams. Int J Sci Eng Technol Res (IJSETR) 2(5)
8. Purushotham A (2013, May–June) Comparative simulation studies on Macpherson suspension system. Int J Mod Eng Res (IJMER) 3(3)
9. Wakjira A, Nallamothu RB (2013) Microcontroller based rear end anti-collision warning system for vehicles. Glob J Eng Des Technol G.J.E.D.T. 2(6):14–21
10. Abebe L, Nallamothu RB, Subrahmanyam KHS, Nallamothu SK, Nallamothu AK (2016) Thermal analysis of disc brake made of different materials. SSRG Int J Mech Eng (SSRG-IJME) V3(6):5–9

11. Feliche E, Nallamothu RB (2017) A study on cause of rollover of sugar cane haulage semitrailer truck in Ethiopia Sugar Estate: case of Wonji Sugar Factory. Int J Eng Trends Technol (IJETT) V43(4):205–211
12. Yesfalgn Damissie H, Ramesh Babu N (2017) Aerodynamics drag reduction on locally built bus body using computational fluid dynamics (CFD): a case study at Bishoftu Automotive Industry. Int J Eng Res Technol (IJERT) 6(11). ISSN: 2278-0181
13. Alemayehu G, Nallamothu RB (2017) Programmable logic controller (PLC) application for hybrid electric vehicle (HEV) simulator. Int J Mech Eng Technol (IJMET) 8(9):281–292
14. Negera DW, Bhaskaran J, Ilmi I, Nallamothu RB (2019) Characterisation of hybrid composite made of false banana fiber and sisal fiber. Int J Eng Adv Technol (IJEAT) 9(2). ISSN: 2249-8958
15. Getu D, Nallamothu RB, Masresha M, Nallamothu SK, Nallamothu AK (2020) Production and characterization of bamboo and sisal fiber reinforced composite for interior automotive body application. Mater Today Proc. https://doi.org/10.1016/j.matpr.2020.08.780
16. Alemayehu Z, Nallamothu RB, Liben M, Nallamothu SK, Nallamothu AK (2020) Experimental investigation on characteristics of sisal fiber as composite material for light vehicle body applications. Mater Today Proc. https://doi.org/10.1016/j.matpr.2020.07.386
17. Ashagrie G, Nallamothu RB, Nallamothu AK, Nallamothu SK (2017) A study on driving stability of bus using computational fluid dynamics (CFD). Int J Res Appl Sci Eng Technol 5(XI)
18. Molla KY, Chul-Ho K, Ramesh Babu N (2017) Aerodynamic design of the Ethiopian train for energy economy under crosswind conditions. 년도 한국철도학회 추계계학술대회 논문집, KSR 2017, South Korea
19. Siraj A, Ramesh Babu N, Srinivasa Reddy K (2019) Static analysis of dump truck chassis frame made of composite materials. Int J Eng Sci Technol 11(2):21–32
20. Kannan R, Rajaganapathy C (2014) Finite element analysis of shock absorber for spring steel and carbon fibre. Int J Eng Sci Res Technol 3(5)

# Design and Analysis of Composite Drive Shaft for Rear-Wheel-Drive Vehicle


**Lelisa Gezu, Ramesh Babu Nallamothu, Seshu Kishan Nallamothu, Anantha Kamal Nallamothu, and Dawit Tafesse**

## 1 Introduction

The composite material technology is very widely used by automotive industries for the construction of structural components of the vehicle for reducing the overall weight of the vehicle for achieving better fuel economy. Reduction of weight of an automobile, with no compromise in the cost, reliability and quality, is the main target of automobile manufacturers. Weight reduction of drive shaft also contributes to the overall weight reduction of the vehicle. Fuel consumption of the vehicle is directly related to the vehicle's weight [1]. The values of specific modulus and specific strength are high for advanced composite materials like glass, Kevlar, carbon and graphite with suitable resins. Due to this, they are used in automobile applications [2]. A drive shaft is a key component of the power train of vehicle, which connects other components of the power train at different angles using universal joints and transmits the power to other components. There is a fuel consumption reduction of about 7% for every weight reduction of 10% of the vehicle 7% [3]. Traditionally, steel (SM45C) is used to make drive shaft. In a vehicle, power gets transferred from the transmission system to rear axle through the drive shaft. All components of drive shaft are rotating and possess a certain amount of mass [4, 5]. In general, energy

L. Gezu
Flower Construction PLC, Addis Ababa, Ethiopia

R. B. Nallamothu (✉)
Mechanical Systems and Vehicle Engineering Department, SoMCME, Adama Science and Technology University, Adama, Ethiopia
e-mail: ramesh.babu@astu.edu.et

S. K. Nallamothu · A. K. Nallamothu
Politecnico di Milano, Bovisa, Milano, Italy

D. Tafesse
Hawassa University, Awasa, Ethiopia



K. Jha et al. (eds.), *Recent Advances in Sustainable Technologies*,
Lecture Notes in Mechanical Engineering,
https://doi.org/10.1007/978-981-16-0976-3_9

**Fig. 1** Two-piece driveline with bearing support in between

loss exists in rotating masses of a vehicle, which is about 17–22% of the total power generated in the vehicle [6]. Heavy rotating parts take more energy in spinning. Mass of the rotating parts is to be reduced to save the energy [7, 8]. The term drive shaft and propeller shafts are used interchangeably [8, 9]. The longer trucks with wheelbases from 3.4 to 4.8 m use drivelines composing of two pieces, consisting of two different shafts with bearing support in between. There may be an overlap depending on the type of the vehicle (Fig. 1) [10, 11].

For meeting the requirements of high-performance vans, light trucks and automobiles, lightweight drive shaft tubes which are made up of graphite/carbon/fibreglass/aluminium were developed by automotive industries [12, 13]. The specific stiffness of the composite material made of carbon fibre epoxy is four times more than that of steel and aluminium. Because of higher stiffness, there is a possibility of usage of composite material in the manufacturing of single-piece drive shaft [14, 15]. Reduction in drive shaft weight is the major significance of using composite material. In recent decades, usage of drive shafts made of composite materials in high-performance race cars is gaining higher attention. Breaking of steel drive shaft creates havoc, splattering the pieces in all directions, damaging the road surface, damaging the body of the vehicle and even throwing the car in the air. But breakage of composite drive shaft does not pose any danger, since it disintegrates into very thin fibres not creating any challenge for the drivers. The composite shaft dampens the vibrations, due to which wear in the components of drive shaft reduces, the traction of the tyre increases and the comfort of the onboard members increases. Part complexity, assembly time, maintenance cost and inventory cost reduce, due to the use of single torque tubes made of composite materials [16–18].

## 2 Design

The properties of steel material are taken from the references.

**Specification of the Problem**

For avoiding the whirling of the drive shaft, the fundamental natural frequency of bending of the drive shaft is to be more than 6500 rpm. The amount of torque transmission is to be more than 3500 N m, in drive shafts of small trucks, passenger

**Table 1** Specifications of the existing vehicle drive shaft [9]

| S. No. | Name | Notation | Value | Unit |
|---|---|---|---|---|
| 1 | Ultimate torque | $T_{max}$ | 3500 | N m |
| 2 | Max. speed of shaft | $N_{max}$ | 5700 | rpm |
| 3 | Length of shaft | $L$ | 1250 | mm |
| 4 | Outer diameter of a shaft | $D_o$ | 90 | mm |
| 5 | Inner diameter of a shaft | $D_i$ | 86 | mm |

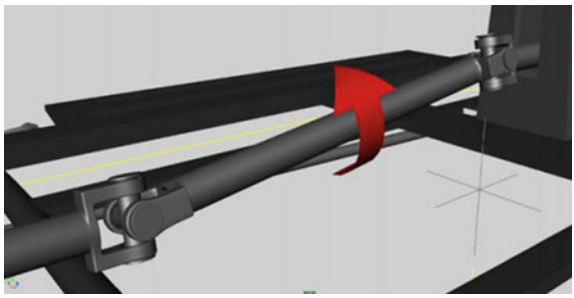

**Fig. 2** Transmission of torque by drive shaft [10]

cars and vans. The maximum size of the outer side diameter of the drive shaft is to be around 100 mm due to space restrictions. In this, outer diameter is fixed as 90 mm. Optimum design of drive shaft used in the transmission of power is necessary. The specified requirements of the drive shaft are given in Table 1.

In general, for drive shafts, steel (SM45C) is used. The properties of this material are taken from the references. The design specifications to be satisfied by drive shaft made of steel are as follows:

1. Capability in transmitting the torque.
2. Torque capability in buckling.
3. Bending natural frequency (Fig. 2).

**Torsional Strength**

Normally, the drive shaft is subjected to torsional load. The maximum shear stress ($\tau_{max}$) at the outer diameter ($D_o$) and inner diameter ($D_i$) of the shaft is given by:

$$\tau = \frac{G \times \theta \times r}{\ell} \tag{1}$$

where

$T$ is the maximum torque applied in N m.
$r$ mean radius of the shaft in m.

$$\text{Total deformation, } \delta = \emptyset * \ell \tag{2}$$

**Torsional Critical Buckling (TCR)**
The cylindrical shell of the composite drive shaft is considered as isotropic, and the buckling torque is given by equation

$$T_{\text{cr}} = \left(2\pi r^2 t\right)(0.272)\left(E_x E_y^3\right)^{0.25}(t/r)^{1.54} \tag{3}$$

**Bending Natural Frequency**
Pinned-pinned beam idealization is used. The equation used to calculate the least natural frequency is

$$f_{\text{nb}} = \frac{\pi}{2}\sqrt{\frac{g E_x I_x}{W L^4}} = \frac{\pi}{2}\sqrt{\frac{E_x I_x}{m_1 L^4}} \tag{4}$$

$W/g =$ the mass per unit length.

**Mass of E-Glass/Epoxy Drive Shaft**

$$m = m_1 \times L \tag{5}$$

**Percentage of Mass Saving**

$$= \left(1 - \frac{\text{mass of composite}}{\text{mass of steel}}\right) \times 100 \tag{6}$$

## 3 Modelling and Analysis

**Modelling in CATIA V5**
CATIA supports multiple stages of product development, conceptualization, engineering (CAE), design (CAD) and manufacturing (CAM).

**Assumptions Considered in ANSYS**
In the mechanical engineering field, for solving different types of problems numerically, ANSYS is widely used. ANSYS is a famous general-purpose finite element analysis software package. Some of the assumptions are made during this analysis like the rotational speed of the shaft is constant, the shaft is of circular uniform cross section, no nonlinear and damping effects are existing, the material is elastic and

linear. It is considered as a plane stress problem since the loads acting out of plane are not applied.

**Modelling and Simulation**

Model of the drive shaft was prepared as per the specifications using CATIA software (Fig. 3). The analysis was done after importing the model into ANSYS and meshing (Fig. 4). The model was analysed for stresses, natural frequencies and deformations after applying boundary conditions and loads. The results were compared among different models. The model which has less torsional stress and with natural frequency closer to steel was selected.

It is observed that there exists a maximum deformation of 0.05 m, and the minimum is 0 m. The diameter of the structural steel shaft is 90–86 mm (Fig. 5). Maximum strain obtained is 0.0033 (Figs. 6 and 7).

The total deformation for the shaft of glass fibre with diameter 90–86 is maximum of 0.157e−5 m and minimum of 0 (Fig. 8).

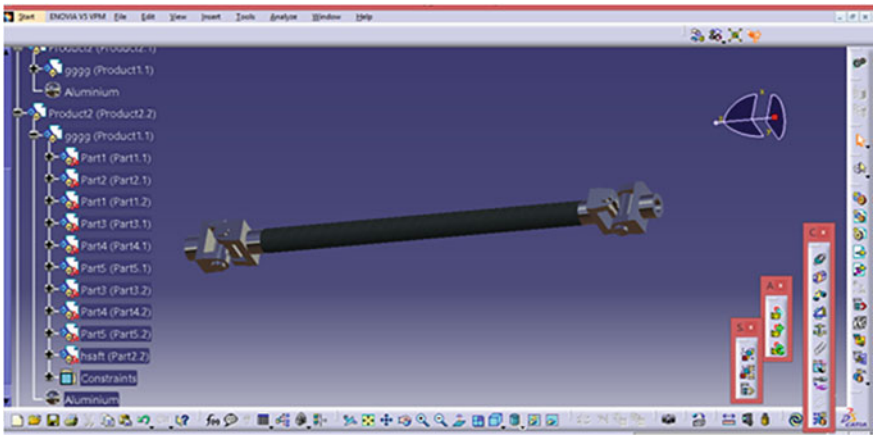


**Fig. 3** CATIA modelled drive shaft

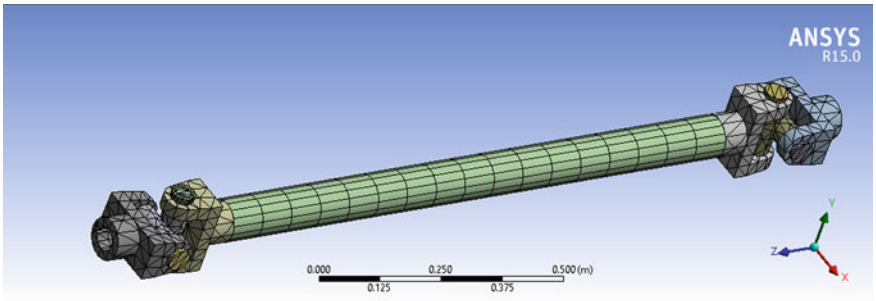


**Fig. 4** Mesh of the drive shaft

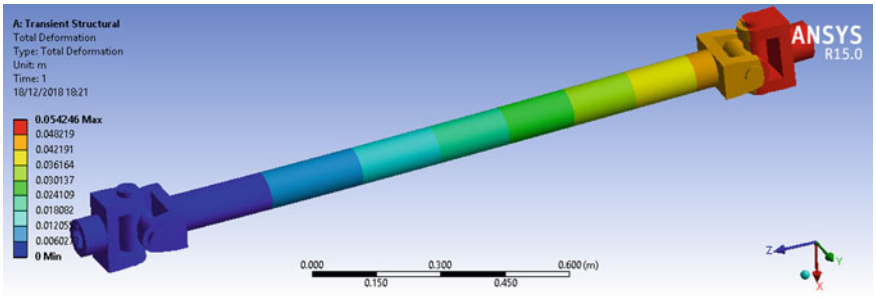


**Fig. 5** Total deformation of steel drive shaft

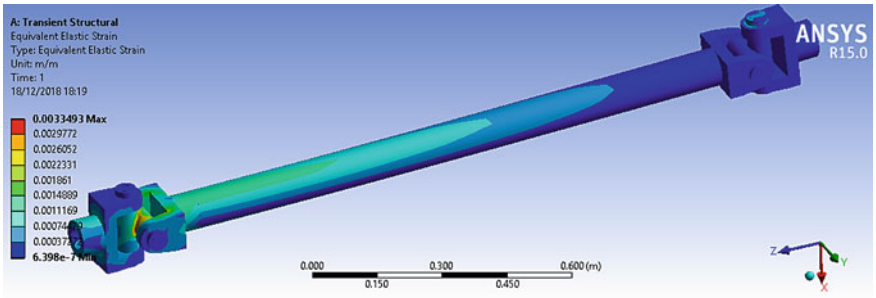


**Fig. 6** Steel drive shaft elastic strain

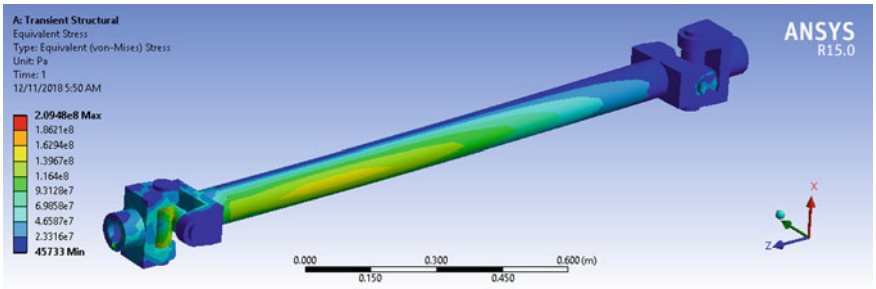


**Fig. 7** Von Mises stress of steel drive shaft

The equivalent elastic strain of the glass fibre of diameter 90-86 is maximum of 0.0080 (Fig. 9).

From the ANSYS analysis, it is observed that the conventional shaft made of steel produced maximum shear and von Mises stresses for a given loading (Fig. 7). The shaft made of E-glass produced maximum stress and deformation (Fig. 10).

There exists a maximum von Mises and shear stress for convectional steel shaft (Fig. 7), with the application of given transmission loads, while there exists maximum

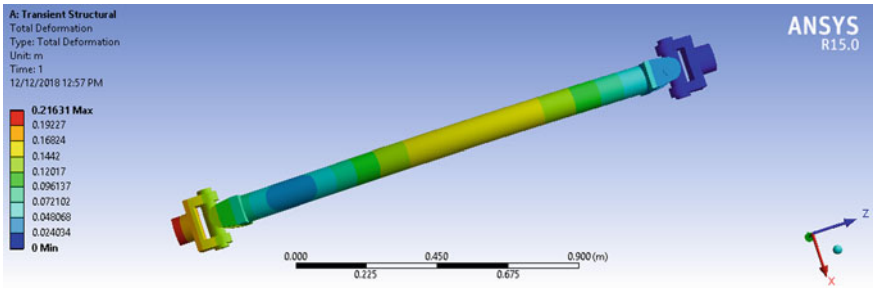


**Fig. 8** Deformation of glass/epoxy fibre drive shaft

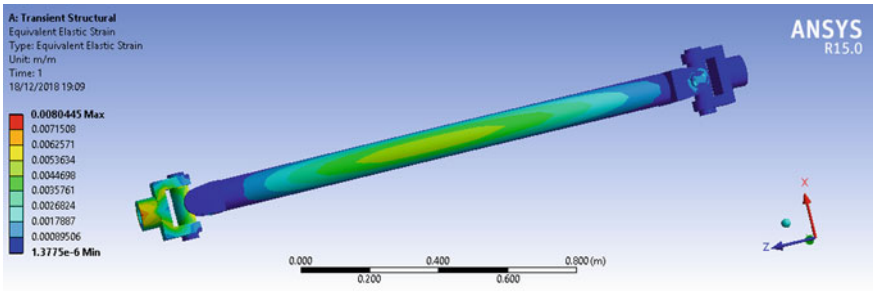


**Fig. 9** Elastic strain of glass/epoxy fibre drive shaft

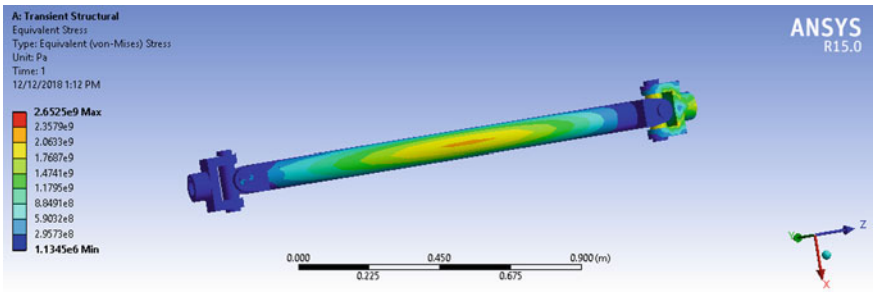


**Fig. 10** Von Mises of glass/epoxy fibre drive shaft

stress in E-glass composite shaft (Fig. 10) for the given load application but it registered the maximum deformation. To minimize the weight, a single-piece composite drive shaft was designed for rear-wheel-drive automobile. A high-strength carbon composite is used for this purpose.

## 4 Results and Discussion

In this work, for carrying out the analysis ANSYS 15.0 was used. In this analysis, nonlinear parameters like inertia and damping effects were neglected. Loading was applied to represent rotational moments. No direct load is acting on the shaft; only it is subjected to a torque. Only static failure was done on the drive shaft (Tables 2 and 3).

From the results, it is observed that the analytical results and FEA results are in good agreement. The analysis was done for composite materials for the sake of weight reduction while checking the von Mises stresses and frequency. About 46% of weight reduction was achieved with composite materials when compared to conventional steel. Whirling of the shaft also can be avoided by rotating the shaft at lower speeds than the first natural bending frequency. The energy lost in rotating of the heavy masses is reduced with this design.

Figure 11 shows that natural frequencies are varying for both materials of E-glass–epoxy composite and steel. It is found that natural frequency increases with an increase in the mode of vibration from software result (Fig. 12).

One-piece composite tubing may replace a two-piece steel setup due to tailor ability of the material. Average vehicle can also be reduced by downsizing vehicles by using an alternative material. Reduction in vehicle size and weight can significantly reduce fuel consumption. Reducing 100 kg weight of vehicles, $CO_2$ emissions can be decreased by about 5 g/km [11].

**Table 2** Validation and comparison of analytical and ANSYS results for steel and composite material

| Results | Steel | | E-glass/Epoxy | |
|---|---|---|---|---|
| | Analytical | ANSYS | Analytical | ANSYS |
| Deformation (m) | 0.0318 | 0.05 | 0.157 | 0.2 |
| Maximum shear strain (m/m) | 0.0255 | 0.0033 | 0.126 | 0.0080 |
| Maximum shear stress (MPa) | 147 | 83 | 50 | 97 |
| Weight (kg) | 8.661 | 8.661 | 4.66 | 4.76 |

**Table 3** Comparison of analytical result for torque and natural frequency

| | Torque transmission capacity (N m) | Torsion buckling capacity (N m) | Natural frequency (Hz) |
|---|---|---|---|
| Specification | 3500 | 3500 | 6500 (rpm) |
| Steel SM45C | 5957.9 | 12,347.7 | 129.9 |
| Glass/Epoxy | 3500 | 14,195 | 124 |

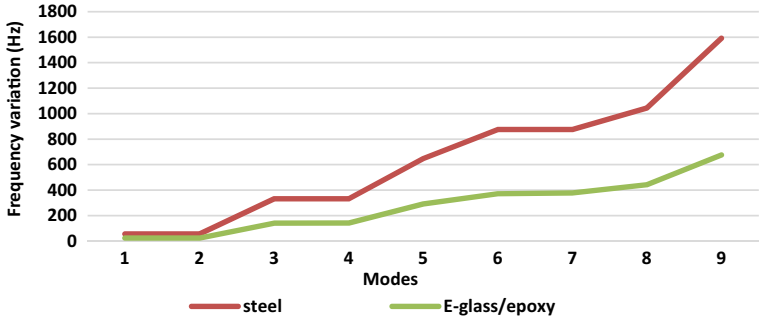


**Fig. 11** Natural frequency variation graph for both materials

**Fig. 12** Chart representation of both drive shaft weights

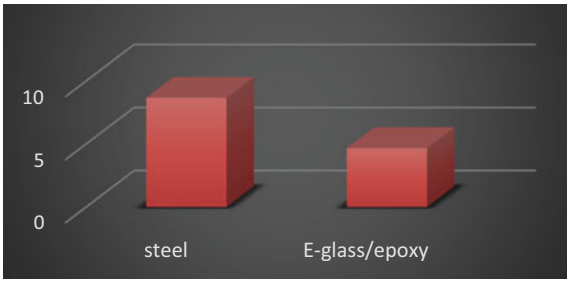


## 5 Conclusion

Based on the finite element analysis and the analytical calculation done, the following conclusions were drawn. Weight saving of about 46% was achieved with the usage of composite material in place of conventional steel. Considering the deformation, resultant frequency, shear stress-induced and also saving in weight, it is clear that the prepared composite is possessing required characteristics for replacing the steel drive shaft by composite drive shaft.

In addition to the benefit of being less weight, the usage of E-glass fibre/epoxy resin also ensures less noise and vibration.

- It can be considered to replace the conventional two-piece steel shaft with a single-piece drive shaft made of composite material.
- There is a considerable weight reduction of about 46%.
- The composites are recyclable, so they can be reused.
- Usage of composite materials gives the benefit of less noise and vibration in addition to the reduction in weight.

## References


1. Sridhar A, Mohan R, Vinoth Kumar R (2016) Design and analysis of composite driveshaft. Int J Sci Eng Res
2. Lee DG, Kim JK, Cho DH (2004) Design and manufacture of an automotive hybrid aluminum/composite drive shaft. J Compos Struct
3. Anup B, Kristian B, Lynette C, Christopher E, Tiffany G, John H, Emmanuel K, Matthew K, Malcolm W (2008) Reducing transportation's petroleum consumption and GHG emissions. MIT
4. Sah MK, Sudhakara D (2018) Design and analysis of composite drive shaft using ANSYS. Int J Comput Eng Res (IJCER)
5. Salzar RS (1998) Design considerations for rotating laminated metal-matrix-composite Shafts. CUNY Graduate School of Civil Engineering, NY 10031, USA
6. Kushwaha D, Saxena G (2014) Optimal design and analysis of composite drive shaft for a light commercial vehicle. IJAERD
7. Khoshravan MR, Paykani A, Design of a composite drive shaft and its coupling for automotive application, Iran
8. EL-Wazery MS, EL-Elamy MI, Zoalfakar SH (2017) Mechanical properties of glass fiber reinforced polyester composites. Int J Appl Sci Eng Egypt
9. Narsaiah J, Venkatesh K, Avinash P (2017) Design & analysis of composite drive shaft made of different materials for application in automobiles. IJSRD 5
10. Virendra VM, Patel AB (2015) Design, analysis and optimization in automobile drive shaft. Int J Innov Res Sci Technol (IJIRST)
11. Sunwenlong C, Lu W (2016) Analysis of energy-saving and emission reduction of vehicles using lightweight materials. Beijing Institute of Technology, China
12. Abebe L, Nallamothu RB, Subrahmanyam KHS, Nallamothu SK, Nallamothu AK (2016) Thermal analysis of disc brake made of different materials. SSRG Int J Mech Eng (SSRG-IJME) V3(6). ISSN: 2348-8360. https://doi.org/10.14445/23488360/IJME-V316P102
13. Ashagrie G, Nallamothu RB, Nallamothu AK, Nallamothu SK (2017) A study on driving stability of bus using computational fluid dynamics (CFD). Int J Res Appl Sci Eng Technol 5(XI)
14. Feliche E, Ramesh Babu N (2017) A study on cause of rollover of sugar cane haulage semi-trailer truck in Ethiopia Sugar Estate: case of Wonji Sugar Factory. IJETT V43(4):205–211. ISSN:2231-5381. https://doi.org/10.14445/22315381/IJETT-V43P235
15. Negera DW, Bhaskaran J, Ilmi I, Nallamothu RB (2019) Characterisation of hybrid composite made of false banana fibre and sisal fibre. IJEAT 9(2). ISSN: 2249-8958
16. Getu D, Nallamothu RB, Muluken M, Nallamothu SK, Nallamothu AK (2020) Production and characterization of bamboo and sisal fibre-reinforced composite for interior automotive body application. Mater Today Proc. https://doi.org/10.1016/j.matpr.2020.08.780
17. Alemayehu Z, Nallamothu RB, Mekonnen L, Nallamothu SK, Nallamothu AK (2020) Experimental investigation on characteristics of sisal fibre as a composite material for light vehicle body applications. Mater Today Proc. https://doi.org/10.1016/j.matpr.2020.07.386
18. Siraj A, Ramesh Babu N, Srinivasa Reddy K (2019) Static analysis of dump truck chassis frame made of composite materials. Int J Eng Sci Technol 11(2):21–32

# Improvement of Structure and Body of Three-Wheeler Vehicle


**Bekele Eromo, Ramesh Babu Nallamothu, Anantha Kamal Nallamothu, and Seshu Kishan Nallamothu**

## 1 Introduction

In urban and rural areas these days, three-wheeler vehicles (TWV) became an important means of transportation. In some of the second-grade cities, these vehicles are used as intermediate public transport (IPT), on selected routes. Even these vehicles are being used as means of transportation between villages, small towns and city borders. Mostly, they operate in the outskirts of the cities. Most of the three-wheelers also designed as a means of transporting goods for transporting goods between cities. These three-wheeler vehicles became very popular due to their ability to manoeuvre in small space in narrow streets. Running cost and the initial cost of the three-wheeler vehicles are very less. Another advantage of these vehicles is the less space required for parking. For short-distance travel, three-wheelers are best and even better and faster than the city busses and travelling expenses are less compared to a four-wheeled taxi. Particularly in India, three-wheeled vehicles are predominantly used in every part of the country. The demand for such vehicles is growing day by day, and even the sales of these vehicles very much higher than sales of all other vehicles together. The usage of these vehicles in African countries also growing at a higher rate [1].

B. Eromo
Mechanical Engineering Department, Wachamo University, Hosaena, Ethiopia

R. B. Nallamothu (✉)
Mechanical Systems and Vehicle Engineering Department, SoMCME, ASTU, Adama, Ethiopia

A. K. Nallamothu · S. K. Nallamothu
Politecnico di Milano, Milan, Italy



K. Jha et al. (eds.), *Recent Advances in Sustainable Technologies*,
Lecture Notes in Mechanical Engineering,
https://doi.org/10.1007/978-981-16-0976-3_10

## 2 Literature Review

The vehicle structure is subjected to various types of static and dynamic loads during its operation. So, the structure of the vehicle is to be designed so that it can withstand such loads to which it is subjected. The outer shape of the body is to be designed aerodynamically to reduce aerodynamic drag, to improve fuel economy and reduce the emissions. The interior space should be able to comfortably accommodate passengers. The suspension system is to be designed to isolate the road vibrations from the body of the vehicle. The vehicle body is to be designed to avoid the transfer of the aerodynamic noise and vibrations to the occupants. The structure of the vehicle has to be integral enough and should be able to protect the occupants during crashes.

The structural design of the vehicles improving year by year to meet the ever-growing needs and requirements of the market. The design of the vehicle structure is a compromise between the contradicting requirements. Many parameters are to be considered while designing a vehicle structure like availability of the materials, type of energy source for propulsion, regulations related to safety and emissions, manufacturing facilities, availability of the funds, access to engineering technology and competition in the market.

There are mainly two types of categories of the structures: one is body over the frame and the second one is uni-body structure. Body over the frame of a sport utility vehicles and passenger cars are consisting of body, frame and front sheet metal. The vehicle body should be rigid enough to provide the necessary resistance to bending and torsion. Passenger cars have a crumple zone, which gets crushed absorbing most of the impact energy and protects the passenger compartment. Crumple zone deforms plastically during the frontal crash and absorbs most of the energy avoiding the transfer of the energy to the passenger compartment safeguarding the passengers. All modules of the structure are bolted together. For the sake of isolating high-frequency vibrations, shock-absorbing body mounts are being used between the body and the frame. Since the early 1980s, the passenger cars produced are mostly uni-body structures. Uni-body structures combine all like body, frame and frontal crumple zone. The parts are constructed with pressed sheet steel and fastened with spot welding and other fastening methods. The major advantages of unit-body are less weight and it is very much rigid [2–4].

### Impact Analysis

**Frontal Impact Analysis**—In general, steel members are used for the construction of the frame. The frame consists of ties and struts. The ties are subjected to tension and struts are subjected to compression. The members are joined with each other so that they are subjected to pure tension and compression. The frontal impact load is estimated by colliding the vehicle at a speed of 65 kmph with a rigid body. Generally, vehicle collision includes two events, primary and secondary. In the primary, vehicle collides with other vehicle or object and the vehicle crumple zone gets crushed absorbing the impact energy [5–7]. The secondary event includes the free movement of the passengers and colliding with other parts inside the vehicle. The secondary

impact may cause injury if restrain systems are not used properly. Torso of the occupants absorbs some part of the energy. The torso releases the energy slowly so that the impact is non-injurious. The energy of the second impact is proportional to the mass of the occupant and the relative speed concerning the interiors. Impact in a short period results in higher force and may cause injuries [8–10].

**Rollover Impact Analysis**—Rollover is another type of crash, during which vehicle turns upside down causing injuries to the occupants. Rollover is the most dangerous crash, in which the fatality rate is very high compared to other types of crashes [11–14]. Rollover may be caused by kerb nudging, collision with kerb wall or collision with another vehicle. This type of rollover is called a tripped rollover. Another type of rollover called untripped, which is generally caused by the speed of the vehicle, instability in steering force input, friction with the ground, etc. [15–18]. When the vehicle slides sideways and strikes kerb, lateral force develops, which causes rollover of the vehicle. When the vehicle slips into soft ground, rollover may occur. Slopes, particularly steeper than 33% also, may cause rollover [19–22]. When one wheel of the vehicle hits a large obstacle, it may roll over. Rollover case is a more serious crash causing a higher rate of deaths. The roof of the vehicle gets crushed towards the heads of the passengers during a rollover and causes serious injuries.

## 3 Methods and Materials

**Methods**—To fulfil the objectives of this study, the method followed includes the following activities.

- *Data Collection*: Data collected from different sources.
- *Preparation of CAD Model*: The CAD model for existing structure and also new structure was prepared by using CATIA V5R19 software.
- *Importing of CAD Model to ANSYS*: The model prepared in CATIA was imported to ANSYS workbench following appropriate procedure before analysis.
- *Structural Analysis*: Structure analysis was done by finite element analysis with ANSYS 16.0 workbench.
- *Impact Analysis*: The impact analysis such as frontal and rollover static impact analysis was done by using finite element analysis.
- *Modal Analysis*: A modal analysis of the vibration characteristics of a structure was done by using ANSYS 16.0 software.

**Modelling Existing Three-Wheeler Structure (CAD Model)**
The model has been done using the overall dimensions length is 2625 mm, width 1300 mm and height 1710 mm and circular cross-sections and diameters of 25 and 3 mm thickness.

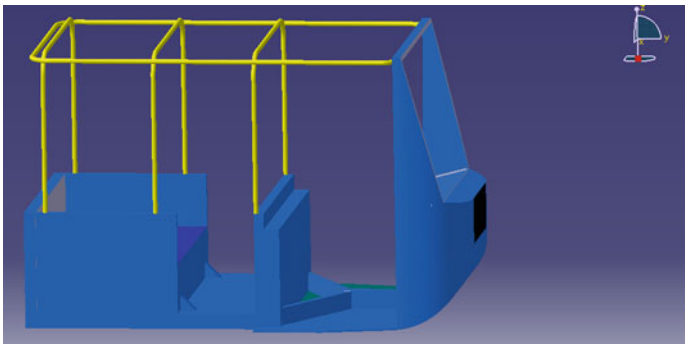

**Fig. 1** 3D CATIA model of the existing structure

**Modelling a New Bajaj Three-Wheeler Structure (CAD Model)**
Circular cross-sections and diameters of 36 and 3 mm thickness have been modelled in CATIA V5R19 software (Figs. 1, 2 and 3).

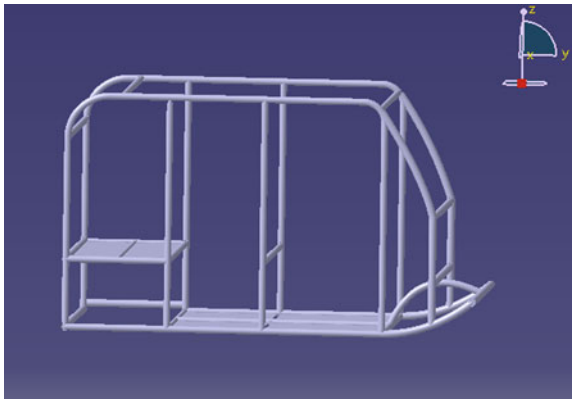

**Fig. 2** 3D CATIA model of new structure

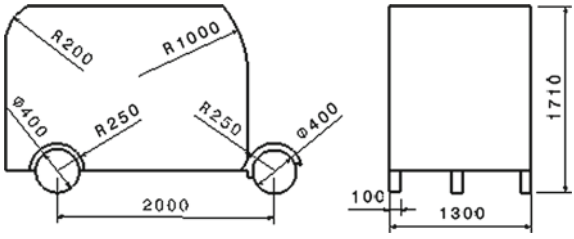


**Fig. 3** CAD drawing for models

## 4 Results and Discussions

Static structural analysis results of existing model are given in Table 1 (Figs. 4 and 5).

**Table 1** Simulation result of static analysis

| Result type | Equivalent or von Misses stress (MPa) | Maximum principal stress (MPa) | Total deformation (mm) | Safety factor |
|---|---|---|---|---|
| Minimum | 2.1829e−5 | −138.01 | 00.16535 | 0.50906 |
| Maximum | 491.1 | 481.43 | 24.421 | – |

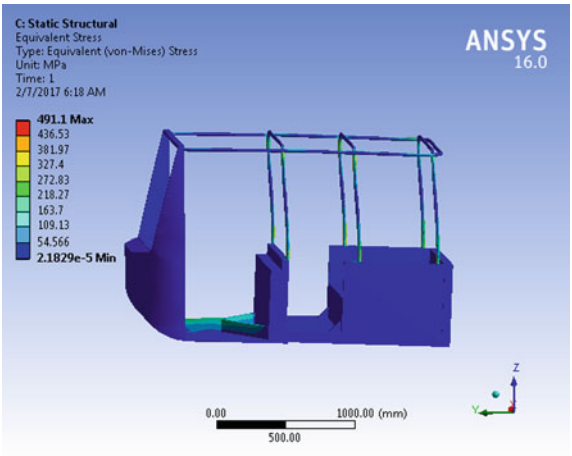


**Fig. 4** Equivalent stress

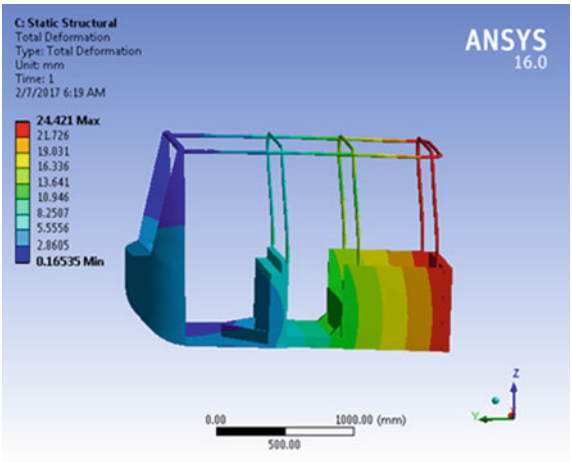


**Fig. 5** Total deformation

**Rollover impact simulation**—For improving passenger safety, the strong roof structure is necessary. A rollover impact analysis is required for this purpose, to know whether the designed roof structure is strong enough to protect the passengers or not. First, side impact and front impact analyses were conducted and the results obtained from this are used as input to roll over-analysis (Figs. 6 and 7). 50% of the frontal impact load is applied for the rollover case (Figs. 8 and 9) [12].

$$\text{Impact force, } F = 0.5 * \text{Frontal impact load.}$$

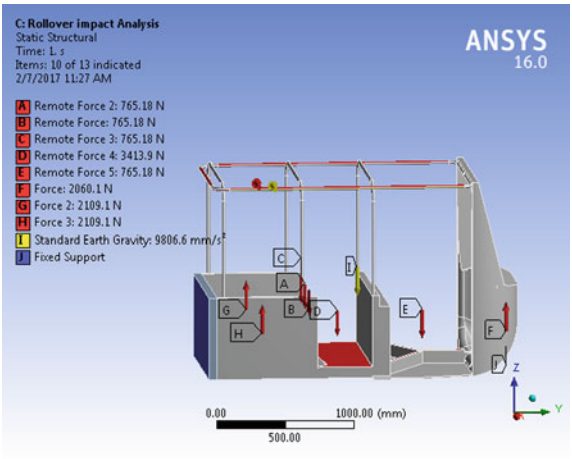


**Fig. 6** Loads and boundary conditions rollover impact of existing model

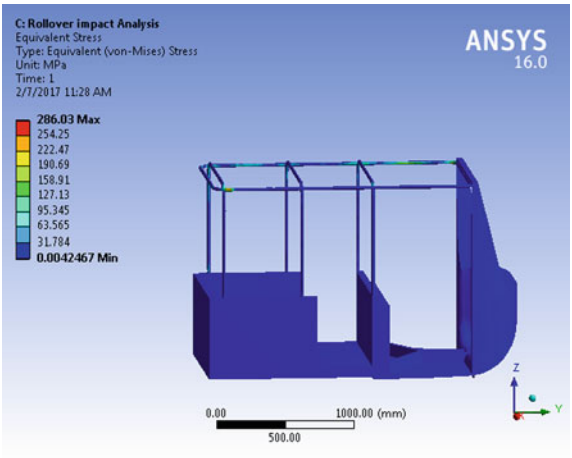


**Fig. 7** Equivalent stress

**Fig. 8** Deformation (total)

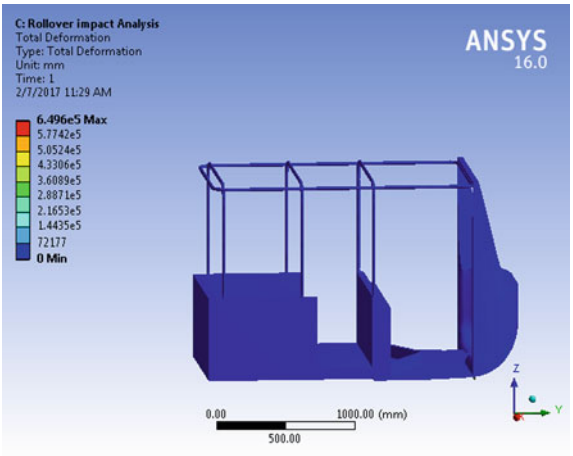


**Fig. 9** Safety factor

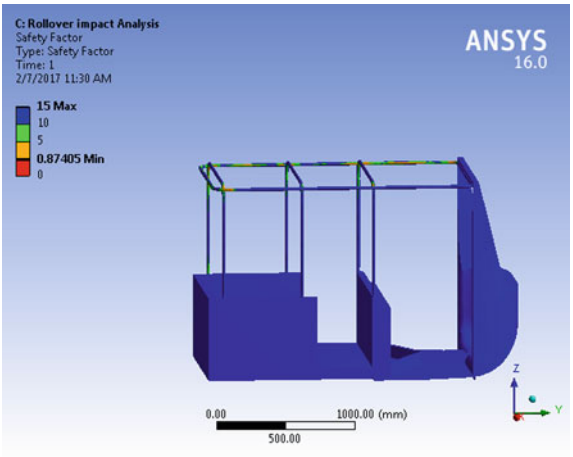


*Static structural analysis of new model*

The results are given in Table 2. The variation of equivalent stress is shown in Fig. 10 and deformation in Fig. 11.

**Table 2** Static simulation result of the modified structure

| Result type | Equivalent or von Misses stress (MPa) | Maximum principal stress (MPa) | Total deformation (mm) | Safety factor |
|---|---|---|---|---|
| Min | 0.14118 | −20.993 | 0.0045389 | 2.0862 |
| Max | 119.84 | 119.89 | 17.29 | – |

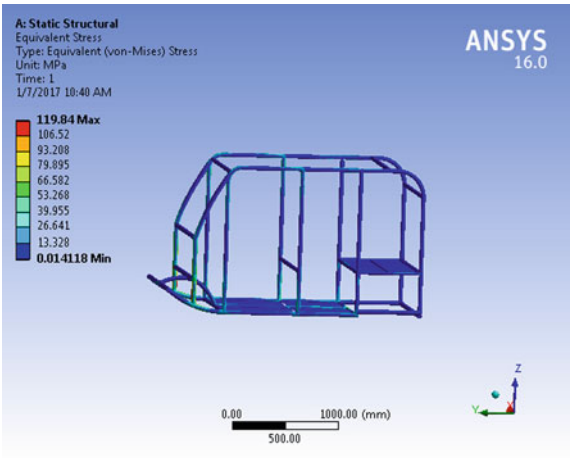


**Fig. 10** Equivalent stress

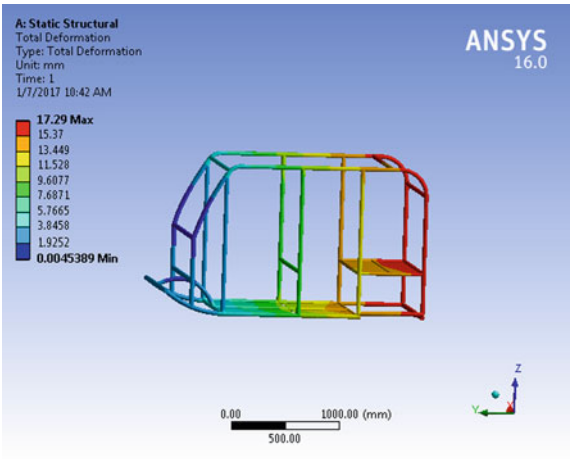


**Fig. 11** Deformation

**Rollover impact analysis**—Strong roof structure for maximum safety during rollover incidents was ensured by performing rollover crash analysis. For impact loading analysis of the rollover, input parameters used are obtained from side impact and front impact analysis (Figs. 12 and 13). The rollover impact analysis load is obtained (Figs. 14 and 15) as follows.

$$\text{Impact force, } F = 0.5 * \text{Frontal impact load.}$$

## Modal Analysis

It is necessary to make a vibrational analysis of the structure to find out the natural frequencies and mode shapes. The following equation is used to calculate natural

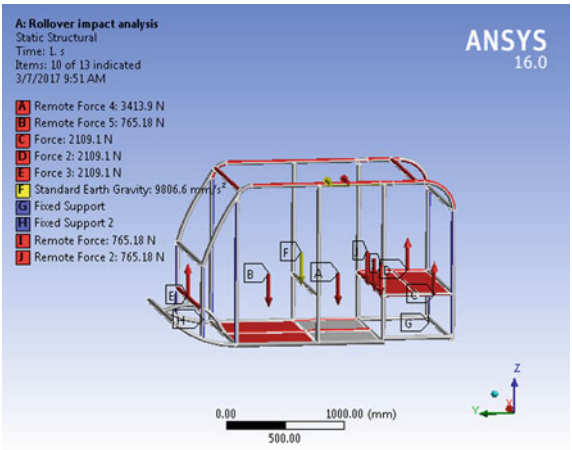


**Fig. 12** Loads and boundary conditions rollover crash static analysis of the new model

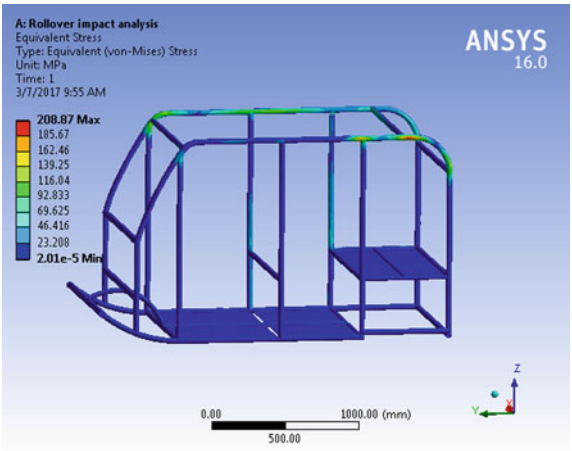


**Fig. 13** Equivalent stress

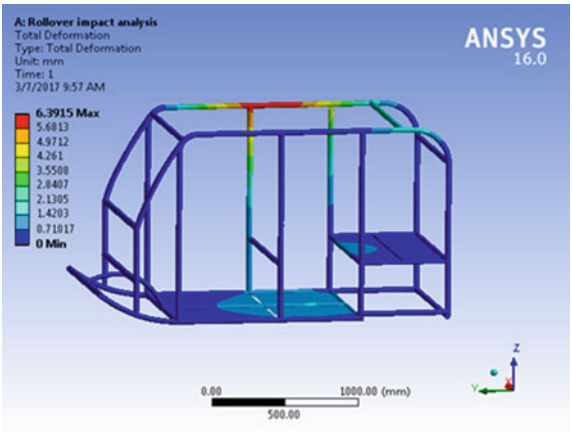


**Fig. 14** Total deformation

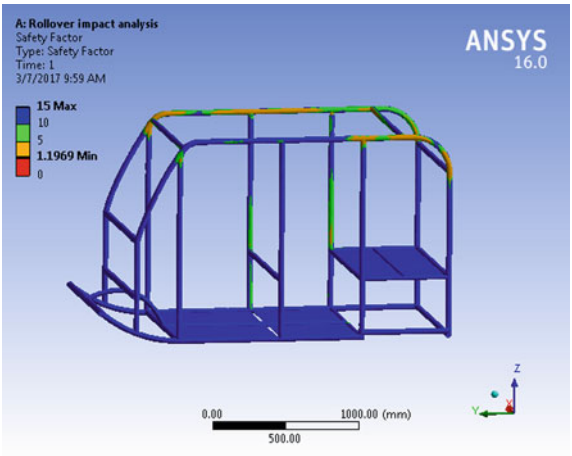


**Fig. 15** Safety factor

frequency.

$$\omega_{\mathrm{n}} = \sqrt{\frac{K}{m}}$$

where $\omega_{\mathrm{n}}$ is natural frequency, m is mass and $k$ is stiffness.

The obtained mode shapes are as follows.

The first mode explains about vibration of rear part of the chassis with a zero natural frequency (Fig. 16).

Second mode is the longitudinal vibration of the frontal part of the frame with zero frequency (Fig. 17).

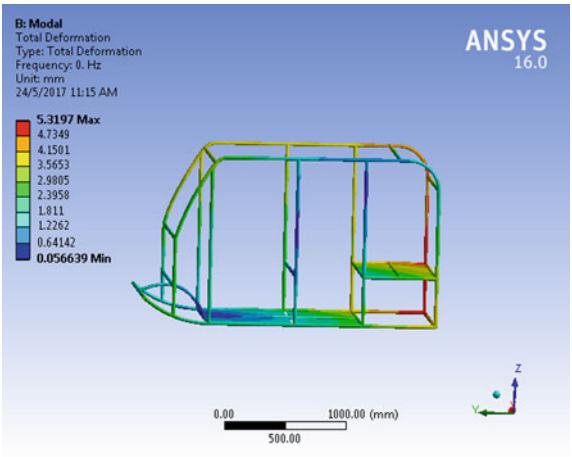


**Fig. 16** First mode

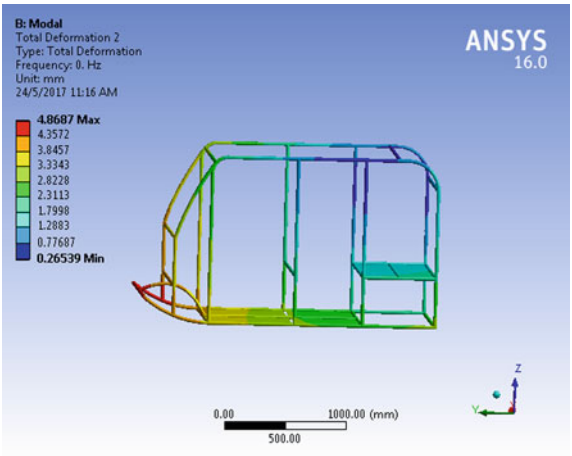


**Fig. 17** Second mode

Third mode is the vibration of entire upper frame and beams connecting them with zero natural frequency (Fig. 18). Fourth mode is the vibration of the frontal structure with a frequency of 3.1412e−003 Hz (Fig. 19).

In the fifth mode, vibration of the entire upper frame and beams connecting them occurs with a natural frequency of 4.4876e−003 Hz (Fig. 20). In the sixth mode, vibration of the upper frame and the beams connecting the rear end occurs with a frequency of 5.5354e−003 Hz (Fig. 21).

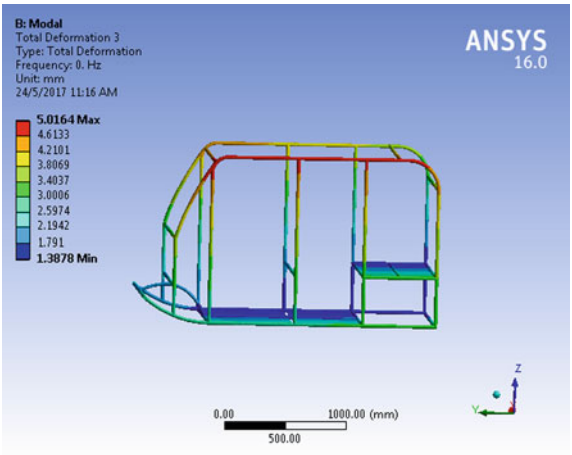


**Fig. 18** Third mode

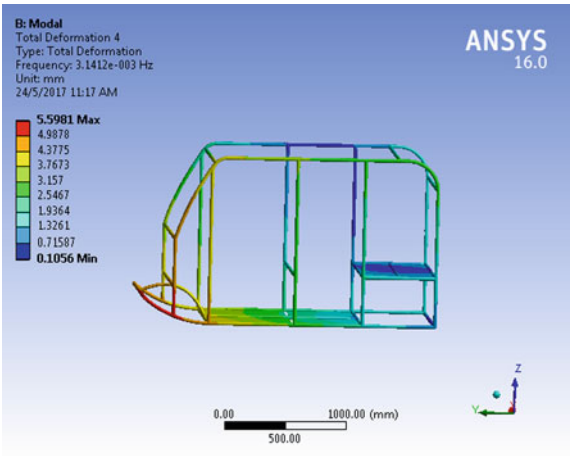


**Fig. 19** Fourth mode

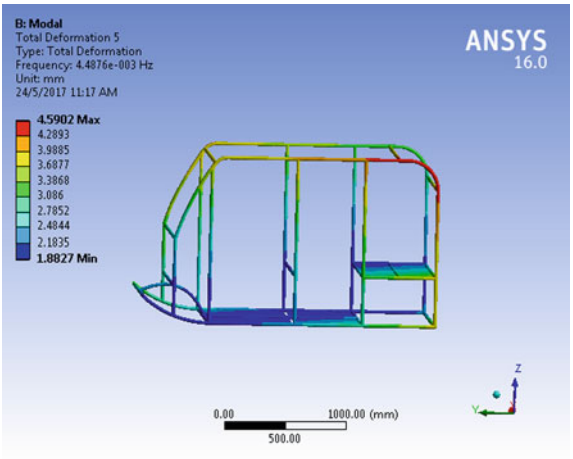


**Fig. 20** Fifth mode

## 5 Conclusions

- This work concerns the following parameters while keeping in mind the strength, performance, weight and safety. The primary goal was to build the lightest frame, to make passenger safety and to maximize the performance of the vehicle.
- The designed structure is analysed for the static and impact loads. The parameters obtained from each analysis are given as input to the next analysis following the order of front, side, rear and rollover impacts, respectively.
- The chassis and body frame was designed as the vehicle can withstand the better crash and static types of loads.

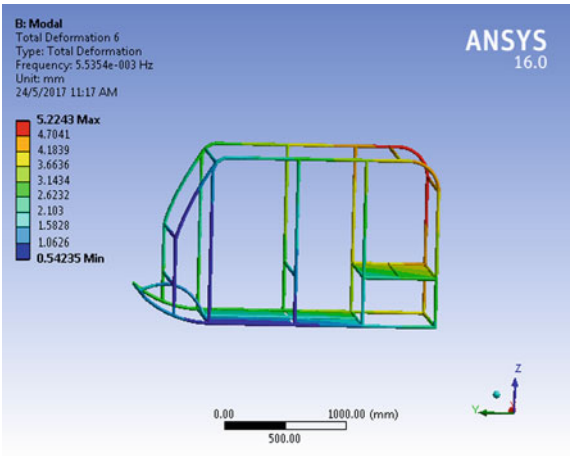


**Fig. 21** Sixth mode

- The body structures have been improved by optimizing the number of tubes using FEA analysis. The important option of the structure of this vehicle is to be performed using the tubular space frame.
- With this work, it is understood that tubular structure increased the strength of the structure with a weight reduction. It can withstand high dynamic stresses with great rigidity. It can also withstand heavy loads with great strength. Bending and torsional loads also can be supported by this system.

## References

1. Iyer NV (2012) A technical assessment of emissions and fuel consumption reduction potential from two and three wheelers in India. In: Prepared for the international council on clean transportation, Washington, DC
2. Butdee S, Vignat F (2008) TRIZ method for lightweight bus body structure design. J Achievements Mater Manuf Eng 31(2):456–462
3. Magee CL (1988) Design for crash energy management—present and future developments. In: The seventh international conference on vehicle structural mechanics
4. Deshpande B, Gunasekar TJ, Morris R, Parida S, Rashidy M, Summers S (1999) Methodology development for simulating full frontal and offset frontal impacts using full vehicle MADYMO models, crashworthiness, occupant protection, and biomechanics in transportation systems. In: ASME mechanical engineering congress and exposition, pp 19–37
5. Huang M, Lawson GP, Powell BK, Walker JH (1977) Characterization of vehicle deceleration time histories in the analysis of impact dynamics. SAE Paper No. 770013
6. Eppinger R (1993) Occupant restraint systems. In: Nahum AM, Melvin JW (eds) Accident injury—biomechanics and prevention, Chapter 8. Springer, Berlin, pp 186–197
7. Rollover. NHTSA. Retrieved 16 Sept 2015
8. Phanomchoeng G, Rajamani R (2012) Prediction and prevention of tripped rollovers. Department of Mechanical Engineering, University of Minnesota
9. (2003) Examination of rollover crash mechanisms and occupant outcomes. National Highway Transportation Safety Administration

10. (2002) Roadside design guide. American Association of State Highway Transportation Officials, pp 3–13
11. Prasad TRK, Static analysis and optimisation of chassis and suspension of an all-terrain vehicle
12. Wakjira A, Nallamothu RB (2013) Microcontroller based rear end anti-collision warning system for vehicles. Glob J Eng Des Technol G.J.E.D.T. 2(6):14–21
13. Abebe L, Nallamothu RB, Subrahmanyam KHS, Nallamothu SK, Nallamothu AK (2016) Thermal analysis of disc brake made of different materials. SSRG Int J Mech Eng (SSRG-IJME) V3(6):5–9
14. Feliche E, Nallamothu RB, Nallamothu SK (2017) A study on cause of rollover of sugar cane haulage semitrailer truck in Ethiopia Sugar Estate: case of Wonji Sugar Factory. Int J Eng Trends Technol (IJETT) V43(4):205–211
15. Yesfalgn Damissie H, Ramesh Babu N (2017) Aerodynamics drag reduction on locally built bus body using computational fluid dynamics (CFD): a case study at Bishoftu automotive industry. Int J Eng Res Technol (IJERT) 6(11). ISSN: 2278-0181
16. Ashagrie G, Nallamothu RB, Nallamothu AK, Nallamothu SK (2017) A study on driving stability of bus using computational fluid dynamics (CFD). Int J Res Appl Sci Eng Technol 5(XI)
17. Molla KY, Chul-Ho K, Ramesh Babu N (2017) Aerodynamic design of the Ethiopian train for energy economy under crosswind conditions. 년도 한국철도학회 추계계학술대회 논문집, KSR 2017, South Korea
18. Siraj A, Ramesh Babu N, Srinivasa Reddy K (2019) Static analysis of dump truck chassis frame made of composite materials. Int J Eng Sci Technol 11(2):21–32
19. Alemayehu G, Nallamothu RB (2017) Programmable logic controller (PLC) application for hybrid electric vehicle (HEV) simulator. Int J Mech Eng Technol (IJMET) 8(9):281–292
20. Negera DW, Bhaskaran J, Ilmi I, Nallamothu RB (2019) Characterisation of hybrid composite made of false banana fiber and sisal fiber. Int J Eng Adv Technol (IJEAT) 9(2). ISSN:2249-8958
21. Getu D, Nallamothu RB, Masresha M, Nallamothu SK, Nallamothu AK (2020) Production and characterization of bamboo and sisal fibre-reinforced composite for interior automotive body application. Mater Today Proc. https://doi.org/10.1016/j.matpr.2020.08.780
22. Alemayehu Z, Nallamothu RB, Liben M, Nallamothu SK, Nallamothu AK (2020) Experimental investigation on characteristics of sisal fibre as a composite material for light vehicle body applications. Mater Today Proc. https://doi.org/10.1016/j.matpr.2020.07.386

# Aerodynamic Analysis of Body of Passenger Bus for $CO_2$ Reduction and Fuel Saving


**Dawit Tafesse, Ramesh Babu Nallamothu, Anantha Kamal Nallamothu, Seshu Kishan Nallamothu, Lelisa Gezu, and Bekele Eromo**

## 1 Introduction

Transportation of the people by bus became one of the most successful commercial activities in the field of transportation. This means of transportation is increasing day by day at a higher rate. The fuel consumption share of the busses and contribution of harmful emissions increasing at an alarming rate. Technology in bus manufacturing is improving. Now, there are busses, which are used for travelling long distances between cities at higher speeds. Due to their bluff body shape, the fuel economy of the busses is very poor compared to other vehicles. As the speed of the bus is increasing, the aerodynamic drag increases drastically in a parabolic manner. Normally, the drag grows with the square of the relative speed of the vehicle concerning the air. At higher speeds, the consumption of the power in overcoming the aerodynamic resistance mounts to 70% of the total brake power produced by the engine. For saving the depleting resources of the fossil fuels and reducing the greenhouse gas emissions and other harmful emissions, the engineers and scientists in automotive industries are vigorously working for improving the fuel economy of the busses by

D. Tafesse
Hawassa University, Awassa, Ethiopia

R. B. Nallamothu (✉)
Mechanical Engineering Department, SoMCME, Adama Science and Technology University, Adama, Ethiopia
e-mail: ramesh.babu@astu.edu.et

A. K. Nallamothu · S. K. Nallamothu
Politecnico di Milano, Milan, Italy

L. Gezu
Flower Construction PLC, Addis Ababa, Ethiopia

B. Eromo
Mechanical Engineering Department, Wachamo University, Hosaena, Ethiopia



K. Jha et al. (eds.), *Recent Advances in Sustainable Technologies*,
Lecture Notes in Mechanical Engineering,
https://doi.org/10.1007/978-981-16-0976-3_11

optimizing the aerodynamic shape of bus outer body. Drag on the body of the vehicle develops in two mechanisms, skin friction drag and pressure drag. About 80% is the contribution of pressure drag and the remaining 20% drag is from skin friction drag [1–3]. Various types of commercial CFD software available in the market can be used for the aerodynamic analysis of the commercial buses. Several researchers are working in the field of the aerodynamics of the vehicles, for reducing the aerodynamic drag coefficient. Various types of numerical and computational methods are being used by the researchers and scientists in the study of vehicle aerodynamics. In this work, the vehicle body is modified by attaching a newly developed device for reducing the drag and for vehicle aerodynamic performance improvement. Lateral guide vanes are attached near the rear end of the vehicle, for the sake of guiding the air smoothly into rear wake zone. Due to entering of the air into the wake zone, the pressure in the wake zone increases, thereby pressure drag reduces, contributing to the vehicle overall drag reduction. Vehicle drag is a very important and necessary activity, as the more than half of the energy is spent in aerodynamic drag.

Aerodynamic drag comprising of skin friction drag and pressure drag. Pressure drag is the major portion of the total drag, which amounts to 80% of the total drag. The geometry of the vehicle shape causes pressure drag, due to separation of the boundary layer where there is a sudden deviation of the contour of the vehicle body, on windscreens of front and rear, on the sides and rooftop, etc. Due to flow separation near the after body, creates a wake zone with very low pressure, causing increased pressure drag. The size of the wake depends on the geometry of the after body and the location of the flow separation [4, 5]. In this present work, novel rear end spoilers are developed and attached to the rear end of the bus. Two different spoilers were attached to the rear end and analysed their influence on bus aerodynamic drag. The obtained results were compared with the baseline model of the existing vehicle. The test was done varying the speed from 80 to 120 km/h.

Flow separation and its control is a very important concept in the various engineering applications of fundamental fluid dynamics. Flow separation from the body of the vehicle aggravates aerodynamic drag. Different types of passive and active flow separation controlling devices are developed. Passive control techniques include modification of the shape of the vehicle, attachment of some add on devices etc. But these methods are dedicated to a particular application.

From the results obtained in the CFD analysis done in this work, it is observed that changes in velocity and pressure near the front and rear parts of the vehicle have a significant influence on lift and drag forces acting on the vehicle. It is observed as the rounding radius of the bus edge is increasing the coefficient of drag gets reduced. Decreasing flow separation is observed with modifications done on the vehicle body.

## 2 Literature Review

On vehicle body aerodynamics, lot of research works are reported in the literature. But, the research works related to heavy vehicle aerodynamics are considerably less.

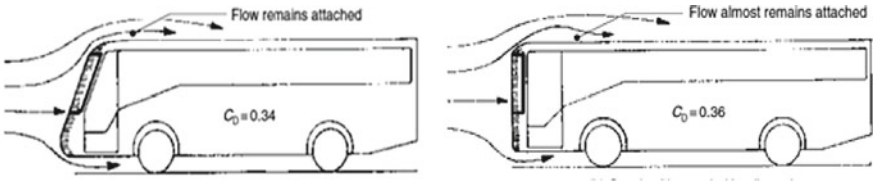


**Fig. 1** Frontal shape design to reduce CD [5, 6]

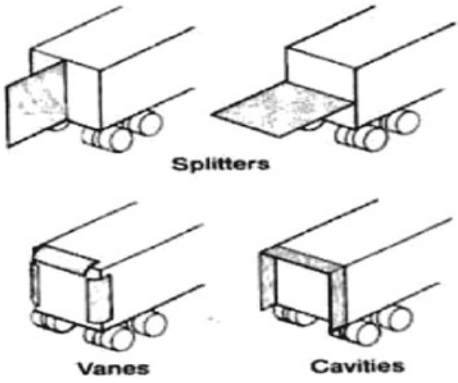


**Fig. 2** Bus body rear side vanes and splitters [7]

This is the motivation behind the execution of this work. With fine-tuning of front edge radii, an optimum radius of the edge was obtained, which is 150 mm. Further increase in radius, observed insignificant influence on aerodynamic drag (Fig. 1) [5, 6].

Add on devices are added on busses and trucks and then experiments were carried out. The influence of extended vertical and horizontal splitter panels extended from the vehicle rear body, non-ventilating cavities and vanes near the rear end was investigated as shown in Fig. 2. It is observed that non-ventilating cavities helped in reduction of drag coefficient by 5% [7].

These days, availability of commercial CFD software packages are very common in the market. These software packages are reliable, rapid and proved to be successful in many engineering applications solving multiple tasks. There are internal and external flow categories in the automotive wind flow. The efficiency of the vehicle is very much dependent on aerodynamic drag. Aerodynamic analysis of vehicle became one of the important and critical research areas these days. In the twentieth century, wind tunnel testing was the most well-known way of analysing vehicle aerodynamics. Due to the recent development of software packages, to deal with aerodynamic analysis, a lot of work is being done by adapting numerical simulations. With such practice, one can save the cost and time in testing [8].

Styling of vehicle outer body is a complex phenomenon which is an integration of artful, stylish and aesthetic appearance besides engineering design requirements of strength and other aspects [9–11]. A vehicle with an aerodynamically designed

body, with less aerodynamic drag, can exhibit higher performance, runs faster and longer with less fuel. Due to this, a great importance is given to aerodynamic body design of a vehicle [12].

Aerodynamic flow simulation is one of the proven conventional methods to see the field of flow around the body of the vehicle which helps in identifying the critical zones where there is a possibility of drag reduction for reducing the fuel consumption [13, 14]. Panels and spoilers are added at the rear end to reduce the drag and altering the front face of the conventional bus model [15–17]. These alterations were done with less investment and without interfering the internal passenger space. The fuel consumption criteria were also studied by many researchers [18, 19].

## 3 Model Preparation and Meshing

### *3.1 Specifications of the Model*

Scaled-down 3D models were prepared using CATIA software. The specifications are given in Table 1. Outer dimensions of the bus are given in Table 2. Bus model was prepared, then converted into STL format and imported to Pheonix CFD software and aerodynamic analysis was done.

**Table 1** Specifications of the model

| S. No. | Model specifications |
|---|---|
| 1 | Front edge radius, minimum of 100 mm |
| 2 | Coverage of underbody and smooth. From 11.5° to 15° |
| 3 | Trailing corner radius. Minimum of 100 mm |
| 4 | Tapering of side panel 100 mm |
| 5 | Tapering o rear roof 1000 mm |
| 6 | Front end curved |
| 7 | Lowering of roof ends |
| 8 | Rake angle increment from 30° to 45° |

**Table 2** Existing bus specifications

| Parameter | Size (mm) |
|---|---|
| Length | 11,955 |
| Width | 2550 |
| Height | 4000 |

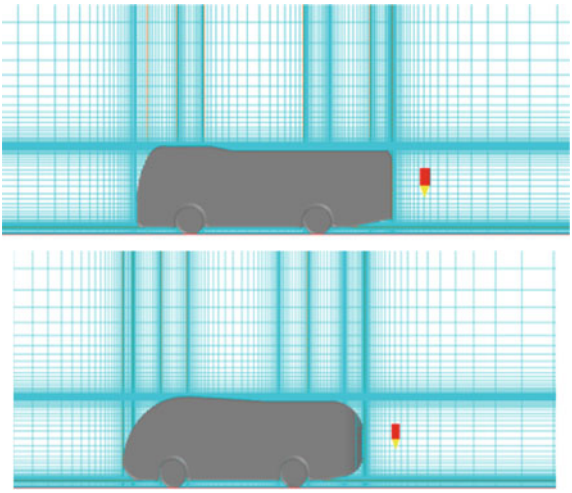

**Fig. 3** Grid convergence

## *3.2 Grid Mesh*

Grid mesh was generated in the selected flow field. Grid was optimized to avoid the difference between two models (Fig. 3). Vehicle has symmetry in the vertical plane along the longitudinal axis. This symmetry made the work simpler.

## *3.3 Application of Initial and Boundary Conditions*

The conditions like rotating wheels, road touching are imposed on the mesh for CFD analysis. The inlet condition was taken as constant velocity and outlet condition was zero-gauge pressure. Atmospheric pressure is the general operating condition. The blue face shows velocity inlet and a red face shows the pressure outlet.

## *3.4 Aerodynamic Drag*

The resistance force due to wind experienced by the vehicle opposite to the motion of the vehicle is called drag. Theoretical estimation of the total drag over the exposed surface area is a very complex task. The drag has two components pressure drag and skin friction drag. CFD helps in making this task simple. But CFD model developed around the body of the vehicle has to be adequately validated.

Comparing the drag and lift acting on two different vehicles does not give good information. Because many parameters like density, projected frontal area, test speed,

etc. influence the drag and lift. So developing a non-dimensional drag is necessary for comparison purpose.

The coefficient of drag in its non-dimensional form is given below [13]

$$F_{\mathrm{d}} = 1/2\rho v^2 C_{\mathrm{d}} A$$

## 4 Simulation Using CFD

### *4.1 Setup*

Using CFD, it is possible to find the solutions of many flow problems like laminar/turbulent, compressible/incompressible, reacting/non-reacting, etc. The problems like chemical reactions, heat transfer, fluid flow and mass transfer can be successfully solved by CFD [14].

Controlled domain size is $X = 80$ m, $Y = 22.55$ m, $Z = 14$ m. Boundary conditions like inlet, outlet and ground plate are set. Importing the model of vehicle with dimensions $L(X) = 11.995$ m, $W(Y) = 2.55$ m, $H(Z) = 4$ m, into CFD software. Initial condition wind velocity was set $V = 27.78$ m/s. Position of the sensor was set at $X = 41.995$ m, $Y = 11.275$ m, $Z = 1.5$ m as shown in Fig. 4. Momentum of the forces calculated at $Z_{\mathrm{pos}} = 1.5$, $X_{\mathrm{pos}} = 25.9975$, and $Y_{\mathrm{pos}} = 11.275$. From all the forces, the drag coefficient was calculated with a reference density of 1.189 kg/m$^3$, reference area in $x$, $y$ and $z$ are $4 \times 2.55 = 10.2$ m$^2$. The fluid in the domain is treated as air at 20 °C, 1 atm. Turbulence model KECHEN was selected. Single-phase simulation, using question formulation ELLIPTIC STAGGERED. Several iterations tried are 1000 with 0.01 global convergence criteria and 0.001 as tolerance.

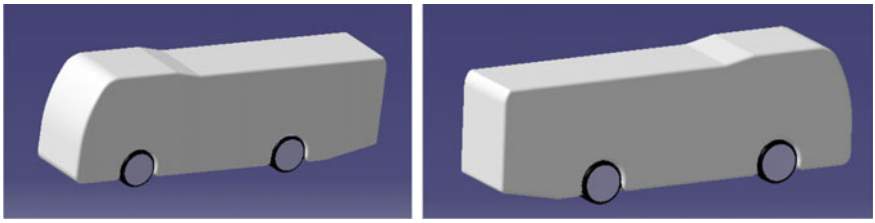

**Fig. 4** Existing bus (Model 1)

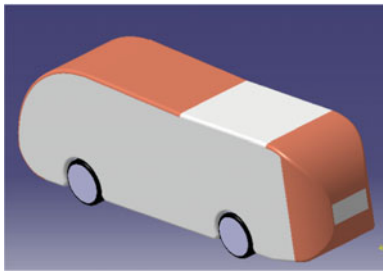

**Fig. 5** Modified bus (Model 2)

### *4.2 Grid Optimization*

Optimization of the grid was done at the position of the probe for pressure and velocity at a speed of 100 km/h (Fig. 3).

### *4.3 Modelling and Testing*

The baseline model was prepared as per the dimensions of the existing bus (Fig. 4). This model is named as Model 1. This model has a relatively flat front surface, sharp corners at rear and front.

Model 2 is a modification of the baseline model. Modifications are done on the roof, frontal area, rear side and rear panel shape (Fig. 5).

## 5 Aerodynamics Analysis

### *5.1 Drag Coefficient ($C_d$)*

$$\frac{C_{\mathrm{d_{Model\,-\,0}}} - C_{\mathrm{d_{Model\,-\,}i}}}{C_{\mathrm{d_{Model\,-\,0}}}} \times 100(\%)$$

See Table 3 and Fig. 6.

### *5.2 Total $F_D$ (N)*

$$F_{\mathrm{d}} = 1/2\rho A C_{\mathrm{d}} V^2$$

See Table 4 and Fig. 7.

**Table 3** $C_d$ at various speeds

| Drag coefficient ($C_d$) at various speed | | | | |
|---|---|---|---|---|
| Speed in km/h | Speed in m/s | Model 1 | Model 2 | $C_d$ percentage reduction (%) from baseline |
| 80 | 22.22 | 0.456279 | 0.421341 | 7.567 |
| 90 | 25 | 0.597414 | 0.559264 | 6.386 |
| 100 | 27.78 | 0.622502 | 0.570847 | 8.298 |
| 110 | 30.56 | 0.702459 | 0.598573 | 14.788 |
| 120 | 33.33 | 0.759947 | 0.632431 | 16.782 |

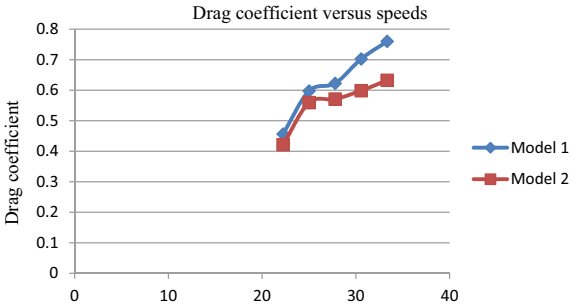


**Fig. 6** $C_d$ versus speed of models

**Table 4** $F_d$ at various speeds

| Drag force ($F_d$) at various speed in N | | | | |
|---|---|---|---|---|
| Speed in km/h | Speed in m/s | Model 1 | Model 2 | Reduction of driving resistance (N) |
| 80 | 22.22 | 1366.063 | 1261.4612 | 104.6018 |
| 90 | 25 | 2264.162 | 2119.576 | 144.586 |
| 100 | 27.78 | 2913.113 | 2671.3835 | 241.7295 |
| 110 | 30.56 | 3978.137 | 3389.814 | 588.323 |
| 120 | 33.33 | 5119.246 | 4567.220 | 552.026 |

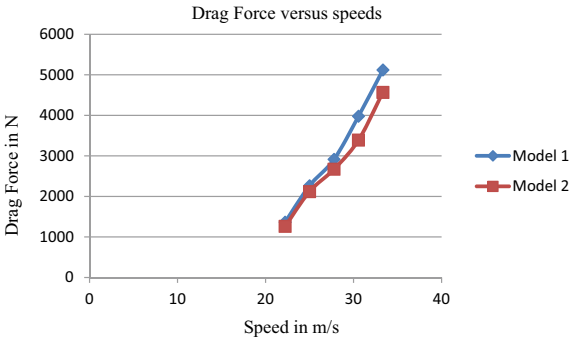


**Fig. 7** $F_d$ versus speed of models

**Table 5** Total resistance

| Total resistance at various in N speeds | | |
|---|---|---|
| Speed in km/h | Model 1 | Model 2 |
| 80 | 1719.123 | 1614.5212 |
| 90 | 2637.542 | 2492.956 |
| 100 | 3306.837 | 2710.7535 |
| 110 | 4392.157 | 3803.834 |
| 120 | 5553.586 | 5001.560 |

**Fig. 8** Total resistance

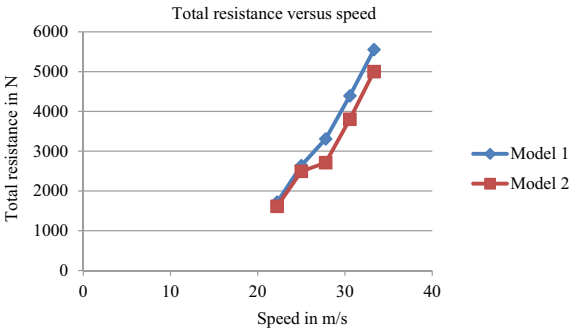


## 5.3 Total Resistance [15]

$$F_t = F_d + F_r + F_g$$
$$F_r = (0.015 + 0.00016V)W$$

Because of the same curb weight, $F_g$ is taken as zero and due to same velocity for both models $F_r$ is treated as constant. Curb weight of the vehicle is 12700 kg, including 70 kg of driver's weight. Variation of total resistance force is given in Table 5 (Fig. 8).

## 5.4 Power Requirement

$$P = F_t V/\eta_t \text{ or}$$
$$\eta_t = \text{Transmission efficiency (taking assume 0.9)}$$
$$P_{sav} = (F_{\text{Model - 1}} - F_{\text{Model - 2}}) \times V_{\text{Bus}}$$

See Table 6 and Fig. 9.

**Table 6** Saving of the power

| Total resistance at various in N speeds | | | Power saving m (kw) |
|---|---|---|---|
| Speed in km/h | Model 1 | Model 2 | |
| 22.22 | 1719.123 | 1614.5212 | 2.324 |
| 25 | 2637.542 | 2492.956 | 3.615 |
| 27.78 | 3306.837 | 2710.7535 | 16.559 |
| 30.56 | 4392.157 | 3803.834 | 17.979 |
| 33.33 | 5553.586 | 5001.560 | 18.399 |

**Fig. 9** Power requirement

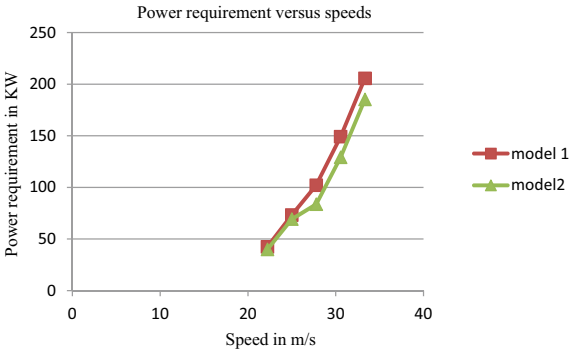


## 5.5 *Consumption of Fuel*

Fuel saving is calculated from power saved.

$$\dot{m}_{\text{fuel}} = \text{Power}_{\text{saved}} / \left( Q_{\text{LHV}} \times \rho_{\text{fuel}} \times \eta_{\text{engine}} \right)$$

The lower heating value of diesel fuel $Q_{\text{LHV}}$ is 42.5 MJ/kg.

The fuel density at ambient temperature is $\rho$ (860 kg/m$^3$). Engine thermal efficiency is 35% (Tables 7 and 8).

**Table 7** Fuel saving (L/h)

| Fuel save (L/h) | | | |
|---|---|---|---|
| Speed in km/h | Power saving (kW) | Model 1 | Model 2 |
| 80 | 2.324 | – | 0.654 |
| 90 | 3.615 | – | 1.017 |
| 100 | 16.559 | – | 4.659 |
| 110 | 17.979 | – | 5.059 |
| 120 | 18.399 | – | 5.178 |

**Table 8** Annual fuel saving

| Annual fuel save (L/year) | | | |
|---|---|---|---|
| Speed in km/h | Power saving (kW) | Model 1 | Model 2 |
| 80 | 2.324 | – | 2354.429 |
| 90 | 3.615 | – | 3662.333 |
| 100 | 16.559 | – | 16,775.817 |
| 110 | 17.979 | – | 18,214.410 |
| 120 | 18.399 | – | 18,639.909 |

### *5.6 $CO_2$ Reduction*

The amount of $CO_2$ from the engine depends on fuel consumption, the carbon content of the fuel and oxidation factor.

$$CO_2 \text{ emission} = A_L * C_L * O_F * 44/12$$

where

$A_L$ combusted fossil fuel amount
$C_L$ fossil fuel carbon content, 0.77 ton/kL
$O_F$ fossil fuel oxidation factor [16].

## 6 Result and Discussion

The analysis by CFD was carried out for the speeds from 80 to 120 km/h for both models at five different speeds. The bus was modified at the front end, corners and at the rear end. Velocity and pressure distributions are shown in Figs. 10 and 11. From Fig. 10, it is observed that the rear wake region is considerably reduced due to the modification done at the rear end.

## 7 Conclusion

3D model of the passenger bus was prepared using the actual dimensions of the existing vehicle. CATIA-V5R20 is used for the preparation of the models. From the CFD analysis, it is observed that the modification of the bus resulted in a reduction of the drag force. Using the CFD, the fluid flow field around the body of the vehicle is visualized. Modification of the vehicle body caused a significant change in velocity and pressure field. The variation near the rear end is very significant, which helped in the reduction of drag. The separation near rear end reduced. The flow field was well modelled. The variation of the flow field is not that much with a variation of

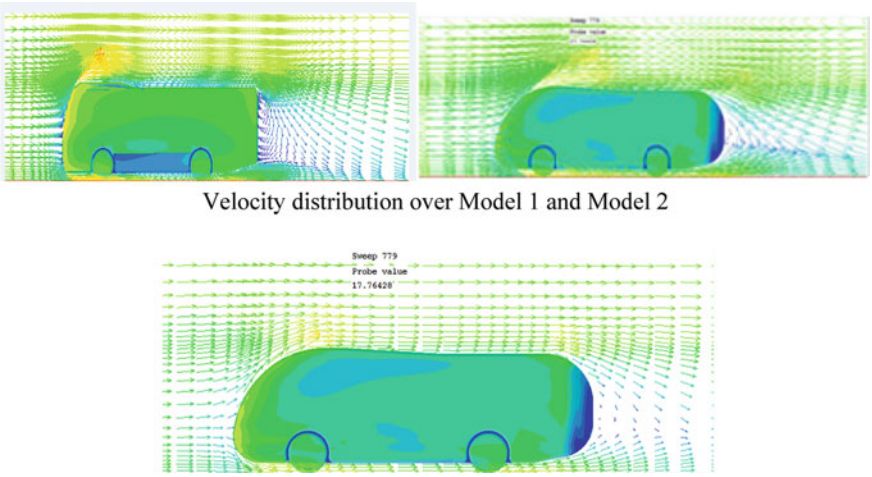


**Fig. 10** Velocity distribution

**Fig. 11** Pressure distribution

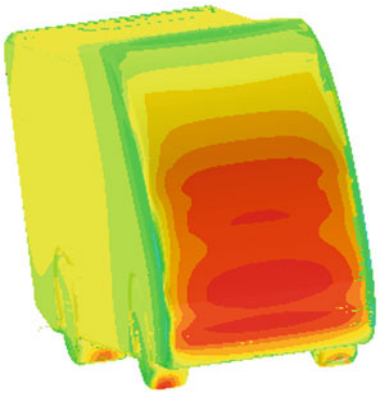

the speed. But body shape modification caused many variations. Coefficient of drag reduced with modification of the bus body. It is found that 18,639.906 L of fuel were saved per year due to modification of the body shape. $CO_2$ emission reduction achieved was 52.1 ton/year.

## References

1. Wood RM (2004) Impact of advanced aerodynamic technology on transportation energy consumption. SAE Technical Paper 2004-01-1306, Washington, DC
2. Barnard RH (1996) Road vehicle aerodynamic design. Addison Wesley Longman Ltd.

3. Kim CH, Yun DG, Lee CM (1998) A numerical study on the aerodynamic effects of a rear-side spoiler on the driving stability of a passenger car. J SNUT 47
4. Hucho WH, Sovran G (1993) Aerodynamics of road vehicles. Annu Rev Fluid Mech 25(1):485–537
5. Götz H (1984) Present and future trends in automotive aerodynamics. In: VKI fluid dynamics vehicle aerodynamics short course 1984-01. Rhode-St.-Genese, Belgium
6. Heisler H (2002) Advanced vehicle technology, 2nd edn
7. Mason WT Jr, Beebe PS (1978) The drag related flow field of characteristics of trucks and buses, aerodynamic drag mechanisms of bluff bodies and road vehicles. In: Symposium held at the general motors research laboratories
8. Parab A et al (2014) Aerodynamic analysis of a car model using fluent—Ansys 14.5. Int J Recent Technol Mech Electr Eng (IJRMEE) 1(4). https://www.ijrmee.org
9. Desai M, Channiwala SA (2008) Experimental and computational aerodynamic investigations of a car. WSEAS Trans Fluid Mech 3(4)
10. Patil CN, Shashishekar KS, Balasubramanian AK, Subbaramaiah SV (2012) Aerodynamic study and drag coefficient optimization of passenger vehicle. Int J Eng Res Technol (IJERT) 1(7)
11. Lloyd B (2012) Dissecting the basic fuel consumption equation into its components to improve adaptability to changing vehicle characteristics. In: 25th ARRB conference-shaping the future: linking policy, research and outcomes, Perth, Australia
12. Berry IM (2010) The effects of driving style and vehicle performance on the real-world fuel consumption of U.S. light-duty vehicles. M.Sc. Mechanical Engineering and M.Sc. Technology and Policy, Massachusetts Institute of Technology
13. Abinesh J, Arunkumar J (2014) CFD analysis of aerodynamic drag reduction and improve fuel economy. Int J Mech Eng Rob Res 3(4). ISSN 2278-0149
14. Anderson JD (2012) Computational fluid dynamics: the basics with application, Revised edn
15. Kim C (2011) A streamlined design of a high-speed coach for fuel savings and reduction of carbon dioxide. Int J Automot Eng Tech Pap 20114633
16. Feliche E, Nallamothu RB et al (2017) A study on cause of rollover of sugar cane haulage semitrailer truck in Ethiopia Sugar Estate: case of Wonji Sugar Factory. IJETT V43(4):205–211
17. Yesfalgn Damissie H, Ramesh Babu N (2017) Aerodynamics drag reduction on locally built bus body using computational fluid dynamics (CFD): a case study at Bishoftu automotive industry. Int J Eng Res Technol (IJERT) 6(11). ISSN: 2278-0181
18. Ashagrie G, Nallamothu RB, Nallamothu AK, Nallamothu SK (2017) A study on driving stability of bus using computational fluid dynamics (CFD). Int J Res Appl Sci Eng Technol 5(XI)
19. Molla KY, Chul-Ho K, Ramesh Babu N (2017) Aerodynamic design of the Ethiopian train for energy economy under crosswind conditions. 년도 한국철도학회 추계계학술대회 논문집, KSR 2017, South Korea

# Computational Evaluation of Aerodynamic Performance of Isuzu Midi Bus Body


**Natnael Bekele, Ramesh Babu Nallamothu, Engidayehu Wotango, Surafel Kebede, Seshu Kishan Nallamothu, and Anantha Kamal Nallamothu**

## 1 Introduction

Only, in designing race cars, vehicle aerodynamics was taken into consideration by automotive industries. In 1973, a group of oil-exporting countries formed a cartel and increased the prices of crude oil drastically. Then, automotive industries started seriously attempting to reduce the aerodynamic drag of vehicles for the sake of reducing the fuel consumption [1]. The automotive industries were very much frightened due to the shortage of fuel in the market at that time. Automotive manufactures started producing higher efficient vehicles with lower fuel consumption. A moving vehicle causes the displacement of the surrounding air and generates a resultant resistive force called drag which accounts for the major parts of the resistance force to the motion.

A major objective of the aerodynamic design of vehicles is to reduce drag and preventing underneath lift forces at high speeds. Focusing on the surface of the body is the most effective approach for the reduction of an aerodynamic drag because the outer surface contributes the largest percentage of the overall drag. Recent mechanisms like drag reduction attachment for both commercial vehicle and passenger cars and aerodynamic streamlining of the outer body surface lead to a reduction of drag acting on the body of the vehicle [2]. With the improvement in outer body shape of the vehicles, there is a significant reduction of drag coefficients from earlier

N. Bekele · R. B. Nallamothu (✉) · S. Kebede
Mechanical Systems and Vehicle Engineering Department, SoMCME, Adama Science and Technology University, Adama, Ethiopia
e-mail: ramesh.babu@astu.edu.et

E. Wotango
Mechanical Engineering Department, Bule Hora University, Bule Hora, Ethiopia

S. K. Nallamothu · A. K. Nallamothu
Politecnico di Milano, Milan, Italy



K. Jha et al. (eds.), *Recent Advances in Sustainable Technologies*,
Lecture Notes in Mechanical Engineering,
https://doi.org/10.1007/978-981-16-0976-3_12

vehicles to recent vehicles. Reduction in drag contributed a lot for the realization of fuel economy. The redesign and modification of car bodies help to reduce the overall aerodynamic drag. Moreover, the add-on devices effectively reduce drag force. Aerodynamic body shape design of cars is very much necessary [3].

Optimal aerodynamic shapes of the vehicle body can be designed by using aerodynamic analysis. Optimum streamlined body shapes help in the reduction of fuel consumption and related harmful emissions [4]. Today's car companies are now basing their vehicles on being more aerodynamically fit with the main goal to develop clean, efficient and sustainable vehicles for urban transport. Moreover, the performance, handling, safety and comfort of a passenger car are significantly affected by its aerodynamic properties. Getting high power under normal conditions is not enough to judge the performance of the car. Aerodynamic properties of a vehicle must be considered for studying the drag and stability performance [5].

There are many motor vehicles available in Ethiopia and most of them are imported from foreign countries, but some of those vehicles are locally fabricated (body) without the engine compartments and chassis layout. Most of the vehicle body-building companies are not considering aerodynamic aspects when designed the outer body shape of the vehicles.

The light truck Isuzu (Fig. 1) is the most commonly available truck in Ethiopia which is imported from a Japanese commercial vehicle and diesel engine manufacturing company found in Japan. However, the outer body of the light truck Isuzu is modified to midi bus without changing the chassis layout at different bus body-building companies and garages as shown in Fig. 2. This study focuses on the vehicle's aerodynamics, especially to reduce the overall aerodynamic drag force of the existing Isuzu midi bus that directly influences fuel consumption. Modifying the outside body design and using drag reduction devices were the main ways of reducing the drag force of this bus [6, 7]. Higher drag reduction can be achieved by diverting the airflow and avoiding flow separation, with the attachment of the extra parts on the outer body


**Fig. 1** Existing Isuzu light truck

**Fig. 2** Existing Isuzu midi bus during an assembly at Kemal bus body building company

of the vehicle. This extra device called "Rear Spoiler", which is aerodynamic equipment that is designed to spoil unfavourable air motion across a car body to decrease the overall drag. The main fixing location is at the rear end of the bus. At higher speeds more than 60 kmph, aerodynamic drag is very high, and it is responsible for the fuel consumption up to 50% of the total fuel consumption of the vehicle [8, 9].

An analysis was done on an intercity bus for body styling and aerodynamic performance by redesigning the outer body of the bus. Fluent, a commercial CFD code was used to compute the aerodynamic performance [10, 11]. There was a drag reduction from 0.53 to 0.29, with redesigning of the exterior body. The combined effect of lowered Cd and frontal area aerodynamic drag reduction by 60% [12, 13].

An examination was done on the flow structure around a bus model using the CFD method. They developed three different models to reduce the drag of the bus [14]. In their study, they determined the drag coefficient of the base model bus as 0.53. They lowered the drag coefficient to 0.49 by modifying the front and rear surface of the bus. They have achieved to decrease the drag coefficient to 0.39 by adding the side panel, 0.40 by the rear spoiler. Thus, they achieved an aerodynamic improvement as 6.57, 25.82, and 24.42%, respectively [15, 16].

They added panels at the rear end of the vehicle along with modification on the front face of one of the conventional bus models and achieved the reduction of the drag. It is observed that, without altering the interior space required for passengers, it is possible to reduce the drag with the least investment [8].

## 2 Methodology

Due to its flat and blunt front surface, the existing Isuzu midi bus has more air resistance to forwarding motion, and it is experiencing higher drag force at higher speeds This work aims to solve this problem, bringing up a novel outer body shape design, with the existing vehicle used as a benchmark. The baseline model of an

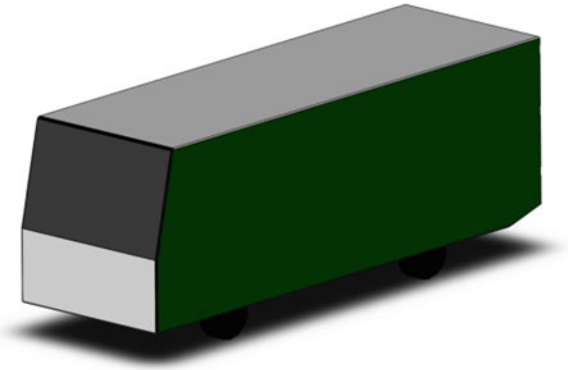

**Fig. 3** The baseline model of an Isuzu midi bus 1/20 scaled down

Isuzu midi bus 1/20 scaled-down model was generated using SolidWorks as shown in Fig. 3. Smooth underbody was used for the model. The analysis was done, with closed wheel wells, with no openings for cooling airflow and with no side-view mirrors.

Four bus body models were prepared for this analysis, with the appearance and exterior body styling. The first bus model "Model I" (Fig. 4a) designed with its front surface tapering more towards the rear end. This model was similar to the baseline model but different in inclination angle of the windshield, and the inclination angle

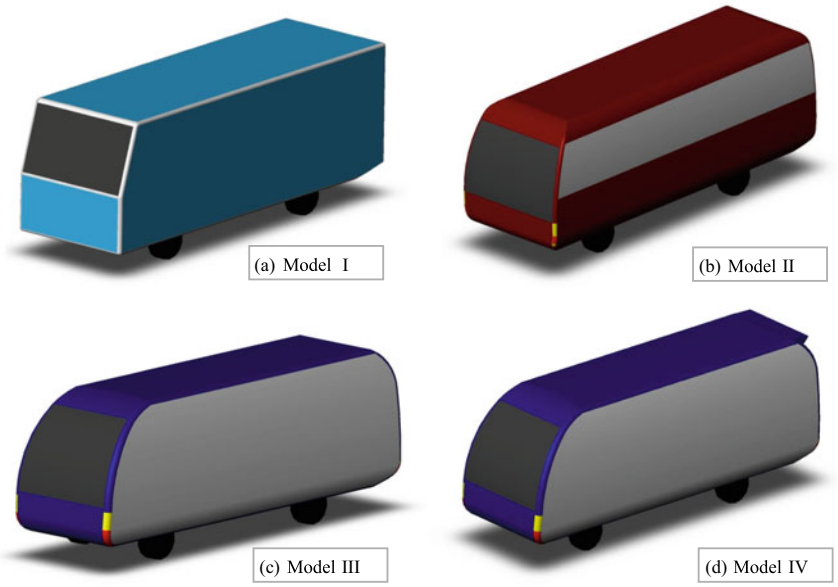


**Fig. 4** CAD models of four modified an Isuzu midi bus

of the baseline model was 11.31° whereas the inclination angle of model one was 15.64°.

The second bus model "Model II" (Fig. 4b) designed with a curved front surface and smooth rounded corners on the front and rear end of the roof. The third bus model "Model III" (Fig. 4c) designed with a more curved front surface and more smooth rounded corners on the front and rear end of the roof. The fourth bus model "Model IV" designed with the same as the third bus model with the rear spoiler at rear end of the roof as shown in Fig. 4d. Rear spoiler, which is externally attached to the rear end of the roof, is meant to push the flow separation a bit rearward and reduce the amount of drag by minimizing the wake region and by throwing the turbulent air behind the bus. The spoiler airfoil shape was selected from NACA catalogue. NACA 4412 airfoil was selected, and the coordinates are imported to SolidWorks for modelling. The main criteria for selecting NACA 4412 airfoil was, becomes it's more efficient for practical application and has lower drag and lift coefficients [9].

The simplified baseline model of an Isuzu midi bus is designed in SolidWorks as shown in Fig. 3. The sizes of the midi bus model are 345 mm long, 110 mm wide, 148.5 mm high and wheelbase of 117.5 mm. After the vehicle model has been uploaded into the ANSYS environment, an enclosure was generated surrounding it. For the experimental study, the enclosure was designed based on a recommendation from Fluent for accurate results. A real wind tunnel is created by a virtual air-box (Fig. 5) created around the 3D CAD model. The size of the bus has a relation to the dimensions of the tunnel. There are ground surface, inlet, an outlet and walls exist in the wind tunnel. From the front of the bus body, the flow inlet plane was located three car lengths away. The outlet of the tunnel exists at a distance of five car lengths from the rear of the vehicle. To provide a very wide simulation domain, the side plane was located sufficiently far from the car body side surface (about two car lengths). The height of the domain is equal to two times the length of the car body [10]. The set distance between the car body bottom surface and ground is 0.0001 m.

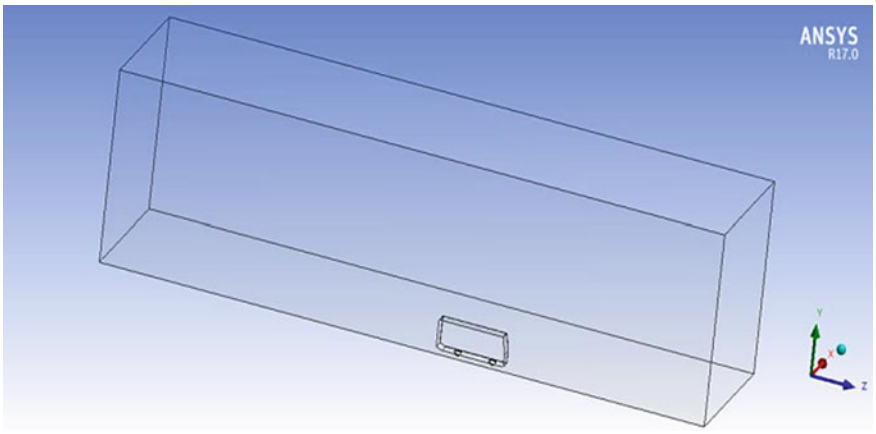


**Fig. 5** Virtual wind tunnel targeted for CFD simulation

The computational domain is discretized by using tetrahedron elements. The triangular mesh is the base format for the established mesh. A fine mesh is necessary to have a converging simulation. The fineness of the entire mesh is described by relevance used. The relevance of 100 means high accuracy and low speed of processing, while a relevance of 100 means low accuracy and higher speed of processing. For this study zero relevance with fine relevance, the centre was used. The advanced size function is curvature and proximity, which is used for progressing from least size of elements, near the curvature of the vehicle to big size elements far away from the vehicle and as approaching the wind tunnel domain walls. Smoothing is done by using smoothing iterations many times. Quality of the elements improved by moving the nodes and elements in the vicinity. In the inflation creation, the vehicle surfaces and ground surfaces are included. The boundary layer formed on the vehicle surfaces and the ground is simulated by meshing called inflation. The default values applied by programme-controlled inflation are enough for accurate simulation of the boundary layer near the surfaces and ground [11]. The growth factor of 20% is used with a maximum layer thickness of 5 mm and one time of 5 levels maximum. Three boxes are developed, to increase the mesh density in critical areas and refining the meshing, underbody and wake-box shown in Fig. 6.

In this work, for analysis, CFD software Fluent was used. Three-dimensional RANS equations are solved by using realizable k-ε turbulence model with non-equilibrium wall function set up. For all developed models, in the simulation using Fluent, the used model is the turbulence model. The simulations were run with a velocity of 80, 100 and 120 kmph.

In the simulation, the airflow is from the velocity-inlet towards the pressure-outlet with a selected amount of velocity. The intensity of the turbulence was reduced to 1%, for velocity inlet. The couples scheme was employed. The set Courant number was 50. Explicit relaxation factor of 0.25 was set for both momentum and pressure. The turbulent viscosity relaxation factor was set to 0.8 during the first upwind and changed to 0.95 for second upwind. The numerical computation was first begins

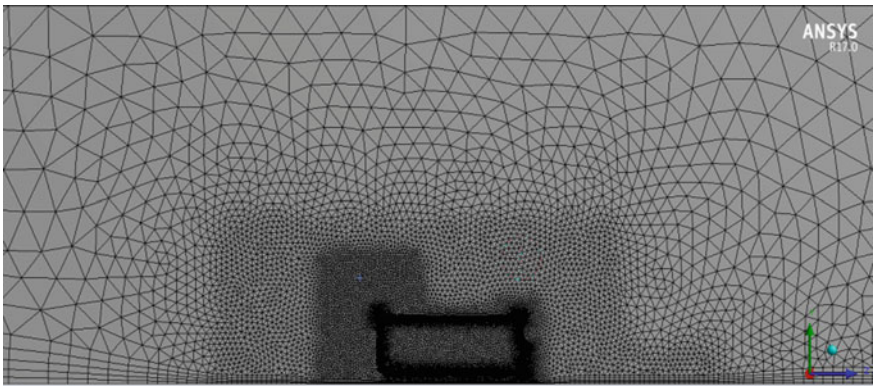


**Fig. 6** Three boxes car, underbody and wake for mesh refining

with the first-order scheme to certain numerical stability. For better truthfulness, the scheme was shifted to the second-order scheme, after the execution of one hundred iterations. This scheme was continued for another 1000 iterations. Most of the scaled residuals and the global aerodynamic quantity such as the drag coefficient converged to 1e-5 long way before the 1000th iteration. Once the convergence was reached, the solution could be analysed to determine which model is effective. The non-slip wall boundary condition is set on the vehicle surface. The boundary conditions on the rest of the wind tunnel surfaces are set as the inviscid wall.

## 3 Result and Discussions

To determine the reduction in the drag coefficient from different models of the bus with modifications, the drag coefficient and flow field of a baseline model examined first. After simulating the baseline model, the modified models were simulated next. After the simulation, all models were compared for the drag coefficient and the flow field of the baseline model.

Due to the stagnation of the approaching air, pressure builds up on the front surface of the vehicle (Fig. 7). Stagnation is the region that comes in contact with the air in the first instance when the car is in motion. Later, as the air is flowing over the body of the vehicle, air accelerates and pressure drops to negative values. Due to sudden deviation of the body surface, flow separation takes place, and wake is created near the rear end of the vehicle. Due to this, the pressure near the rear end is lower than the pressure on the front side of the vehicle. The pressure drag, which is a pulling of the vehicle towards back develops due to the pressure difference between the front

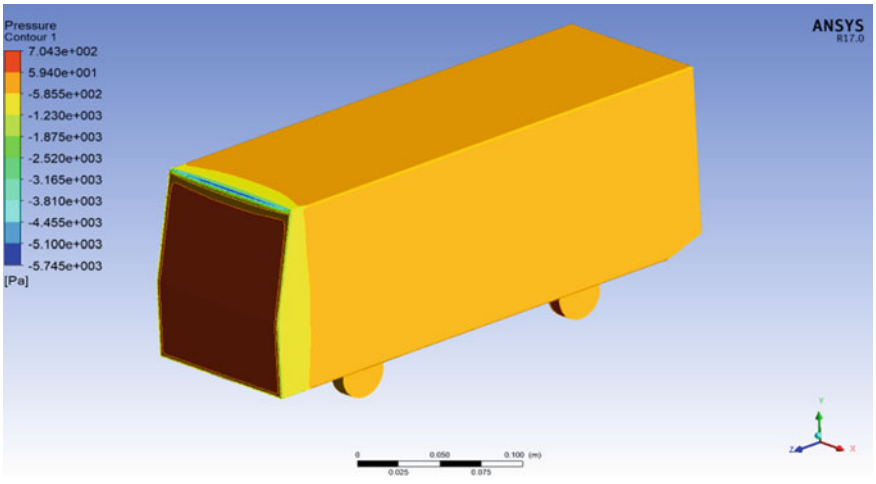


**Fig. 7** Pressure contour of the baseline model at 120 kmph

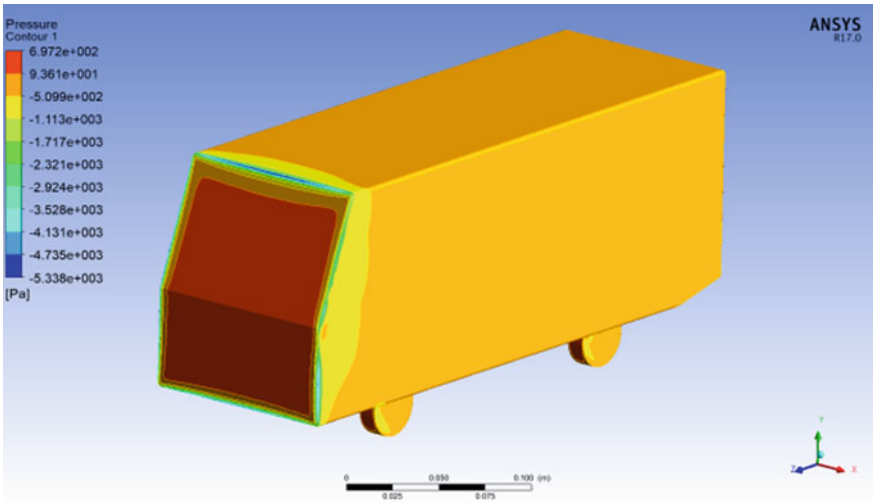


**Fig. 8** Model I pressure contour at 120 kmph

and rear sides of the vehicle. The size of the low-pressure wake zone near the rear end is to be reduced for the sake of reducing pressure drag. The concepts like radius improvement, roof tapering, roof end lowering, etc., are tried with the reduction of the pressure drag, as reported in the literature.

Due to the pressure variations on the surface of the vehicle body, the pressure drag developed is higher than the other form of drag called skin friction drag. In particular, the pressure difference between the front and rear parts of the vehicle is very high. Pressure contour of all models indicates that flow stagnation caused high pressure on the frontal surface of the vehicle (Figs. 8, 9, 10 and 11). Wake formation due to flow separation near rear end leading to reduction of the pressure. On the other hand, a low level of static pressure takes place where separated flow exists at the back of the bus model. It is known that the pressure differences between forwarding and backward faces of the bus model cause drag force. The maximum pressure increases with increasing speed. The increase in the surface pressure increases the drag coefficient which can be seen from Table 1.

The pressure difference of baseline, model I, model II, model III and model IV are 6449.3, 6035.2, 4843.5, 4096.8 and 3409.4 Pa at speed of 120 kmph, respectively. The proposed modified design resulted in a reduction of the pressure difference. The pressure difference of model III is lowest than all the baseline model, model I and model II. The presence of a rear spoiler in the rear upper part of the bus, the pattern of the flow behind the bus has slightly improved than model III. Consequently, which minimize the low-velocity area in the wake region and delay the turbulence zone away from the bus model. In all models of the bus velocity streamline contour shows that the wake region gets stronger and wider as the speed increases.

The locations where the flow is disturbed can be identified by the visualization of the airflow around the vehicle. The most significant is the nature and the formation

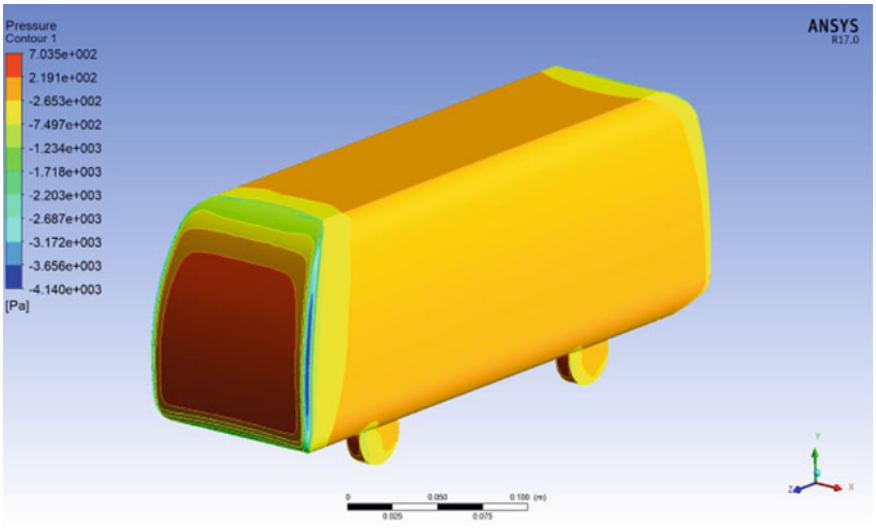


**Fig. 9** Model II pressure contour at 120 kmph

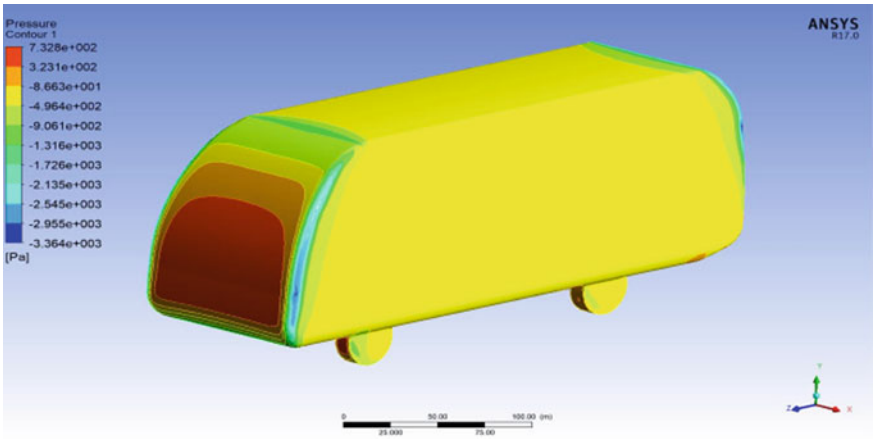


**Fig. 10** Model III pressure contour at 120 kmph

of the flow. Flow structure information can be obtained by visualization of path lines. The nature of the flow can be completely understood by visualizing the locations of streamlined flow, separation, and recirculation, vorticity generation, etc. Streamlines are the lines that are tangential to the flow velocity. As can be seen, the streamlines are in direction with the car surface and some streamlines tend to bend towards the rear side of the car. Also, the wake region in the back of the bus can be observed clearly. The colours indicate the velocity magnitude. The velocities close to inlet velocity are indicated by green colour and red colour indicates high-velocity zones.

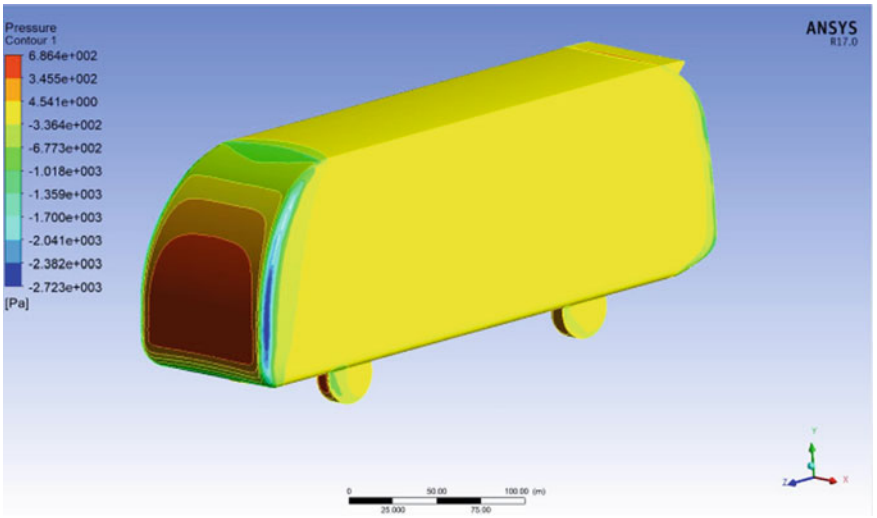


**Fig. 11** Model IV pressure contour at 120 kmph

**Table 1** Comparative coefficients of drag for all models

| Models | Speed (kmph) | Drag coefficient ($C_{d)}$ | Average $C_d$ value | Percent of $C_d$ reduction from the baseline model (%) |
|---|---|---|---|---|
| Baseline Model | 80 | 0.72872 | 0.72881 | – |
| | 100 | 0.72877 | | – |
| | 120 | 0.72895 | | – |
| Model I | 80 | 0.54672 | 0.56010 | 25.01 |
| | 100 | 0.54906 | | 24.66 |
| | 120 | 0.58452 | | 19.81 |
| Model II | 80 | 0.38114 | 0.38293 | 47.69 |
| | 100 | 0.38354 | | 47.37 |
| | 120 | 0.38412 | | 47.31 |
| Model III | 80 | 0.33598 | 0.34184 | 54.01 |
| | 100 | 0.34142 | | 53.15 |
| | 120 | 0.34813 | | 52.24 |
| Model IV | 80 | 0.33014 | 0.33266 | 54.69 |
| | 100 | 0.33239 | | 54.39 |
| | 120 | 0.33547 | | 53.98 |

However, blue colour sections in the contour represent low-velocity areas present on the bus body. The low-velocity area can be seen on the front of the bus at the stagnation point, underbody of the bus, and on the back of the bus. Drag acting on the bus increases with the development of turbulence in low-velocity areas.

From the velocity distribution shown in Figs. 12 and 13, it is seen that sudden change in the shape near the rear end caused flow separation. Recirculation and vertices are observed in the flow separation zone. Flow accelerates on the roof of the bus causing a reduction in the pressure due to converging flow. Pressure drag


**Fig. 12** Baseline model velocity contour at 120 kmph

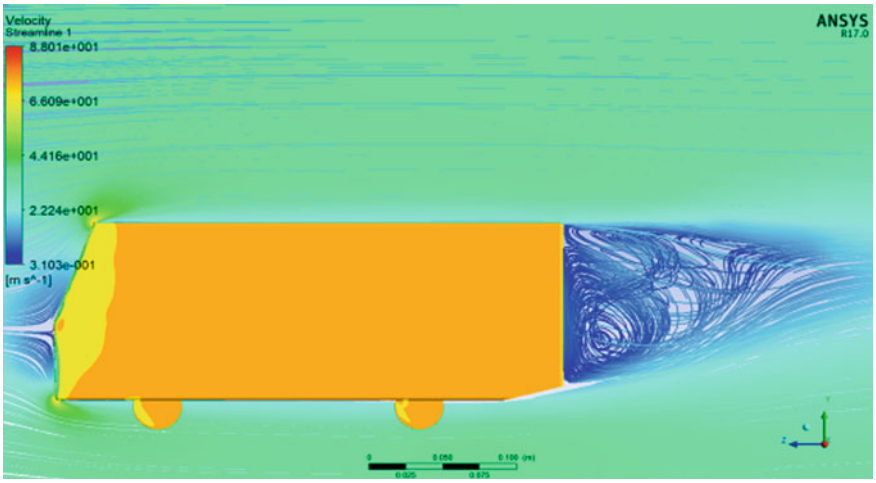


**Fig. 13** Model I velocity contour at 120 kmph

is induced due to the separation of high-speed flow near the rear end. In model IV (Fig. 16), due to the presence of a rear spoiler in the rear upper part of the bus, there is a slight improvement of the flow pattern behind the bus than model III (Fig. 15). Consequently, which minimize the low-velocity area in the wake region and delay the turbulence zone away from the bus model. In all models of the bus velocity streamline contour shows that the wake region gets stronger and wider as the speed increases (Fig. 14).

The comparison between the drag coefficient of the baseline model with the other four models at speeds of 80, 100 and 120 kmph was summarized in Table 1.

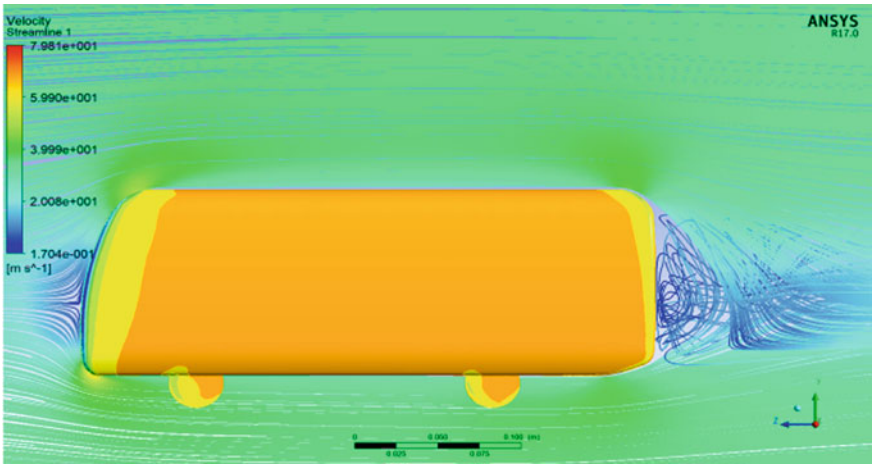


**Fig. 14** Model II velocity contour at 120 kmph

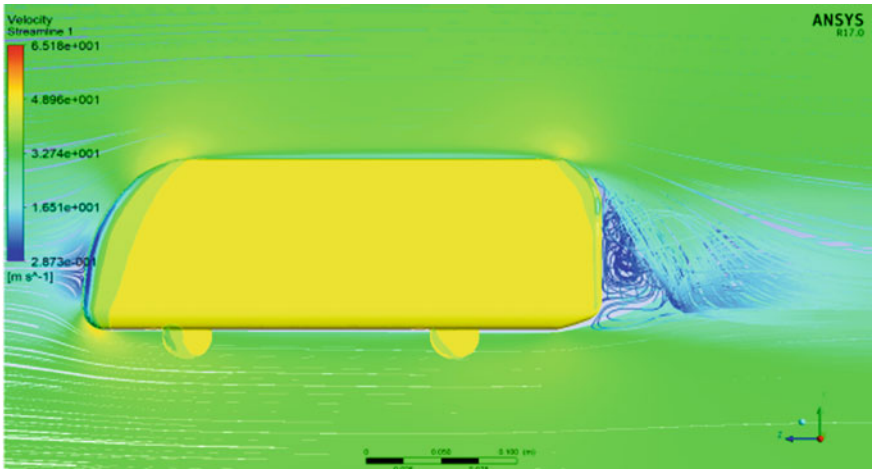


**Fig. 15** Model III velocity contour at 120 kmph

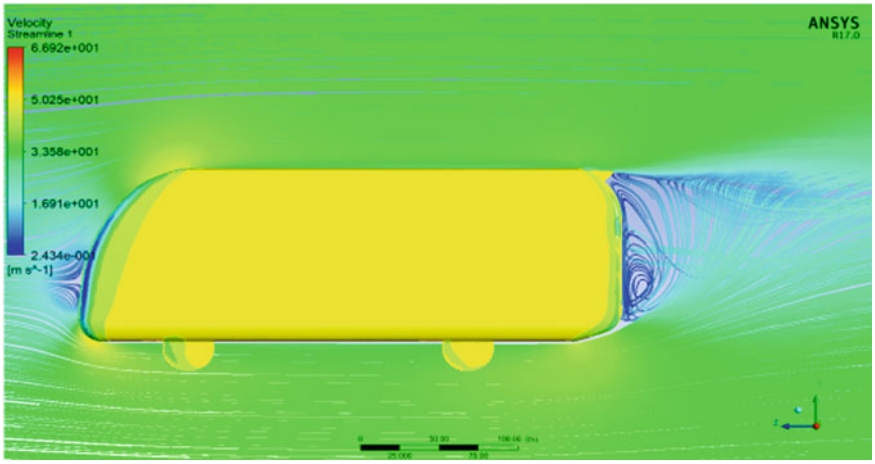


**Fig. 16** Model IV velocity contour IV at 120 kmph

Also summarizes the drag coefficient of four models with the percentage difference from the baseline model. Both at low and high speeds, model IV has the lowest drag coefficient, and the baseline model has the highest drag coefficient. Due to the exterior body modifications on the baseline model, the coefficient of drag reduced by model I, model II, models III and IV were approximately 23.15%, 47.46%, 53.09%, and 54.35%, respectively.

There is a maximum of 32.81% fuel can be saved in model IV from a baseline model at 80 kmph and 32.61% of fuel can be saved in model IV at three average speeds from a baseline model. The other high reduction was from model III with 32.41%, 31.89% and 31.34% at speed of 80, 100 and 120 kmph, respectively. Model II reduces the amount of fuel consumption with 28.61%, 28.42% and 28.38% relative to a baseline model at speeds of 80, 100 and 120 kmph, respectively. However, model I has the least fuel reduction with 15.01%, 14.79% and 11.88% of fuel when compared to the baseline model at speed of 80, 100 and 120 kmph, respectively.

## 4 Conclusions

After the analysis of all models, the modified models and a model with rear spoiler reduced the amount of swirling air in the back of the bus and hence reduced the amount of drag coefficient compared to the baseline model. On the backside of the baseline model of Isuzu midi bus, there is a formation of a large wake zone and it caused higher pressure difference between the front and the rear of the bus, causing high drag. To improve the aerodynamic performance of the existing bus, four modifications of the exterior body were prepared. The last prepared model employed rear spoiler, which was meant to push the flow separation a bit rearward and decrease

the amount of drag by minimizing the wake region and by throwing the turbulent air behind the vehicle.

- The results show that by modifying the exterior shape of the bus body, it is possible to improve aerodynamic performance. Also, by using add on a device like a spoiler, one can improve the performance of the bus. These modifications helped considerably in reducing the coefficient of drag, i.e. Cd which improved fuel consumption and reduced to exhaust emission.
- It was found that model IV has the least drag force. Bus model II and III gave an intermediate result. The average drag coefficient of the baseline model, model I, model II, model III, and model IV were 0.72881, 0.56010, 0.38293, 0.34184 and 0.33267, respectively. Due to the exterior body modifications on the baseline model, the coefficient of drag reduced by model I, model II, models III and IV were approximately 23.15%, 47.46%, 53.09%, and 54.35%, respectively.
- The maximum of 32.81% fuel can be saved in model IV from a baseline model at 80 kmph and 32.61% of fuel can be saved in model IV at three average speeds. This reduction in exhaust emission has a significant effect on the environment.

## References

1. Barnard RH (2009) Road vehicle aerodynamics design, 3rd edn. Mech Aero Publishing
2. Hucho WH (1998) Aerodynamics of road vehicles, 4th edn. Society of Automotive Engineers, Warrendale
3. Bansal R, Sharma RB (2014) Drag reduction of a passenger car using add-on devices. J Aerodyn 2014, Article ID 678518 (Hindawi Publishing Corporation)
4. Muthuvel A, Murthi MK, Sachin NP, Koshy VM, Sakthi S, Selvakumar E (2013) Aerodynamic exterior body design of bus. Int J Sci Eng Res (IJSER) 4(7)
5. Ramasekhar Reddy P, Lokanadham R (2017) CFD analysis on aerodynamic effects on a passenger car. Int Res J Eng Technol (IRJET) 04(09)
6. Barnard RH (2001) Road vehicle aerodynamic design, 2nd edn. Mech. Aero Publishing
7. Raveendran A et al (2009) Exterior styling of an intercity transport bus for improved Aerodynamic performance. SAS TECH 8(2)
8. Patil CN, Shashishekar KS, Balasubramanian AK, Subbaramaiah SV (2012) Aerodynamic study and drag coefficient optimization of passenger vehicle. Int J Eng Res Technol (IJERT) 1(7)
9. Raiyan MF, Hossain S, Akanda MNU, Jony NH (2014) A comparative flow analysis of NACA 6409 and NACA 4412 Aerofoil. Int J Res Eng Technol 03(10). ISSN: 2319-1163 | pISSN: 2321-7308
10. Mahdi Al-Obaidi AS, Otten WA (2018) Aerodynamic analysis of personal Vehicle side mirror. J Eng Sci Technol 52–64 (School of Engineering, Taylor's University, 7th EURECA)
11. Seibert W, Lanfrit M, Hupertz B, Kruger L (2002) A best practice for high-resolution aerodynamics simulation around a production car shape. In: Fourth MIRA international vehicle aerodynamics conference in Warwick, UK
12. Feliche E, Nallamothu RB, Nallamothu SK (2017) A study on cause of rollover of sugar cane haulage semitrailer truck in Ethiopia Sugar Estate: case of Wonji Sugar Factory. Int J Eng Trends Technol (IJETT) 43(4):205–211

13. Yesfalgn Damissie H, Ramesh Babu N (2017) Aerodynamics drag reduction on locally built bus body using computational fluid dynamics (CFD): a case study at Bishoftu automotive industry. Int J Eng Res Technol (IJERT) 6(11). ISSN: 2278-0181
14. Ashagrie G, Nallamothu RB, Nallamothu AK, Nallamothu SK (2017) A study on driving stability of bus using computational fluid dynamics (CFD). Int J Res Appl Sci Eng Technol 5(XI)
15. Molla KY, Chul-Ho K, Ramesh Babu N (2017) Aerodynamic design of the Ethiopian train for energy economy under crosswind conditions. 년도한국철도학회추계계학술대회논문집, KSR 2017, South Korea
16. Siraj A, Ramesh Babu N, Srinivasa Reddy K (2019) Static analysis of dump truck chassis frame made of composite materials. Int J Eng Sci Technol 11(2):21–32

# Wear Characteristics of Aluminum Composite Reinforced by Multiwall Carbon Nanotubes


**Sunil Kumar Tiwari, Ankit Dasgotra, Vishal Kumar Singh, Akula Umamaheswararao, and Jitendra Kumar Pandey**

## 1 Introduction

Many researchers have shown their interest in the area of metal matrix nanocomposites more specifically toward aluminum composite because of their enhanced properties as compared to the involved individual components [1, 2]. Increased properties of composites like strength, hardness, corrosion resistance, dimensional stability, thermal stability, etc., make them suitable for their use in automotive industries [3–5]. In addition to this, low density, low specific weight, stiffness, and wear resistance properties of aluminum composites make them an appropriate candidate for aerospace and marine industries [1, 6, 7]. They are mostly used in the parts where reciprocating and rotating motions are common to happen like, piston, brakes, drive shafts, etc. [8]. Researchers have opted several methods to fabricate aluminum composite broadly liquid and solid processing. They have used SiC, B4C, Pb, $TiB_2$, $Al_2O_3$ in micro- and nanosize as reinforcing material for fabricating aluminum composite [6]. Looking in the scenario of introducing new and

S. K. Tiwari · A. Dasgotra · V. K. Singh · J. K. Pandey (✉)
Department of Research and Development, University of Petroleum and Energy Studies, Dehradun, Uttarakhand 248007, India
e-mail: jkpandey@ddn.upes.ac.in

S. K. Tiwari
e-mail: sktiwari@ddn.upes.ac.in

A. Dasgotra
e-mail: adasgotra@ddn.upes.ac.in

V. K. Singh
e-mail: vk.singh@ddn.upes.ac.in

A. Umamaheswararao
Department of Mechanical Engineering, Lovely Professional University, Jalandhar, Punjab 144411, India



K. Jha et al. (eds.), *Recent Advances in Sustainable Technologies*,
Lecture Notes in Mechanical Engineering,
https://doi.org/10.1007/978-981-16-0976-3_13

emerging nanoreinforcements, authors have synthesized aluminum composite with carbon nanotubes. Particularly, they have used multiwall carbon nanotubes reinforced aluminum composite for industrial applications because of the decreased cost of production of MWCNT [9, 10]. Carbon nanotubes possesses excellent mechanical, thermal, and wear resistance properties [7, 8, 11, 12]. Researchers have successfully fabricated Al-CNT composite through different fabrication routes but they have found the common problem of agglomeration of CNT in aluminum matrix, poor wettability, and porosity in final part [2, 13]. Many researchers have found enhanced mechanical, thermal, electrical, and corrosion resistance properties when they reinforced aluminum with CNT, and few studies have also reported enhanced wear resistance properties of the composite. Bustamante et al., have fabricated Al-2024-CNT composite through milling process, and they have found that with highest weight percent of carbon nanotube in aluminum matrix, better wear resistance property of the composite was achieved [6]. Choi et al., have also explained that the presence of CNT shows effective contribution toward improving the wear resistance properties of Al-CNT composite [9]. Aranke et al., found that addition of CNT has not shown positive effect in enhancing wear resistance properties of the composite. Moreover, reinforcing aluminum with CNT beyond 0.7wt% resulted in decreased wear resistance [2]. Kim et al., have also explained that excessive CNT in aluminum resulted in decreased hardness and increased wear in the composite [14]. It has been studied that, along with the CNT dispersion, CNT agglomeration, size and fraction of CNT, carbide formation in the composite, wear-resistant property of the material also depends upon the working environmental conditions and load applied on the material [15, 16]. Xu et al., proclaimed that addition of CNT in aluminum strengthens the matrix and thereby enhances the wear resistance property of the composite. This study reflects the fabrication of aluminum composite through melting process and also explains the effect of reinforced carbon nanotube on wear resistance property of composite.

## 2 Materials and Methods

In present study, Al-7075-t6-51 and multiwall carbon nanotubes (MWCNT) were used as matrix and reinforcing material, respectively. MWCNTs (with > 99% purity, diameter 10–12 nm, and length 4–8 μm) were reinforced in matrix through stir casting technique in open environment at room temperature as shown in Fig. 1 [17–19]. Crucible, mold, and stirrer were prepared from graphite to prevent contamination in the composite. Four class of composites, Al-0 wt%CNT, Al-0.1 wt%CNT, Al-0.15 wt%CNT, and Al-0.2 wt%CNT, were prepared to compare and study their wear properties. Samples for wear test were prepared according to ASTM G99 standards (Φ 6 mm, length 30 mm). The contact surfaces of prepared samples were polished and cleaned using different grades of silicon carbide grit papers (from 120 to 1000). They were cleaned prior testing using acetone. Test was performed on pin-on-disk tribometer in dry sliding condition. Parameters used for conducting wear tests for all

**Fig. 1** Stir casting setup and operating processes

samples were, track diameter 70 mm, load-10 N, RPM 454, time 15 min and disk of high-speed steel. Experiment was conducted at room temperature at constant load, RPM and for same time. Figure 2 shows the setup of pin-on-disk tribometer along with disk and samples.


**Fig. 2** Pin-on-disk setup with samples and disk

## 3 Results and Discussion

Results of wear and friction force obtained from the instrument has been shown in Figs. 3 and 4, respectively, as (a) Al-0 wt%CNT, (b) Al-0.1 wt%CNT, (c) Al-0.15 wt%CNT, and (d) Al-0.2 wt%CNT. Data points on *X*-axis represent time in seconds. From Fig. 3, it can be clearly seen that, the pure sample (without reinforced CNT) has shown the maximum wear after 15 min of continuous sliding on the disk. With increase in reinforcement (by wt%), wear loss decreased and composite with 0.2 wt% CNT has shown the minimum wear loss.

From the results obtained, we can say that the overall impact of reinforced CNT on wear resistance properties of composites is nearly same for all samples. This can be understood well in the way that the wear characteristic of the Al-CNT composite depends on the homogeneous mixing of CNT in the matrix and synthesis process

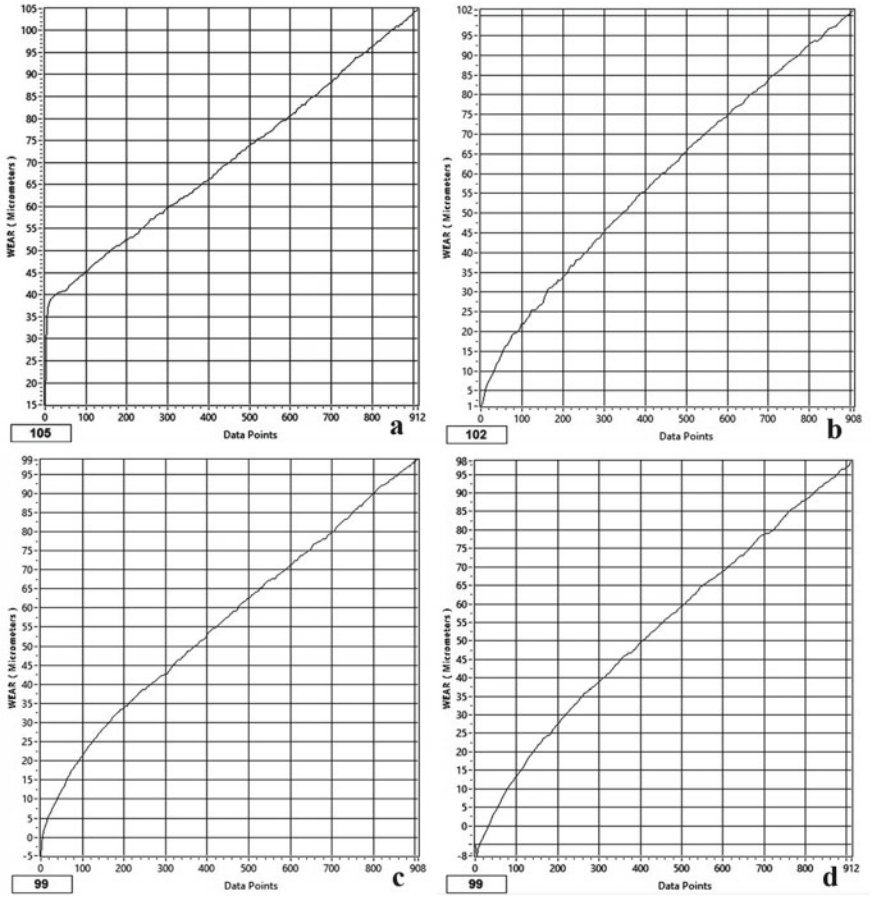


**Fig. 3** Wear results of the composites

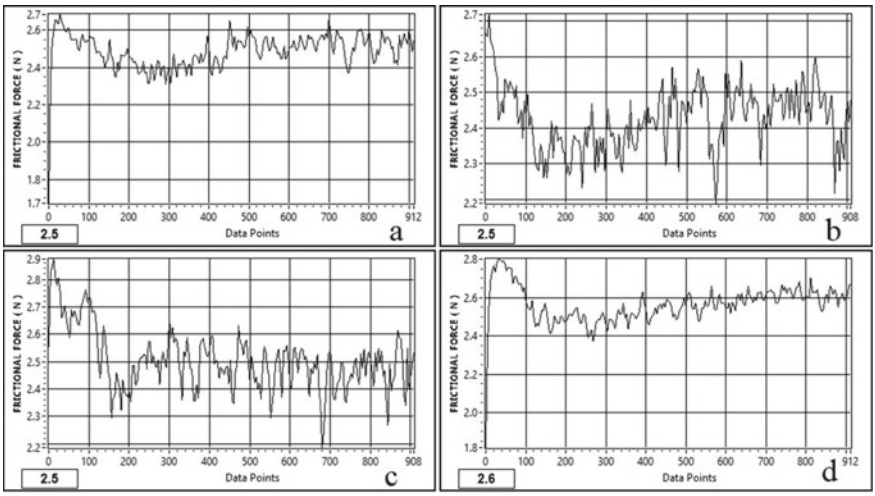


**Fig. 4** Frictional results of the composites

[6]. One of the good properties of CNT is to provide self-lubricating property, which resist wear in the material. Inhomogeneous mixing and clustering of CNT in Al matrix results are non-uniform distribution of reinforcement and thus decrease the lubricating effect while fabricating through stir casting technique. Because of this, less impact of CNT on the tribological property in the composite has been observed. This decrease in the wear loss of the composite with increase in reinforcement can also be the result of depth of wear groove or flatness of the wear track of the disk due to its continuous rotation. Shivaramu et al. have explained a relevant theory related to this technique. Result of microhardness test has shown a gradual increase in the hardness of the composites as the ratio of reinforcement in the composite was increased up to 0.15 wt%CNT. Beyond this the hardness was decreased due to the agglomeration of CNT [19]. Results of hardness test have been summarized in Table 1. It can be explained in the way that the presence of CNTs in aluminum matrix results in increasing the brittleness and hardness of the composite. Microscopic results show that the size and structure of grains are almost same in every samples when seen at 100× Fig. 5. More microcracks and pits were seen in samples reinforced with carbon nanotubes as shown in Fig. 6. Due to the presence of microcracks near grain boundaries in reinforced samples, the bond between reinforcement and matrix

**Table 1** Hardness of composites

| S. No. | Sample | Hardness value (Hv) |
|---|---|---|
| 1 | Al-0 wt%CNT | 54.483 |
| 2 | Al-0.1 wt%CNT | 68.625 |
| 3 | Al-0.15 wt%CNT | 72.808 |
| 4 | Al-0.2 wt%CNT | 61.933 |

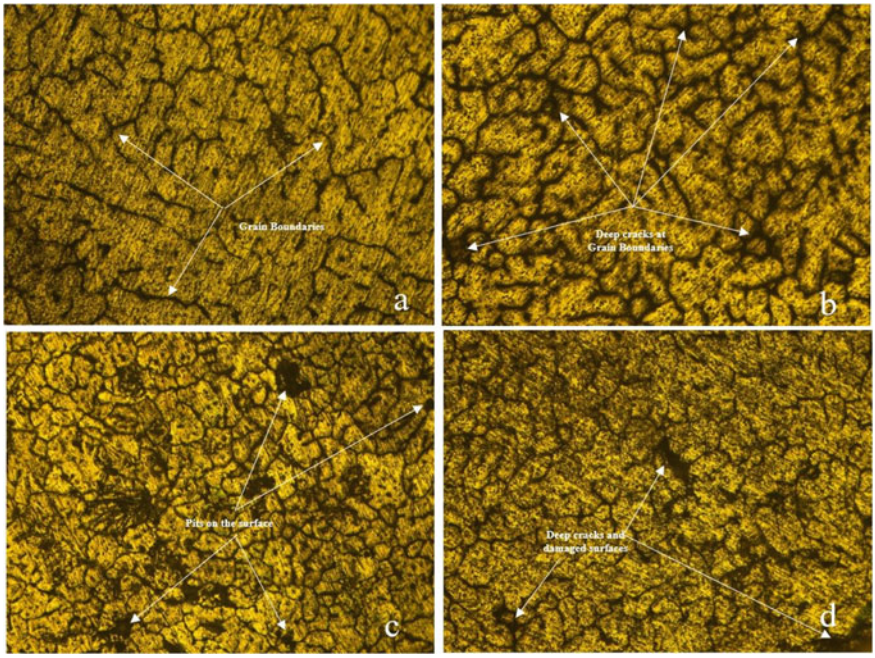


**Fig. 5** Surface structure of **a** Al-0 wt%CNT, **b** Al-0.1 wt%CNT, **c** Al-0.15 wt%CNT, and **d** Al-0.2 wt%CNT at 100×

was weak which minimized the effect of reinforcement in the composite. From the results of frictional force obtained from the setup, it can be seen that at the starting of every sample testing, we have observed increased frictional force. This is due to the uneven surface finish in disk and tip of pin and due to the formation of debris at worn surfaces. Once sliding time from 100 to 200 s passed, approximately constant range of frictional force has been obtained. This is due to the smoothing of contact surface of pin while sliding on the disk due to constant amount of temperature generated at the contact surfaces.

## 4 Conclusion

- Composites with different ratio of CNTs were fabricated using stir casting technique.
- Composite with 0.2 wt%CNT has shown better wear results as compared to other samples.
- Results obtained from the experiment suggest that reinforcement of CNTs in the matrix has not shown a remarkable result differences due to inhomogeneous mixing of CNT in the matrix.

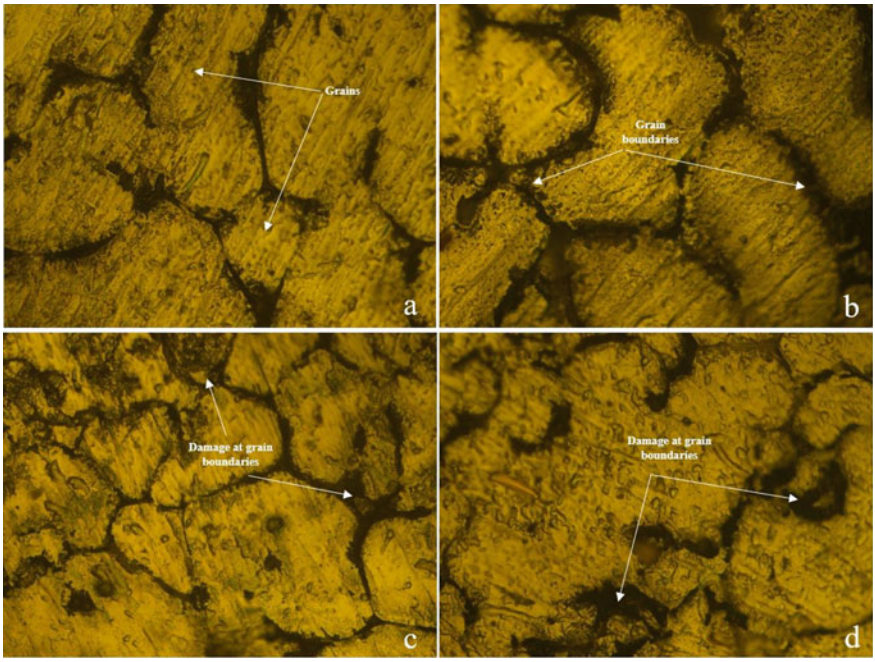


**Fig. 6** Surface structure of **a** Al-0 wt%CNT, **b** Al-0.1 wt%CNT, **c** Al-0.15 wt%CNT, and **d** Al-0.2 wt%CNT at 500×

- Temperature rise between sample and disk was approximately same for all the samples.
- Presence of MWCNT in the matrix is responsible for reflecting good results of wear in the composite.

**Acknowledgements** Authors are thankful for the support and help from Central Instrumentation Centre, University of petroleum and Energy Studies, Dehradun, India, and Department of Science and Technology, Ministry of Science and Technology, Government of India (DST/TM/WTI/2k16/245(G).

## References

1. Coyal A, Yuvaraj N, Butola R, Tyagi L (2020) An experimental analysis of tensile, hardness and wear properties of aluminium metal matrix composite through stir casting process. SN Appl Sci 2(5). https://doi.org/10.1007/s42452-020-2657-8
2. Aranke O, Gandhi C, Dixit N, Kuppan P (2018) Influence of multiwall carbon nanotubes (MWCNT) on wear and coefficient of friction of aluminium (Al 7075) metal matrix composite. Mater Today Proc 5(2):7748–7757. https://doi.org/10.1016/j.matpr.2017.11.452

3. Manikandan P, Sieh R, Elayaperumal A, Le HR, Basu S (2016) Micro/nanostructure and tribological characteristics of pressureless sintered carbon nanotubes reinforced aluminium matrix composites. J Nanomater 2016. https://doi.org/10.1155/2016/9843019
4. Meenakshi SU, Mahamani A (2015) Development of carbon nanotube reinforced aluminum matrix composite brake drum for automotive applications
5. Nam DH et al (2014) Hardness and wear resistance of carbon nanotube reinforced aluminum-copper matrix composites. J Nanosci Nanotechnol 14(12):9134–9138. https://doi.org/10.1166/jnn.2014.10084
6. Pérez-Bustamante R et al (2012) Wear behavior in Al 2024-CNTs composites synthesized by mechanical alloying. Wear 292–293:169–175. https://doi.org/10.1016/j.wear.2012.05.016
7. Singh S, Singh R, Gill SS (2020) Investigations for wear characteristics of aluminium-based metal matrix composite prepared by hybrid reinforcement. Proc Natl Acad Sci India Sect A—Phys Sci. https://doi.org/10.1007/s40010-020-00683-z
8. Sahoo B, Narsimhachary D, Paul J (2019) Tribological characteristics of aluminium-CNT/graphene/graphite surface nanocomposites: a comparative study. Surf Topogr Metrol Prop 7(3). https://doi.org/10.1088/2051-672x/ab3025
9. Choi HJ, Lee SM, Bae DH (2010) Wear characteristic of aluminum-based composites containing multi-walled carbon nanotubes. Wear 270(1–2):12–18. https://doi.org/10.1016/j.wear.2010.08.024
10. Shrivastava P, Alam SN, Panda D, Sahoo SK, Maity T, Biswas K (2020) Effect of addition of multiwalled carbon nanotube/graphite nanoplatelets hybrid on the mechanical properties of aluminium. Diam Relat Mater 104: https://doi.org/10.1016/j.diamond.2020.107715
11. Saleh B, Jiang J, Ma A, Song D, Yang D, Xu Q (2020) Review on the influence of different reinforcements on the microstructure and wear behavior of functionally graded aluminum matrix composites by centrifugal casting. Met Mater Int 26(7):933–960. https://doi.org/10.1007/s12540-019-00491-0
12. Yadav V, Harimkar SP (2011) Microstructure and properties of spark plasma sintered carbon nanotube reinforced aluminum matrix composites. Adv Eng Mater 13(12):1128–1134. https://doi.org/10.1002/adem.201100132
13. Kim HH, Babu JSS, Kang CG (2013) Fabrication of A356 aluminum alloy matrix composite with CNTs/Al2O3 hybrid reinforcements. Mater Sci Eng, A 573:92–99. https://doi.org/10.1016/j.msea.2013.02.041
14. Kim IY, Lee JH, Lee GS, Baik SH, Kim YJ, Lee YZ (2009) Friction and wear characteristics of the carbon nanotube-aluminum composites with different manufacturing conditions. Wear 267(1–4):593–598. https://doi.org/10.1016/j.wear.2008.12.096
15. Al-Qutub AM, Khalil A, Saheb N, Hakeem AS (2013) Wear and friction behavior of Al6061 alloy reinforced with carbon nanotubes. Wear 297(1–2):752–761. https://doi.org/10.1016/j.wear.2012.10.006
16. Carvalho O, Buciumeanu M, Madeira S, Soares D, Silva FS, Miranda G (2015) Dry sliding wear behaviour of AlSi-CNTs-SiCp hybrid composites. Tribol Int 90:148–156. https://doi.org/10.1016/j.triboint.2015.04.031
17. Tiwari SK, Singh H, Midathada A, Sharma S, Ravella UK (2018) Study of fabrication processes and properties of Al-CNT composites reinforced by carbon nano tubes—a review. Mater Today Proc 5(14):28262–28270. https://doi.org/10.1016/j.matpr.2018.10.109
18. Tiwari SK, Sharma H, Deepmala KM, Umamaheswararao A (2019) Investigation of mechanical and tribological properties of aluminum composite reinforced by boron carbide. Silicon Carbide and Carbon Nanotubes, pp 5494–5498
19. Tiwari SK, Sharma H, Umamaheswararao A, Sharma S (2020) Synthesis and characterization of aluminum composite reinforced by multiwall carbon nanotubes. In: Advances in materials science and engineering. Springer, Singapore, pp 115–124

# Advancement in Digital Flight Control System


**J. V. Muruga Lal Jeyan, Akhila Rupesh, Sabiha Parveen, and Ajith Kumar**

## 1 Introduction

The main aim of the paper is to create an aircraft which gives the expected actuation by overcoming the overloading. This is to be done with the help of microcontroller and to design the feedback unit using comparators. In aircraft with hydraulic and pneumatic actuators, it requires an additional air or oil chamber in order to provide the required actuation. This increases the size and cost of construction. The expected actuation may not be obtained due to the aerodynamic loading in the control surfaces. So, in commercial aircrafts, the pilot in the cockpit has to move the control stick until the required actuation is obtained. In order to overcome these difficulties, in this paper, electronic actuators with digital flight control system and light intensity are implemented [1–4].

J. V. Muruga Lal Jeyan
Department of Aerospace Engineering, Lovely Professional University, Phagwara, Punjab, India

A. Rupesh (✉) · A. Kumar
Department of Aeronautical Engineering, Mangalore Institute of Technology and Engineering, Moodbidri, Karnataka, India

A. Kumar
e-mail: ajithkumar@mite.ac.in

S. Parveen
Manav Rachna International Institute of Research and Studies, Faridabad, India



K. Jha et al. (eds.), *Recent Advances in Sustainable Technologies*,
Lecture Notes in Mechanical Engineering,
https://doi.org/10.1007/978-981-16-0976-3_14

## 1.1 Flight Control Systems (FCS)

A system that includes all aircraft subsystems and components used by the pilot or other sources to control one or more of the following:

- Aircraft flight path
- Altitude
- Airspeed
- Aerodynamic configuration
- Structural modes.

## 1.2 Flight Control Surfaces

An airplane usually has control surfaces and its controls, which enables the controlling of an aircraft and its stability. The control surfaces are having its own operating mechanisms, which works with cockpit controls [5].

The primary control surfaces are aileron, elevator, and rudder as shown in Fig. 1. There are three axes of rotation, namely roll axis, yaw axis, and pitch axis. An airplane may turn about three axes. Whenever the altitude of the airplane changes in flight (with respect to the ground or other fixed object), it will rotate about one or more of these axes. The three axes intersect at the center of gravity and each one is perpendicular to the other two. These three movements of the aircraft with respect to the corresponding axis are shown in Fig. 2.

The three primary control surfaces are responsible for the movement of the aircraft in the above-mentioned axes. The rolling, pitching, and yawing motion are controlled by aileron, elevator, and rudder, respectively, as shown in Fig. 3.

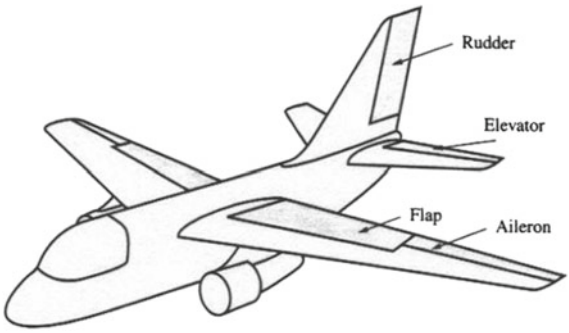


**Fig. 1** Location of control surfaces in the aircraft

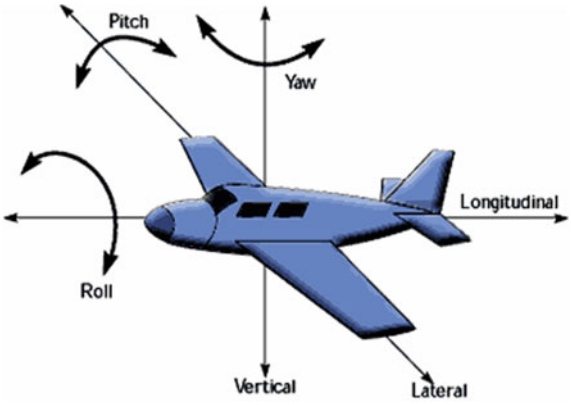


**Fig. 2** Movement with respect to corresponding axes

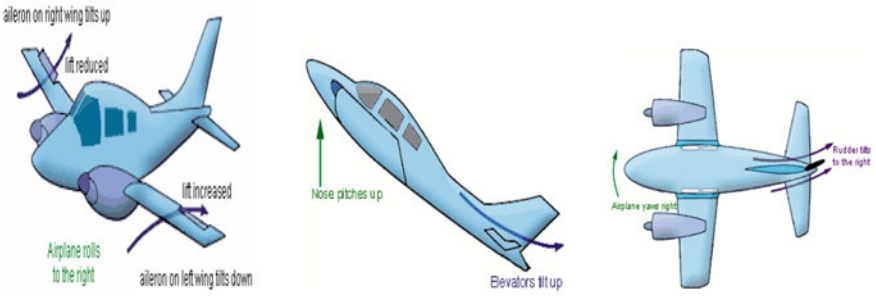


**Fig. 3** Control surfaces and its corresponding movements

## *1.3 Mechanical Control Systems(MCS)*

The mechanical systems are based on hydraulic actuators, pneumatic actuators, intelligent system, and mechanical systems with feedback. These existing systems and its disadvantages are discussed below, and also this paper deals with the control unit implemented in the proposed system in order to overcome the drawbacks of existing system. The main disadvantage of hydraulic actuators is that it requires separate oil chamber in order to perform actuation. It can leak and also requires position feedback for repeatability. In the case of pneumatic actuators, the force required by the stem is large, and hence, it may make the stem system to fail. It also requires a separate air chamber.

## 2 Methodology

### *2.1 Digital Flight Control System*

In order to overcome the drawbacks faced in the above mechanisms, we are going for the digital system. The digital flight control system is designed using electronic actuators with feedback system and digital micro controllers. The digital flight control systems are implemented using digital technology, and the pilot input signals are transmitted as serial digital data using avionics data bus networks. The signals data are subsequently processed by digital microcontrollers in the flight control computers (Fig. 4).

The advantages of digital flight control systems over the mechanical systems are easy installation and maintenance. Digital systems do not have the problem of friction. Digital systems are not affected by bending or vibration of aircraft.

The main advantages of digital flight control systems are as follows:

- Weight reductions
- Hardware economy
- Flexibility
- Digital avionics data buses.

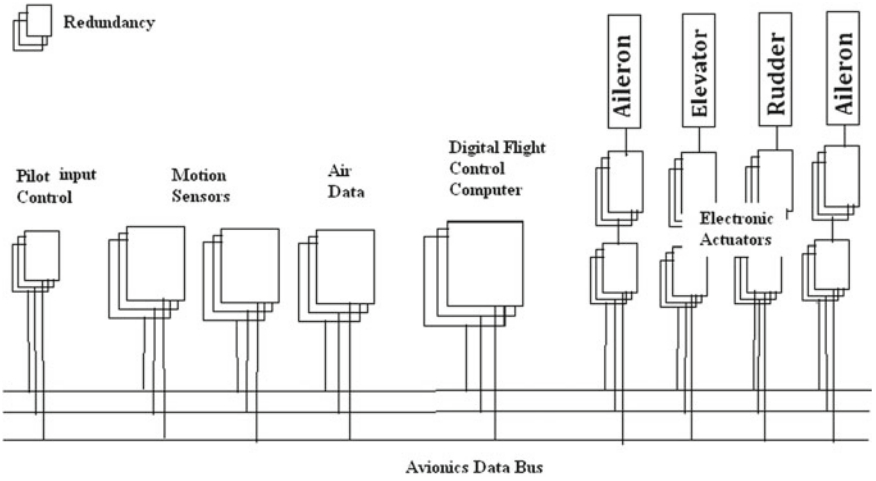


**Fig. 4** Systematic block diagram for maneuvering aircraft using digital flight control system

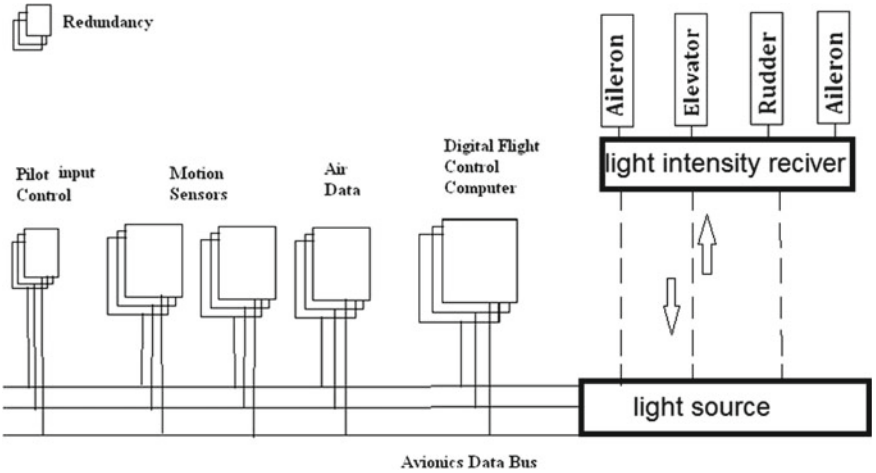


**Fig. 5** Systematic block diagram for maneuvering aircraft using light intensity

## *2.2 Fly by Light System*

With the intensity of the light reflected, control surface actuation can be done more effectively. Moreover, the usage of wires can be eliminated. The advantages of fly by light flight control systems over the digital systems are as follows:

- Easy installation and maintenance
- Light systems do not have the problem of friction
- Light systems are not affected by bending or vibration of aircraft.
- Weight reductions
- Hardware economy
- Flexibility
- Reliable
- Quick and accurate (Fig. 5).

## *2.3 Fly by Acoustics*

With the intensity of the sound reflected, control surface actuation can be done more effectively. Moreover, the usage of wires can be eliminated (Fig. 6).

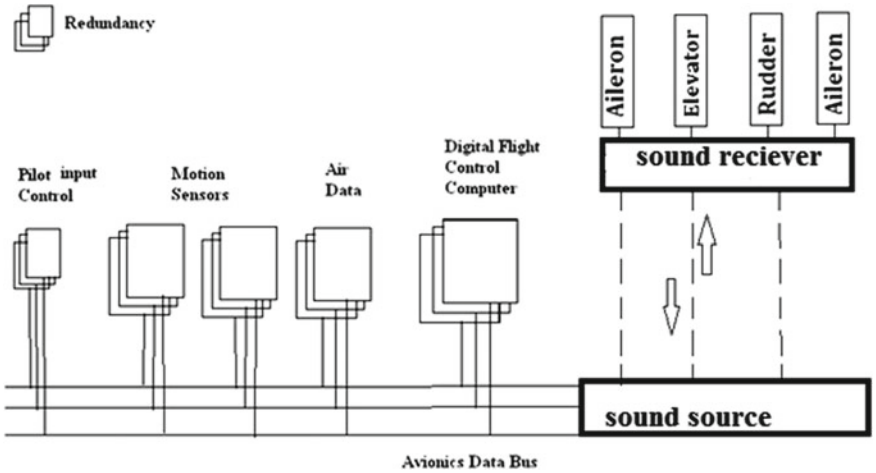


**Fig. 6** Systematic block diagram for maneuvering aircraft using sound source

## 3 Interfacing

The platform used for interfacing the microcontroller with the system is .NET. The combination of C# and Visual Basic is used as the programming language in .NET platform. Figure 7 shows the overview of the common language infrastructure. In our programming, we have used the combination of C# and VB.net codes.

## 4 Conclusion

With our analysis, we had concluded that digital flight control system, fly by light, and acoustics are more effective in actuation and feedback and this system reduces size and weight of the existing control systems.

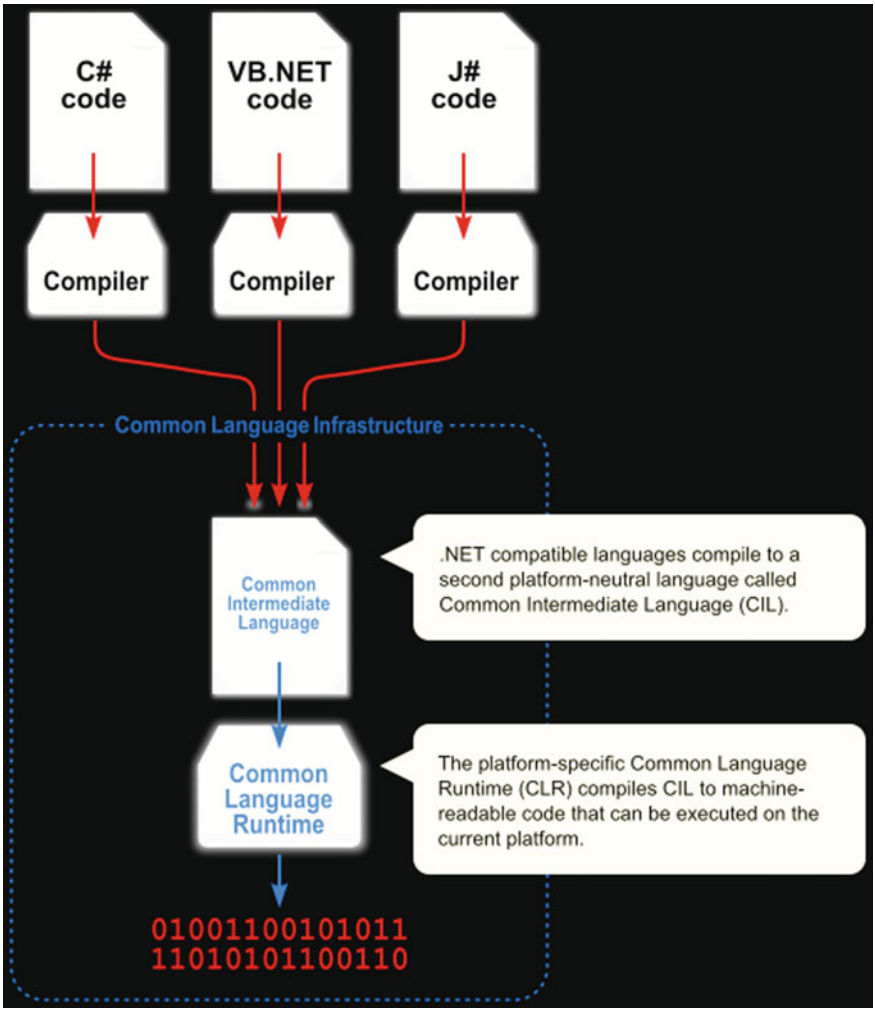


**Fig. 7** Overview of the common language infrastructure

## References

1. Johnson C (2001) Process control instrumentation technology, 4th edn., pp 1–30
2. Johnson EN et al (2004) Development and test of highly autonomous aerial vehicles. J Aerosp Comput Inf Commun 1
3. Gayakwad RA (1994) Op-amps and linear integrated circuit, 3rd edn. Prentice Hall, pp 343–345
4. Hage RE, Perkins CD, Airplane performance stability & control, pp 1–152
5. Nelson RC, Flight stability and control, 2nd edn., pp 100–170

# An Approach to Acquire Vibration Signals for Gear Fault Detection


**Vikas Sharma and Anand Parey**

## 1 Introduction

For sustainable power generation, health monitoring and fault diagnosis of a gearbox are very important for wind turbines (WTs) because these machines operate under harsh operating conditions. The speed and load of WTs keep on changing under real-time operating conditions [1] and can cause serious damage to them. Vibration-based health monitoring is one of the simplest and easiest ways to monitor gearbox health and detect an early fault, but it becomes complicated under varying operating conditions [2–4].

Primarily, techniques such as time synchronous averaging or fast Fourier transform (FFT) are limited to stationary operating conditions. The FFT exhibits the fault transient by virtue of the appearance of the sidebands and their density. Under varying speed conditions, the frequencies in FFT smears, and thus, the interested frequency components are difficult to mark [5]. With a course of time, many other signal-processing techniques such as wavelet transform, empirical mode decompositions, filter-based analysis, and many more have been developed to deal with the problem of varying speed conditions. All of these techniques have been developed to improve the overall representation of FFT and to display the variation in energy present in the gearbox vibration signal. These techniques have been also observed inefficient due to some of the assumptions made [2–4].

A major observation noted is the negligence of considering the transmission path of gear vibrations [6, 7]. Transmission path is the path by which gear tooth vibrations travels from the excitation source to the point of their reception [8, 9]. Conventionally,

V. Sharma (✉)
Department of Mechanical Mechatronics Engineering, The LNM Institute of Information Technology, Jaipur, India

A. Parey
Discipline of Mechanical Engineering, Indian Institute of Technology Indore, Indore, India



K. Jha et al. (eds.), *Recent Advances in Sustainable Technologies*,
Lecture Notes in Mechanical Engineering,
https://doi.org/10.1007/978-981-16-0976-3_15

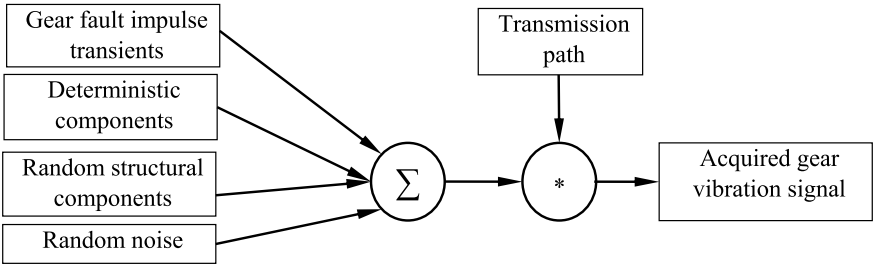


**Fig. 1** Role of the transmission path in gear vibration signal

an accelerometer is kept outside the gearbox and gear vibrations thus travels through numerous components such as gear, key, shaft, bearing, gearbox case, and bearing case before recorded. In this way, the vibrations of non-rotating parts, independent of speed variation, will also be recorded due to transmission path effect. Few researches have highlighted that the transmission path convolutes the actual gear vibration signal [10] as shown in Fig. 1. Further, the transmission path not only distorts [11] but also modulates the gear vibration signal [12]. Both the distance and different possible ways to travel the gear vibration signal also contributes to transmission path [13].

Few studies have discussed about mounting an accelerometer close to the gear pair, to acquire the strong vibration signals [14–16]. However, the methods have significant drawbacks such as use of slip rings causes electrical interference in the acquired vibration signals. Thus, there is a chance of getting erroneous results and misleading the fault detection. Therefore, an attempt has been made by mounting an accelerometer close to the gear pair, thereby minimizing the transmission path as well as overcoming the problem of interference. An experimental investigation has been carried out to exhibit the capability of proposed approach as well as detecting gear faults at varying speed conditions. In addition to this, two condition indicators (CI) have been used in the investigation to support the fault diagnosis [4]. These CIs viz. FM0 and sideband energy ratio (SER) quantifies the level of vibrations caused by the faults.

## 2 Proposed Novel Approach to Acquire Vibration Signal

In a gearbox, major components comprises of gear pair, shafts, keys, bearings, gearbox casing, and bearing case. Let an accelerometer, i.e., Accelerometer 1 ($Acc_1$) is mounted conventionally, and during meshing of a gear with tooth fault, the ensuing vibrations will travel through the different possible paths as shown in Fig. 2a. It shows that keeping accelerometer at a distance will increase transmission paths (i.e., TP-1 and TP-2 in Fig. 2a) which would not acquire purely gear vibration signals, but a composition of signals. Further, lubricating oil will also damp the gear vibration, since gear pair always remains in the lubricating oil present in the sump. It is further

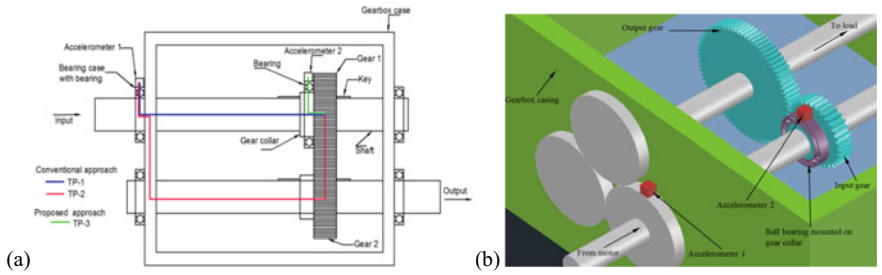


**Fig. 2** Proposed arrangement of placing an accelerometer, 3D model of the proposed arrangement

possible that due to these transmission paths, vibration signals may lose some significant information. Therefore, mounting of an accelerometer on the collar of a gear using a bearing (TP-3) has been proposed. Accelerometer 2 ($Acc_2$) is fixed to outer race of the bearing which remains free and steady during rotation, and the inner race of the bearing is press fit to the surface of gear collar, thus locked with the gear to rotate. It enables the fault induced vibrations to travel from the gear tooth to the $Acc_2$, as shown by green color in Fig. 2a. It would minimize the effects of the transmission path and damping of vibrations by lubrication.

A 3D model of the proposed arrangement exhibiting how to place an accelerometer inside the gearbox is shown in Fig. 2b. $Acc_1$ shows the conventional position of an accelerometer placed outside gearbox on bearing case. $Acc_2$ is mounted inside the gearbox, on a newly installed fresh ball bearing on the gear collar. This way weak transients due to early localized faults can be easily perceived by $Acc_2$ without being adulterated. Acquiring gear vibration signals via both the accelerometers will help to contrast the effect of the transmission path. Further, it is also expected that $Acc_2$ will not acquire the vibrations caused by non-rotating components or the structural vibrations.

To evaluate the acquired signals statistically, the CIs: FM0 and SER were used and their responses were noted against the fault. FM0 highlight the changes in meshing pattern. For a signal $x$, FM0 is expressed as the ratio of maximum peak-to-peak amplitude ($PP_x$) to summation of amplitude ($P_N$) of $N$th harmonics, and $H$ being the total number of harmonics analyzed in the frequency spectrum [4]:

$$\text{FM0} = \frac{\text{PP}_x}{\sum_{N=0}^{H} P_N}$$

SER is the ratio of the summation of the sideband amplitudes to the amplitude of the center mesh frequency. SER is a crucial parameter to analyze the FFT statistically and therefore used in this study to validate the results of the FFT. It is expressed as [17]:

$$\text{SER} = \frac{\sum_{i=1}^{6} \text{Sideband amplitude}_i}{\text{center mesh frequency amplitude}}$$

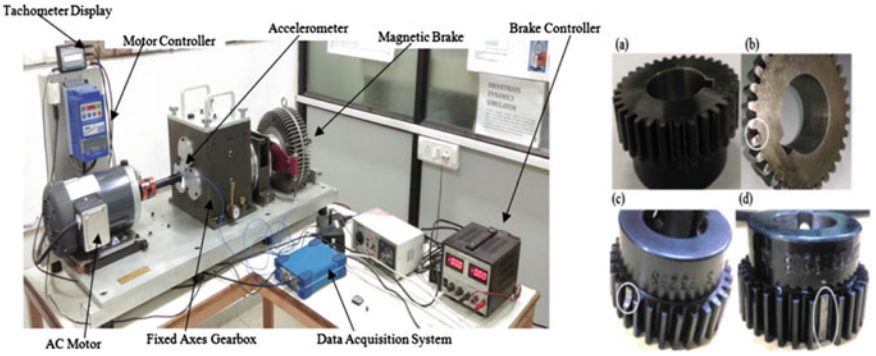


**Fig. 3** Experimental setup and different gears, **a** Healthy gear; **b** cracked tooth gear; **c** chipped tooth; **d** missing tooth gear

## 3 Experimental Investigation

### *3.1 Test Setup*

The experimental investigations were performed on a drivetrain diagnostic simulator (Fig. 3), which utilizes a 2.237 kW, 3phase, 0–3000 rpm AC drive motor simulating a WT. The operational speed and load can be varied at the same time with the help of a VFD. The vibration signals were acquired from single stage gear set encompassing a gear-pinion pair of 20° pressure angle, further specifications of gearbox are mentioned [5]. Gear tooth faults, i.e., cracked tooth, chipped tooth, and missing tooth (Fig. 3) have been considered. Experiments were performed at no load, 40% load, i.e., 32 Nm and 80% load, i.e., 64 Nm, respectively.

### *3.2 Arrangement of Accelerometers*

In the present setup, the gears had an extended collar; therefore, such an arrangement of placing bearing was made. As earlier mentioned, two accelerometers were mounted as shown in Fig. 4. The zoomed view of $Acc_2$ mounted on the gear collar inside the gearbox is shown in Fig. 4b. The accelerometer is fixed by means of an adhesive on the outer race of bearing. Similarly, the outer race of bearing was hold by means of an adhesive arrangement such that its outer race is locked, and the inner race is allowed to rotate freely. Another view of $Acc_2$ mounted on the gear collar using ball bearing is shown in Fig. 4c. PCB-based ICP type uniaxial accelerometers have been used in this study (Table 1). The effect of installed bearing will also be observed; however, its effect will be insignificant. Thus, this arrangement will lead to an efficient fault detection for incipient faults.

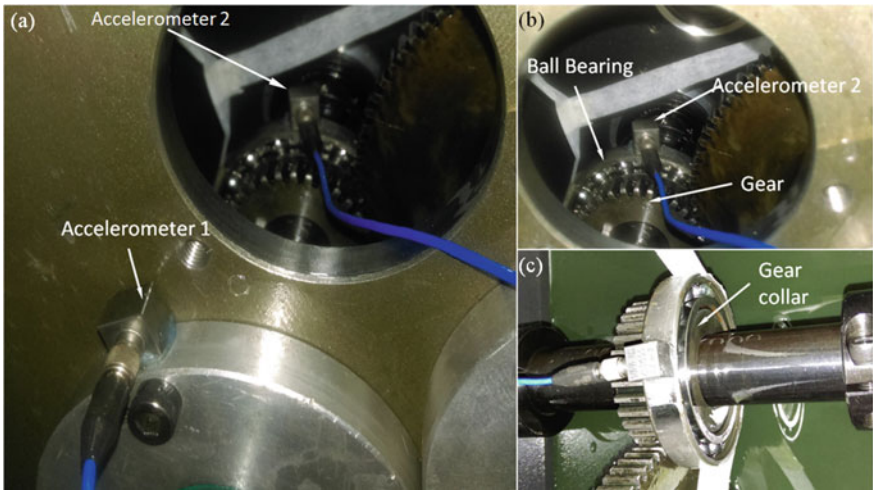


**Fig. 4** Arrangement of accelerometers, **a** zoomed view of $Acc_2$, **b** another view of $Acc_2$

**Table 1** Accelerometer specification

| Model No. | Sensitivity (mV/(m/s$^2$)) | Frequency range (Hz) | Measuring range (m/s$^2$ pk) |
|---|---|---|---|
| PCB 333B32 | ($\pm$10% )10.2 | ($\pm$5% )0.5 $-$ 3000 | $\pm$490 |

## *3.3 Speed Fluctuation*

The prime objective of the investigation was to acquire vibration signals of a greater strength and simultaneously minimizing the effect of transmission path. To record the vibration signals, a sampling rate of 25.4 kHz and at constant loads, following are the speed profiles used to record the vibration signals [18]:

**Sinusoidal speed variation**: Sinusoidal speed variations are more prominent in gearbox. Figure 5a shown the sinusoidal speed variation governed by $f_i = 5 + (\sin(2\pi 5t))$, where $f_i$ is the input speed and $t$ is time.

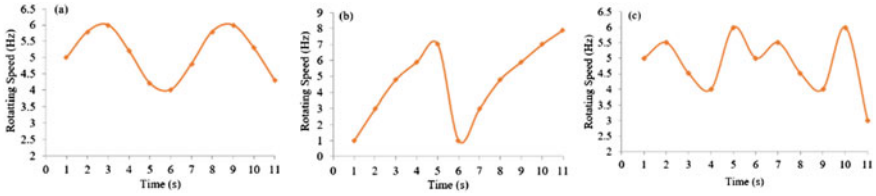


**Fig. 5** Variation in speed; **a** sinusoidal speed, **b** quadratic speed, **c** random speed

**Quadratic speed variation**: A quadratic fluctuating profile of speed, expressed as $f_i = -12.9t^2 + 20t + 1$, (Fig. 5b), is also noticed in WT as run-up speed conditions.

**Random speed variation**: $T$ the input speed $f_i$ is fluctuated around 20% of $f_i = 5$ Hz to imitate random, expressed as $f_i = [5, 5.5, 4.5, 4, 6, 5, 5.5, 4.5, 4, 6]$ and plotted as Fig. 5c.

## 4 Result and Discussion

The vibration signals were acquired at varying speed conditions under different loads of 0%, 40%, and 80% for all the considered gear tooth faults. Figure 6 shows the vibration signals acquired at the aforementioned speed by both the accelerometers. It is noted that there is a marginal increase in the amplitude of the vibration signals acquired by $Acc_2$ for the healthy gear as compared to corresponding responses of $Acc_1$. For faulty gear conditions, the amplitude of the signals for $Acc_2$ is twice of the amplitude of signals perceived by the $Acc_1$ for all the varying speeds at different loads. This implies a loss of the amplitude in the gear vibration signal for the faulty gears, which is possible due to the negative effect of the transmission path. In other words, it can be said that the signal strength is higher when the signal is monitored close to the fault-prone location/excitation source, as displayed by $Acc_2$. Further, for comparative analysis, signal-to-noise ratio (SNR) was also computed and marked

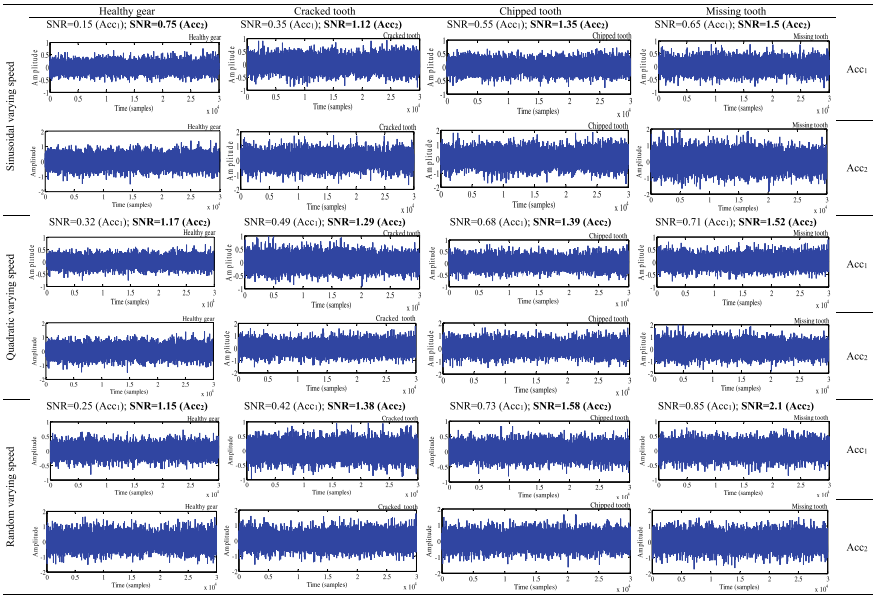


**Fig. 6** Time-domain signal for different gear health under varying speed at 40% load

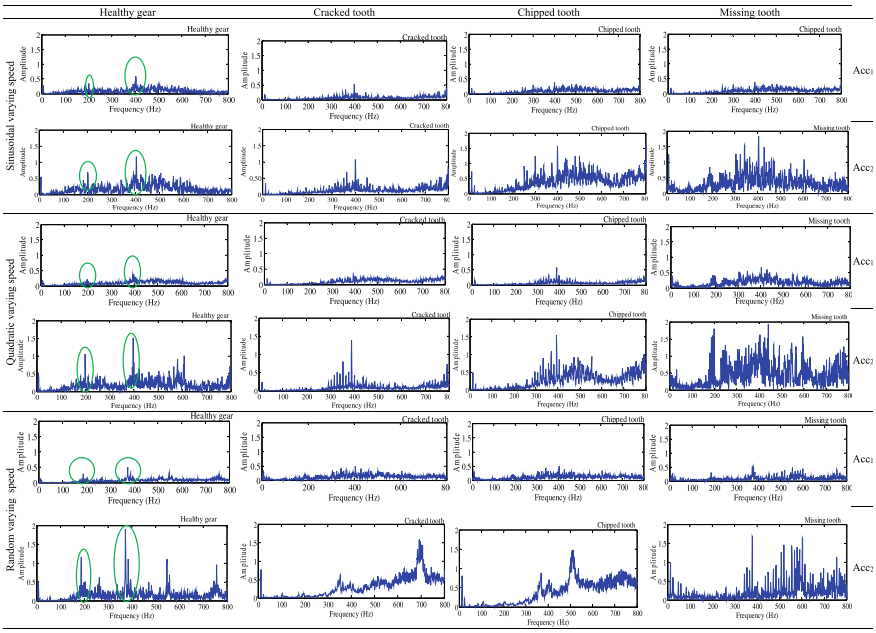


**Fig. 7** FFT for different gear health under varying speed at 40% load

in Fig. 6. The signals acquired by the $Acc_2$ have a higher SNR value for all the gear health conditions under different speed conditions. Considering both SNR and amplitude of signals by $Acc_2$ exhibits that placing of accelerometer close to the gear will increase the signal strength and reduce the negative effects caused due to the lengthy and multiple vibration transmission paths.

Detection of a gear tooth fault fundamentally depends on the identification of the GMF, sidebands, and their amplitude. The FFT of the time-domain gear vibration signals is displayed in Fig. 7. On observing the responses of $Acc_2$ for healthy gear, the first dominating peak was appeared at 180 Hz, which on reverse calculation deduces a mean shaft speed of 5.625 Hz (180 Hz $\div$ 32 $=$ 5.625 Hz). It is well known that with increasing fault severity, the sidebands around the central frequency (i.e., GMF) components increases. This behavior is very well observed for cracked tooth, chipped tooth, and missing tooth fault under sinusoidal speed conditions for the vibration signals of $Acc_2$. The response of $Acc_2$ seems to be less affected under sinusoidal fluctuating speed. For quadratic speed fluctuation profile, the healthy gear FFT again exhibits the clear peaks, i.e., GMF and its harmonics, however, in this case, GMF appears at 190 Hz that corresponds to shaft rotation speed of 5.93 Hz. Similarly, for random speed variation, the FFT of the healthy gear exhibits the clear frequency components for the $Acc_2$. This satisfies the objective of acquiring vibration signals of more strength from close to the point of vibration excitation.

Afterward, FM0 and SER were employed to distinguish the gear health and validate the fault based on their values. Their responses for the externally placed

accelerometer were found trivial; however, the responses for the internally placed accelerometer were impressive. This shows that $Acc_2$ has a superior performance in recognizing the localized gear tooth faults. Table 2 lists the value obtained of FM0 and SER for all the localized faults. It has been observed that the FM0 ranges within 0.01–0.07, with an average increase of 27% from healthy to initial crack for all the specified conditions of load and speed. SER ranges from 2.5 to 16, with an average increase of 27% from healthy to initial crack, showing both the indicators diagnosing different faults under fluctuating speed.

Figure 8 exhibits the responses of FM0 and SER, respectively, for 0%, 40%, and 80% load under the fluctuating profiles of speed. The deflection and vibrations in a gear pair will increase in the order of healthy gear tooth, cracked gear tooth, chipped gear tooth, and missing gear tooth. Therefore, there is a substantial increase in the CIs with the fault can be noted from Fig. 8. The measurements were captured with the utmost care and using state-of-the-art instrumentation. The signals acquired using the proposed method show advantages over the conventional method of acquiring gear vibration signals.

## 5 Conclusion

A new arrangement of placing an accelerometer in the gearbox for better signal quality as well as for enhanced fault detection without using complicated signal-processing techniques is demonstrated. An accelerometer is mounted internally on the gear collar of one of the gears of a gear pair. The responses of the proposed arrangement of accelerometer have been compared by evaluating SNR value, the amplitude of time domain signals, FFT spectrum, and responses of CIs to the conventional arrangement of mounting accelerometer. It has been found that the vibration signals acquired from an accelerometer placed internally were strong and capable to exhibit the fault features/symptoms. Further, responses of two CIs, i.e., FM0 and SER validate the capability of mounting accelerometer internally and detects the presence of gear tooth fault under varying speed conditions.

**Table 2** Performance of CI for different localized gear tooth faults

| Features | | | Gear | | | | | | | |
|---|---|---|---|---|---|---|---|---|---|---|
| | | | No crack | | Initial crack | | Chipped tooth | | Missing tooth | |
| | | | $Acc_1$ | $Acc_2$ | $Acc_1$ | $Acc_2$ | $Acc_1$ | $Acc_2$ | $Acc_1$ | $Acc_2$ |
| 40% load conditions | (a) | Sinusoidal varying speed | | | | | | | | |
| | | FM0 | 0.0629 | 0.2121 | 0.1004 | 0.2951 | 0.1492 | 0.4112 | 0.2117 | 0.5051 |
| | | SER | 3.4561 | 3.2014 | 5.0014 | 6.7714 | 6.7918 | 9.2514 | 7.1014 | 12.9821 |
| | (b) | Quadratic varying speed | | | | | | | | |
| | | FM0 | 0.0211 | 0.2998 | 0.0414 | 0.3114 | 0.0866 | 0.5152 | 0.1251 | 0.5995 |
| | | SER | 3.6114 | 3.1141 | 4.5578 | 6.7132 | 5.9814 | 8.9919 | 7.0141 | 11.0141 |
| | (c) | Random varying speed | | | | | | | | |
| | | FM0 | 0.0477 | 0.2751 | 0.0711 | 0.3292 | 0.1291 | 0.3715 | 0.2014 | 0.486 |
| | | SER | 3.5114 | 3.2151 | 4.7151 | 6.5795 | 6.8881 | 9.0019 | 8.0101 | 11.8417 |

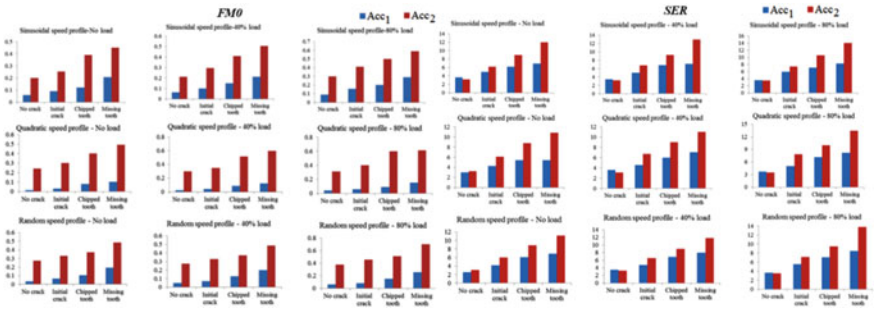


**Fig. 8** Responses of FM0 and SER under varying speed at different loads

## References


1. Feng Z, Liang M (2014) Fault diagnosis of wind turbine planetary gearbox under nonstationary conditions via adaptive optimal kernel time–frequency analysis. Renew Energy 66:468–477
2. Salameh JP, Cauet S, Etien E, Sakout A, Rambault L (2018) Gearbox condition monitoring in wind turbines: a review. Mech Syst Signal Process 111:251–264
3. Maheswari RU, Umamaheswari R (2017) Trends in non-stationary signal processing techniques applied to vibration analysis of wind turbine drive train—a contemporary survey. Mech Syst Signal Process 85:296–311
4. Sharma V, Parey A (2016) A review of gear fault diagnosis using various condition indicators. Procedia Eng 144:253–263
5. Sharma V, Parey A (2017) Frequency domain averaging based experimental evaluation of gear fault without tachometer for fluctuating speed conditions. Mech Syst Signal Process 85:278–295
6. Huang W, Sun H, Dou H, Wang W (2017) Study of transmission path of wind turbine gearbox fault vibration signal based on power flow finite element method. Adv Mech Eng 9(5):1687814017703899
7. Vanhollebeke F, Peeters J, Vandepitte D, Desmet W (2015) Using transmission path analysis to assess the influence of bearings on structural vibrations of a wind turbine gearbox. Wind Energy 18(5):797–810
8. Liu L, Liang X, Zuo MJ (2016) Vibration signal modeling of a planetary gear set with transmission path effect analysis. Measurement 85:20–31
9. McFadden PD, Smith JD (1986) Effect of transmission path on measured gear vibration. J Vib Acoust Stress Reliab Des 108(3):377–378
10. Jardine AK, Lin D, Banjevic D (2006) A review on machinery diagnostics and prognostics implementing condition-based maintenance. Mech Syst Signal Process 20(7):1483–1510
11. Borghesani P, Pennacchi P, Randall RB, Ricci R (2012) Order tracking for discrete-random separation in variable speed conditions. Mech Syst Signal Process 30:1–22
12. Stander CJ, Heyns PS (2006) Transmission path phase compensation for gear monitoring under fluctuating load conditions. Mech Syst Signal Process 20(7):1511–1522
13. Feng Z, Zuo MJ (2012) Vibration signal models for fault diagnosis of planetary gearboxes. J Sound Vib 331(22):4919–4939
14. Ning S, Han Z, Wang Z, Wu X (2016) A novel fault diagnosis approach of gearbox using an embedded sensor fixed gear body. J Vibroeng 18(7)
15. Smith W, Deshpande L, Randall R, Li H (2013) Gear diagnostics in a planetary gearbox: a study using internal and external vibration signals. Int J Cond Monit 3(2):36–41
16. De Smidt MR (2008) Internal vibration monitoring of a planetary gearbox. Doc. dissertation, University of Pretoria

17. Pattabiraman TR, Srinivasan K, Malarmohan K (2015) Assessment of sideband energy ratio technique in detection of wind turbine gear defects. Case Stud Mech Syst Signal Process 2:1–11
18. Sharma V, Parey A (2016) Gear crack detection using modified TSA and proposed fault indicators for fluctuating speed conditions. Measurement 90:560–575

# Review on Emerging Trends and Future Perspectives of Green Roof Buildings


**Swarn Veer Singh Jaral and Manpreet Singh**

## 1 Introduction

Green rooftops are typically intended to build the vital nature of their homes, even though there are different favorable circumstances moreover. It is sometimes called green roofs, live roofs, or roof gardens, which are simply planted roofs in the last level. It is a layered structure composed of a waterproofing substrate, a growing medium, and a plant layer itself. Green rooftops likewise incorporate a layer of root boundary, a drainage sheet, and where the environment demands, a water system framework. Initially, green roofs present certain problems concerning their structures, such as water lodging, water infiltration within the building, etc. Such drawbacks of green roofs demonstrate the attention of several researchers on finding new layers in green roofs and modifying current layers with different materials used for them. This paper explores the development of green roofs with the latest developments in science on its additional layers and different materials used. Past and current work on green roof construction suggests that it is divided into many layers, such as concrete base, waterproofing sheet, ICB, filter, drainage, substrate, vegetation, which is shown in a schematic representation in Fig. 1.

## 2 Concrete Slab

A solid section is an average auxiliary component of current structures, comprising of a smooth and level surface built of poured concrete. Energy conservation has become a prime concern for the design of modern structures, and the proliferation

S. V. S. Jaral · M. Singh (✉)
School of Mechanical Engineering, Lovely Professional University, Phagwara 144411, India
e-mail: manpreet.20360@lpu.co.in



K. Jha et al. (eds.), *Recent Advances in Sustainable Technologies*,
Lecture Notes in Mechanical Engineering,
https://doi.org/10.1007/978-981-16-0976-3_16

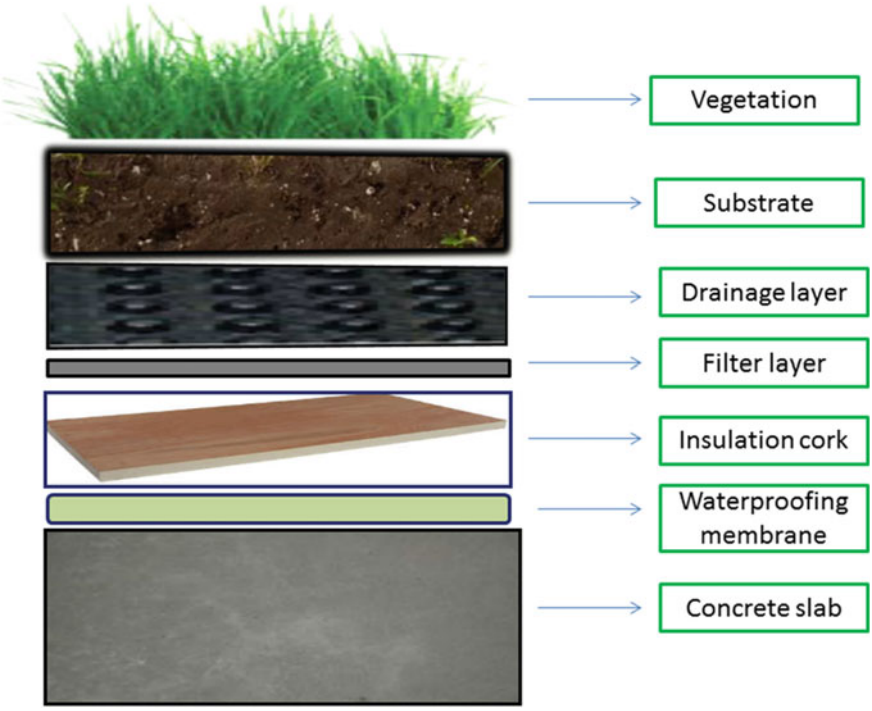


**Fig. 1** Schematic representation of different layers in green roofs

of concrete slabs calls for close analysis of the thermal properties to reduce carbon loss. Concrete has identical thermal properties of masonry goods since it has a fairly small thermal mass and is a strong conductor of heat. Without insulation, directly ground-mounted concrete slabs may induce a large amount of extraneous energy transmitted through conduction, resulting in either heat loss or excessive heat. For modern building, concrete slabs are typically poured over a sheet of insulation, such as expanded polystyrene and the slab can contain underfloor heat tubing. Green roofing starts with a concrete slab which is typically around 12–16 cm thick [1]. While more research is needed to improve the insulation by determining the appropriate thickness of the concrete slab.

## 3 Waterproofing Sheet

Waterproofing is a vital aspect of structural security and is essential to the efficient design of green roofs. This could be a layer or covering of bitumen, asphalt on a building, or another sort of liquid waterproofing. Such waterproofing solutions may be added to concrete decks or the screeds of sand/cement. A green roof can be

constructed with any kind of waterproofing device, but single-ply membranes have become very common in recent years and are listed for their cost-effectiveness and usability of nearly all green roofing companies. As such the waterproofing coating is generally believed to be a membrane [2]. It was also suggested that membrane cover that is resistant to root penetration should be used for waterproofing membranes and vary from 10 cm or more [3]. Several researchers have struggled with the treatment of flat roofs with flexible sheets for waterproofing layer (SBS bitumen, PVC-P layer) and concentrated on membrane defects and water tightness and concluded that avoidance of potential defects is most effective [4]. The raised surface temperature of the waterproofing layer encourages certain analysts to handle the topic of the surface temperature of level rooftops, where the waterproofing layer is utilized as an elastic waterproofing film of delicate PVC and spotlights on the shading impact of the plasticized PVC film on the surface temperature and characterizes a definitive surface temperature of the polymeric PVC layers in shading reliance on test estimations [5]. Table 1 beneath addresses a portion of the rising waterproofing medicines.

## 4 Insulation board membrane

Several scientists implement a current layer and use it as water draining and storage sheet, and it has been discovered that this additional layer has higher insulation efficiency, while the introduction of layers has contributed to increased thermal insulation. The utilization of more fruitful and greener improvement materials is a procedure that is being looked for after to make more sufficient essentialness powerful structures. A few scientists explore the warm action, water spillover, and plant improvement of two green rooftop frameworks. The standard strategy, containing polystyrene and polyethylene expelled, and the elective plug-based framework, seen that the all-encompassing stopper covering showed a more articulated temperature stretch and more productive treatment of precipitation measures under dry conditions. Likewise, it is also found that the development and well-being of plug-based green rooftop plants were equivalent to that of the reference strategy, proposing the solid proficiency of the stopper gadget [15]. A few scientists have set up a green material gadget that substitutes customary waste and water stockpiling polyethylene films with protection plug sheets (ICBs), and it has additionally been seen that both the layers (cork and substrate) lost aspect of protection capacity during the hot structure, yet it was re-established to the ICB layer inside a couple of hours [16]. ICB samples with various thicknesses and densities were also studied and found that lower density ICB is more effective in the system [17]. As this new layer is being added, so many of the research initiatives need to find new products from natural resources that are eco-friendly, cost-effective, and more popular in their mode of operation. Whereas some scientists have also uncovered various content, although others have proposed new uses of materials utilizing a green roof sheet seen in a tabular type in Table 2.

**Table 1** Water proofing medicines

| Type | Description | Advantage | Disadvantage | References |
|---|---|---|---|---|
| Fluid-applied elastomeric | Consists of polyurethane elastomers of high-solid material | Superb elastomeric materials, to cross holes or cracks smoothly | Not acceptable on wet or untreated surfaces, dangerous chemical contaminants | [6] |
| Polyurethane liquid membrane waterproofing | Consists of two constituents: foundation and reactor. Polyol serves as the basis, while isocyanide is a part of the reactor | Optimum elasticity, good tolerance to UV radiation | Temperature effect on the rate of polymerization by adding the substance to the surface | [7] |
| Bituminous coating waterproofing method | Method of coating is used according to the degree of formulation and polymerization | No solvent flames, water-based coatings do not harm bitumen, non-toxic | Washed away if the rain comes on a newly painted water-based coating | [8] |
| Coal-tar built-up membrane (ASTM D 450, Type II, ASTM D 450, Type I) | Consist of alternating carbon tar layers and plywood reinforcement layers | Excellent bonding of coal-tar tapes and pipe surfaces with enhanced electrical insulating properties, easy to adhere, avoid humidity | Higher cost | [9] |
| Hot-fluid-applied polymer-modified asphalt membrane | Made of treated asphalt, plastic rubbers, and extensions | No seams | Reflective splitting, shortage of blinking tools | [10] |
| Polymer-modified bitumen sheet membrane | Composed of polymer-modified asphalt and one or more layers of strengthening material | Less versatile | Site prone configuration, limited sheet size results in a wide range of seams | [11] |
| Butyl rubber membrane | Consist of sheets of strengthened butyl rubber manufactured by the factory | High porosity against organic solvents and reactive chemicals, chemically extremely stable | The low permeability of water vapor | [12] |
| Ethylene propylene diene monomer (EPDM) membrane | Designed to waterproof exposed and unexposed applications | Likely to be rated as root resistant, UV sensitive and weather tolerant for long life | Condensation of moisture can soften the glue | [13] |

(continued)

**Table 1** (continued)

| Type | Description | Advantage | Disadvantage | References |
|---|---|---|---|---|
| Polyvinyl chloride (PVC) membranes | The preferred material for roofing systems and ventures involving complicated curvatures of the roof | PVC membranes are likely to be marked as root resistant | Moisture condensation can soften the glue, raising the risk of wind uplifting | [14] |

**Table 2** Materials used for green roof sheets

| Material used | Examination | Finding | References |
|---|---|---|---|
| Polystyrene, polyethylene, and an elective stopper-based framework | Warm conduct, water seepage, and vegetation development | Indicating a more articulated temperature deferral and plant development and well-being in the green plug rooftop | [15] |
| Insulation cork board (ICB) | Drainage determination of ICB of different thickness and densities | Lower thickness ICB has been utilized as a waste layer, and the framework has outflanked | [16–19] |
| | Characterize ICB that swaps the polyethylene membranes | ICB and substrates lose part of their protection limit when the framework is wet, even though it has been completely re-established inside a couple of hours in the ICB layer | |
| | Examines mechanical performance medium density cork board | Suitable for uncoated external insurance of improvement façades and rooftops, as it has well-automated implementation without compromising its hygrothermal direct | |
| Aerogel-enhanced HGB, aerogel-enhanced blanket | Thermal performance of aerogel-enhanced HGB | The higher the aerogel content, the lower the density, and thermal conductivity of an HGB enhanced with aerogel | [20–22] |
| | Thermal performance of aerogel-enhanced blanket | Effective thermal conductivity of aerogel covers considering various materials for fastening them | |

(continued)

**Table 2** (continued)

| Material used | Examination | Finding | References |
|---|---|---|---|
| Rice husk and expanded cork by-products | Energy consumption | Building arrangements dependent on these composite materials can be utilized in structures, in this manner assisting with diminishing vitality utilization during the administration life of the structures | |
| Ceramic board (seashell and fly ash, rice husk ash, rice husk and Portland cement) | Attainability of utilizing shell and fly debris | All the properties of CB and the squanders got from feasible CB can be utilized for the inner warm protection coating of the structure | [23] |
| Wood fiber (melamine-urea-formaldehyde (MUF), phenol-formaldehyde (PF), emulsifiable 4,4′ methylene diisocyanate (eMDI), and latex resins, lime) | Thermal insulation of wood fiber | Using wood fiber as a vacuum insulation panel core material has broad application prospects | [24] |
| | Physical and heat insulation properties, toxic chemical emissions, and combustion characteristics | MUF adhesive is the best choice for wood-fiber insulation boards | [25] |
| | Hygrothermal behaviors | Higher insulation performance and higher water vapor resistance factor | [26] |
| Flax and agglomerated cork | Thermal behavior | Lower thermal conductivity | [27] |
| Novel sawdust biomass | Insulation | New biomass-based protection material with great physical execution can help moderate vitality, cleaner creation, and practical turn of events | [28] |

(continued)

**Table 2** (continued)

| Material used | Examination | Finding | References |
|---|---|---|---|
| Mussel shells | Feasibility, thermal, and acoustic characteristics | Suitable for using it as building insulation material | [29] |
| | Cement-coating mortars in which conventional aggregates are partially replaced by mold shell aggregates | Mussel shell achievability in concrete coatings at an ideal replacement pace of 25% of the regular total | [30] |
| Natural fibers (fibers cork, jute, kapok, pineapple leaves, tea leaves, coconut husk, etc.) | Natural composite fiber panels for buildings' thermal insulation | Filaments, for example, plug, jute, pineapple leaves, tea leaves, and coconut husk are the most productive natural materials and are appropriate for warm protection | [31] |
| | Thermo-hygrometric behavior | Coconut fiber insulations are equally comparable to natural and synthetic materials | [32] |
| Beet pulp and potato starch | Portrayal of an imaginative 100% plant-based green composite | Genuine effect on hygrothermal and acoustic properties of the examined material because of porosity of both starch and moistness content | [33] |
| Agglomerated and expanded black | Desirable properties of two different cork materials | Black cork was characterized by superior thermal stability | [34] |
| Reused waste sheets | Warm, acoustic, hygrothermal, and ignitability properties | Fascinating warm and acoustic execution portrayed the cowhide cutting waste boards and affirmed the possible application in building protection | [35] |

(continued)

**Table 2** (continued)

| Material used | Examination | Finding | References |
|---|---|---|---|
| Silica aerogels | Thermal, hydric, mechanical, acoustic, and fire | Fulfill the requirements of insulation | [36] |
| Giant reed and cork residues | Building elements | Innovative uses of wastes | [37] |
| Bamboo particleboards | Thermal performance | Significant hygrothermal properties | [38] |

## 5 Filter Layer

The channel layer's key activity is to perceive the advancement establishment of leakage sheet and consequently prevent little components like vegetation trash, soil fines from coming to and impeding the waste sheet underneath. For basic use, geotextile materials are typically found in green rooftops [39, 40]. The channel materials should have a solid elasticity to withstand the above burden. Likewise, tight pores are required to permit sensible water penetrability, the standard way while hindering the progression of medium soil particles into the channel layer. The channel material likewise fills in as a root-boundary layer for plants with low and little roots. It was likewise proposed in the writing that non-woven polymer-based texture [41] and non-woven geotextile channel texture [42] adequately treated dampness and isolated substrate layers, which added to the foundation of local herbaceous plants and expended roughly 1.5 L of water per square meter, individually.

## 6 Drainage Layer

The seepage layer is basic for the manageability of each green rooftop. Because of the way that most green rooftop layer needs circulated air through and non-water-logged soil for a profitable turn of events, the seepage layer assists with eliminating abundance soil water to safeguard high-impact substrate consistency. Seepage covering likewise secures the permeable surface and upgrades the warming properties of the green rooftop [39]. In present day times, two primary sorts of seepage layers are utilized in green rooftops: straightforward waste boards: produced using high-quality materials like polyethylene with water-holding compartments which require overabundance water release. Grain removal items: These include some WHCs just as wide pore spaces for putting away the soil and models include lightweight extended mud totals (LECAs), extended shale, broken stones, unpleasant rock, and stone chips. The decision of a reasonable waste layer relies vigorously upon the cost, development necessities, plant shape, and size of the green rooftop. In examining, granular things follow the necessities for private ventures, for example, high rises. It may be seen as the most popular drainage process, but it might be appropriate to lift the soil layer above the liquid surface in certain cases. Many researchers utilize different materials for making drainage layer such as 5–15 mm clay pebbles [43], rubber crumbs [44], Nophadrain 5 [42], BioRemeGree drainage cell [45] and concluded that these materials have significant water-holding capacity of 4.3 L/$m^2$. The greatest drawback with granular materials, however, is that they must be applied to level rooftops or to profoundly turned surfaces. Seepage frameworks are best worked for huge scope establishments and are reasonable for the level and respectably slanted surfaces. Cost and last removal are the main drawbacks of the seepage modules; in any case, their speedy establishment and the chance of opening parts during the redesign of rooftops favor them in present day green rooftops.

## 7 Substrate Layer

The soil explicitly affects the development of plants and the efficiency of green roofs. The selection of an appropriate substratum is also vital to the sustainability of any green roof. Huge numbers of the upsides of green rooftops are legitimately identified with the development foundation property, including water quality upgrade, top stream disposal, warm preferences, and sound protection. Aside from this, extreme conditions exist in rooftop settings, allowing soil to have certain special properties. It is, therefore, not realistic to assume that one substance contains all the characteristics appropriate to shape a green roof substrate. It is common practice to mix multiple components at defined ratios of different characteristics to form a medium of growth. Various materials are included in the substrate and are well discussed in the literature, such as 3 to 10% of the peat content [46]. It has also been suggested that there is a substantial difference between the media and natural soils, depending on composition, degree of compaction, and the internal moisture content [47]. A few analysts measure the capacity of reused and locally available materials such as broken concrete, squashed stones, urban waste fertilizer, etc., and pumice, perlite, sheep excrement as green rooftop substrates, and it was seen that the effectiveness of substrate blends made out of black-top, broken stones, volcanic pillar, balanced with sawdust, and compost was acceptable in specific circumstances, which could be utilized as a green rooftop substrate [48]. Although some suggest that interactions between plant and pollinator on green roofs are modulated by substrate height, substrate depth, and plant population [49]. It is also found that vegetation cover and the depth of the substrate affect the reduction of runoff, and in case of saturation, there is an excess runoff generation mechanism [50]. It has been additionally discovered that conceivable utilization of recovered items (modern green rooftop seepage sheet, bamboo stems and roots, and polyethylene terephthalate (PET) bottle tops and bottoms) as an alternate resource for urban soil and irrigation systems and the value of understanding the initial soil and drainage layer utilizing reclaimed materials for the creation of renewable, and low-cost green roofs was presented [51]. While working on the substrate layer, it was suggested that phosphates have been selected as a water quality measure based on their possible detrimental effects on water quality in urban rainwater collections, and it is believed that polypropylene mats and aggregates establish specific conditions for leachate production, both in terms of volume and chemistry [52]. Limit assimilation might be a useful resource for the development medium to improve the nature of the overflow. It is recommended that the growth medium be prepared using locally available materials while reading the literature and that native plants be screened for eventual green roof success. The commonly used substrates (organic, inorganic, and commercial) are shown in tabular form in Table 3.

**Table 3** Various substrate materials used for green roof

| Substrate | Composition | Observation | References |
|---|---|---|---|
| Organic | Perlite, vermiculite, coco-peat, mulch | Low-mass thickness, high ability to hold water, air filled porosity and pressure driven conductivity and greatest plant uphold | [47, 53–56] |
| Inorganic | Crushed bricks and tiles | Improved physical properties for development and endurance of the plants, water maintenance, and establishment of green rooftop | [55, 57] |
| Commercial substrate | Zinco Sedum, DAKU | sustainable plant growth, runoff quality | [44, 58] |

## 8 Vegetation

The uppermost sheet, which brings energy to the green roof network, is vegetation. The effectiveness of every green roof relies on how good the plants are. Plants boost the efficiency of runoff [47], air purify [58, 59], and thermal performance [60]. It ought to be recalled that green rooftops are not a decent natural surroundings for plant development [61, 62]. Water is likewise a limiting component in housetop conditions, and its quality varies altogether during precipitation occasions. Contemplating the serious atmosphere on the housetops, the attractive plant attributes for wide green rooftops are as per the following, the ability to endure dry season conditions flourish under decreased supplement loads, solid soil quality, less successive water system, little and medium roots phytoremediation. While it is trying to recognize a plant, animal category with every single alluring component, significant advancement has been made in the location of suitable green rooftop plants. Vegetation goes under delicious kinds, some of which are the most seriously considered taxa on green rooftops [63]. Distinctive delicious assortments are there; however, sedum plants are more normal and tough for broad rooftops all over the globe [62] as a result of their ability to stifle happening and store overabundance water [64] to withstand dry situations. A few analyses have exhibited the capacity of the sedum variety to withstand an extended period without water [60]. Many experts have suggested different plant varieties with various characteristics when working on the selection of plants as a vegetative layer such as sedum spp. (strong photosynthetic metabolism and stayed active even after 4 months without water and 7 cm of substratum depth was sufficient for greater growth and absolute coverage) [65, 66], *Sedum rubrotinctum* (existed without water for two years) [67]. It is also beneficial to use natural plants for green roofs [68, 69]. It is described that local plants may also be used as vegetative layer like rose moss succulent plants [47] as ideal green roof vegetation for tropical wet and dry climates with related characteristics to sedum, *Aptenia cordifoliaas* [70] as dry productive and absorbs less water, grasses such as belongs from poaceae family

[71] performed successfully. A few analysts likewise call attention to that both the area and the developing medium profundity will influence the underlying populace of unmanaged green rooftops, however, with contrasting effects on network get together and propose the achievement of unmanaged empty rooftops as supplies of local and intrusive plant decent variety in urban regions [72]. It is consequently important that plant type choice for green rooftops be delivered in consistence with neighborhood climatic conditions and accessibility of supplements, just as the impact of the plant on the living spaces. It has been also found that the different types of plantations usage may help to improve the productivity of green roofs. It is advised that instead of using grass or sedum species as a plant foundation, there is also a chance of growing vegetables (underground or above ground), fruit, etc. More research is needed to know the different vegetation materials that show significant properties when being used in green roofs. Figure 2 includes the different plants that are used in vegetation layer.

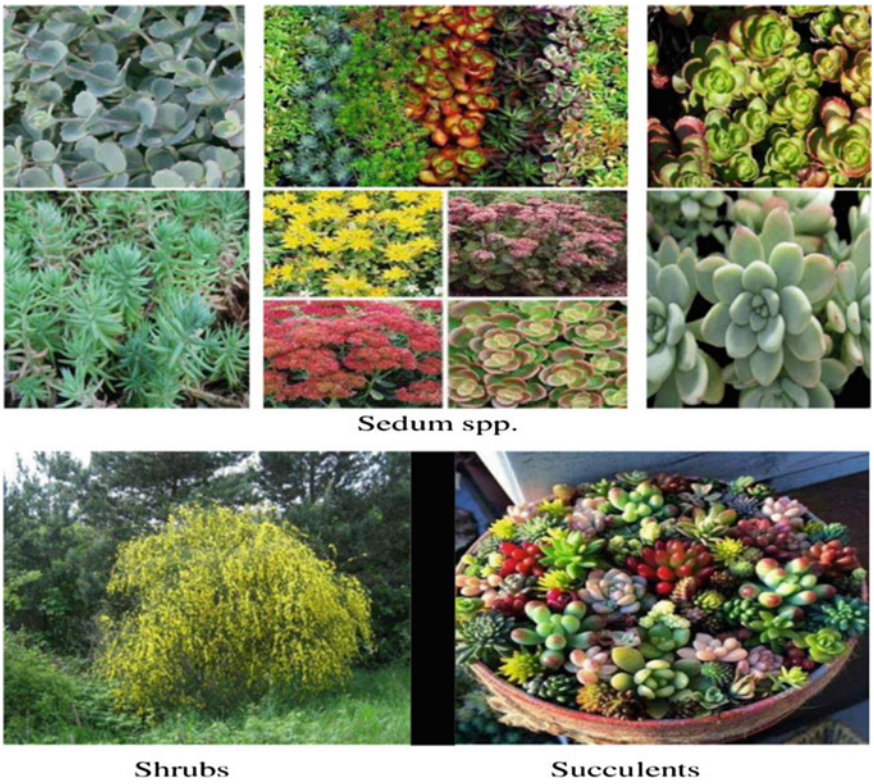


**Fig. 2** Plants use for green roofs

## 9 Conclusion

Green material has been proposed as a sheltered strategy to diminish the negative effects of urbanization. As an outcome, a few nations are giving chances to house proprietors to introduce green rooftops with appealing auxiliary expense. More cost-effective green material practices should be made for various advantages (natural, monetary, and so forth). In any case, more inside and out, reasonable logical work on every part of the green rooftop is required, and multidisciplinary study participation in illuminating the difficulties is inescapable. The essential target of this investigation was to portray the current work of materials utilized for the development of various layers, and there is a need later on to change the various layers with the investigation and modification of various materials for better warm protection, cost-adequacy, and so forth.

- In the insulation sheet, the material from the hilly areas can offer a good alternative to the oak tree.
- In the case of a runoff pad, a substance that is less susceptible to the environment should be used to minimize the leakage of harmful chemicals.
- A lot of study is needed to know the scope of growing vegetables, fruits in the vegetative layer.
- In the case of the substrate layer, further work is needed to know the actual depth and the materials used for better insulation.

## 10 Future Recommendations

Green roofs are a relatively recent and evolving field, as is obvious from the literature. Green rooftop research is required to keep on developing as a few researchers overall comprehend the favorable circumstances and results of green material. More expenditure in research on various layers and their structure is therefore needed to analyze this technology. Shortly, we should foresee green roofs in any area of the country.

## References

1. Castleton HF, Stovin V, Beck SB, Davison JB (2010) Green roofs; building energy savings and the potential for retrofit. Energy Build 42(10):1582–1591
2. Wark CG, Wark WW (2003) Green roof specifications and standards. Constr Specif 56(8)
3. Hejl M, Mohapl M, Bříza L (2020) Modular green roofs and their usage in the world. Int J Eng Res Afr 47:103–108 (Trans Tech Publications Ltd.)
4. Sutliak S, Plachý J (2020) Diagnostics of flat roofs with flexible sheets for waterproofing. MS&E 728(1):012004
5. Plachý J, Vysoká J (2020) Surface temperature of flat roofs with waterproofing polymer membranes. MS&E 728(1):012006

6. Fogel J (1976) Cold-applied fluid elastomeric waterproofing membranes. In: Building Seals and Sealants. ASTM International
7. Pisello AL, Fortunati E, Fabiani C, Mattioli S, Dominici F, Torre L, Cabeza LF, Cotana F (2017) PCM for improving polyurethane-based cool roof membranes durability. Solar Energy Mater Solar Cells 160:34–42
8. Nehdi ML, Soliman AM (2013) Novel green roofing membrane system made with recycled leftover paint. Green Mater 1(4):231–241
9. Rossiter WJ, Mathey RG (1978) Elastomeric roofing: a survey, vol 13. Department of Commerce, National Bureau of Standards, National Engineering Laboratory, Center for Building Technology
10. Snodgrass EC, McIntyre L (2010) The green roof manual: a professional guide to design, installation, and maintenance. Timber Press
11. Jang DH, Kim HS, Choi SK (2011) Greenhouse test results for two years of sheet shaped root barrier materials apply to green roof system for sustainable building construction. J Korea Inst Build Constr 11(6):634–644
12. Ishimatsu K, Ito K (2013) Brown/biodiverse roofs: a conservation action for threatened brownfields to support urban biodiversity. Landsc Ecol Eng 9(2):299–304
13. Moustafa H, Lawandy SN, Rabee M, Zahran MA, Jasiunas L (2020) Effect of green modification of nanoclay on the adhesion behaviour of EPDM rubber to polyester fabric. Int J Adhes Adhes 102617
14. Yong M, Zhang Y, Sun S, Liu W (2019) Properties of polyvinyl chloride (PVC) ultrafiltration membrane improved by lignin: hydrophilicity and antifouling. J Membr Sci 575:50–59
15. Simoes N, Almeida R, Tadeu A, Brett M, Almeida J (2020) Comparison between cork-based and conventional green roof solutions. Build Environ 106812
16. Almeida R, Simoes N, Tadeu A, Palha P, Almeida J (2019) Thermal behaviour of a green roof containing insulation cork board. An experimental characterization using a bioclimatic chamber. Build Environ 160:106179
17. Tadeu A, Simoes N, Almeida R, Manuel C (2019) Drainage and water storage capacity of insulation cork board applied as a layer on green roofs. Constr Build Mater 209:52–65
18. Simoes N, Fino R, Tadeu A (2019) Uncoated medium density expanded cork boards for building façades and roofs: Mechanical, hygrothermal and durability characterization. Constr Build Mater 200:447–464
19. Fino R, Tadeu A, Simoes N (2018) Influence of a period of wet weather on the heat transfer across a wall covered with uncoated medium density expanded cork. Energy Build 165:118–131
20. Yang W, Liu J, Wang Y, Gao S (2020) Experimental study on the thermal conductivity of aerogel-enhanced insulating materials under various hygrothermal environments. Energy Build 206:109583
21. Berardi U, Ákos L (2019) Thermal bridges of metal fasteners for aerogel-enhanced blankets. Energy Build 185:307–315
22. Marques B, Tadeu A, António J, Almeida J, de Brito J (2020) Mechanical, thermal and acoustic behaviour of polymer-based composite materials produced with rice husk and expanded cork by-products. Constr Build Mater 239:117851
23. Hossain SKS, Roy PK (2019) Fabrication of sustainable ceramic board using solid-wastes for construction purpose. Constr Build Mater 222:26–40
24. Wang B, Li Z, Qi X, Chen N, Zeng Q, Dai D, Fan M, Rao J (2019) Thermal insulation properties of green vacuum insulation panel using wood fiber as core material. BioResources 14(2):3339–3351
25. Lee M, Lee S, Kang E, Son D (2019) Combustibility and characteristics of wood-fiber insulation boards prepared with four different adhesives. BioResources 14(3):6316–6330
26. Park JH, Kang Y, Lee J, Chang SJ, Wi S, Kim S (2019) Development of wood-lime boards as building materials improving thermal and moisture performance based on hygrothermal behavior evaluation. Constr Build Mater 204:576–585
27. Prabhakaran S, Krishnaraj V, Sharma S, Senthilkumar M, Jegathishkumar R, Zitoune R (2020) Experimental study on thermal and morphological analyses of green composite sandwich made of flax and agglomerated cork. J Therm Anal Calorim 139(5):3003–3012

28. Zou S, Li H, Wang S, Jiang R, Zou J, Zhang X, Zhang G (2020) Experimental research on an innovative sawdust biomass-based insulation material for buildings. J Clean Prod 121029
29. Carolina MG, Belen GF, Diego CL, Luis POJ (2020) Mussel shells: a canning industry by-product converted into a bio-based insulation material. J Clean Prod 122343
30. Garcia MC, Fonteboa GB, Lopez CD, Abella MF (2019) Design and properties of cement coating with mussel shell fine aggregate. Constr Build Mater 215:494–507
31. Denes TO, Gavrea DR, Tiuc AE, Istoan R (2019) Natural fibre composite panels for thermal insulation of buildings: a review. Sci Pap Ser-Manage Econ Eng Agric Rural Dev 19(4):71–78
32. Fabbri K, Tronchin L, Barbieri F, Merli F, Manfren M, La Gennusa M, Peri G, Cirrincione L, Panzera MF (2020) On the hygrothermal behavior of coconuts fiber insulators on green roofs. In: 2020 IEEE international conference on environment and electrical engineering and 2020 IEEE industrial and commercial power systems Europe (EEEIC/I&CPS Europe). IEEE, pp 1–6
33. Karaky H, Maalouf C, Bliard C, Moussa T, El Wakil N, Lachi M, Polidori G (2018) Hygrothermal and acoustical performance of starch-beet pulp composites for building thermal insulation. Materials 11(9):1622
34. Kaczynski P, Ptak M, Fernandes F, Chybowski L, Wilhelm J, Sousa R (2019) Development and testing of advanced cork composite sandwiches for energy-absorbing structures. Materials 12(5):697
35. Barbanera M, Belloni E, Buratti C, Calabro G, Marconi M, Merli F, Armentano I (2020) Recycled leather cutting waste-based boards: thermal, acoustic, hygrothermal and ignitability properties. J Mater Cycles Waste Manage 1–13
36. Ibrahim M, Nocentini K, Stipetic M, Dantz S, Caiazzo FG, Sayegh H, Bianco L (2019) Multi-field and multi-scale characterization of novel super insulating panels/systems based on silica aerogels: thermal, hydric, mechanical, acoustic, and fire performance. Build Environ 151:30–42
37. Barreca F, Gabarron AM, Yepes JAF, Pérez JJP (2019) Innovative use of giant reed and cork residues for panels of buildings in Mediterranean area. Resour Conserv Recycl 140:259–266
38. Nguyen DM, Grillet AC, Bui QB, Diep TMH, Woloszyn M (2018) Building bio-insulation materials based on bamboo powder and bio-binders. Constr Build Mater 186:686–698
39. Townshend D (2007) Study on green roof application in Hong Kong. Final Report, pp 42–53
40. Vijayaraghavan K, Raja FD (2015) Pilot-scale evaluation of green roofs with Sargassum biomass as to improve runoff quality. Ecol Eng 75:70–78
41. Licht J, Lundholm J (2006) Native coastal plants for northeastern extensive and semi-intensive green roof trays: substrates, fabrics and plant selection. In: Paper presented at the fourth annual greening rooftops for sustainable communities conference
42. Wong GKL, Jim CY (2014) Quantitative hydrologic performance of extensive green roof under humid-tropical rainfall regime. Ecol Eng 70:366–378
43. Vijayaraghavan K, Joshi UM, Balasubramanian R (2012) A field study to evaluate runoff quality from green roofs. Water Res 46:1337–1345
44. Perez G, Coma J, Solé C, Castell A, Cabeza LF (2012) Green roofs as passive system for energy savings when using rubber crumbs as drainage layer. Energy Procedia 30:452–460
45. Vijayaraghavan K, Joshi UM (2014) Can green roof act as a sink for contaminants? A methodological study to evaluate runoff quality from green roofs. Environ Pollut 194:121–129
46. Emilsson T, Rolf K (2005) Comparison of establishment methods for extensive green roofs in southern Sweden. Urban For Urban Green 3:103–111
47. Bellazzi A, Barozzi B, Pollastro MC, Meroni I (2020) Thermal resistance of growing media for green roofs: to what extent does the absence of specific reference values potentially affect the global thermal resistance of the green roof? An experimental example. J Build Eng 28:101076
48. Eksi M, Sevgi O, Akburak S, Yurtseven H, Esin İ (2020) Assessment of recycled or locally available materials as green roof substrates. Ecol Eng 156:105966
49. Dusza Y, Kraepiel Y, Abbadie L, Barot S, Carmignac D, Dajoz I, Raynaud X (2020) Plant-pollinator interactions on green roofs are mediated by substrate characteristics and plant community composition. Acta Oecologica 105:103559

50. Soulis KX, Ntoulas N, Nektarios PA, Kargas G (2017) Runoff reduction from extensive green roofs having different substrate depth and plant cover. Ecol Eng 102:80–89
51. Nagase A (2020) Novel application and reused materials for extensive green roof substrates and drainage layers in Japan-Plant growth and moisture uptake implementation. Ecol Eng 153:105898
52. Baryła A, Karczmarczyk A, Brandyk A, Bus A (2018) The influence of a green roof drainage layer on retention capacity and leakage quality. Water Sci Technol 77(12):2886–2895
53. Vijayaraghavan K, Raja FD (2014) Design and development of green roof substrate to improve runoff water quality: Plant growth experiments and adsorption. Water Res 63:94–101
54. Kotsiris G, Nektarios PA, Ntoulas N, Kargas G (2013) An adaptive approach to intensive green roofs in the Mediterranean climatic region. Urban For Urban Green 12:380–392
55. Nagase A, Dunnett N (2011) The relationship between percentage of organic matter in substrate and plant growth in extensive green roofs. Landsc Urban Plan 103:230–236
56. Molineux CJ, Connop SP, Gange AC (2014) Manipulating soil microbial communities in extensive green roof substrates. Sci Total Environ 493:632–638
57. Ondoño S, Bastida F, Moreno JL (2014) Microbiological and biochemical properties of artificial substrates: a preliminary study of its application as technosols or as a basis in green roof systems. Ecol Eng 70:189–199
58. Speak AF, Rothwell JJ, Lindley SJ, Smith CL (2012) Urban particulate pollution reduction by four species of green roof vegetation in a UK city. Atm Environ 61:283–293
59. Dvorak B, Volder A (2010) Green roof vegetation for North American ecoregions: a literature review. Landsc Urban Plan 96:197–213
60. Cook-Patton SC, Bauerle TL (2012) Potential benefits of plant diversity on vegetated roofs: a literature review. J Environ Manag 106:85–92
61. Rowe DB (2011) Green roofs as a means of pollution abatement. Environ Pollut 159:2100–2110
62. Farrell C, Mitchell RE, Szota C, Rayner JP, Williams NSG (2012) Green roofs for hot and dry climates: interacting effects of plant water use, succulence and substrate. Ecol Eng 49:270–276
63. Gabrych M, Kotze DJ, Lehvävirta S (2016) Substrate depth and roof age strongly affect plant abundances on sedum-moss and meadow green roofs in Helsinki, Finland. Ecol Eng 86:95–104
64. Rowe DB, Getter KL, Durhman AK (2012) Effect of green roof media depth on Crassulacean plant succession over seven years. Landsc Urban Plan 104:310–319
65. Durhman AK, Rowe DB, Rugh CL (2006) Effect of watering regimen on chlorophyll fluorescence and growth of selected green roof plant taxa. Hort Sci 41:1623–1628
66. Getter KL, Rowe DB (2008) Media depth influences Sedum green roof establishment. Urban Ecosyst 11:361–372
67. Terri J, Turner M, Gurevitch J (1986) The response of leaf water potential and crassulacean acid metabolism to prolonged drought in *Sedum rubrotinctum*. Plant Physiol 81:678–680
68. Nagase A, Dunnett N (2010) Drought tolerance in different vegetation types for extensive green roofs: effects of watering and diversity. Landsc Urban Plan 97:318–327
69. Schweitzer O, Erell E (2014) Evaluation of the energy performance and irrigation requirements of extensive green roofs in a water-scarce Mediterranean climate. Energy Build 68:25–32
70. Nektarios PA, Amountzias I, Kokkinou I, Ntoulas N (2011) Green roof substrate type and depth affect the growth of the native species *Dianthus fruticosus* under reduced irrigation regimens. Hort Sci 46:1208–1216
71. Yang J, Yu Q, Gong P (2008) Quantifying air pollution removal by green roofs in Chicago. Atm Environ 42:7266–7273
72. Aloisio JM, Palmer M, Tuininga AR, Lewis JD (2020) Introduced and native plant species composition of vacant unmanaged green roofs in New York City. Urban Ecosyst

# PCCI Combustion for Better Emissions in Diesel Engines


**Getachew Alemayehu, Deresse Firew, Ramesh Babu Nallamothu, and Sung Kyu Kang**

## 1 Introduction

Considering its most efficiency of diesel engine, investigations were done to minimize its emission by applying different practical strategies of low-temperature combustion: HCCI, PCCI, PCI and RCCI. LTC purpose in decreasing $NO_x$ and PM simultaneously in diesel engines; even in avoiding the need of exhaust after-treatment technologies, were confirmed by different researchers but the challenge of hydrocarbon and carbon mono-oxide increments is still an unsolved problem. PCCI under LTC modes of combustion strategy indicated promising outputs in lowering oxides of nitrogen in conventional and biodiesel fuels. The potential of PCCI compared to the conventional diesel combustion in reducing $NO_X$ and smoke simultaneously at partial load conditions including the possibility of reducing emissions in CI engines was investigated [1].

In PCCI diesel engines, the strategy of advanced injection to get sufficient time for mixture formation before combustion was discussed the resulting reduction of smoke and $NO_x$ with increased HC and CO emissions [2]. The maximum lower start of injection that could make PCCI combustion operational irrespective of the degree of exhaust gas recirculation, and the reductions in $NO_x$ and Soot concerning a significant increase in HC and CO were studied on conventional CI engine [3]. Studies indicated that proper matching in time of injection with the fuel type in LTC strategies including PCCI which are emerging ideas of modern combustion science

G. Alemayehu · D. Firew · R. B. Nallamothu (✉)
Mechanical Systems and Vehicle Engineering Department, SoMCME, Adama Science and Technology University, Adama, Ethiopia
e-mail: ramesh.babu@astu.edu.et

S. K. Kang
Mechanical Engineering Department, Jimma University, Jimma, Ethiopia



K. Jha et al. (eds.), *Recent Advances in Sustainable Technologies*,
Lecture Notes in Mechanical Engineering,
https://doi.org/10.1007/978-981-16-0976-3_17

could lower HC and CO. PCCI operation utilizes the injection of fuel on ports or through DI of fuel early or lately [4].

Results from using EGR on PCCI operation indicated that the more the degree of EGR the greater the indicated mean effective pressure, and due to dilution and thermal effects of EGR, $NO_x$ were decreased [5]. Further efforts of investigation in making the best emission and performance results of LTC strategies will make it to be the most appropriate and near-future environmental friendly technology of combustion including adopting different fuels in PCCI combustion.

## 2 PCCI for Diesel Engines

More CO and HC were resulted from poor combustion phasing because of the decreased temperature inside the combustion chamber. This result forced investigators in working on different LTC technique that they name it as PCCI operation, i.e., the improvement of homogeneous charge compression ignition (HCCI) combustion concept concerning combustion stability. Considering better control over the combustion events researchers discussed that PCCI mode of operation shows improved combustion than HCCI resulting in enhanced engine performance, lower $NO_x$, PM and significant CO and HC cuts [6].

Toyota Central Research had developed engine in PCCI with higher efficiency together with lower $NO_x$ emissions from combustion of premixed lean mixture [7]. Various experimental investigations on PCCI combustion of diesel engines in low-load ranges were carried out since PCCI operation at high load leads to knocking, and from the results, the possibilities of reductions of soot and $NO_x$ emissions at the same time were confirmed. Experimental investigations and comparisons were carried out among the PCCI combustion and the conventional diesel in controlling emissions [8].

The study mentioned that the greater charge of the premix fraction and the decreased temperature of the PCCI operation were important features for the results in comparison to the diesel mode [8]. Results in Fig. 1a shows PM in RCCI dual fuel and shows 40% reduction compared with the conventional diesel combustion; however, relating with the PCCI diesel, it is two times greater. Other experiments were carried out using n-pentanol diesel 60% by volume with isobutanol diesel mixtures to promote partly premixed LTC in less level of EGR and tuned time of injection on diesel engine with direct injection type targeting minimizing oxides of nitrogen and particle matter simultaneously [10]. Low-compression ratio technique was applied for PCCI advanced combustion system on diesel engines, and the results showed the possibility of reducing oxides of nitrogen by 15%. 3% reduction in consumption of fuel also attained [11].

The possibility of reducing oxides of nitrogen and soot through keeping greater efficiency of thermal conditions during partial load settings by applying the PCCI combustion technique needs solving various challenges related to emission and efficiency of combustion. EGR was found important in PCCI to increase load range

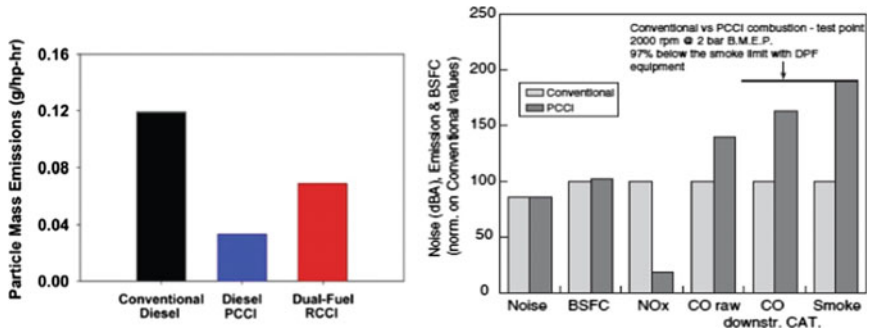


(a) (b)

**Fig. 1** **a** PM percentage in PCCI, CDC and RCCI, **b** Conventional and PCCI mode assessment concerning emission and performance of the engine for the indicated speed and brake mean effective pressure [8, 9]

and reduce oxides of nitrogen. The study also indicated that using high EGR during lower load of the engine resulted in a simultaneous decrease in oxides of nitrogen, unburned hydrocarbon, carbon mono-oxide and soot. Extending the load of an engine could be achieved by increasing $P_b$ using multi-pulse injection through the opportunity of enhanced fuel molecule collisions with oxygen resulting advancement of ignition timing. In minimizing engine emissions, prominent engine parameters in LTC through multiple injection approach were identified [12, 13].

Most commonly in the LTC operations, fuel is injected possibly through ports or else injecting early in the combustion chamber which promotes mixing for both combustion modes.

The study Fig. 2a showed temperature ranges in which $NO_x$ is formed which is at temperatures higher than 2000 K. Also by decreasing cylinder temperature and minimizing fuel-rich local zones, it indicated the possibility of eliminating emissions of soot and $NO_x$. From the $\varphi$-T map, researchers explained the temperature range in which there is combustion under low-temperature conditions being under the

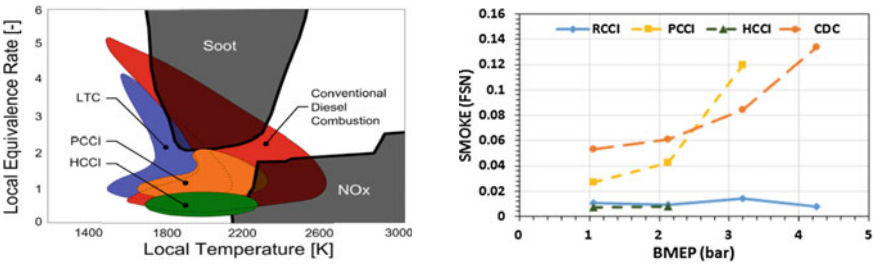


(a) (b)

**Fig. 2** **a** Areas of diesel conventional ignition and low-temperature combustion, **b** smoke emissions in conventional and LTC modes [14, 15]

temperature ranges for the development of oxides of nitrogen and at $\varphi$ values less than diesel soot formation zone. The two distinct zones for soot and $NO_x$ emissions formation were clearly shown in the plot [14].

These LTC strategies of reducing $NO_x$ and soot emissions in parallel are an advanced combustion concept lowers the high temperature leading to $NO_x$ formation zone together with minimizing excess fuel in the mix leading to the formation of soot. Researchers implemented several techniques to avoid fuel-rich pockets inside the cylinder by forming a premixed mixture through port fuel injections, various direct injection approaches, the pressure of injection, premixed ratio, time of injection and spray angle. Figure 2b shows conventional and LTC conditions with their smoke emissions at varying loads [15].

Though challenges of high HC and CO emissions were faced, the combustion concept of PCCI in achieving low emissions at part load operations was effectively applied with minor engine modifications on conventional direct injection engines. Studies showed PCCI operations are accompanied with more hydrocarbon and carbon monoxide than conventional diesel operations for several factors. Attachment of the fuel spray and charge with wall were considered among the factors. Minimizing production of NOx with 13% during PCCI operation applying EGR of 30% resulted in comparison with the conventional diesel operation. Delaying also controlling the combustion applying EGR were made a possible and more increment of EGR rate caused combustion instability and greater carbon monoxide and hydrocarbon outputs. By changing engines into the operating condition of PCCI results indicated a decrease in smoke and NOx productions in comparison to the usual diesel combustion for certain load range operations [16].

PCCI direct injection mode of combustion is also a technique in which both port injection and direct injection are used in supplying the fuel into the combustion chamber. This technique helps to work on fuels in dual mode and showed better combustion features and ranges of operations. Studies indicated the possibility of 28% reduction in oxides of nitrogen by using PCCI-DI technique. Studies indicated also that it helps in increasing the operation load and speed ranges. PCCI-DI combustion also lowers carbon dioxide productions but carbon monoxide and hydrocarbon productions increased [17].

Experiments were conducted on this mode of operation by modifying time of injection, level of EGR, and pressure of the injection. Duration of combustion and PM Metalit after-treatment devices were also applied [18].

As shown in Fig. 3, emission analysis using the mode-13 ESC cycle of test engine taken as a reference applying direct injection operation, and combination of PCCI-DI technique was conducted. Results indicated the possibility of reduction of oxides of nitrogen and soot by 33%, 19%, 36% and 90 [18].

The combustion, emission and performance features of an engine in PCCI-direct injection combustion operation by premixing gasohol 90% and ethanol 10% accompanied by direct injecting the diesel were experimentally studied. The study found a greater delay of the ignition together with less duration of combustion and also a higher heat release rate in comparison to diesel. More UHC and CO productions obtained during medium and part load conditions but reduced slowly to a diesel

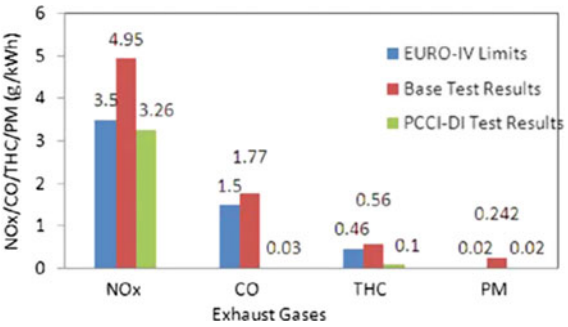


**Fig. 3** Evaluation of emissions in conventional DI operation and combination of PCCI-DI conventional operation [18]

condition during full loads. Premixing ethanol and gasohol by 20% and from this 70% and 67% reduction of smoke are obtained compared to directly injected diesel fuel. This investigation which used a premixed gasohol and ethanol fuel has also resulted in a decrease in $NO_x$ emission to 30% and 24% [19].

## 3 Injection Timing in PCCI Combustion

Introduction of air-fuel premixing through advanced injection resulting retarded fuel pulse injection was obtained in PCCI approach which enables controlling of the start of ignition. Literatures explained that injecting the fuel in advance helps in stratifying the fuel in the combustion chamber combining in the air that HCCI like condition could be created near TDC position of the piston [20].

The performance, combustion and emission characteristics using biodiesel blends on diesel engine applying PCCI through varying injection timing were analysed by researchers. In reducing $NO_x$, combustion at low temperature appears a promising combustion concept and research works said that the concept holds true including biodiesel fuels although producing greater $NO_x$. To get better $NO_x$ emissions in biodiesel combustions studies mentioned that retarded SOI is better than advanced SOI. Since biodiesel is having a greater oxygen ratio. Greater cetane value makes it to withstand greater EGR. Starting injection lately results improved low-temperature combustion which reduces oxides of nitrogen [4].

The impacts of advanced ($25^0$bTDC chosen) and retarded injection timing ($21^0$bTDC chosen) were compared with the conventional injection timing (baseline diesel at $23^0$BTDC) under similar operating conditions. The experimental study indicated that CO emissions at full load for advanced (25 deg BTDC) injection timing were 25% less than the baseline diesel while UHC emissions were high during injecting the fuel lately comparing with the normal and advanced timings. For this advanced injection timing mentioned above, $NO_x$ emissions were 10% higher when compared with the standard injection timing, whereas $NO_x$ emission was found 10% lower than the normal time of injection at the late time of injection (21 deg before top dead centre). Also, the PCCI mode of operation through advanced injection

timing decreases the smoke and CO in an increment of UHC and $NO_x$ at fully or completely loaded conditions whereas retarded injection timing decreases the CO and $NO_x$ emissions with an increase in unburnt hydrocarbon and smoke emissions at fully or completely loaded conditions [9, 15, 21]. On the contrary, other findings also confirmed that excess values of the start of injection increase HC and CO emissions above acceptable ranges. So, proper and optimized combination of the combustion parameters in LTC engines working in PCCI mode can provide acceptable values of emissions and load ranges. Current and ongoing research efforts in making LTC technology efficient through biodiesel and other alternative fuels developed hope for further reduction investigation on HC and CO emissions. These tuning of fuel properties also helps to improve greater load ranges and hazardous exhaust gasses in PCCI operations.

Experimental exploration of combustion, performance and emission characteristics using different test fuels (20% biodiesel blended with mineral diesel (B20), (B40), and baseline mineral diesel were carried out on PCCI engine. Impacts of different fuel injection factors, particularly timings of 24°, 20°, 16° and 12° before top dead centre and fuel injection pressures; 1000, 700 and 400 bars were analysed. The following results were obtained from the analysis; during 1000 bar fuel injection pressure, HRR and $P_{max}$ showed the maximum. Due to extreme noise of the cylinder including the knock, the study did not recommend 1000 bar fuel injection pressure for the PCCI combustion. Also, the investigation indicated that the early time of injection indicated higher combustion of the premix, which resulted in shorter burning duration with the advanced phasing of combustion. The behaviour of the combustion among the three fuels used in the test indicated no significant differences. Minor higher $P_{max}$ was shown in B20 due to retarded SoC. The experimental investigation compared the three test fuels, and the results indicated that B20 was having the maximum heat release rate, $R_{max}$ result, and noise of the cylinder, B40 showed superior biodiesel having advanced combustion phasing. The other essential point of the investigation revealed was the less impact of fuel properties at higher FIPs. Less CO and HC resulted in B20 comparing among three test fuels; on the other hand, an opacity of smoke and $NO_x$ showed marginally greater in the mixtures of biodiesel. Besides, B40 and B20 showed greater PM amounts in comparison to the diesel; though at advanced SoMI, the difference decreased. The study found out the optimized FIP for PCCI combustion mode which is 700 bar FIP, and better combustion and emission characteristics were obtained from B20 even though the performance of PCCI operation using B20 resulted somewhat lower comparing with diesel [22–24].

## 4 Exhaust Gas Recirculation (EGR) in PCCI Combustion

Applying EGR in upper levels together with a good start of injections, help for the realization of LTC technologies and these keep soot and NOx low in-cylinder

combustions. Applying higher EGR makes the delay of ignition long. From investigations, it was mentioned how this will make the premix in good condition resulting in lower rich pockets following the LTC condition. This will enable the engine to simultaneously reduce $NO_x$ and soot level. EGR interrupts $O_2$ amount which enters the combustion chamber making the temperature of the flame locally to reduce, that contributes for the reduction of $NO_x$, and also studies showed that through the extension of the ignition delay, EGR would delay the start of combustion. Studies found out the application of the large amount of EGR up to 54% in a PCCI combustion retards the ignition timing by diluting the gas mixture. In alleviating the premature ignition challenge through increasing EGR rate, its impact and maximum possible limits on CO, and THC emissions should be identified [25–28].

Another study of PCCI combustion through the proper matching of high-EGR rate and advanced combustion was investigated. This finding showed that to allow engines to enter the PCCI combustion mode SOI should not be lower than 16°CA bTDC regardless of the EGR level. On the other hand, the study explained that significant increases in HC and CO have always resulted during the reductions of $NO_x$ and soot which is also accompanied by an undesirable increase of basic and CN. Besides, the investigation discovered the possibility of reducing simultaneously soot and $NO_x$ in 99% and 90% correspondingly [29–31].

High temperature formed in the combustion chamber leads $NO_x$ emission generation in the exhaust. Controlling this peak combustion temperature helps to reduce $NO_x$ and studies showed that exhaust gas recirculation (EGR) is one of the effective methods in overcoming this challenge by forming a lean air-fuel mixture. Investigations indicated that by recirculating exhaust gas into the combustion cylinder dilution can take place which decreases the $O_2$ concentration in the combustion cylinder. Based on temperature, EGR is classified into the followings: Hot EGR in which the exhaust gas is re-circulated without being cooled, EGR of full cooled type where the recirculating gas become cold before entering cylinder employing heat exchanger mostly cooled through water, and the other type is EGR of partially cooled type.

Various investigations indicated that in applying EGR, there is a trade-off between the increase in soot, CO and UHC and a reduction in $NO_x$. The finding showed more than 50% of EGR applications increased PM amount. Applying EGR at higher loads was found difficult since the weakening of diffusion type combustion which resulted in more PM and smoke. Whereas during light loads, UHC in EGR may combust again, making better BTE. Besides, EGR of the hot type may increase the temperature of the premix, which would affect the combustion and exhaust emissions [32, 33]. Most researchers recommend EGR rate, not more than 30%. Extra increase of EGR amount resulted in CO and HC to be higher and the stability of combustion suffers [34–36]. To make the engine to operate in PCCI condition needs proper start of injection. It is mentioned in one study that start of injection which is lower than 16° crank angle before top dead centre was not in a position to make the engine to start PCCI operation unless EGR is applied [37–39].

## 5 Port Fuel Injection in PCCI Combustion

Formations of premixed mixture outside the combustion chamber are required in PCCI combustion mode. Studies and literature indicated that certain amount of fuel needs to be sprayed inside the ports in forming the premix which will enter the cylinder, and the usual conventional direct injection will be used to supply the remaining fuel. These will improve the homogeneous property of the mixture inside the combustion cylinder. Experimental studies of PCCI combustion mode using two diesel fuel types in which one is heated and the other not heated were carried out on CI engine to investigate its impact on the performance and emissions. The study revealed the following conclusions: 3–4 bar increase of injection pressure improved the spray atomization at high temperatures of the diesel. Particularly at 80 °C, temperature of the fuel and 4 bar pressure of injection resulted in a spray approaching gasoline. 35% proportion of diesel port injection using a PCCI mode of combustion showed improved thermal efficiency at high loads. By making the fuel temperature high, which is of a diesel type sprayed in the inlet port indicated a significant reduction of carbon monoxide and hydrocarbon. However, diesel temperature rises from 40 to 60 °C increased $NO_x$ [40–42].

Port fuel injection using a mixture of n-butanol and biodiesel were tested on PCCI operation technique, and the study showed promising results to simultaneously lower soot and oxides of nitrogen during speeds of idle, and its trade-off was modified favourably. The study also pointed out that future research studies to focus on techniques of EGR in increasing LTC operation level in minimizing soot and $NO_x$ productions. Increased outputs of oxides of nitrogen and hydrocarbon are found in the study showing the negative side effects of PCCI operation using n-butanol as indicated in the analysis primarily for the reason of the premix burning stage of combustion which is not completed inside the cylinder implying increasing up to 20 times depending on the speed and load situations [43]. Studies using methane port injection supply engines using two fuels found the promising technique in minimizing UHC as well as $NO_x$. The technique of port fuel supply increases $NO_x$ but lower in HC amounts. Results from the study revealed that a reduction amount of 7.69% smoke and 13.33% hydrocarbon and also 31.81% carbon monoxide whereas 1.45% increment of $NO_X$ resulted [44–46].

## 6 Challenges of PCCI Combustion

Overcoming the traditional $NO_x$–soot trade-off and reduction of specific fuel consumption in conventional diesel combustion through diesel PCCI combustion technique and other advanced combustion concepts for internal combustion engines was found fruitful. Researchers indicated that there are still challenges in PCCI

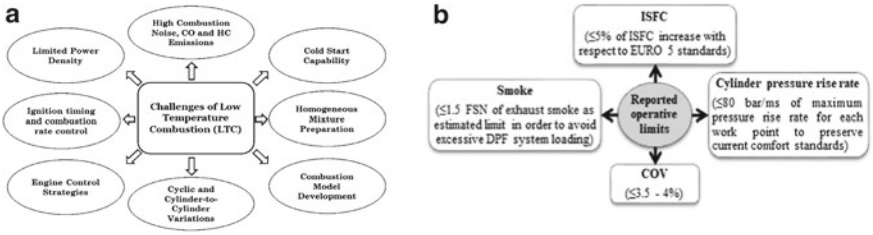


**Fig. 4** **a** Challenges of LTC, **b** reported PCCI combustions operative limits [23, 43]

combustion within in its success which hinders the LTC technology for commercialization. Time of ignition and rate of combustion controls indicated the major parameters of challenge which resulted in limited operating ranges greater production of hydrocarbon and carbon monoxides being the main challenges which need further investigations [44]. Unless efficient and proper controlling of the appropriate combustion rate being not sustained, excessively early or excessively delayed combustion would be resulted in the cylinder resulting in noise and engine damage. Other studies also revealed that smoke emission and premature ignition were challenges which need further studies for the betterment of thermal efficiency [25]. Numerous practical challenges were developing in the execution of LTC techniques. Studies found out that controlling the start of combustion is the key challenge and important parameter to make LTC strategy efficient. Limitation of LTC due to greater combustion levels particularly during big loads including misfiring during light loads was also challenging. Preparing the premixed charge makes better dilution of the air-fuel mixture which results in efficient burn rates. Figure 4 shows basic challenges faced in realizing LTC engines including PCCI combustion.

## 7 Conclusions

The PCCI principle, under LTC condition, showed comparatively an innovative technique possessing greater efficiency and maintaining lower production of soot and oxides of nitrogen suiting the global regulations of emission that has yet to find commercial success. Characteristics of local concentration and temperature stratification in the cylinder could be achieved through PCCI combustion. The mixture stratification could control the time of ignition and rate of combustion that could extend ignition duration and maximum load and all these affects the engine efficiency of combustion and emission results. Various results of experimental and simulation studies being examined and results indicated PCCI technique showed improved outcomes and acceptable values of emission characteristics than the conventional engine particularly with the addition of EGR. Port fuel injection also showed a promising strategy for PCCI mode of combustion which needs further optimization works through

applying alternative fuels in addition to the conventional fuels. Applying the flexibility nature of fuels affects the chemical kinetics which is having an important feature in LTC mode of combustions, and also research findings confirmed that modifications of fuel properties have a significant role in auto-ignition characteristics. Injection timing in PCCI operation mostly involves advanced or retarded time of injection which aims parallel decrease in both soot and oxides of nitrogen, unlike diesel usual combustions.

From the results, it is indicated that PCCI combustion on diesel engines brought the following emission improvements; applying low compression ratio technique resulted in 15% $NO_x$ emission reduction and a 3% of fuel consumption reduction, applying high EGR during light load conditions of the engine resulted in a parallel reduction of carbon monoxide, soot, unburned hydrocarbon and oxides of nitrogen with increased thermal efficiency, applying PCCI-DI operation mode enables reduction of 33%, 19%, 36% and 90% of $NO_x$, and soot emissions, respectively, applying pre-mixture of gasohol together with ethanol with 20% ratio resulted in 70% and 67% smoke emission reduction, applying B20 fuelled PCCI operation resulted in better combustion and emission characteristics, implementing methane port injection supply resulted in 0.5% increase in BTE, 13.33% decrease in HC, 31.81% decrease in CO, 1.45% increase in $NO_X$.

This review work tried to discuss PCCI combustion including what has been done, and the contributions of PCCI combustion which could help for further research efforts in overcoming the challenges of low-temperature combustion engines particularly PCCI combustion that the authors believe important in realizing their commercialization and look for other schemes in reducing the challenges under PCCI combustion mode.

## References

1. Dipak Kisan D, Nitin Parashram G (2020) Effect of combustion parameters on performance, combustion and emission characteristics of a modified small single cylinder diesel engine. Int J Recent Technol Eng (IJRTE) 8(5)
2. Liang X, Zheng Z, Zhang H, Wang Y, Yu H (2019) A review of early injection strategy in premixed combustion engines. Appl Sci (Published by MPDI)
3. Yusaf T, Hamawand I, Baker P, Najafi G (2013) The effect of methanol-diesel blended ratio on CI engine performance. Int J Automot Mech Eng (IJAME) 8:1385–1395. ISSN: 2180-1606 (Online)
4. Imtenan S, Varman M, Masjuki HH, Kalam MA, Sajjad H, Arbab MI, Rizwanul Fattah IM (2014) Impact of low-temperature combustion attaining strategies on diesel engine emissions for diesel and biodiesels: a review. Centre for Energy Sciences, Faculty of Engineering, University of Malaya, 50603 Kuala Lumpur, Malaysia
5. Park Y, Bae C (2011) Influence of EGR and pilot injection on PCCI combustion in a single-cylinder diesel engine. SAE Tech Pap Ser. https://doi.org/10.4271/2011-01-1823.
6. Singh AP, Agarwal AK (2018) Low-temperature combustion: an advanced technology for internal combustion engines. Adv Internal Combust Engine Res Energy Environ Sustain. https://doi.org/10.1007/978-981-10-7575-9_2

7. Aoyama T, Hattori Y, Mizuta J, Sato Y (1996) An experimental study on premixed-charge compression ignition gasolineengine. SAE960081
8. Beatrice C, Avolio G, Bertoli C, Del Giacomo N, Guido C, na Migliaccio M (2007) Critical aspects on the control in the low temperature combustion systems for high performance DI diesel engines
9. Paykani A, Kakaee A-H, Rahnama P, Reitz RD (2015) Progress and recent trends in reactivity-controlled compression ignition engines. Int J Engine Res. MechE
10. Kumar R, Saravanan S (2016) Partially premixed low-temperature combustion using dimethyl carbonate (DMC) in a DI diesel engine for favourable smoke/NOx emissions. Fuel 180:396–406
11. Catania AE, d'Ambrosio S, Finesso R, Spessa E, Cipolla G, Vassallo A (2009) Combustion system optimization of a low compression-ratio PCCI diesel engine for light-duty application. SAE Int J Engines 2(1):1314–1326
12. Lu Y, Yu W, Su W (2011) Using multiple injection strategies in diesel PCCI combustion: potential to extend engine load, improve trade-off of emissions and efficiency. SAE International. https://doi.org/10.4271/2011-01-1396
13. Sonawane YD, Deore ER (2020) Low-temperature combustion with multiple injection strategies in single cylinder diesel engine. Int J Innov Technol Explor Eng (IJITEE). 9(7). ISSN: 2278-3075
14. Neely GD, Sasaki S, Huang Y, Leet JA, Stewart DW (2005) New diesel emission control strategy to meet US Tier 2 emissions regulations. SAE Technical Paper; 2005-01-1091
15. Murugesa Pandian M, Anand K (2018) Comparison of different low-temperature combustion strategies in a light-duty air cooled diesel engine. Appl Thermal Eng 142:380–390
16. Bhiogade GE, Suryawanshi JG (2017) A comparative experimental study on engine operating on PCCI and CI mode
17. Ying W, Li H, Longbao Z, Wei L (2010) Effects of DME pilot quantity on the performance of a DME PCCI-DI engine. Energy Convers Manage 51(4):648–654
18. Juttu S, Mishra P, Thipse SS, Marathe NV, Gajendra Babu MK (2011) Combined PCCI-DI combustion to meet EURO-IV norms on LCV engine experimental and visualization study. SAE International, 2011-26-003; SIAT, India
19. Saravanan S, Pitchandi K, Suresh G (2015) An experimental study on premixed charge compression ignition-direct ignition engine fueled with ethanol and gasohol. Alex Eng J
20. Inagaki K, Fuyuto T, Nishikawa K, Nakakita K, Sakata I (2006) Combustion system with premixture controlled compression ignition. R&D Review of Toyota CRDL, pp 35–46
21. Purusothaman M, Teja NS, Sai NJ, Reddy V, Ram OP, Subrahmanyam KR (2020) Experimental validation on PCCI engine fuel with *Madhuca indica* blends. Int J Sci Technol Res 9(01)
22. Singh AP, Jain A, Agarwal AK (2017) Fuel-injection strategy for PCCI engine fueled by mineral diesel and, biodiesel blends. Energy Fuels. https://doi.org/10.1021/acs.energyfuels.6b03393. ACS Publications, pubs.acs.org/EF
23. Di Blasio G (2011) Premixed combustion in a light-duty compression ignition engine through fuel and injection system design. UniversitàDegliStudiDi Napoli
24. Nallamothu RB, Teferra A, Appa Rao BV (2013) Biogas purification, compression and Bottling. Glob J Eng Des Technol G.J.E.D.T., 2(6):34–38
25. Bao Z, Pan W, Yokoyama T, Hirayama K, Horibe N, Kawanabe H, Ishiyama T (2020) Study on characteristics of combined PCCI and conventional diesel combustion. Int J Automot Eng 11(2)
26. Kanda T, Hakozaki T, Uchimoto T, Hatano J, Kitayama N, Sono H (2005) PCCI operation with an early injection of conventional diesel fuel. SAE paper no. 2005-01-0378
27. Nallamothu RB, Tegegne T, Appa Rao BV (2013) Performance evaluation of caster methyl easter in direct injection four stroke diesel engine. Glob J Eng Des Technol G.J.E.D.T. 2(6):22–28
28. Wakjira A, Nallamothu RB (2013) Microcontroller based rear end anti-collision warning system for vehicles. Glob J Eng Des Technol G.J.E.D.T. 2(6):14–21
29. d'Ambrosio S, Iemmolo D, Mancarella A, Vitolo R (2016) Preliminary optimization of the PCCI combustion mode in a diesel engine through a design of experiments

30. Nallamothu RB, Fekadu G, Appa Rao BV (2013) Comparative performance analysis of gasoline and its blends with ethanol in gasoline engine. Glob J Biol Agric Health Sci G.J.B.A.H.S. 2(4):100–106
31. Ramesh Babu N, Wakjira A (2014) Investigation on the performance of fuel stick fuel conditioner in diesel vehicle. Int J Sci Res 3(11)
32. Varshney VK, Gaurav K, Tripathy S, Agrawal AK, Design of an experimental EGR system for a two cylinder diesel engine. I. I.T. Kanpur, Kanpur 208016, India
33. Abebe L, Nallamothu RB, Subrahmanyam KHS, Nallamothu SK, Nallamothu AK (2016) Thermal analysis of disc brake made of different materials. SSRG Int J Mech Eng (SSRG-IJME) 3(6):5–9
34. Bhiogade G, Suryawanshi JG (2016) Investigations on premixed charge compression ignition engine with external mixture formation and exhaust gas recirculation technique. J Mech Sci Technol 30(11):5269–5274
35. Akanaw TT, Moges HG, Babu R, Bisrat D (2014) Caster seed from Melkasa Agriculture Research Centre, East Showa, Ethiopia, and it's Biodiesel Performance in Four Stroke Diesel Engine. Int J Renew Energy Dev 3(2):99–105
36. Neway S, Nallamothu RB, Nallamothu SK, Nallamothu AK (2016) Investigation on pollution caused by gasoline and diesel fuelled vehicles. Int J Eng Trends Technol (IJETT) 36(7):376–381
37. d'Ambrosio S, Iemmolo D, Mancarella A, Vitolo R (2016) Preliminary optimization of the PCCI combustion mode in a diesel engine through a design of experiments. Energy Procedia
38. Firew D, Ramesh Babu N, Didwania M (2016) The performance evaluation of diethyl-ether (DEE) additive with Diesel blends using Diesel Engine test rig. Int J Sci Eng Res 7(6)
39. Nallamothu RB, Nallamothu AK, Nallamothu SK, Niranjan Kumar IN, Appa Rao BV (2018) Experimental investigation on effect of injection timing in multiple injection on NOx and smoke from CRDI diesel engine fueled with biodiesel blend. Ethiopian J Sci Sustain Dev (EJSSD) 5(2)
40. Sankaralingam RK, Ferroskhan SI, Venugopal T (2018) Experimental studies on premixed charge compression ignition (PCCI) engine using port injection of heated diesel. J Eng Sci Technol 13(11):3457–3472
41. Nallamothu RB, Nallamothu AK, Nallamothu SK, IN NK, Rao BVA (2018) Experimental investigation on NOx and smoke emission from CRDI diesel engine operated with biodiesel blend varying dwell between main and pre-injection. Ethiopian J Sci Sustain Dev (EJSSD) 5(2)
42. Nallamothu RB, Niranjan Kumar IN, Appa Rao BV, Anantha Kamal N, Seshu Kishan N (2018) Emission analysis of CRDI diesel engine fueled with cotton seed oil biodiesel with multiple injection strategy. Int J Emerg Technol Innov Res 5(9):707–712
43. Valentino G, Corcione FE, Iannuzzi SE (2012) Effects of gasoline-diesel and n-butanol-diesel blends on performance and emissions of an automotive direct-injection diesel engine. Int J Engine Res 13:199
44. Agarwal AK, Singh AP, Maurya RK, Evolution, challenges and path forward for low-temperature combustion engines
45. Nallamothu RB, Geremewbirbirsa, Niranjan Kumar IN, Appa Rao BV, Seshu Kishan N (2019) A review on performance of biodiesel in engines with and without addition of nanoparticles. Int J Manage Technol Eng IJMTE/1592 IX(II)
46. Nallamothu RB, Lemma M, Niranjan Kumar IN, Appa Rao BV, Anantha Kamal N, Seshu Kishan N (2019) Performance of cotton seed biodiesel with nano additives in diesel engines: a review. J Appl Sci Comput VI(II):142–147

# Design and Analysis of Front Axle of Truck at Different Driving Conditions

**Daniel Hambissa Datti, Ramesh Babu Nallamothu, Gamachisa Mitiku, Adem Siraj, and Getachew Fentaw**

## 1 Introduction

An axle is a rod or shaft used for turning of the wheel. The axles accomplish the transmission of driving rotational moment to the Wheel. Axle maintains the relative distance between the wheels and also relative position of the wheels with respect to the body. In addition to supporting the weight of the vehicle, it also carries cargo and any other load. Axles can be classified into three different types, namely rear axles, front axle, and stub axle. Generally, the front axle has a function of supporting the front portion of the vehicle, simplify steering, and absorb shocks from the road (Fig. 1).

D. H. Datti · R. B. Nallamothu (✉)
Mechanical Systems and Vehicle Engineering Department, SoMCME, Adama Science and Technology University, Adama, Ethiopia
e-mail: ramesh.babu@astu.edu.et

G. Mitiku
Department of Mechanical Engineering, Bule Hora University, Bule Hora, Ethiopia

A. Siraj
Mechanical Engineering Department, Addis Ababa Science and Technology University, Addis Ababa, Ethiopia

G. Fentaw
Mechanical Engineering Department, Woldia University, Woldia, Ethiopia



K. Jha et al. (eds.), *Recent Advances in Sustainable Technologies*,
Lecture Notes in Mechanical Engineering,
https://doi.org/10.1007/978-981-16-0976-3_18

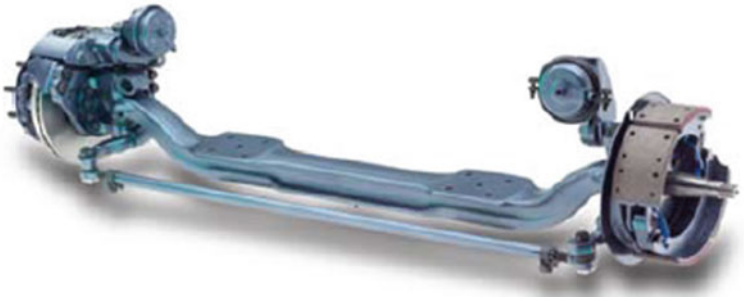

**Fig. 1** Front axle with the steering assembly

### *1.1 Front Axle*

Most often, front axle can have I-section in the mid-section (spring seat to spring seat) and circular or elliptical section or I-section at the ends. This cross-sectional shape of the axle can resist bending loads and torques due to the weight of the vehicle and braking, respectively. When the vehicle is accelerating, shifting of load takes place from front to rear and while decelerating, vice versa happens [1]. The front dead axle of trucks was designed and analyzed when the truck is accelerating on different road conditions (level road, uphill, and downhill).

Types of the front axle are listed below:

(i) Dead axle
(ii) Line axle.

The front axles are called dead axles as they do not make any rotational motion with the wheels and only used for support purposes. Unlike live axle, dead axles do not transmit any motion. There is a different mechanisms used for spinning the wheels. At the wheel mounting points, near the end of axle half shafts, there is a difference exists between live axles and gear axles. Front portion weight of the vehicle is safely carried by the rigid and strong front dead axle. The front dead axles are usually mounted on heavy-duty trucks.

## 2 Literature Review

Various analytic, experimental, and numerical researches were done for the front axle beam. For different types of a heavy commercial vehicle, the design and analysis of the front axle were done by using the analytic and FEA method. The axles were modeled on any of the modeling software and imported to ANSYS software for a numerical result. FEA results are well in agreement with numerical calculations as observed from different literatures. Ashok Leyland 1612 Comet heavy commercial vehicle axle model was analyzed for two materials namely as ductile cast iron and

SAE 1020 under static condition. To perform the analytic and numerical analysis, for finding deflection and stresses vehicle payload, gross weight and other specifications were used. By comparing the FE results with analytical design, it was observed that SAE 1020 is a better material for the manufacturing of axle than ductile cast iron [2]. The axle could also be optimized by initially considering different I cross-section area models and then selecting the best material among SAE 4310, AISI 1020, SAE-AISI 1018, and cast iron materials. The results show that SAE1018 is the best material [3] and also, for the manufacturing of the axle, aluminum alloy is better and a suitable material than gray cast iron [4–7]; in addition to this, the axle could also be designed by considering glass carbon and S—2 glass epoxy glass carbon and steel materials under dynamic condition. For each material, transient analysis and modal analysis were done on the axle to determine displacement, stress, vibration, and strain [8–11]. The deformation and strain values are more for composite material S2 glass than steel and glass carbon. The stress value is less for S2 glass material [12, 13].

The vibrations are more for the front axle when glass carbon is used. So, it was observed that considering the weight and strength, using S2 glass is better than glass carbon [14, 15]. Moreover, by using structural steel material with an I-beam shape, the front axle was analyzed to determine its behavior under transient and static loading conditions and also to determine the load capacity of the front side rigid axle of an LCV. Modal analysis was also done. Even though performance requirements are met by front axle, as the analysis results indicate, but failure may occur in the welded region of front axle and sleeve of the coil spring under the condition of emergency braking because of inadequate tensile and yield strength. It leads to difficulty for the vehicle to change the direction. According to the natural frequency values and excitation frequency range, there is a much difference between natural frequency values and excitation frequency, indicating very fewer failure chances [16, 17]. Another survey was done for ISUZU CYZ 400 heavy-duty vehicles by considering various forces acting on the axle. The design includes vertical, braking, and cornering load which cause static and dynamic conditions. The beam was considered as a simply supported beam and the stress and deflection of the axle are analyzed [18, 19]. The results showed the modified Good Mann Line Diagram [20–22]. And also, the shape optimization was carried out for all three load cases to minimize the mass of the axle beam. The stress, strain, and displacement values due to three loading cases such as vertical load, vertical and cornering combined load and the vertical and braking combined load were analyzed by considering design parameters such as wheel track, axle weight, rated load of the axle, kingpin center, and spring center. Improved strength-to-weight ratio is obtained. The fatigue life result shows the highest reliability [23, 24].

**Table 1** Vehicle specification

| | |
|---|---|
| Wheelbase | 5.48 m |
| Track width | 1.76 m |
| Overall length (OL) | 9.19 m |
| GVWR | 10,432.62 kg |
| Chassis weight | 3975.73 kg |
| Gross payload | 6456.88 kg |
| Front axle | GAWR 3798.836 kg |
| | Axle Type "I" Beam |
| | Shock Absorbers Telescopic Type |
| | Suspension Semi-elliptic Leaf Springs |
| Rear axle | GAWR 6998.93 kg |
| | Axle Type Full-floating Banjo Housing |

## 3 Analytic Calculation

### *3.1 Vehicle Required Specifications (UD Truck UD2300LP)*

See Table 1.

### *3.2 Analytical Load Calculation*

This design includes analysis of the front axle of the truck at two driving conditions. These are

(1) An accelerating truck on a level pavement
(2) An accelerating truck on grade (uphill or downhill) pavement.

**Accelerating vehicle on a Level Road**. When the truck (no trailer) accelerates on level ground at a low speed, such that the force due to aerodynamic force is zero, and the loads on the front axles become:

$$\text{LOAD ON AXLE}(F_A) = w\left(\frac{a_2}{2} - \frac{h}{l}\frac{a}{g}\right) \tag{1}$$

where:
$w$ is weight of the truck
$g$ is the gravity and $a$ is the acceleration at which the vehicle is traveling
$a_2$ is the horizontal distance of the rear axle from the center of gravity of the truck
$h$ is the height center of the gravity.

At a normal range of driving speeds, maximum accelerations are 0.05 g $\left(\frac{a}{g} = 0.05\right)$ or less [25]. Typical values of CG height of truck is between 1.14 and 2.16 m [1]. By using the above parameters, the longitudinal position of the truck can be found from the equation of maximum acceleration for rear-wheel drive [5].

$$\frac{a_{rwd}}{g} = \frac{a_1 \mu_x}{l - h\mu_x} \quad \text{i.e. } a_1 = \frac{a_{rwd}}{g}\left(\frac{1}{\mu_x} - \frac{h}{l}\right) \tag{2}$$

where $\mu_x$ is the coefficient of kinetic friction between the tire and road surface. For dry pavement, $\mu_x = 0.5$ [6].

**Loads on Grades**. The front axle is also influenced by different topographies (slopes or grades). The grade is the "rise" over the "run." The value of road gradient (in per cent) obtained by dividing vertical rise by the horizontal distance. The maximum recommended slope for light trucks running at a moderate speed (30–40 km/h) on mountainous topography is 15% [9]. Thus, the axle loads as influenced by grades will be:

$$\text{load on front axle}(F_A) = w\left(\frac{a_2}{l}\cos\theta \pm \frac{h}{l}\sin\vartheta\right) \pm \frac{h}{l}ma) \tag{3}$$

where $\pm$ sign is used to indicate the uphill and downhill conditions, plus (+) sign stands for downhill, and a negative sign is for uphill condition). The values of the longitudinal center of the position of the truck can always vary with the condition of the road pavement (level, uphill, and downhill) for the current condition, and the equation for center of gravity positions can be evaluated by two equations.

$$F_x = \mu_x * \text{normal force under the two wheel} = \mu_x 2F_z \tag{4}$$

By using Newton second low of motion along longitudinal direction, we have:

$$F_x = ma \pm mg\sin\theta \tag{5}$$

where $2F_z$ is equal with the total load on the axle, and by equating Eqs. 6 and 7, we got the equation for the position of the center of gravity from the front axle as follow:

$$\text{For uphill driving } a_1 = \left(\frac{a}{g}\left(\frac{1}{\cos\theta\mu_x} - \frac{h}{l\cos\theta}\right) - \frac{h}{l}\tan\theta + \frac{\tan\theta}{\mu_x}\right)l \tag{6}$$

$$\text{For downhill driving } a_1 = \left(\frac{a}{g}\left(\frac{1}{\cos\theta\mu_x} + \frac{h}{l\cos\theta}\right) + \frac{h}{l}\tan\theta - \frac{\tan\theta}{\mu_x}\right)l \tag{7}$$

Therefore, the value of $a_2$ become: $a_2 = l - a_1$.

The value of accelerations for slow pulls up steep grades would be limited to approximately 0.15 g's [1].

## 4 Analysis for Front Axle Beam

The software selected for the structural analysis is ANSYS mechanical which is mostly used as a finite element analysis tool. The analysis is carried out after modelling the front axle on another CAD software. The obtained computer simulation results are used to predict the behavior of the front axle with those driving condition.

### *4.1 Design and Modeling Using Catia V5 Software*

To perform the analysis of the axle beam in ANSYS, first, the axle beam must be modeled in any of commercially available modelling software like CATIA or Solid Works, etc. CATIA V5 modelling software is preferred for modelling in this thesis. CATIA is mechanical modelling software which allows 3D modelling and 2D drafting of elements. 3D solid models can be created for capturing design intent with or without constraints while utilizing automatic or user-defined. The 3D modeling of the front axle is as shown below Fig. 2.

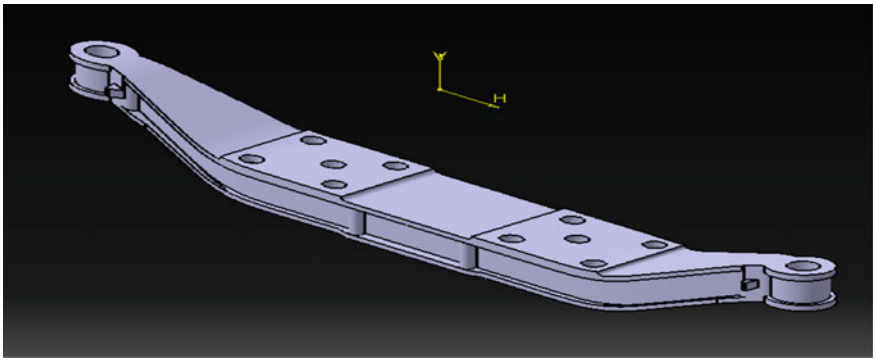

**Fig. 2** 3D modeling of the axle

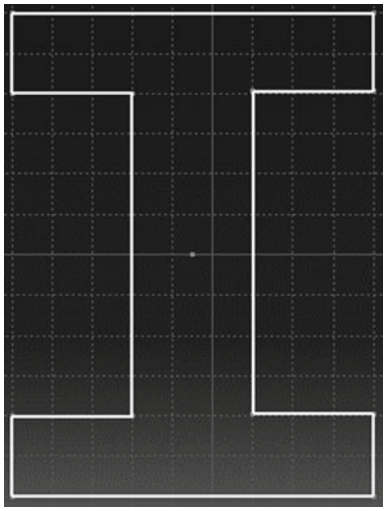

**Fig. 3** Section of the axle

## 4.2 ANSYS Simulation of Static Condition of Front Axle

It is necessary to investigate the behavior of the axle beam in response to dynamic and static loads. Both shear and bending stresses exist in front axles. The axle is treated as a beam supported vertically upward at the ends [3]. Here, the 3D model of the simplified geometry is imported to ANSYS software where the model is meshed and analyzed in response to a static load.

**Material description**. The material which is chosen for the front axle beam is SAE-AISI 1018 material which is best for front axle beam [3]. Standard properties of SAE-AISI 1018 are taken from the tables.

*Cross-section of the beam.* The I cross-section of the beam is designed based on the density of the material, length, and GAWR of the front axle [3] (Fig. 3).

$$v_{fa} = \frac{\text{GAWR}}{\rho_{\text{material}}}, \quad \text{Area}_{\text{cross section}} = {}^{v_{fa}}\!/_{l_{\text{axle}}} \tag{7}$$

where $v_{fa}$ is the volume of the cross-section of the axle and $l_{\text{axle}}$ is the length of the axle.

## 4.3 Finite Element Analysis

The current 3D model was meshed using tetrahedral elements. The model consists of 188,870 nodes and 118,354 elements. Proper boundary conditions are integrated into the analysis (Fig. 4).

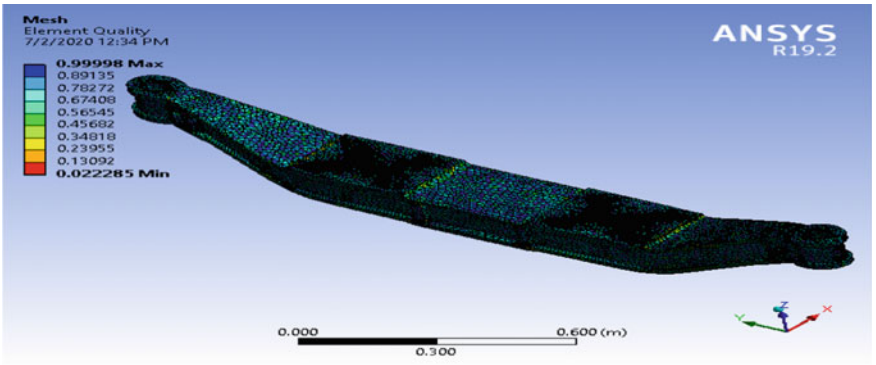


**Fig. 4** Mesh quality

(A) **For level road driving**
*Maximum stress*
*Maximum deformation.*

From the above result, we can see that the maximum stress (equivalent stress) and deformation on the axle are $4.23 \times 10^7$ Pa and $9.14 \times 10^{-5}$ m, respectively (Figs. 5, and 6).

(B) **Uphill driving**
*Maximum stress*
*Deformation.*

During uphill driving, the front axle is subjected to maximum stress (equivalent stress) and deformation of $2.5 \times 10^7$ Pa and $5.33 \times 10^{-5}$ m, respectively (Figs. 7, and 8).

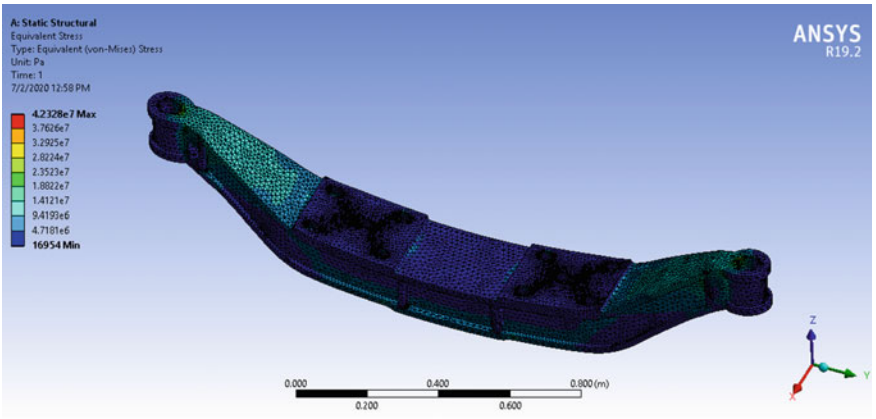


**Fig. 5** von Mises stress on the axle

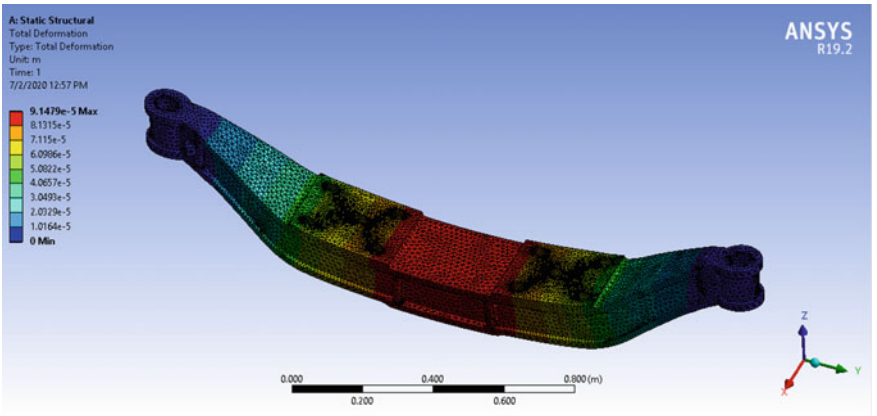


**Fig. 6** Total deformation

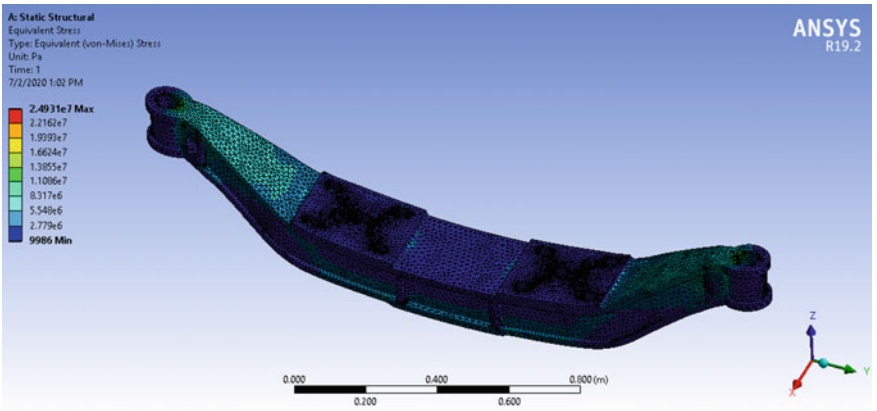


**Fig. 7** von Mises stress

(C) *Downhill driving condition stress*
See Fig. 9
Deformation.

From this result, it can be observed that the equivalent stress and deformation on the axle are $4.4 \times 10^7$ Pa and $9.5 \times 10^{-5}$ m, respectively. By comparing with the other driving condition, maximum stress and deformation on the axle occur when the truck moves on the downhill road (Fig. 10).

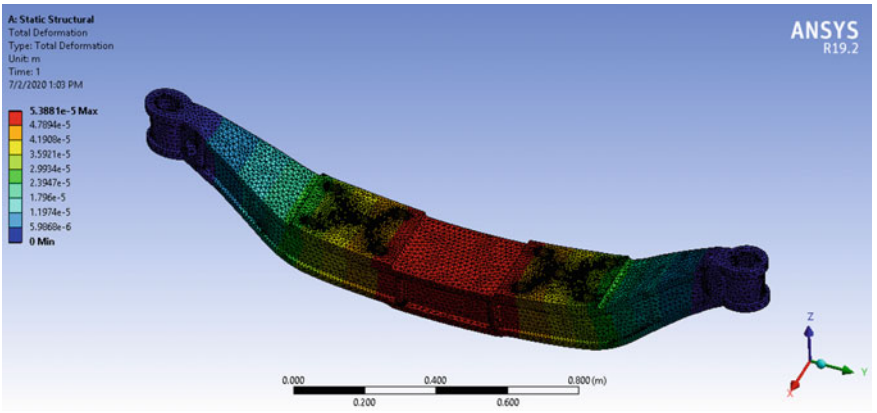


**Fig. 8** Total deformation

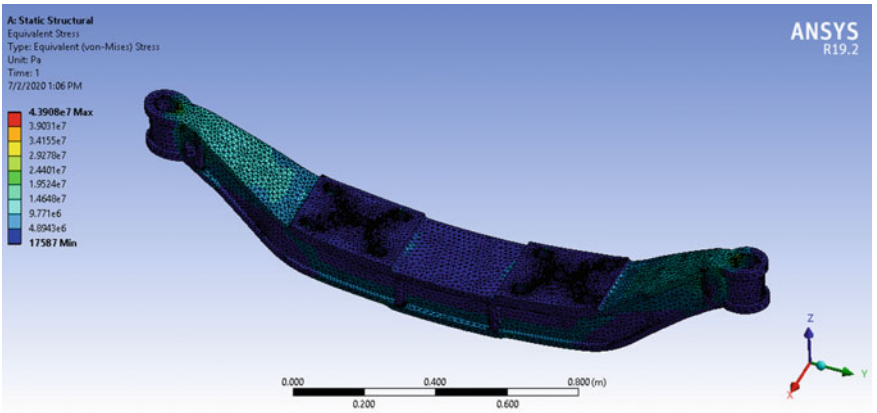


**Fig. 9** von Mises stress

## 5 Conclusion

In this research, the front axle of the heavy-duty vehicle was analyzed numerically for SAE-AISI 1018 at the different driving conditions. The results indicate that the maximum or critical condition for the axle occurs when it is derived on the downhill road and the values of the maximum von Mises stress and total deflection during these conditions are $4.4 \times 10^7$ Pa and $9.5 \times 10^{-5}$ m, respectively**.** The design is safe since the indicated von Mises stress is below the yield strength of the material.

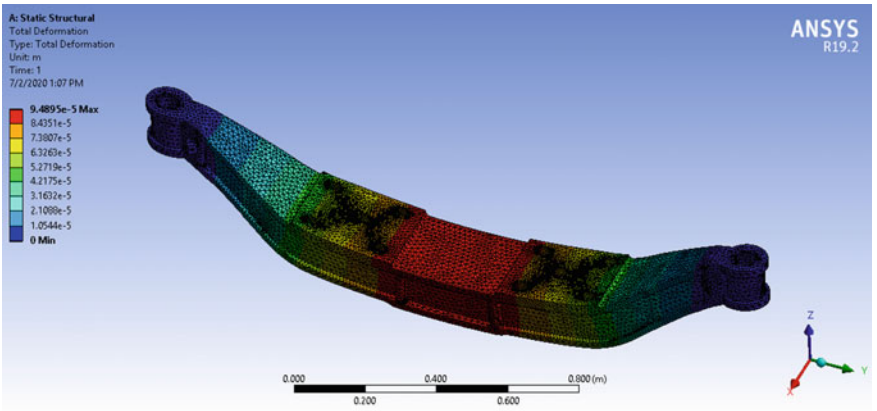


**Fig. 10** Total deformation

## References


1. Gillespie, TD (1992) Fundamentals of vehicle dynamics, vol 400. Society of Automotive Engineers, Warrendale, PA
2. Dhande, KV, Ulhe P (2014) Design and analysis of front axle of heavy commercial vehicle. Int J Sci, Technol Manag 03
3. Maddewad K, Jadhav T, Bhosale A, Yemle S, Jadhav N (2017) Optimization of front axle for heavy commercial vehicle by analytical and FEA method. Int Res J Eng Technol (IRJET)
4. Raju KP, Kumar BJ Design and analysis of a heavy vehicle front axle
5. Jazar RN (2008) Vehicle dynamics. In: Theory and application. Springer Science
6. Rievaj V, Vrábel J, Synák F, Bartuška L (2018) The effects of vehicle load on driving characteristics. Adv Sci Technol Res J 12
7. Ruban M, Sivaganesan S (2016) Design analysis and optimization of front axle for commercial vehicle using CAE. ARPN J Eng Appl Sci 11(13):8511–8516
8. Wint KZ, Htoo AM, Thwin ST (2018) Stresses analysis of various force for front axle beam in heavy Duty. Int J Sci, Eng Technol Res (IJSETR) 7(10).
9. Dey S, PRVVV Sri Rama Chandra Murthy D, Baskar P (2014) Structural analysis of front axle beam of a light commercial vehicle (LCV). Int J Eng Trends Technol (IJETT) 11(5)
10. Sessions J (2007) Forest road operations in the tropics. Springer, Berlin, Heidelberg, New York
11. Buhari R, Rohani MM, Abdullah ME (2013) Dynamic load coefficient of tyre forces from truck axles. Appl Mech Mater 405:1900–1911
12. Jiang K, Pavelescu A, Victorino A, Charara A (2014) Estimation of vehicle's vertical and lateral tire forces considering road angle and road irregularity.In: 17th international IEEE conference on intelligent transportation systems (ITSC), pp 342–347
13. Tuononen AJ (2009) Vehicle lateral state estimation based on measured tyre forces. Sensors 9(11):8761–8775
14. Jayaprakash V, Rohit AK (2018) Design and dynamic analysis of a heavy vehicle front axle under bending loads. IJSART 4(10)
15. Ud trucks Homepage, https://www.udtrucks.com/. Last accessed 2020/08/10.
16. Ermias Feliche, Ramesh Babu Nallamothu, Seshu Kishan Nallamothu (2017) A study on cause of rollover of sugar cane haulage semitrailer truck in Ethiopia Sugar Estate: case of Wonji Sugar Factory. Int J Eng Trends Technol (IJETT) 43(4):205–211
17. Yesfalgn Damissie H, Ramesh Babu N (2017) Aerodynamics drag reduction on locally built bus body using computational fluid dynamics (CFD): a case study at Bishoftu automotive industry. Int J Eng Res Technol (IJERT) 6(11)

18. Ashagrie G, Nallamothu RB, Nallamothu AK, Nallamothu SK (2017) A study on driving stability of bus using computational fluid dynamics (CFD). Int J Res Appl Sci Eng Technol 5(XI)
19. Kibret Yilak Molla, Kim Chul-Ho, N.Ramesh Babu: Aerodynamic Design of the Ethiopian Train for Energy Economy under Crosswind Conditions. 년도 한국철도학회 추계계학술대회 논문집, KSR 2017, South Korea (2017).
20. Siraj A, Ramesh Babu N, Srinivasa Reddy K (2019) Static analysis of dump truck chassis frame made of composite materials. Int J Eng, Sci Technol 11(2):21–32
21. Getachew Alemayehu, Ramesh Babu Nallamothu, " Programmable Logic Controller (Plc) Application for Hybrid Electric Vehicle (Hev) Simulator.International Journal of Mechanical Engineering and Technology (IJMET). Volume:8, Issue: 9 (2017); 281–292.
22. Negera DW,. Bhaskaran J, Ilmi I, Nallamothu RB (2019) Characterisation of hybrid composite made of false banana fibre and sisal fibre. Int J Eng Adv Technol (IJEAT), 9(2). ISSN: 2249-8958
23. Getu D, Nallamothu RB, Masresha M, Nallamothu SK, Nallamothu AK (2020) Production and characterization of bamboo and sisal fibre-reinforced composite for interior automotive body application. Mater Today: Proc. Elsevier
24. Alemayehu Z, Nallamothu RB, Liben M, Nallamothu SK, Nallamothu AK (2020) Experimental investigation on characteristics of sisal fibre as a composite material for light vehicle body applications. Mater Today: Proc
25. Gillespie TD (1993) Effects of heavy-vehicle characteristics on pavement response and performance, vol 353. Transportation Research Board

# Spectroscopic and Structural Investigation of Graphene Oxide Synthesized via Hummers' Method


**Nipom Sekhar Das, Koustav Kashyap Gogoi, Suma Das, and Avijit Chowdhury**

## 1 Introduction

The carbon nanostructures have attracted growing attention recently due to their remarkable properties and affluent applications in diverse fields [1]. The graphene oxide (GO), one of the allotropes of carbon nanomaterials, owns a 2-D hexagonal planar sheet-like structure and shows enormous interest because of its large specific area, easy accessibility, and low-cost production. In addition, the GO displays some incredible characteristics such as high thermal and electrical conductivity, flexibility, tunable energy bandgap, and high mechanical strength. Hence, GO is a very promising material in modern science and nanodevice technology and found applications in bio-sensing, catalysis, energy storage, resistive memories, etc. In view of the above, therefore, the synthesis of GO with few numbers of layered sheets is very crucial to harness their exceptional characteristics at the nano regime [2–4]. The preparation of GO from natural graphite is simple and safe, and it can be easily exfoliated into single- or few-layer thick sheets by breaking the weak bonds present between the layers using the liquid-phase exfoliation method [5]. The Hummers' method is broadly used for the preparation of GO in an eco-friendly and efficient way. However, many oxygen functional groups like carboxylic, epoxy, hydroxyl, and carbonyl groups [6–8] are induced during the synthesis process. The presence of these substantial numbers of functional groups makes GO an excellent water-soluble and high ease of functionalization. However, the oxygen functional groups present in GO are accountable for poor performances as it mainly affects the carrier transport process. The GOs possess large number of oxygen functional groups which is amorphous in nature and hence not suitable for applications, especially for electronic devices. Therefore, the synthesis of GOs using Hummer's method via controlling the

N. S. Das · K. K. Gogoi · S. Das · A. Chowdhury (✉)
Organic Electronics and Sensor Laboratory, Department of Physics, National Institute of Technology Silchar, Silchar, Assam 788010, India



K. Jha et al. (eds.), *Recent Advances in Sustainable Technologies*,
Lecture Notes in Mechanical Engineering,
https://doi.org/10.1007/978-981-16-0976-3_19

synthesis parameter is very crucial to obtain high-quality GOs with reduced oxygen functionalities. Therefore, the exfoliation of GO and the reduction of functional groups are crucial factors for the performance enhancement, especially to meet the expectation and functionalities similar to graphene. The novelty of the proposed work lies in the synthesis of exfoliated GO using a cost-effective a straight-forward solution processing technique. Such an efficient and environment-friendly technique facilitates a few-layered thick GO sheets with a large specific area. It can be used as templates to graft various nanomaterials with desired functionalities. Functional GO displays a wide range of applications in energy storage, energy conversion, electronic and optoelectronic devices, including memory devices, [9, 10] due to the synergistic interfacial effect at the percolated structure. Herein, the GO is synthesized using conventional Hummer's method via controlling the synthesis parameter to obtain GO sheets with reduced oxygen functionalities.

## 2 Experimental Procedure

The GO was synthesized via conventional Hummers' method by using graphite flakes as the starting material [11–13]. The procedure for the synthesis of GO is shown schematically in Fig. 1. Briefly, 0.24 g of graphite flakes was added with 0.24 g $NaNO_3$ and dispersed in 13.56 mL of $H_2SO_4$. After 6 h of continuous stirring, 1.23 g of $KMnO_4$ was mixed into the solution, and temperature of the solution was kept below 12 °C. Then, $H_2O$ (26.54 mL) was added after heating the solution at 35 °C. After overnight stirring, the solution was heated further to 96 °C for 15 min and brought it down to room temperature. Then, 56.64 mL of deionized water was mixed to the solution. Then, the solution turned yellow after the addition of 5.64 mL of $H_2O_2$. The yellowish solution was then centrifuged by HCl followed by DI $H_2O$ several

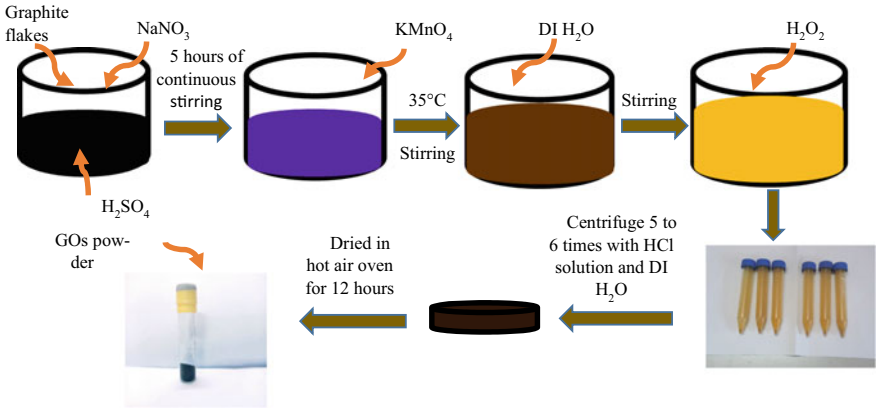


**Fig. 1** Synthesis of GO by using Hummers' method

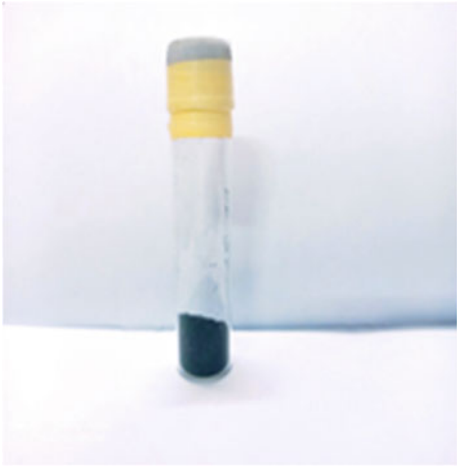

**Fig. 2** Synthesized GO powder

times. Finally, the brown-colored solution was heated in an oven for 12–15 h to obtain wafer-like sheet. After grinding the sheet, a fine powder of GO was obtained as shown in Fig. 2. The liquid-phase exfoliation of GO is done using a tip sonicator for an hour at 40 W before the spectroscopic analysis. The GO is then characterized through UV–visible spectroscopy (Agilent Technologies, Model: Cary 60), photoluminescence spectroscopy (Fluoromax-4C Spectrofluorometer, HORIBA), X-ray diffractometer (XRD) (Panalytical), and scanning electron microscopy (Model: ZEISS EVO-MA 10).

## 3 Result and Discussions

### *3.1 Optical Analysis of Graphene Oxide*

#### 3.1.1 UV–visible Absorption Spectroscopy of GO

The UV–visible spectroscopy of GO is carried out in the wavelength region of 200–800 nm, and the corresponding spectra are shown in Fig. 3a. An absorption peak is appeared at 228 nm which is evolved because of the transition between $\pi$–$\pi^*$ in $sp^2$ hybridized carbon atoms present in the aromatic C–C ring [14]. Another peak found at 312 nm which is resulted due to the transition of $n$–$\pi^*$ in the energy levels of C=O bonds present in the carbonyl group [15]. The Tauc's plot is used as shown in Fig. 3b to obtain the optical bandgap energy, and estimated values are found to be 4.08 eV and 3.43 eV, respectively [16].

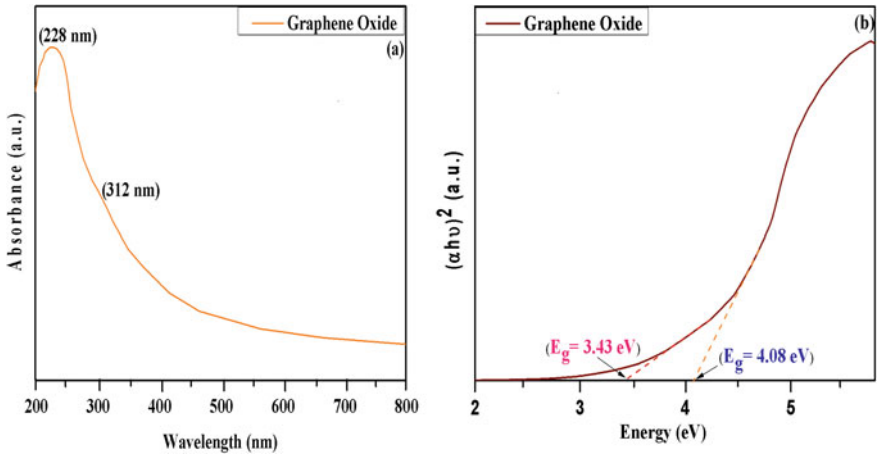


**Fig. 3** **a** UV–visible spectroscopy, and **b** Tauc's plot of GO

### 3.1.2 Photoluminescence (PL) Spectroscopy of GO

The PL spectroscopy of GO is carried out with an excitation wavelength $\lambda_{ex}$ ~ 228 and 312 nm, respectively. A broad peak appears at 433 nm for the excitation wavelength 312 nm as shown in Fig. 4a [17, 18]. A deconvoluted photoluminescence spectrum is shown in Fig. 4b which shows the deconvoluted emission peaks center at 367 nm, 398 nm, 422 nm, 434 nm, 452 nm, 474 nm corresponding to emission energies of 3.37 eV, 3.11 eV, 2.93 eV, 2.85 eV, 2.74 eV, and 2.61 eV, respectively [19]. The emission energy for the broad peak is estimated to be 2.86 eV, from the emission energy curve as shown in Fig. 4c.

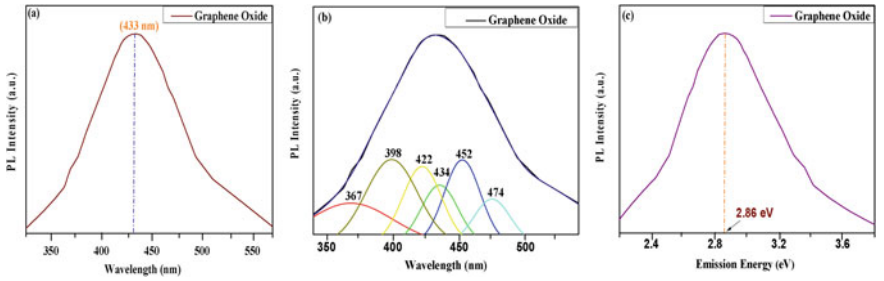


**Fig. 4** **a** Photoluminescence (PL) spectra of GO **b** deconvoluted photoluminescence (PL) spectra of GO, and **c** emission energy curve of graphene oxide

## *3.2 Structural Studies of Graphene Oxide*

### 3.2.1 X-ray Diffraction (XRD)

The XRD analysis of GO is performed to study the structural phase and to estimate the inter-planar spacing of GO. It was performed by using $CuK_{\alpha}$ radiation with $\lambda = 1.54$ Å in a $2\theta$ range (5–60°) as shown in Fig. 5a [20]. A sharp peak appears at $2\theta = 9.89°$ which is originated due to the reflection from (001) plane of GO [21]. The hexagonal structure of GO is confirmed by the (001) plane [21]. Another small peak centered at $2\theta = 42.60°$ corresponds to the reflection from (101) plane [22]. The inter-planar spacing of GO is estimated using Bragg's law, and it is found to be 8.93 Å [22].

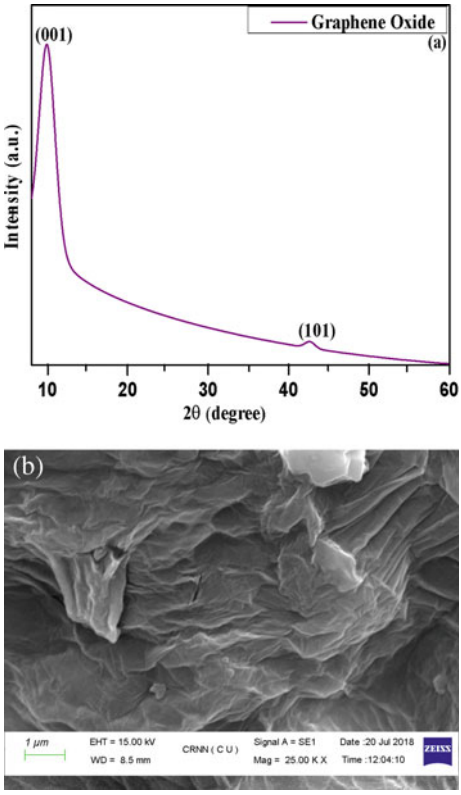


**Fig. 5** **a** XRD spectra of GO, **b** SEM image of GO

### *3.3 Morphological Analysis of Graphene Oxide*

#### 3.3.1 Scanning Electron Microscopy (SEM) of GO

The SEM image of GO is shown in Fig. 5b. The GO sheets are found with irregular morphology throughout the surface. These types of irregular structures may be attached to the multiple stacked sheets at different places. It can be concluded from the figure mentioned below that there are various layers of GO overlap in an irregular manner [22]. The energy-dispersive X-ray spectroscopy (EDAX or EDS) analysis (figure not shown) confirms that the synthesized material contains carbon and oxygen.

## 4 Conclusion

GO was synthesized economically and efficiently by using the Hummers' method. The optical energy gaps are estimated to be 4.08 and 3.43 eV, respectively, from Tauc's plot, and emission energy is found to be 2.86 eV for the broad peak that appears at 433 nm in PL spectra. It is also observed that the optical energy gap 3.43 eV is almost comparable with the emission energy 3.37 eV at the lower wavelength region ($\lambda \sim 367$ nm) obtained from the PL spectra. The synthesized GO has an inter-planar spacing of about 8.93 Å that is estimated using Bragg's law, and also, XRD analysis confirms the hexagonal structure of GO. The SEM analysis suggests that GO contains 2–3 sheets for a thickness of 2 nm.

**Acknowledgements** We are grateful to Central Instrumentation Facility, NIT Silchar, for giving us the characterization facilities.

## References

1. Alam SN, Sharma N, Kumar L (2017) Synthesis of graphene oxide (GO) by Modified Hummers method and its thermal reduction to obtain reduced graphene oxide (rGO). Graphene 6(1):1–18
2. Gurunathan S, Han JW, Kim E, Kwon D-N, Park J-K, Kim J-H (2014) Enhanced green fluorescent protein-mediated synthesis of biocompatible graphene. J Nanobiotechnol 12(1)
3. Siburian R, Sihotang H, Raja SL, Supeno M, Simanjuntak C (2018) New route to synthesize of graphene nano sheets. Orient J Chem 34(1):182–187
4. Johra FT, Lee J-W, Jung W-G (2014) Facile and safe graphene preparation on solution-based platform. J Ind Eng Chem 20:2883–2887
5. Du D, Song H, Nie Y, Sun X, Chen L, Ouyang J (2010) Blue photoluminescence from chemically derived graphene oxide. Adv Mater 22(4):505–509
6. Luo L, Peng T, Yuan M, Sun H, Dai S, Wang L (2018) Preparation of graphite oxide containing different oxygen-containing functional groups and the study of ammonia gas sensitivity. Sensors 18(11):3745

7. Mondal K, Balasubramaniam B, Gupta A, Lahcen AA, Kwiatkowski M (2019) Carbon nanostructures for energy and sensing applications. J Nanotechnol 1–3.
8. Yu H, Zhang B, Bulin C, Li R, Xing R (2016) High-efficient synthesis of graphene oxide based on improved Hummers method. Sci Rep 6(1)
9. Mohan VB, Lau K-T, Hui D, Bhattacharyya D (2018) Graphene-based materials and their composites: a review on production, applications and product limitations. Compos B 142:200–220
10. Long W-J, Gu Y-C, Xiao B-X, Zhang Q-M, Xing F (2018) Micro-mechanical properties and multi-scaled pore structure of graphene oxide cement paste: synergistic application of nanoindentation, X-ray computed tomography, and SEM-EDS analysis. Constr Build Mater 179:661–674
11. Gogoi KK, Chowdhury A (2019) Highly stable write-once-read-many times switching behavior of graphene oxide -polymer nanocomposites. AIP Conf Proc 2142:150028
12. Guerrero-Contreras J, Caballero-Briones F (2015) Graphene oxide powders with different oxidation degree, prepared by synthesis variations of the Hummers method. Mater Chem Phys 153:209–220
13. Gogoi KK, Chowdhury A (2019) Electric field induced tunable electrical hysteresis in poly (methyl methacrylate)/graphene oxide heterostructure. AIP Conf Proc 2100:020022
14. Mamo MA, Sustaita AO, Coville NJ, Hümmelgen IA (2013) Polymer composite of poly (vinyl phenol)-reduced graphene oxide reduced by vitamin C in low energy consuming write-once–read-many times memory devices. Org Electron 14(1):175–181
15. Marcano DC, Kosynkin DV, Berlin JM, Sinitskii A, Sun Z, Slesarev A, Alemany LB, Lu W, Tour JM (2010) Improved synthesis of graphene oxide. ACS Nano 4(8):4806–4814
16. Das RC, Gogoi KK, Das NS, Chowdhury A (2019) Optimization of quantum yield of highly luminescent graphene oxide quantum dots and their application in resistive memory devices. Semicond Sci Technol 34(12):125016
17. Gan Z, Xiong S, Wu X, Xu T, Zhu X, Gan X, Guo J, Shen J, Sun L, Chu PK (2013) Mechanism of photoluminescence from chemically derived graphene oxide: role of chemical reduction. Adv Opt Mater 1(12):926–932
18. Shukla S, Saxena S (2011) Spectroscopic investigation of confinement effects on optical properties of graphene oxide. Appl Phys Lett 98(7):073104
19. Chien C-T, Li S-S, Lai W-J, Yeh Y-C, Chen H-A, Chen I-S, Chen L-C, Chen K-H, Nemoto T, Isoda S, Chen M, Fujita T, Eda G, Yamaguchi H, Chhowalla M, Chen C-W (2012) Tunable photoluminescence from graphene oxide. Angew Chem Int Ed 51(27):6662–6666.
20. Jia MS, Chang SY, Hua XL, Dong LS, Te H, Bo TH(2013): X-ray diffraction pattern of graphite oxide. Chin Phys Lett 30(9):096101
21. Gogoi KK, Chowdhury A (2019) Electric field induced tunable memristive characteristics of exfoliated graphene oxide embedded polymer nanocomposites. J Appl Phys 126:025501
22. Gogoi KK, Das NS, Chowdhury A (2019) Tuning of electrical hysteresis in PMMA/GOs/PMMA multi-stacked devices. Mater Res Express 6:085108

# IOT-Based Online FIR Assistance System with Two-Way Security Using Image Processing


**Sandeep Singh and Manpreet Singh**

## 1 Introduction

India is now the fastest developing country in the world. So, a lot of new innovations are being developed for our glamorous living styles. The technologies are used in the fields of education, banking, industry, etc [1]. Our nation has more population compared to other countries. This ensures that public safety is the most critical aspect of our country's defense and security structure. The department of Indian Police is often readily available for service of the citizens, but often due to certain circumstance, they have neglected to do so. The government is reducing the burden with the use of advance technologies and digitalization and thus saves time and effort. The Indian Police Force is the only big part of our society that remains completely devoid of this privilege yet. The Indian Police Department has, for most of its routine operations, been manually controlled ever since. The officials also followed the basic methods of conducting the trials, with the conventional "pen and paper" approach being very prevalent. In earlier days, when population was much lower, these traditional activities were relaxed, and crime rates were also comparatively low. But in today's India, where society's crimes are in a peak and so many cases are reported every day, manual handling of the case and all of its associated records has become a very cumbersome process. FIR is a vital first step toward complaint registration. The procedure for filing an FIR is mentioned under Section 154 of Criminal Procedure Code, 1973. According to CPC, usually, one needs to visit the police station to file a complaint or an FIR. The report can be forwarded to the police either orally or in writing. A person can file a complaint for a criminal matter according to the Indian Jurisdiction and Legislation. For any other crime, either the perpetrator of the offense or someone else on his/her behalf can file an FIR. As after, FIR has been

S. Singh · M. Singh (✉)
School of Mechanical Engineering, Lovely Professional University, Phagwara, India
e-mail: manpreet.20360@lpu.co.in



K. Jha et al. (eds.), *Recent Advances in Sustainable Technologies*,
Lecture Notes in Mechanical Engineering,
https://doi.org/10.1007/978-981-16-0976-3_20

filed that the police can begin investigation into the crime committed. But nowadays, we faced many problems while registering a complaint against any crime. Some people despise going to police station when there is a crime taking place. There is usually a feeling that registering a complaint is a tedious process or the police will not be cooperative; police will ask inappropriate questions and misbehave; sometimes, they ask money for filing the FIR. Thus, digitalization of the police department is required for the betterment of public as well as for department. To file an incident report and get updates, the conventional way of visiting a police department has to be replaced with an online procedure [2]. Therefore, an e-police system is being built that gathers the data of the FIR through an online FIR assistance system that transfers the information on server of the nearest police department, and then, the whole process takes place online, with information exchanged between the device and the data server. In the present scenario, most of the states like Delhi, Haryana, Tamil Nadu, Himachal Pradesh, Jharkhand, Maharashtra and Madhya Pradesh had launched E-FIR online services for the public [3]. In E-FIR services, states had launched an online portal Web site which provides the facility to the public to lodge their complaint via Internet-connected device. According to the literature survey, we found that an individual needs to create their user ID and password on the portal and login into their account to register a complaint. In this process, individual needs to scan their documents and needs to upload on the portal for the verification of identity. This is very tedious and time-consuming process. In the existing system, there are further scopes of improvement which are mentioned as follows:

- India, which has the world's second largest population, lags behind in technology. Besides, some people are not trained enough to use these services and some of them do not have those tools to use the online services [4].
- There is no security in the system as anyone can login with others' credential to lodge the FIR.
- There is no hardware model available for this type of the system.
- User must have a smartphone or laptop with good Internet connection.
- It is also not accessible to everyone.

For the betterment of the existing system, we are introducing IOT-based online FIR assistance system with two-way security using image processing in this paper. Through this system, user can easily lodge the complaint against crime. This machine is user friendly and can be operated by a common man by following certain simple steps. Once the FIR is registered, then the image captured by the camera is stored by the camera for the future reference [5]. If same person came again, then by using face detection, he/she can see their application status automatically, and they need not to verified themselves again.

## 2 FIR Registration

This system looks like an AVTM machine which can be installed in all public places for their ease of access. This IOT-based online FIR assistance system is directly connected to the nearest police station HQ database via Internet and can serve as a client for that server which can post the FIR to the database and also able to fetch the data as per the user requirement [6]. In this machine, two-way security system is implemented which avoid any individual to lodge fake complaints. The working of the machine is as follows:

- User needs to visit to the public booth to access this service and needs to verify him/herself first.
- Firstly, user needs to enter his Aadhaar Card No. for identity verification.
- After Aadhaar verification, he/she needs to verify their thumbprint for identity verification [7].
- A camera is mounted on the top of the system which will capture the image of the person and process the image.
- Image taken is processed and is been stored in the database for the future reference.
- Then, user can select the appropriate crime type and can lodge the E-FIR by typing from the keyboard input.
- After that, the FIR is sent to the nearest police station database along with the image captured during Aadhaar verification.
- User gets a successfully registered message on the mobile no. which is registered in the Aadhaar database which contains complaint number.

## 3 Methodology

### *3.1 Raspberry Pi 3 Model B+*

In this machine, Raspberry Pi 3 Model B+ acts as a heart of the system. It runs on Linux operating system and also provides a set of general-purpose input/output (GPIO) pins that allow you to control electronics components for physical computing and explore the Internet of things (IoT). The Raspberry Pi operates in the open-source ecosystem: It runs Linux and its main supported operating system, Raspbian [8].

### *3.2 Open CV*

It is an open-source computer vision library that mainly aimed at real-time computer vision. This library is used to carry out image transformations in the system. The camera is used in the system that will capture the image, and then, further process is carried out by this library. It will convert the RGB image to grayscale image and

that detect the face and crop that particular area from the image and store the image into the database. There are certain other libraries also used for image processing like numpi, dlib, etc [9].

### *3.3 Tkinter*

This is a Python library which provides us to create a simple graphical user interface (GUI) that consists of various input buttons, notification bar, menu bar and other dialog boxes which make it more easy to operate effectively. This library helps to connect the software with the hardware and also triggers the machine to perform various actions.

## 4 Face Detection and Recognition

The face is the most significant feature of the body of humans so that can represent a person's emotions [10]. Years ago, people used the non-living stuff like smart cards, plastic cards, PINS and tokens for authentication. Nose, eyes and mouth, which are related to facial extraction, are the most significant features of facial image. In this device, the image of the user will be taken and the computer vision software added to identify and recognize human faces [5]. There are many approaches to accomplish and get the most important features from facial images in face recognition. Haar cascade feature detection is the most popular algorithm for face detection [11]. OpenCV library is used for face recognition since it is the best open-source library that can be used for image processing, which is not too complex. The Haar cascade algorithm looks for particular Haar-like features of a human face. A face candidate is a rectangular segment of the original image called a sub-window. The sub-window size is usually around $24 \times 24$ pixels. The sub-window is also rotated in an attempt to get a range of different sizes of faces. Through this window, the Haar cascade algorithm scans the complete image and denotes all of the respective parts as face candidates [12]. The algorithm for face detection mainly has four phases: integral image estimation, hair-like characteristics, AdaBoost training, cascade classifier. The Haar-like algorithm's beginning step is to transform the input image into an integral image. The definition of the integral image is defined by the arrangement of the pixel values of the original images. The integral image is used to detect quick feature detection. AdaBoost is a machine learning algorithm capable of constructing a strong classifier from a weighted set of helpless classifiers [13, 14]. AdaBoost algorithm provides needless context to a good field of the stuff repercussion. A significant portion of the AdaBoost algorithm is determining the best function, threshold and polarity. Depending on the weighted error, it selects the better output function produces. The final for Viola–Jones face detection algorithm is cascade classifier phase. Cascade

**Fig. 1** System is detecting the face of the use

stage is used for speedy elimination of face candidates. In cascade classifier, the sub-window goes through various phases of filter and determines that the sub-window is a face or not. The classifier will directly reject the area if input area fails, and if it passes, then face can be detected [15].

## 5 Result and Analysis

The result of this system is analyzed and recorded. When a user is standing in front the machine, then after authentication, the camera will turn on and capture the image of the user and collect the samples and stored the same in the database. After that from the image, the face is detected by OpenCV library and crop the face from the image and stored in the database. When the next time same person came, then it will automatically start searching that user face in the database. If found successfully, then it displayed all the data and history of the user application, and user can see the application status also. The following images show the output of the system Figs. 1, 2 and 3.

The face detection system of this machine is working very fine; with the accuracy of 92%, the whole system is working efficiently. This system is very helpful for the public and also upgrades the existing system with two-way security so that no false complaint can be done. Another major important need of this system is that this will upgrade the police department and reduce their work efficiently.

## 6 Conclusion

In this paper, we have proposed a smart IoT-based online FIR system with two-way security system and upgrade the existing system with full security. In this proposed

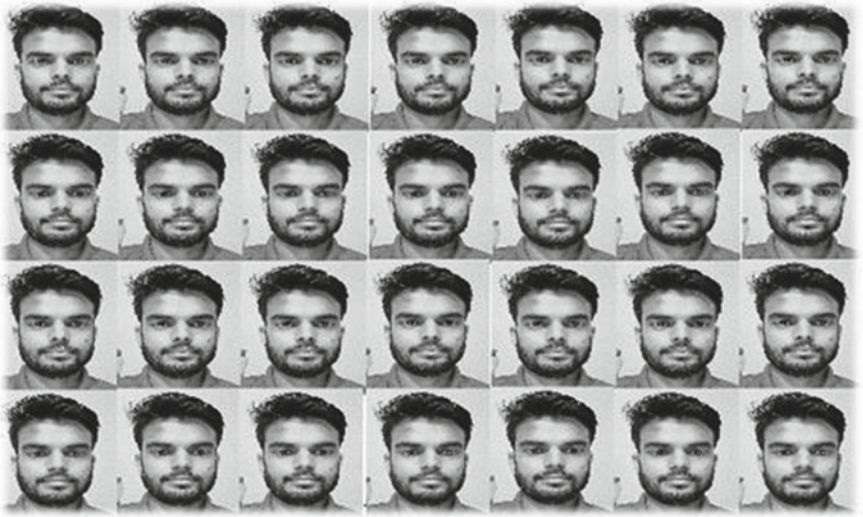

**Fig. 2** System takes up to 60 frames and converts from RGB to grayscale image and stored into the database for future reference

**Fig. 3** Image is taken by system when the same person comes next time and then compares it with the images in database

system, we have tried to overcome difficulties faced by conventional FIR system in India.

- In the proposed system, the person need not to go to the police station for filing the FIR.
- The proposed system is easily accessible like an ATM machine.
- In this proposed system, two-way security system is implemented to overcome the problem of false complaint.
- In the proposed system, Haar cascade-based image processing technique has been implied to verify the identity of the person filing the FIR utpo 92% accuracy.
- In the proposed system, all the information is saved in the cloud where a person can take a follow-up at any time.

## References


1. Othman NA, Aydin I (2017) A new IoT combined face detection of people by using computer vision for security application. IEEE
2. Khade A, Yerigeri S, Sonde K, Pillai S (2016) Onlie FIR registration system and SOS system. Int J Eng Comput Sci 5(04)
3. Bhavsar S, Deshpande SS (2019) Online FIR management system. Int J Sci Dev Res (IJSDR) 04(02)
4. Al-Ali AR, Al-Rousan M (2004) Java-based home automation system. IEEE Trans Consum Electron 50(2):498–504
5. Othman NA, Aydin I, A face recognition method in the Internet of Things for security applications in smart homes and cities. In: International Istanbul smart grids and cities congress and fair (ICSG): 2018
6. Vaidya B, Patel A, Panchal A, Mehta R, Mehta K, Vaghasiya P (2013) Smart home automation with a unique door monitoring system for old age people using Python, OpenCV, Android and Raspberry pi. In: International conference on intelligent computing and control systems ICICCS 2017.
7. Deshmukh SV, Kshirsagar UA (2017) Face detection and face recognition using Raspberry Pi. Int J Adv Res Comput Commun Eng 6(4). ISO 3297:2007 Certified
8. Suchitra, Suja P, Tripathi S (2016) Real-time emotion recognition from facial images using Raspberry Pi II. In: 2016 3rd international conference on signal processing and integrated networks (SPIN), IEEE
9. Syed Navaz AS, Dhevi Sri T, Mazumdar P (2013) Face recognition using principal component analysis and neural networks. Int J Comput Netw, Wirel Mob Commun (IJCNWMC), 3(1):245–256. ISSN 2250-1568. TJPRC Pvt. Ltd.
10. Patil A, Shukla M (2014) Implementation of classroom attendance system based on face recognition in class. Int J Adv Eng Technol
11. Gupta I, Patil V, Kadam C, Dumbre S. Face detection and recognition using Raspberry Pi. In: 2016 IEEE international WIE conference on electrical and computer engineering (WIECON-ECE) 19–21 Dec 2016, AISSMS, Pune, India
12. Lienhart R, Maydt J (2002) An extended set of Haar-like features for rapid object detection. In: Proceedings. International conference on image processing, vol. 1, 2002, pp I-900–I-903
13. Rajesh M, Rajan BK, Roy A, Almaria Thomas K. Text recognition and face detection aid for visually impaired person using Raspberry Pi. In: 2017 international conference on circuits power and computing technologies [ICCPCT], IEEE
14. Deniz O, Bueno G, Salido J, De la Torre F (2011) Face recognition using histograms of oriented gradients. Elsevier, pp 1598–1603.
15. Viola P, Jones M (2001) Rapid object detection using a boosted cascade of simple features. In: Proceedings of the 2001 IEEE computer society conference on computer vision and pattern recognition. CVPR 2001, 2001, pp I-511–I-518

# Experimental Investigation of Sound-Absorbing Material of Different Surface Shapes on Noise Reduction Performance of an Acoustic Enclosure

**Pavan Gupta and Anand Parey**

## 1 Introduction

Noise pollution of the factory and the industrial workspace is a serious concern. The environment of intense noise plays a major role in a worker's performance. The high exposure to noise not only impacts the adverse effects on psychological health but also causes hearing damage, poor voice communication, and impaired efficiency [1]. The noise generated from cutting tools during machining is one of the main sources of noise in the factory workspace such as portable saw, spindle, drilling machine [2–4]. The acoustic enclosure is one of the most important engineering designed structures for modifying the sound transmission path and suppressing the airborne noise effectively by adding sound-absorbing materials [5]. Cole et al. [6] and many other researchers [7–10] demonstrated theoretically and experimentally the effectiveness of acoustic absorbing materials on the noise reduction characteristics for the acoustic enclosure made of different materials. Recently, Cao et al. [11] and several other researchers [12–14] predicted analytically and experimentally the noise reduction capability of complex structures by incorporating the acoustic absorbing materials in the studies.

The literature survey has shown that the implementation of sound-absorbing materials has a significant role in the noise control of an enclosure and other complex structures. Airborne noise transmission can be diminished by adding the sound-absorbing material which is directly linked with the energy of the acoustic waves. The noise reduction performance of acoustic enclosure depends on many factors such

P. Gupta (✉) · A. Parey
Discipline of Mechanical Engineering, Indian Institute of Technology Indore, Indore, Madhya Pradesh 453552, India
e-mail: phd1701203006@iiti.ac.in

A. Parey
e-mail: anandp@iiti.ac.in



K. Jha et al. (eds.), *Recent Advances in Sustainable Technologies*,
Lecture Notes in Mechanical Engineering,
https://doi.org/10.1007/978-981-16-0976-3_21

as material, geometry, panel thickness, location of the source, the thickness of sound-absorbing material, and location of the implementation of acoustic material on the structure. However, it has been found that limited work is focused on the use of sound-absorbing material with different surface shapes on the acoustical performance of the cutting tool enclosure. By optimization of acoustic material properties in a defined range of frequency, it is possible to maximize the noise reduction of the structure by making use of an adequate amount of sound-absorbing material of different surface shapes. In the current study, therefore, an experimental work is presented for investigating the influence of sound-absorbing material of different surface shapes for the applications of improving the acoustic performance of the cutting tool enclosure. The polyurethane foam (PU) is considered as a sound-absorbing material in the present study. The commercially available acoustic material of three surface shapes, i.e., plane, wedge, and pyramid surfaces are chosen for the analysis.

## 2 Methodology

The acoustic enclosure performance is defined by noise reduction. The noise reduction (NR) of the acoustic enclosure is expressed in decibel (dB) as follows [15]:

$$NR = L_{\mathrm{O}} - L_{\mathrm{W}}, \tag{1}$$

where $L_{\mathrm{O}}$ is the sound pressure level from an unenclosed noise source and $L_{\mathrm{W}}$ from the enclosed noise source.

The various commercially acoustic materials used in the experimental work are shown in Fig. 1. The technical properties of acoustic material are given in Table 1.

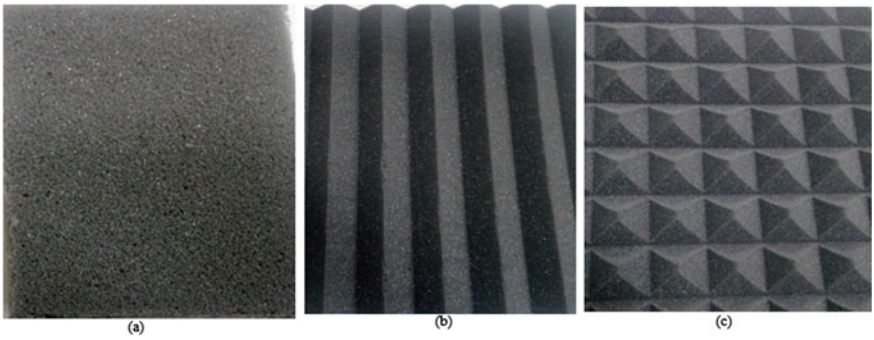


**Fig. 1** Polyurethane sound-absorbing material of various shapes **a** plane **b** wedge **c** pyramid

**Table 1** Technical properties of acoustics foams available from suppliers

| Sl. No. | Parameters | Plane shape PU foam | Wedge shape PU foam | Pyramid shape PU foam |
|---|---|---|---|---|
| 1 | Thickness (mm) | 50 | 50 | 50 |
| 2 | Bulk density ($kg/m^3$) | 32 | 32 | 32 |
| 3 | Bulk Poisson's ratio | 0.39 | 0.39 | 0.39 |

**Table 2** Different conditions of noise measurement

| Condition | Noise measurement condition details |
|---|---|
| Case-1 | Enclosed source |
| Case-2 | Enclosed source by adding plane shape PU foam |
| Case-3 | Enclosed source by adding wedge shape PU foam |
| Case-4 | Enclosed source by adding pyramid shape PU foam |

The initial noise level of the noise sources was measured without an enclosure to have a reference value for comparison purposes. Thereafter, all the iterations have been implemented as per Table 2.

## 3 Experimental Work

The noise measurement was conducted in a large volume of noise and vibration control laboratory at IIT Indore.

An enclosure made of steel material was employed in the experimental work which consisted of five flexible panels welded together. The enclosure has dimensions of 1 m $\times$ 0.8 m $\times$ 1 m, and the thickness of each panel was 1.15 mm. The polyurethane foam of different shapes was used in the study. Four piezotronics microphones (PCB made) were employed around the enclosure. The sound pressure level (SPL) measurement is taken at a distance of 1 m for each surface of the enclosure. The spatial mean average value of the sound pressure level was taken. The measurement data was acquired using the 16 channel LMS data acquisition system in the range of frequency between 63 and 8000 Hz of 1/3 octave band.

Noise radiated by the cutting tools is the prime cause of noise pollution in the factory environment. In the present study, therefore, hand-held circular saw of model GKS 7000 with a rated power input of 1100 W is considered as a noise source for the experimental work which is shown in Fig. 2. The sound pressure level value of the noise source is measured to be 88.75 dB(A). The background noise was measured to be 45 dB(A) which is far lesser than the sound pressure level of the noise source. Therefore, background noise has a negligible influence on the noise measurement


**Fig. 2** Noise source: handheld circular saw

of the source. All the measurements were repeated for ensuring the reliability of measurement.

The measurement set-up and schematic diagrams for the implementation of PU foam are shown in Figs. 3 and 4, respectively.

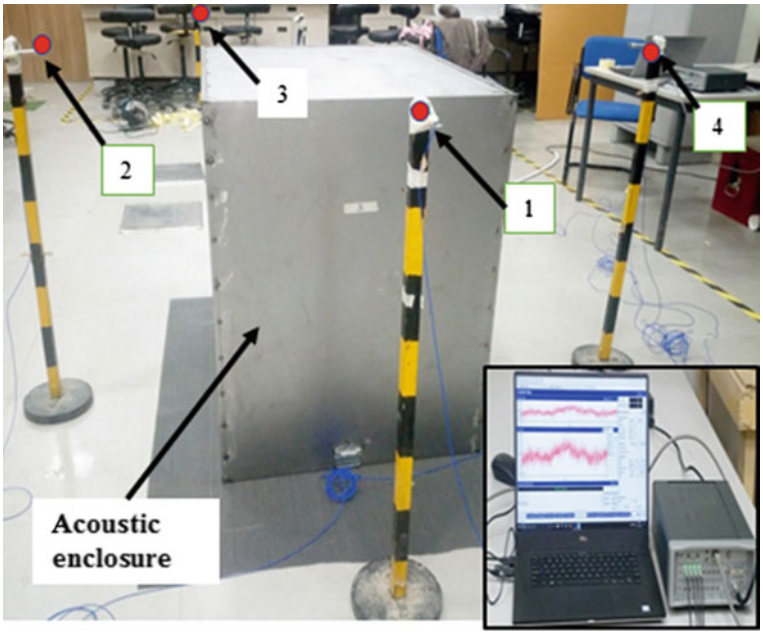


**Fig. 3** Experimental set-up using microphones (1–4) with LMS data acquisition system and noise source inside the enclosure

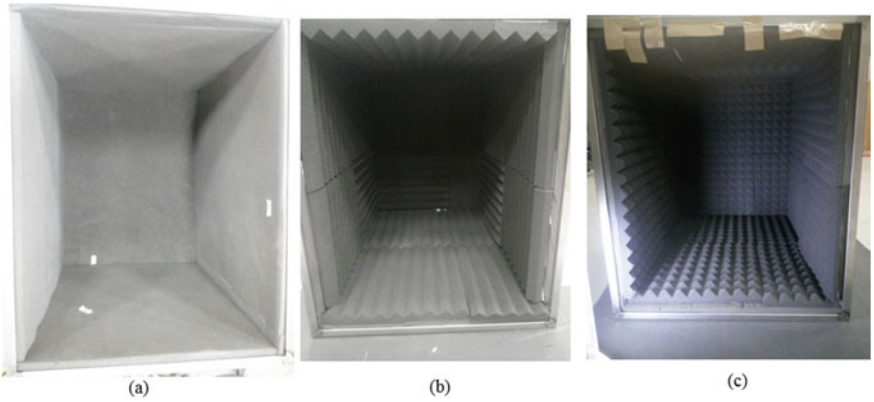


**Fig. 4** Schematic diagrams for the implementation of PU foam: **a** Enclosed source by adding plane shape PU foam, **b** enclosed source by adding wedge shape PU foam, **c** enclosed source by adding pyramid shape PU foam

## 4 Results and Discussion

The overall SPL values in various cases of the measurement are shown in Fig. 5. It is observed from Fig. 5 that adding the sound-absorbing PU foam inside the enclosure reduces the noise-level efficiently. The acoustic materials not only suppress the acoustic resonance inside the enclosure but also demise the magnitude of standing waves with an increment of the frequencies of the resonance of the standing wave. It can be seen from Fig. 5 that surface shapes of the acoustic material inside the enclosure directly influence the acoustical performance of the enclosure. The overall value of SPL for the noise source was observed is 88.75 dB(A) which is maximum. The minimum SPL is achieved in the case of using pyramid shape PU foam which is 65 dB(A).

The noise reduction for various conditions is shown in Fig. 6. It is found that adding a pyramid shape PU foam inside the acoustic enclosure causes a larger noise attenuation of 23.75 dB(A).

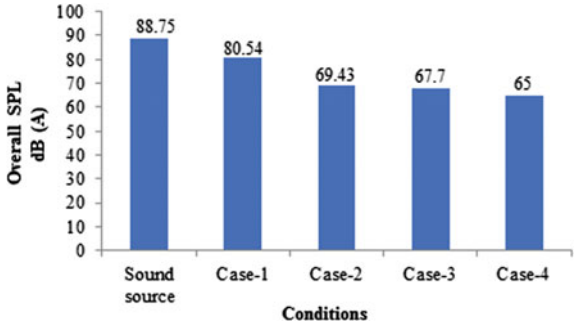


**Fig. 5** Overall sound pressure level values of various measurement conditions

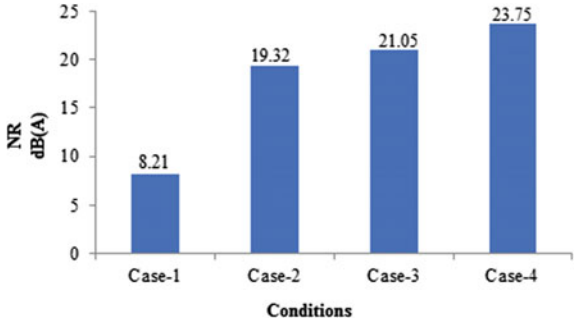


**Fig. 6** Noise reduction values of various measurement conditions

It can be observed directly from Fig. 6 that the plane shape and wedge shape PU foams cause a noise reduction of 19.32 dB(A) and 21.05 dB(A), respectively.

The 1/3 octave analysis is carried out to study the effect of various shapes of acoustic material in the different frequency bands [6, 12]. The 1/3 octave analysis shows that wedge shape and pyramid shape acoustic materials have an overall better effect in comparison to plane PU foam in the entire frequency region as shown in Fig. 7. One-third octave band analysis shows that the wedge and pyramid shape PU foams have a similar effect in the frequency range between 500 and 2000 Hz. The pyramid shape PU foam is very efficient in the high-frequency region between 2000 and 8000 Hz. It is clear from the experimental results that the pyramid shape PU foam is very effective for improving the acoustic performance of the enclosure.

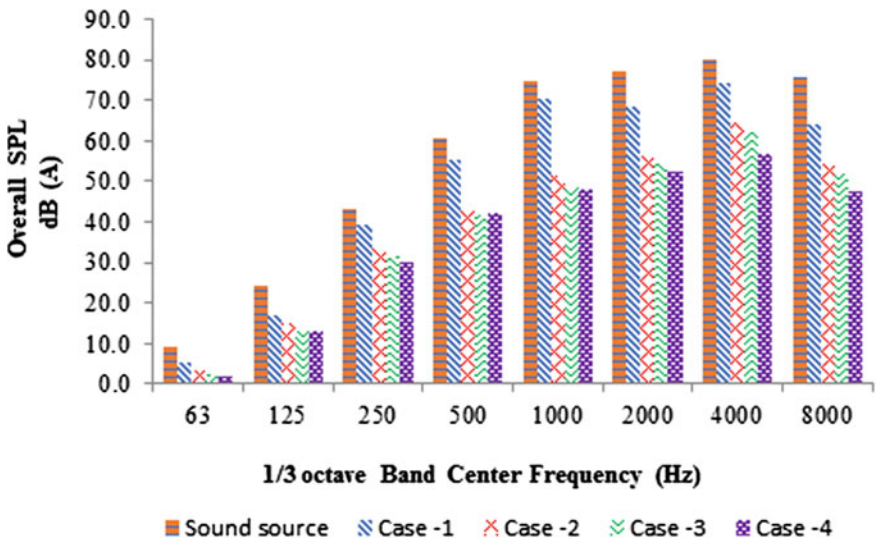


**Fig. 7** Overall sound pressure level values at the center frequency of 1/3 octave band

## 5 Conclusion

Noise control of the factory workspace is a serious issue. The noise generated from cutting tools during machining is one of the main sources of noise in the factory workspace such as portable saw, spindle, drilling machine. The surroundings of intense noise radiated from the cutting tool and machining operations impact directly on the worker's performance. Therefore, an appropriate design of the cutting tool enclosure using sound-absorbing material is imperative from the acoustical point of view.

In the present paper, an experimental study in the laboratory was carried out for investigating the effect of various shape acoustic materials on the noise reduction efficiency of an enclosure for cutting tools applications. The noise source was considered as a handheld saw. The various conditions have been considered for the measurement by using the different shapes of sound-absorbing polyurethane foam. Therefore, commercially available acoustic material of three surface shapes, i.e., plane, wedge, and pyramid surfaces, are chosen for the analysis. It is found from the experimental results that surface shapes of the acoustic material influence the acoustical performance of the enclosure greatly. The experimental result shows that a larger noise reduction of about 23.75 dB(A) is achieved for the case of using pyramid shape PU foam. The 1/3 octave analysis is also carried out to study the effect of various shapes of acoustic material in the different frequency bands. The 1/3 octave analysis shows that wedge shape and pyramid shape acoustic materials have a better effect on the acoustic performance of enclosure in comparison to plane PU foam in the entire frequency region. The pyramid shape PU foam is very efficient in the high-frequency region between 2000 and 8000 Hz. Therefore, it can be concluded from the experimental results that the pyramid shape PU foam is very effective for improving the acoustic performance of the enclosure. The present experimental study demonstrates that the implementation of sound-absorbing material of different surface shapes would be an appropriate method for improving the acoustical performance of the enclosure.

## References

1. Lazarus H, Sehrndt GA, Jacques J (1992) European standards for occupational and machinery noise control. Saf Sci 15:375–386. https://doi.org/10.1016/0925-7535(92)90026-V
2. Barbosa AAR, Bertoli SR (2017) Noise generated by portable saw in different construction materials. Am J Civ Eng Archit 5:17–24. https://doi.org/10.12691/ajcea-5-1-3
3. Cao H, Kang T, Chen X (2019) Noise analysis and sources identification in machine tool spindles. CIRP J Manuf Sci Technol 25:26–35. https://doi.org/10.1016/j.cirpj.2019.04.001
4. Licow R, Chuchala D, Deja M, Orlowski KA, Taube P (2020) Effect of pine impregnation and feed speed on sound level and cutting power in wood sawing. J Clean Prod 272:122833. https://doi.org/10.1016/j.jclepro.2020.122833
5. Tandon N, Nakra BC, Ubhe DR, Killa NK (1998) Noise control of engine driven portable generator set. Appl Acoust 55:307–328. https://doi.org/10.1016/S0003-682X(98)00004-8

6. Cole V, Crocker MJ, Raju PK (1983) Theoretical and experimental studies of the noise reduction of an idealized cabin enclosure. Noise Control Eng J 20:122–132. https://doi.org/10.3397/1.2827608
7. Oldham DJ, Hillarby SN (1991) The acoustical performance of small close fitting enclosures, part 1: theoretical models. J Sound Vib 150:261–281
8. Oldham DJ, Hillarby SN (1991) The acoustical performance of small close fitting enclosures, part 2: experimental investigation. J Sound Vib 150:283–300
9. Ming R, Pan J (2004) Insertion loss of an acoustic enclosure. J Acoust Soc Am 116:3453–3459. https://doi.org/10.1121/1.1819377
10. Osman TA (2003) Design charts for the selection of acoustical enclosures for diesel engine generator sets. Proc Inst Mech Eng Part A J Power Energy. 217:329–336. https://doi.org/10.1243/095765003322066556.
11. Cao L, Fu Q, Si Y, Ding B, Yu J (2018) Porous materials for sound absorption. Compos Commun 10:25–35. https://doi.org/10.1016/j.coco.2018.05.001
12. Bolton JS, Shiau NM, Kang YJ (1996) Sound transmission through multi-panel structures lined with elastic porous materials. J Sound Vib 191:317–347. https://doi.org/10.1006/jsvi.1996.0125
13. Panneton R, Atalla N (1996) Numerical prediction of sound transmission through finite multilayer systems with poroelastic materials. J Acoust Soc Am 100:346–354. https://doi.org/10.1121/1.415956
14. Atalla N (2014) Modeling the sound transmission through complex structures with attached noise control materials. Wave Motion 51:650–663. https://doi.org/10.1016/j.wavemoti.2013.11.001
15. Kim HS, Kim JS, Lee SH, Seo YH (2014) A simple formula for insertion loss prediction of large acoustical enclosures using statistical energy analysis method. Int J Nav Archit Ocean Eng 6:894–903. https://doi.org/10.2478/IJNAOE-2013-0220

# A Comparative Numerical Study of Transient Thermal Behaviour of Water-Cooled Metallic Plates


**Sunil Kumar, Gurdyal Singh, Gaurav Jain, and Sachin Bhogal**

## 1 Introduction

Steels and aluminium alloys are widely used materials in mechanical industries due to their excellent mechanical, physical, and chemical characteristics. The major applications of these materials as thick plates are in agriculture machinery and underwater machine parts. Welded submarine structures and pressure vessels are fabricated using thick metallic plates. In the recent past, thermal simulation of metallic plates has been performed by the investigators to study the heat transfer response under variable ambient conditions [1–4]. Both theoretical and experimental observations are recorded and compared [5–8]. The present study deals will the transient thermal response of thick metallic plates.

Transient heat transfer behaviour between flat metallic plates was analysed numerically considering uniform wall temperature [9]. The transient cooling of metallic plate from 400 to 100 °C with water jet was studied by Kumagai et al. [10]. The temperature at plate–water interface was found to be high near stagnation line with high jet sub-cooling. Combined convection and radiation heat transfer of nano-fluids flowing between parallel plates was studied by Narahari et al. [11]. The analysis was performed to obtain the exact solution for temperature, velocity and Nusselt number.

Transient thermal analysis of laser welding of SS 304 thin plates was performed by Pankaj et al. [12] and observed that the transient cooling was influenced by welding speed and laser power. Water jet cooling of stainless steel plates was performed by Aamir et al. [13] to obtain high heat transfer rate. Influence of plate thickness on heat transfer rate, cooling time and convection co-efficient was studied at constant

S. Kumar · G. Singh (✉) · G. Jain
Chitkara University Institute of Engineering and Technology, Chitkara University, Punjab, India
e-mail: gurdyal.singh@chitkara.edu.in

S. Bhogal
Chitkara College of Hospitality Management, Chitkara University, Punjab, India



K. Jha et al. (eds.), *Recent Advances in Sustainable Technologies*,
Lecture Notes in Mechanical Engineering,
https://doi.org/10.1007/978-981-16-0976-3_22

flow rate. Correlation was developed between plate thickness and spray dynamics. Aamir et al. [14] performed evaporative cooling using water spray to improve the heat transfer rate for different geometries of steel. Boiling number for smooth plate was observed to be low as compared to narrow fin and wide square fin geometry. Fast increase in convection co-efficient was observed in nucleate boiling regime. Increase in cooling rate, burnout point and critical heat flux point was observed for wide square fin compared to other geometries.

Transient cooling behaviour of aluminium plate from 137 to 37 °C was analysed experimentally and the correlation for Nusselt number was developed. The results were compared with modelled results [15]. Numerical analysis of aluminium alloy welding was conducted by Riahi and Nazari [16]. Das et al. [17] analysed the thermal behaviour of aluminium 6061 plates during friction stir welding considering heat generation into account. Bajpei et al. [18] analysed the transient thermal response of aluminium 6061-T6 and aluminium 5052-H32 plates using ANSYS software. High temperature and low residual stresses were observed for aluminium 5052-H32 plate as compared to aluminium 6061-T6. Owadano et al. [19] performed the heat transfer cooling simulation of aluminium plate, round bar and sphere using 'Decimal Basic' software. The temperature difference between the surface and centre during cooling was found to be the product of surface temperature and half of the Biot number. The temperature distribution was observed as parabolic with negative curvature at centre.

The present analysis focuses on the time-dependent thermal behaviour of thick metallic plates. Water is used as a cooling medium. The plates of SS 316 (austenitic stainless steel) and aluminium 6061 are considered for present thermal investigation. Transient simulation has been performed to show the temperature distribution in these metallic plates. LISA software is used for finite element analysis.

## 2 Problem Formulation

In the transient heat transfer of metallic plates, the temperature varies with time and space. It is assumed that the heat transfer is in one direction only, i.e., through the plate thickness. One-dimensional transient heat transfer case can be expressed as Eq. 1 [5];

$$T = f(x, t) \tag{1}$$

Plate length, width and thickness ($L$) are considered as 1 m, 0.6 m and 0.2 m, respectively. The non-dimensional temperature at mid-plane can be expressed as Eq. 2 [5];

$$\frac{T_t - T_a}{T_o - T_a} = e^{-(mt)} \tag{2}$$

In this equation, $(T_t)$ is the temperature at time $(t)$, $(T_a)$ is the temperature of cooling water, $(T_o)$ is the initial temperature and the reciprocal of time constant $(m)$ can be written as Eq. 3 [5].

$$m = \frac{h}{\rho C_p (L/2)} \text{ s}^{-1} \tag{3}$$

For both plates, the values of $(T_a)$ and $(T_o)$ are considered as 20 °C and 300 °C, respectively. Convective heat transfer co-efficient of water is taken as 500 W/m$^2$K. For steel plate, thermal conductivity $(k) = 15$ W/mK, density $(\rho) = 8000$ kg/m$^3$ and $(C_p) = 500$ J/kgK. For aluminium plate, thermal conductivity (k) = 202 W/mK, density $(\rho) = 2707$ kg/m$^3$ and $(C_p) = 897$ J/kgK. During analysis using LISA 8.0.0, the heat flow domain is discretised into 4-noded 32 elements having total 45 nodes. At the extreme end, the heat flux through convection and conduction is taken as equal. Initially, whole plate is at uniform temperature. Both materials are assumed to be isotropic. Total cooling time is selected as 10 min.

## 3 Results and Discussion

Finite element analysis software LISA 8.0.0 has been used in present transient heat transfer study. The numerical results are checked for the accuracy using analytic approach (Eqs. 1–3). The approximation of simulated results is found to be in close agreement with analytic approach.

The simulated results for the temperature distribution in the SS 316 plate are shown in Fig. 1. The values of temperature are written in °C and time in seconds. It has been shown that during this 10 min cooling process, the minimum temperature will be 107.1 °C. Table 1 shows values of temperature at mid-section and extreme end during the time interval of 60 s for SS 316 plate.

The simulated results for heat flux in the SS 316 plate are shown in Fig. 2. The values of heat flux are written in W/m$^2$ and time in seconds. It has been shown that during cooling process, the maximum heat flux will be attained as $4.198 \times 10^4$ W/m$^2$ at extreme end and minimum as 4664 W/m$^2$ at the mid-section. Heat flows from the mid-section towards extreme end in X-direction.

The simulated results for temperature distribution in the aluminium 6061 plate are shown in Fig. 3. The values of temperature are written in °C and time = 480 s (8 min). It has been shown that during this 10 min cooling process, the minimum temperature will be 102.5 °C.

Table 2 shows values of temperature at mid-section and extreme end during the time interval of 60 s for aluminium 6061 plate.

The simulated results for heat flux in the aluminium 6061 plate are shown in Fig. 4. The values of heat flux are written in W/m$^2$ and time in seconds. It has been shown that during cooling process, the maximum heat flux will be attained as $9.119 \times 10^4$ W/m$^2$ at extreme end and minimum as $1.013 \times 10^4$ W/m$^2$ at mid-section.

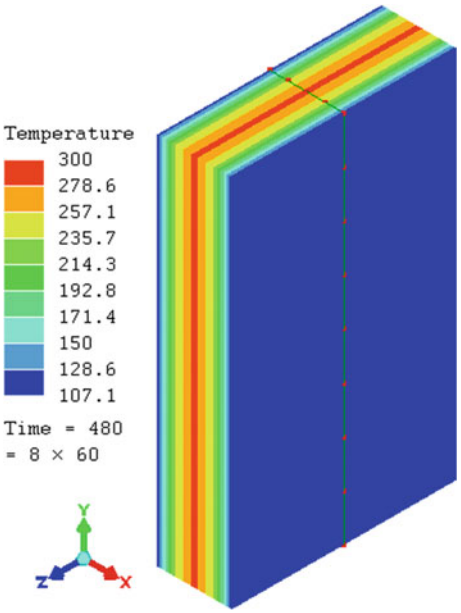


**Fig. 1** Modelling of steel plate (Temperature in °C)

**Table 1** Temperature distribution for SS 316 plate

| Time (min) | Temperature at mid-section (°C) | Temperature at extreme end (°C) |
|---|---|---|
| 0 | 300 | 300 |
| 1 | 298.5 | 200.9 |
| 2 | 296.6 | 168.3 |
| 3 | 294.2 | 150.4 |
| 4 | 292.6 | 138.5 |
| 5 | 291.3 | 130.1 |
| 6 | 289.8 | 123.7 |
| 7 | 287.1 | 118.6 |
| 8 | 284 | 114.3 |
| 9 | 277.6 | 110.6 |
| 10 | 269.2 | 107.1 |

The cooling effect of both metallic plates is compared and shown in Fig. 5. It is clear that aluminium 6061 is more thermal effective compared to SS316 when used as a thick plate. The temperature at extreme end is almost same for both metallic plates during cooling process. But, at the mid-section, the cooling of aluminium 6061 is found to be very fast compared to SS 316. At extreme end, there is a gradual cooling in case of aluminium alloy but for stainless steel, the cooling rate is very fast initially at the plate surface and its intensity decreases afterwards. For austenitic

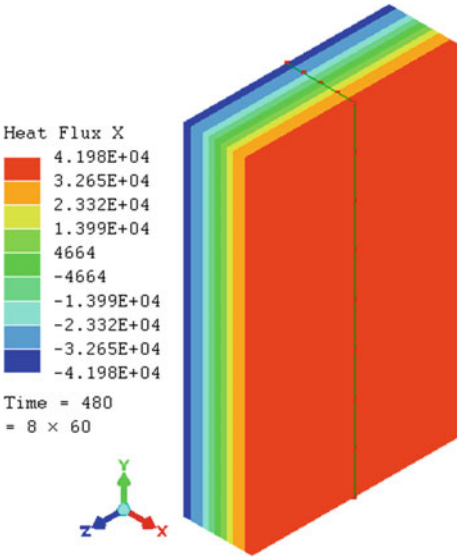


**Fig. 2** Modelling of steel plate (Heat flux in W/m$^2$)

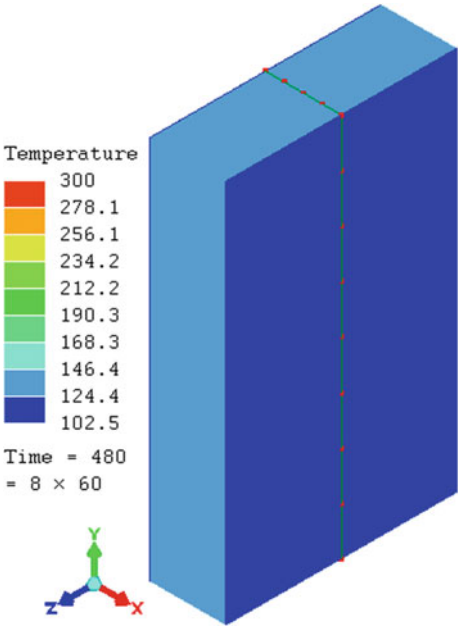


**Fig. 3** Modelling of aluminium plate (Temperature in °C)

**Table 2** Temperature distribution for aluminium 6061 plate

| Time (min) | Temperature at mid-section (°C) | Temperature at extreme end (°C) |
|---|---|---|
| 0 | 300 | 300 |
| 1 | 280.4 | 251.3 |
| 2 | 252.2 | 226.2 |
| 3 | 227.1 | 203.4 |
| 4 | 204.7 | 184 |
| 5 | 184.7 | 166.3 |
| 6 | 166.9 | 150.4 |
| 7 | 151 | 136.3 |
| 8 | 136.8 | 123.7 |
| 9 | 124.1 | 112.5 |
| 10 | 112.9 | 102.5 |

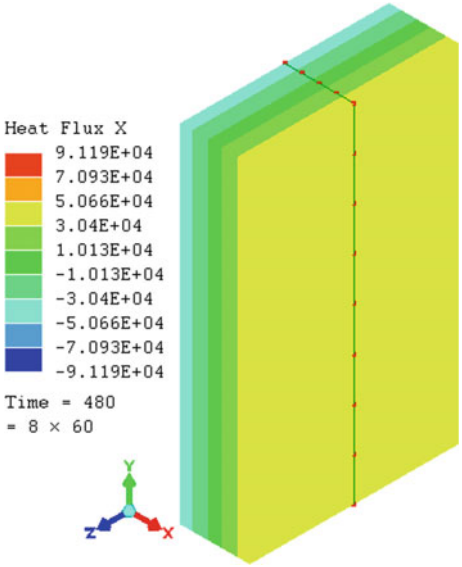


**Fig. 4** Modelling of aluminium plate (Heat flux in W/m$^2$)

stainless steel, the thermal cooling behaviour is not appreciable at the mid-section of the plate due to its more heat storage capacity and low thermal diffusivity compared to aluminium alloy.

Finally, it can be observed from the transient thermal analysis that one should look for aluminium alloy if more heat is required to release. Results shows that the heat flux is high for aluminium 6061 compared to SS 316. Aluminium alloys are preferred over stainless steels in such situations where low weight requirement is the main concern. Both these materials are best for the water-based applications due to high corrosiveness and good strength.

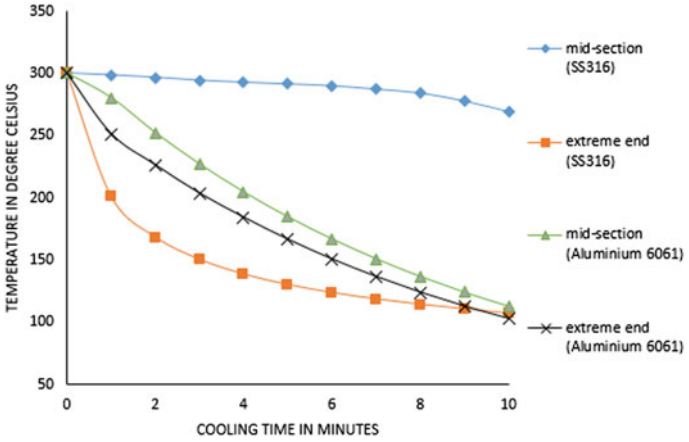


**Fig. 5** Comparison curves for temperature verses cooling time

## 4 Conclusion

Comparative study for transient thermal behaviour of metallic plates has been conducted in present work. It has been concluded that the aluminium 6061 plate shows more fruitful results compared to SS 316 when subjected to cooling. By using finite element analysis software, much computational time has been saved to achieve the results. The values of heat flux are observed to be high for aluminium 6061 compared to SS 316. All the materials should be analysed numerically, analytically and experimentally before using them in specific application where heat transfer phenomenon is involved.

## References

1. Liu L, Xie G, Wang Y, Chu J, Wang Q (2012) Optimizing accelerated cooling processes of thick plates by using numerical simulation. Mater Manuf Processes 28(1):56–60
2. Kotresha B, Gnanasekaran N (2019) Numerical simulations of fluid flow and heat transfer through aluminum and copper metal foam heat exchanger—a comparative study. Heat Transfer Eng 41(6–7):637–649
3. Kerme ED, Fung AS (2020) Transient heat transfer simulation, analysis and thermal performance study of double U-tube borehole heat exchanger based on numerical heat transfer model. Appl Thermal Eng, 115189
4. Akpan P, Njiofor T (2014) Transient simulation of a metal cooling process. J Energy Technol Policy 4(2):13–21
5. Roncati D (2013) Iterative calculation of the heat transfer coefficient, pp 1–9. Retrieved from https://mafiadoc.com/iterative-calculation-of-the-heat-transfer-coefficient-lisa-fea_5ba79e6d097c470b5d8b47e0.html

6. XiongC MB, Li H, Zhang F, Wang Y (2015) Modeling and analysis of transient temperature field in finite thickness plate under symmetrically located moving heat sources. Adv Mech Eng 7(11):1687814015619554
7. Poirier DR, Geiger G (eds) (2016) Transport phenomena in materials processing. Springer
8. Chiba R (2018) An analytical solution for transient heat conduction in a composite slab with time-dependent heat transfer coefficient. Math Probl Eng. https://doi.org/10.1155/2018/4707860
9. Joshi HM (1988) Transient effects in natural convection cooling of vertical parallel plates. Int Commun Heat Mass Transfer 15(2):227–238
10. Kumagai S, Suzuki S, Kubo R, Kawazoe M (1995) Transient cooling of a hot metal plate with an impinging water jet. Heat Transf-Jpn Res 24(6). https://doi.org/10.1299/kikaib.61.3749
11. Narahari M, Alaparthi N, Pop I (2017) Exact analysis of the transient free convection flow of nanofluids between two vertical parallel plates in the presence of radiation. Canad J Chem Eng 95(11):2186–2198
12. Pankaj P, Tiwari A, Biswas P (2019) Transient thermal analysis of $CO_2$ laser welding of AISI 304 stainless steel thin plates. In: Manufacturing engineering. Springer, Singapore, pp 49–65
13. Aamir M, Qiang L, Xun Z, Wang H, Ullah R (2016) Study on ultra-fast cooling behaviors of water spray cooled stainless steel plates. Exp Heat Transf 29(3):299–321
14. Aamir M, Qiang L, Hong W, Xun Z, Wang J, Sajid M (2017) Transient heat transfer performance of stainless steel structured surfaces combined with air-water spray evaporative cooling at high temperature scenarios. Appl Therm Eng 115:418–434
15. Venugopal G, Balaji C, Venkateshan SP (2008) A correlation for laminar mixed convection from vertical plates using transient experiments. Heat Mass Transf 44(12):1417
16. Riahi M, Nazari H (2011) Analysis of transient temperature and residual thermal stresses in friction stir welding of aluminum alloy 6061–T6 via numerical simulation. Int J Adv Manuf Technol 55(1–4):143–152
17. Das NK, Kadian AK, Tiwari A, Pankaj P, Biswas P (2019) Transient thermal analysis on friction stir welding of AA6061. In: Manufacturing engineering. Springer, Singapore, pp 67–82
18. Bajpei T, Chelladurai H, Ansari MZ (2016) Numerical investigation of transient temperature and residual stresses in thin dissimilar aluminium alloy plates. Procedia Manuf 5:558–567
19. Owadano T (2018) Cooling of aluminumplate, cylinder and sphere induced by heat transfer. J Jpn Inst Met Mater 82(6):183–187

# Comparative Analysis of Tensile Strength for Corroded and Un-corroded Friction Stir Processed Aluminum Alloy Surface Composites


**A. Nihal, Piyush Gulati, Jaiinder Preet Singh, Manpreet Singh, Rajeev Kumar, and Harpinder Singh**

## 1 Introduction

Finding a material with particular properties is a standout among the most imperative issues in numerous mechanical applications, particularly in the aviation and transportation ventures. So there is a need of outlining material with the specific properties. High strength combined with high ductility is conceivable with materials having fine and homogenous grain structures. Be that as it may, there are numerous restrictions regarding expense and time of generation with traditional preparing methods such as rock well, powder metallurgy processes and hot rolling which contains thermo-mechanical processing and high energy laser-melt treatment, high energy electron beam irradiation, plasma spraying, cast sinter and casting which requires high energy consumptions and time consuming. But in these above-mentioned processes, the material is subjected to liquid phase at extremely high temperature due to which interfacial reaction takes place between the metal matrix and reinforcement, and also, there is formation of some detrimental phases which results into poor microstructure of the surface layer.

In order to avoid that problem, a new technique was introduced in which the processing takes place at temperature below melting point of the material and the process was termed as friction stir processing (FSP) due to which solidified microstructure is obtained in the surface layer [1, 2]. Friction stir processing (FSP) uses the same procedure of friction stir welding (FSW), whereas FSP is for modifying the local microstructures and FSW is for combining materials together permanently. FSP modifies the internal material structure through severe, localized plastic deformation resulting in desired mechanical properties. FSP is a multipurpose

A. Nihal · P. Gulati (✉) · J. P. Singh · M. Singh · R. Kumar · H. Singh
School of Mechanical Engineering, Lovely Professional University, Phagwara, Punjab 144411, India
e-mail: piyush.14775@lpu.co.in



K. Jha et al. (eds.), *Recent Advances in Sustainable Technologies*,
Lecture Notes in Mechanical Engineering,
https://doi.org/10.1007/978-981-16-0976-3_23

method, because it has extensive applications like processing, fabrication and materials synthesis [3]. Required specific properties can be achieved by choosing proper reinforcements in FSP. Since its development by Mishra et al. [3], several authors have explored FSP as a technique for the development of surface composites. Wang et al. [4] developed SiCp reinforced aluminum matrix composites and had observed excellent bonding between the inserted particles and the base material.

Aluminum, the second most abundant metallic component on earth, turned into a monetary rival in engineering applications as of late as the end of the nineteenth century. Even though aluminum compounds came after steel and copper, however because of exceptional combination of certain mechanical properties, they have turned into the most generally utilized nonferrous metal [5]. High quality aluminum AA7075 (Al–Zn–Mg–Cu) is a precipitate hardenable alloy generally utilized as a part of the aviation, marine and vehicle ventures [6].

The aluminum alloy AA7075 has great mechanical properties yet it is prone to corrosion due to large number of intermetallic particles, which are either developed purposely to improve the mechanical properties or are present as impurities that can lead to localized corrosion, i.e., pitting and intergranular attack which will unfavorably impact its mechanical properties [7, 8]. In order to increase corrosion resistance of the alloy, many surface protection methods have been applied [9]. However, these protecting methods have not significantly reduced the corrosion problems without affecting the other properties of the alloy. Therefore, in the present work, focus is to investigate the tensile strength of AA7075 surface composite with $B_4C$ particles as reinforcement without compromising its corrosion resistance.

## 2 Experimentation

FSP process carried out on TAL V—350 vertical machining center, which is easy, efficient and controllable as it is a computer controlled machine. The friction stir processing setup is shown in Fig. 1. Investigation of tensile strength of FSPed aluminum alloy reinforced composites in a corrosive environment was accomplished with a several series of processes. Corrosion on the samples was carried out by using sodium hydroxide solution, as represented in Fig. 3, which is highly corrosive and alkaline in nature. The tools used for FSP and capping are represented in Fig. 2.

Aluminum 7075 with 5 mm thickness sheet was used as our plate and $B_4C$ powders were used as reinforcement. Distinctive type of processing will be held by certain proportion of $B_4C$, tool pass and parameters. For dispersal of $B_4C$, a small groove of 1.5 mm wide and 2 mm depth was provided on aluminum sheet. After filling the groove with $B_4C$, a pass of pin less tool as shown in Fig. 2 was carried out in order to close the groove known as capping. Capping is to avoid spattering of $B_4C$ away from groove during processing. Further processing with pin and shoulder tool was completed. In order to achieve a defect free FSP, the input parameters viz: rotational speed and the transverse speed of the tool need to be carefully selected. During processing, the temperature range of the material around the tool is locally

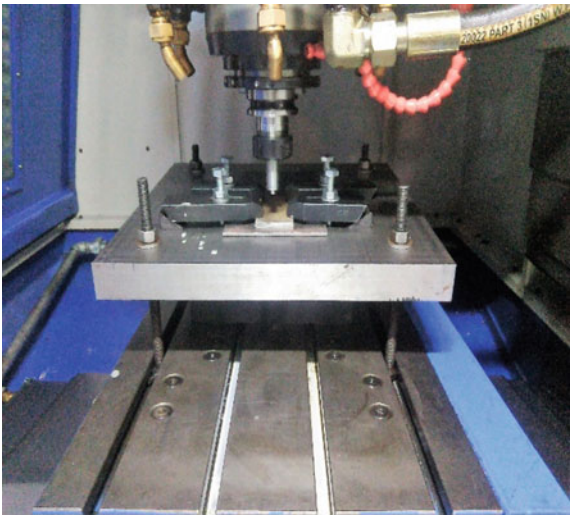

**Fig. 1** Friction stir processing setup

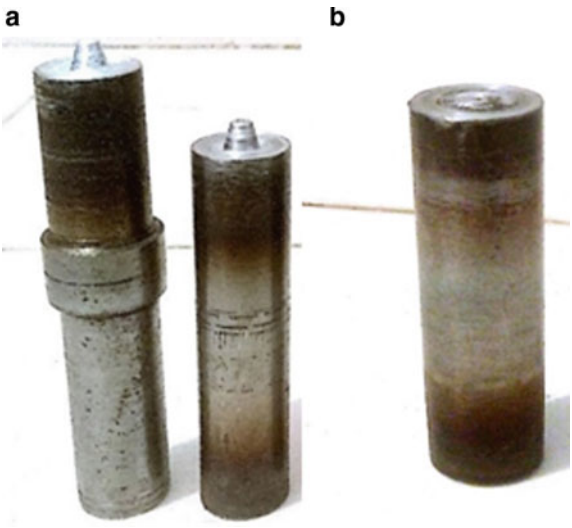


**Fig. 2** Tool used for present work, **a** for processing, **b** for capping

**Fig. 3** Corrosion setup used in present work

**Table 1** Finalized processing parameters

| S. No. | Processing | Traverse speed (mm/min) | Rotational speed (rpm) |
|---|---|---|---|
| 1 | None (base) | None | None |
| 2 | | | 1400 |
| 3 | | 30 | 1500 |
| 4 | Yes | | 1600 |
| 5 | With boron | | 1400 |
| 6 | Carbide | 40 | 1500 |
| 7 | | | 1600 |
| 8 | | | 1400 |
| 9 | | 50 | 1500 |
| 10 | | | 1600 |
| 11 | | | 1400 |
| 12 | Yes | 30 | 1500 |
| 13 | | | 1600 |

raised to a level in which severe plastic deformation can readily occur and simultaneously minimizing the forces acting on the tool. In general, the heat input increases with higher rotation speed or decreasing transverse speed. The finalized processing parameters after a series of trials are represented in Table 1.

For friction stir processing, there is a need to outline a reasonable and precise tool. H13 steel molybdenum-chromium hot work steel was utilized as tool due to properties like good hot hardness, thermal fatigue cracking resistance and toughness will reduce those effects made us to choose H13 as our tool material. Tool consists of shoulder and tapered pin. Taperness is provided in order to reduce stress concentration else there is a change of breakage of pin. A small concavity also provides to the tool shoulder that results in reduction of chips out.

All specimens of tensile test were kept in alkaline solution for 8 h (until reaction complete) as shown in Fig. 4 and kept in atmosphere for drying.

## 3 Results and Discussion

### *3.1 Tensile Test*

Tensile test was conducted on all the FSPed specimens to measure ultimate tensile strength (UTS) for corroded as well as non-corroded specimens. There is a need to know the impact of corrosion on tensile strength for different parameter so from each plate, two specimens were taken for tensile tasting as shown in Table 1. From each

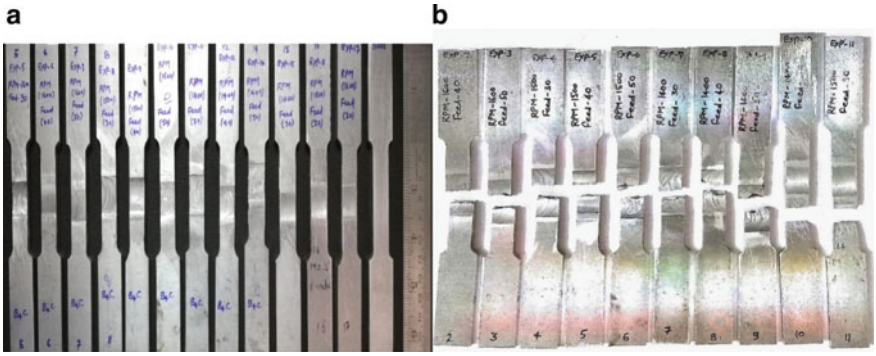


**Fig. 4** Non-corroded tensile specimens: **a** before test, **b** after test

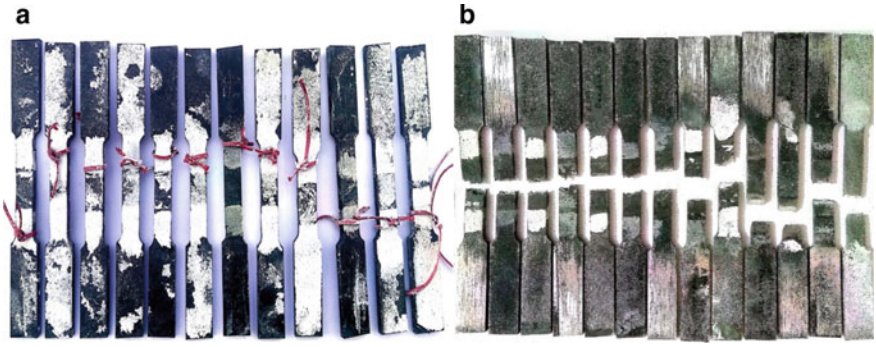


**Fig. 5** Corroded tensile specimens: **a** before test, **b** after test

plate, one specimen is corroded another left un-corroded and subjected to tensile testing.

Figure 5 shows corroded tensile specimens before and after fracture. White powder coating present on specimen is aluminum oxide film produced as a result of corrosion. Tensile results as shown in Fig. 6 reveal that by increasing rpm, there is a decrement in tensile strength as a result of increase in grain size by increase in temperature. If the temperature is below crystallization temperature, then there will be strain hardening and dislocation of grains resulting in improvement of tensile strength; this can occur by using low rpm and high traverse speed rate. But here due to high rotational and traverse speed, heat is more that soften material by grain growth and refining of dislocation by recrystallization resulting in decrease in UTS. The UTS of specimens processed without particles also having the same phenomenon, whereas it has high UTS than processed with $B_4C$ particles. It was observed that UTS of processed zone without particle was more than the given value because breakage occurred away from the processed zone as seen in Figs. 4 and 5 which means processed zone has

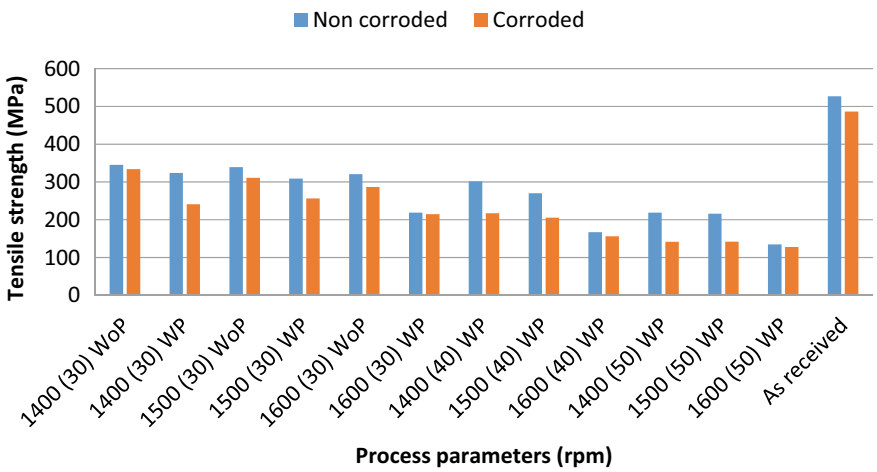


**Fig. 6** Tensile strength of non-corroded and corroded specimen

more strength than the broken zone. From the result, 1400 rpm at 30 traverse speed without particles has the better tensile strength.

## *3.2 Impact of Corrosion on Tensile Strength*

By choosing proper parameters, effect of corrosion can be reduced. So for knowing that reduction in UTS of corroded sample with respect to non-corroded samples is calculated by taking difference of both samples at same parameters as shown in Fig. 7.

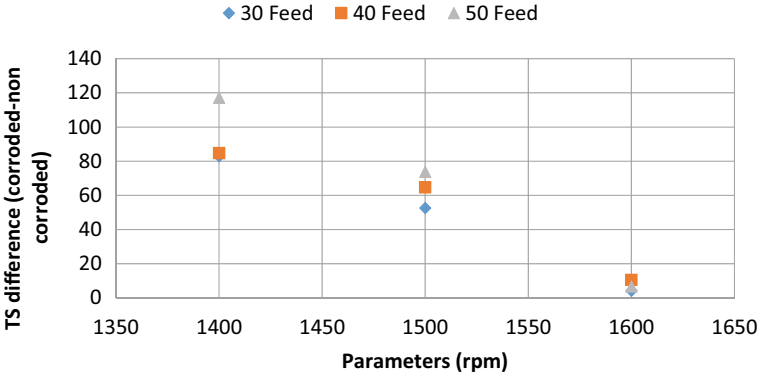


**Fig. 7** Tensile strength in corroded samples

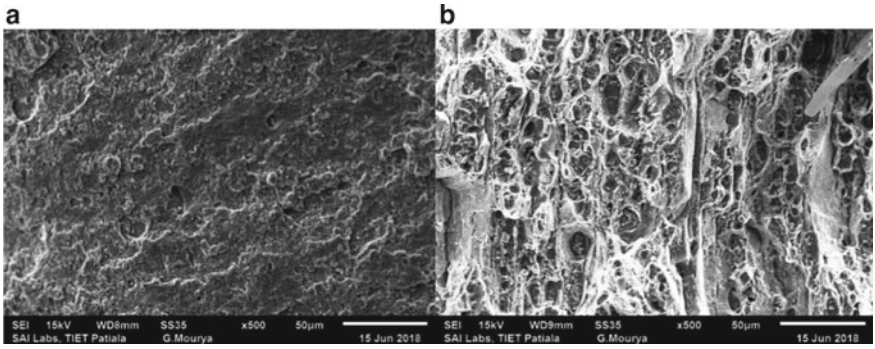


**Fig. 8** Fractrography image by using SEM, **a** without $B_4C$ particles, **b** with $B_4C$ particles

By increasing rpm, there is a drop in tensile strength due to corrosion effect at all traverse speed rates. It means by decreasing rpm, corrosion attacks on specimen were increasing due to low surface finish, voids and low interface bonding between base material and $B_4C$ obtained at lower rpm; thereby, chemicals can penetrate and attack specimen deeply. So 1600 rpm at 30 traverse speed was having lowest effect of corrosion on tensile strength followed by 1600 rpm at 50 and 40 traverse speed, respectively, and 1400 rpm at 50 traverse speed has highest effect of corrosion on tensile strength.

Fractrography images as shown in Fig. 8 of tensile specimens clearly revealed the images of breakzone and presence of $B_4C$ was identified in many place which is processed with particles. And also specimen processed without particles has very lesser amount of voids or pits in comparison to processed with $B_4C$. FSPed with $B_4C$, pits are visible due to pull out of $B_4C$ as a result of tensile loads due to less interface bonding between $B_4C$ and parent metal. This resulted in reduction of UTS of FSPed specimen.

## 4 Conclusion

Aluminum alloy metal matrix composites were fabricated by friction stir processing using $B_4C$ as reinforcements at varying process parameters. The FSPed specimens were tested for tensile test with and without corrosion. It was observed that impact of corrosion is high for FSPed specimen with $B_4C$ than without particles. By increasing rpm, impact of corrosion was reducing and thereby 1600 rpm has lowest reduction in wear resistance after corrosion. Tensile strength of FSPed specimen was lowered by about 35% as compared to base. FSPed with $B_4C$ has lower tensile strength as compared to without particles. Tensile fracture occurred for specimens without particles is away from processed zone. For tensile also, impact of corrosion was lowered by increasing rpm. It is as a result of increase in temperature results in

higher peak temperature which helps in reduction of defects in processed zone and good interface bonding among $B_4C$ and base materials; thereby, material can resist the penetration of chemicals into the work. Lowest rpm (1400) with lowest traverse speed (30) accomplished better tensile strength as compared to others. By increasing rpm, due to more stirring action, higher amount of frictional and deformation heat is generated which results in higher grain size and thereby reduction in the strength.

## References

1. Ma ZY, Sharma SR, Mishra RS (2006) Effect of multiple-pass friction stir processing on microstructure and tensile properties of a cast aluminum–silicon alloy. Script Mater 54:1623–1626
2. Karthikeyan L, Senthilkumar VS, Balasubramanian V, Natarajan S (2009) Mechanical property and microstructural changes during friction stir processing of cast aluminum 2285 alloy. Mater Des 30:2237–2242
3. Gulati P, Shukla DK (2017) Investigation of the effects of plunge depth on the resulting temperature distribution, microstructure and mechanical properties of friction stir welded AZ31B magnesium alloy. Adv Mater Manuf Charact 7(2):53–59
4. Mishra RS, Mahoney M, McFadden S, Mara N, Mukherjee A (1999) High strain rate superplasticity in a friction stir processed 7075 Al alloy. Scripta Mater 42:163–168
5. Wang W, Shi Q-y, Liu P, Li H-k, Li T (2009) A novel way to produce bulk SiCp reinforced aluminum metal matrix composites by friction stir processing. J Mater Process Technol, 2099–2103
6. Starke EA, Staley JT (1996) Application of modern aluminum alloys to aircraft. Aerospace, 131–172
7. Aruri D, Adepu K, Adepu K, Bazavada K (2013) Wear and mechanical properties of 6061-T6 aluminum alloy surface hybrid composites [(SiC + Gr) and (SiC + $Al_2O_3$)] fabricated by friction stir processing. J Mater Res Technol 2:362–369
8. Navaser M, Atapour M (2017) Effect of friction stir processing on pitting corrosion and intergranular attack of 7075 aluminium alloy. J Mater Res Technol, 155–165
9. Yahalom J (2003) Corrosion protection methods. In: Encyclopedia of materials: science and technology, pp 1710–1713

# Wear Analysis of Friction Stir Processed Aluminium Alloy Surface Composites


**Piyush Gulati, A. Nihal, Dinesh Kumar Shukla, Jaiinder Preet Singh, Harpinder Singh, and Gurveen Singh**

## 1 Introduction

The demand to lighten the automobiles leads to the development of new materials. Finding a material with particular properties is a standout amongst the most imperative issues in numerous mechanical applications particularly in transportation ventures. Aluminium alloys possess high specific strength and good corrosion resistance which makes them a suitable choice for lightening of vehicles' components as well improving the efficiency.

However, during service, the components experience wear which can affect its service life. To improvise upon the wear characteristics, the surface properties need to be improvised [1, 2]. This can be achieved by using the surface composites in which the surface layer experiences modification and the original composition is retained by the substrate. There are various conventional techniques to fabricate aluminium matrix composites (AMCs) like anodizing, physical vapour deposition, etc. which improves the surface properties of the aluminium alloys [1, 3–6]. Despite yielding satisfactory results, there are certain short comings in these techniques such as toxic emissions, higher processing time and use of expensive consumables [7].

Friction stir processing (FSP) is another promising technique capable of fabricating AMCs and that too with desirable range of distribution of added particles [8]. FSP is a solid state processing technique in which a solid non-consumable rotating tool, comprised of a pin and a shoulder, is inserted in the parent metal up to depth for

P. Gulati · A. Nihal (✉) · J. P. Singh · H. Singh
School of Mechanical Engineering, Lovely Professional University, Phagwara, Punjab, India

D. K. Shukla
Department of Mechanical Engineering, Dr. B R Ambedkar NIT Jalandhar, Jalandhar, Punjab, India

G. Singh
Department of Mechanical Engineering, DAVIET, Jalandhar, Punjab, India



K. Jha et al. (eds.), *Recent Advances in Sustainable Technologies*,
Lecture Notes in Mechanical Engineering,
https://doi.org/10.1007/978-981-16-0976-3_24

the modification in its microstructure and properties. The main source of heat generation during FSP is the friction between rotating tool and workpiece and the plastic deformation which causes recrystallization. Most of the FSP applications such as repairing of cast defects [9, 10] or fabrication of metal matrix composites [11–16] are limited to planar surfaces [7]

Since its development by Mishra et al. [17], several authors have explored FSP as a technique for the development of surface composites. Wang et al. [18] developed SiCp reinforced aluminium matrix composites and had observed excellent bonding between the inserted particles and the base material. It was also reported that the developed surface composite revealed 10% higher microhardness values in comparison to the base material. Higher hardness values of surface composites in comparison with base material, fabricated through FSP, were also reported by R. Ramesh et al. [19]. They had used Aluminium 7075 as the base metal and reinforcement as B4C particles. Rana et al. [20] also used Aluminium 7075 as the base material for fabricating AMCs using B4C particles as the reinforcement particles. They have evaluated the wear properties and microhardness of the AMCs. As per the reported results, they observed excellent improvement in the wear resistance (100%) of the surface composite in comparison to the parent metal. Moreover, hardness was also found to increase by 40–70% for the surface composites. The improved properties were attributed to fine distribution of B4C particles in the aluminium matrix.

As per the published literature, most of the surface composites fabricated using friction stir processing evaluated the surface properties such as wear and hardness. However, the effect of corrosion on various properties of developed surface composites is not touched upon. In the present research work, an effort is made to successfully fabricate aluminium matrix surface composites through FSP using Aluminium 7075 as the substrate and B4C particles as the reinforcements. The surface composites were then tested for wear and the effect of corrosion on the properties of AMCs is also highlighted in the current work.

## 2 Experimentation

Aluminium alloy 7075 plates 5 mm thick were friction stir processed using $B_4C$ particles to fabricate aluminium matrix surface composites. The set up used for performing the FSP is represented in Fig. 1. The $B_4C$ particles were layered into a 1.5 mm $\times$ 2 mm small groove on the surface which was then capped using pin less FSP tool so as to avoid spattering of the particles. The FSP tool with a conical pin and the pin less tool is shown in Fig. 2.

Corrosion on the samples was carried out by using sodium hydroxide solution. All specimens of wear test were kept in alkaline solution for 8 h (until reaction complete). The wear tests were performed on pin on disc apparatus. The corroded and non-corroded samples prepared for wear test are represented in Fig. 3. During processing, the material around the tool will have to be locally raised to a temperature range in which severe plastic deformation can readily occur, and at the same time

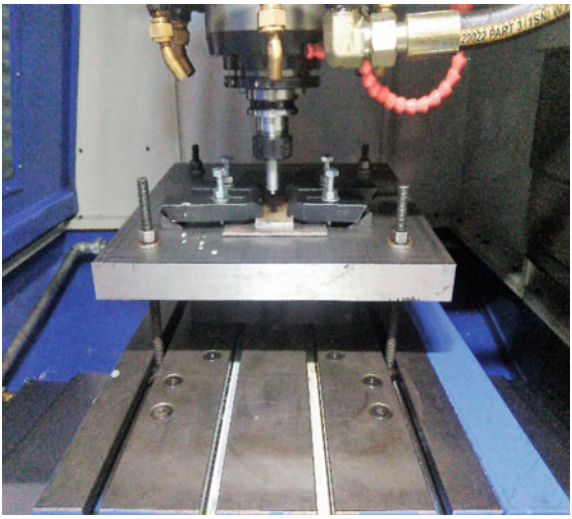

**Fig. 1** Friction stir processing set up

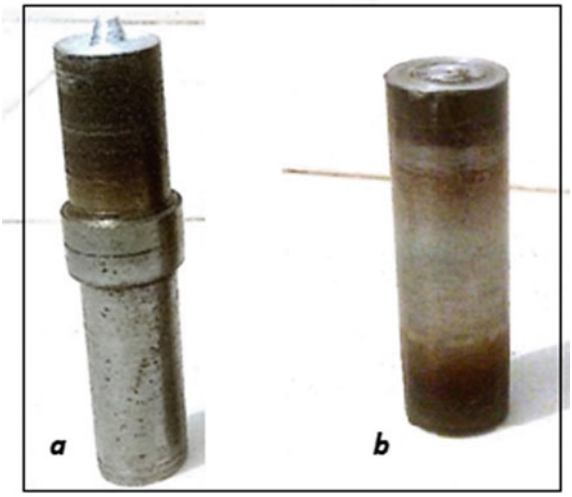


**Fig. 2** FSP tool, **a** conical pin, **b** pinless tool

minimizing the forces acting on the tool. In general, the heat input to the work piece increases with higher rotation speed or decreasing transverse speed. The finalized processing parameters after a series of trials are represented in Table 1.

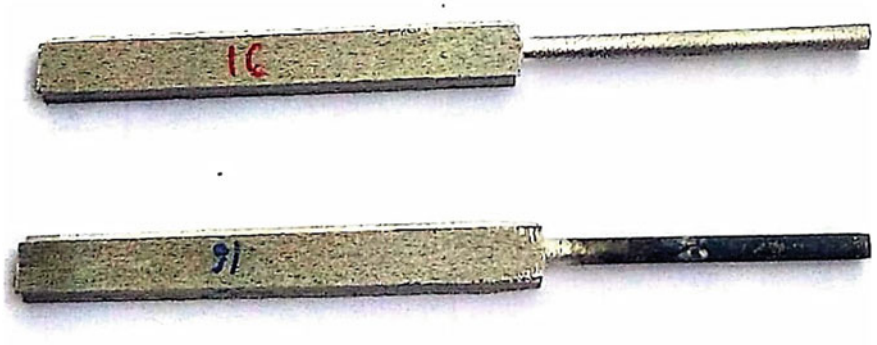

**Fig. 3** Wear specimen (pin) of non-corroded and corroded

**Table 1** Finalized processing parameters

| S. No. | Processing | Traverse speed (mm/min) | Rotational speed (rpm) |
|---|---|---|---|
| 1 | None (Base) | None | None |
| 2 | | | 1400 |
| 3 | | 30 | 1500 |
| 4 | Yes | | 1600 |
| 5 | With boron | | 1400 |
| 6 | Carbide | 40 | 1500 |
| 7 | | | 1600 |
| 8 | | | 1400 |
| 9 | | 50 | 1500 |
| 10 | | | 1600 |
| 11 | | | 1400 |
| 12 | Yes | 30 | 1500 |
| 13 | | | 1600 |

## 3 Results and Discussion

### *3.1 Wear Test*

Pin on disc tribometer was considered for the study of wear behaviour of a specimen. It has an immobile pin by a load in touch with a disc which is in rotation. Frictional coefficient is measured by the proportion of the frictional power to the power stacking on the pin. The pin on disc test was demonstrated its capacity in giving a straightforward wear and erosion test. Linear wear rate 'h' is plotted by utilizing a linear variable differential transducer. From linear wear rate, volumetric wear rate is found by using cylinder formula $= \pi/4 \times d^2 h$.

The wear graphs for base sample and FSPed sample at 1600 rpm are represented in Figs. 4, 5 respectively. These results reported that by increasing rpm of processed specimen without $B_4C$, wear rate was also increasing with respect to it. The results were validated from Devaraju et al. [21] that increase in rpm will soften material due to over ageing and grain size growth occurred by temperature rise by increasing rpm. More the size of grain reduce material hardness and strength. From the volumetric wear rate as represented in Tables 2 and 3, it is clear that wear resistance dropped for all corroded specimens from non-corroded as obvious that corrosion attacks will weak the specimen and reduce area of contact by degrading surface.

Whereas from these corroded friction stir processed specimens, 1400 rpm has better wear resistance than non-corroded base. From that linear wear rate obtained volumetric wear rate is reported in Table 2. Only 1400 rpm without particles enhanced wear resistance than base material due to reason of strain hardening occurred by deformation with low temperature. Also by increasing rotational speed of tool at same traverse speed, there is an increment in wear resistance with particles, whereas without particles show opposite way that is by increasing rotational speed, there is a

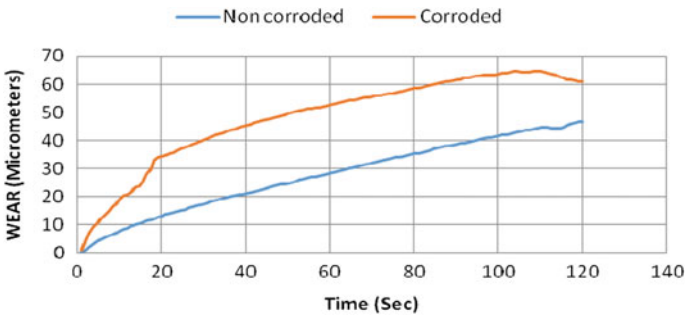


**Fig. 4** Wear versus time graph of base sample

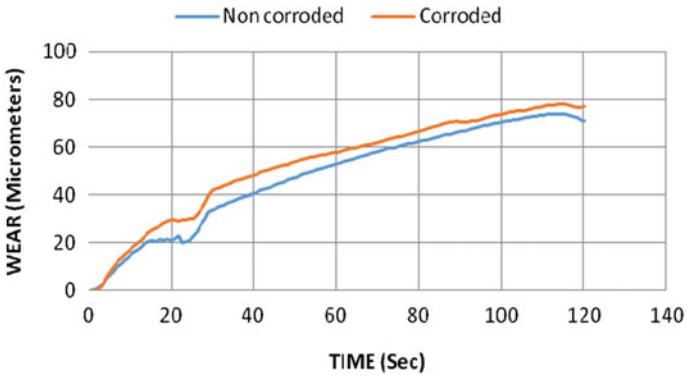


**Fig. 5** Wear versus time graph of 1600 rpm without $B_4C$

**Table 2** Volumetric wear rate of FSPed specimens without reinforcement

| RPM | Traverse speed | Volumetric wear rate $mm^3/s$ | |
|---|---|---|---|
| | | Non-corroded | corroded |
| 1400 | 30 | 0.2424 | 0.3443 |
| 1500 | | 0.3367 | 0.4337 |
| 1600 | | 0.5003 | 0.5442 |

**Table 3** Volumetric wear rate of FSPed specimens with $B_4C$ as reinforcement

| RPM | Traverse speed | Volumetric wear rate $mm^3/s$ | |
|---|---|---|---|
| | | Non-corroded | corroded |
| 1400 | 30 | 0.2854 | 0.5293 |
| 1500 | | 0.2600 | 0.4869 |
| 1600 | | 0.1574 | 0.3451 |

decrement of wear resistance. And increment of wear resistance by increasing rpm in the specimens was due to proper distribution $B_4C$ in the processed area. Wear resistance improved for FSPed material with particles at all processing parameter.

Volumetric wear rate of corroded and non-corroded samples calculated from wear graph is listed in Table 3. Volumetric wear rate is high for 1400 followed by 1500 then 1600 rpm. This means 1600 rpm processed with $B_4C$ has better wear resistance than other two lower rpms. And also, wear resistance was improved on all processing parameters specimens processed with $B_4C$ than as received. So addition of $B_4C$ into AA7075 by utilizing FSP is good for improving wear resistance, whereas there is high drop in wear resistance after corrosion of specimen subjected to wear testing tells that in a corrosive environment without FSPed without $B_4C$ is preferred.

It is clear from the results obtained base materials and FSPed with $B_4C$ particles has higher wear rate increment than FSPed without $B_4C$ after corrosion. Due to this reason, there is a high drop in wear resistance after corrosion of FSPed with and without $B_4C$ particles, whereas before corrosion, the wear resistance was much higher. From the linear wear rate, volumetric wear rate of non-corroded and corroded base was 0.3303 and 0.4308 $mm^3/s$. It is clear that drops in wear resistance higher for FSPed samples with $B_4C$ than FSPed without $B_4C$, and due to this reason, corroded 1400 rpm and 1500 rpm processed without $B_4C$ has better wear resistance than with $B_4C$. Interestingly, FSPed with $B_4C$ at 1600 rpm and FSPed without particles has more wear resistance than corroded base samples.

## *3.2 Impact of Corrosion on Wear Resistance*

Drops in wear resistance of corroded samples from non-corroded samples of different plates of various process parameters are shown in Fig. 7. This will provide effects of corrosion on wear resistance by all parameters.

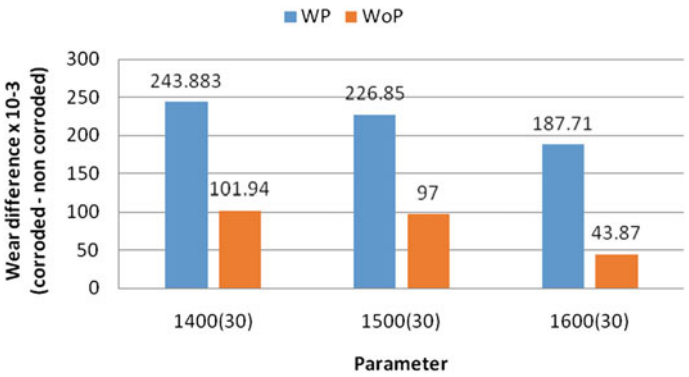


**Fig. 7** Impact of corrosion by FSP on wear rate

By increasing rpm, effect of corrosion on wear resistance was decreasing; this also validated from Navaser et al. [22] that by increasing rpm, the extent of IGC was reducing in TMAZ and HAZ of AA7075. It is due to reason that when we utilize reinforcements, there is a chance of occurrence of small pores and less interface bonding between foreign particles in processed area, if stirring or heat not occurred properly. So corrosion attacks more rapidly, that is why corrosion affected wear resistance adversely by decreasing order of rpm. If rpm is more, particles will distribute in a better way, and by high temperature, metal will soften more and by cooling better bonding between $B_4C$ and parent metal will occur and corrosion attack will reduce. However, this impact due to reinforcements can be reduced by increasing rpm which will enhance interface bonding between $B_4C$ particles and parent alloy. So if the application of material is under corrosive environment, then FSPed without out particle or less amount of $B_4C$ with high rpm up to a limit is preferred.

## *3.3 Processing Parameter Relation on Coefficient of Friction*

Coefficient of friction is one of the important properties in tribology. This value can derive from friction force because normal load was known that is 10 N. Dividing mean value of friction force by normal load will give coefficient of friction value. So it is evident from Fig. 8 that processed specimen without particle has more coefficient of friction than with particles, so, it has more contact area than without particles. Also it observed that coefficient of friction was increasing by increasing rpm because of the availability of more stirring time and thereby particles will also breakdown resulting better interface bonding and high temperature results in reduction of defects and thereby more contact area. When rpm is increasing, coefficient of friction of with particles and without particles is coming more closure.

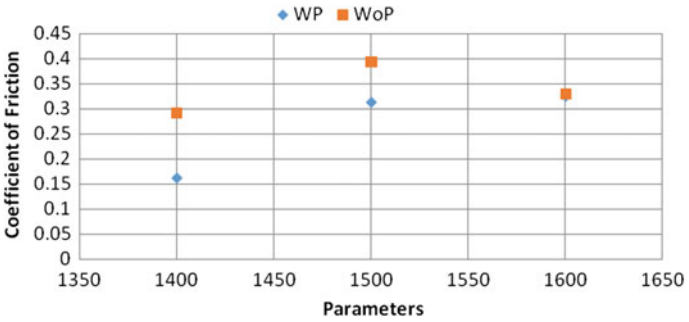


**Fig. 8** Influence of processing parameter on coefficient of friction

## 4 Conclusions

Aluminium matrix surface composites were successfully fabricated through friction stir processing using $B_4C$ as reinforcement particles. Wear specimens prepared from the friction stir processed composites and were tested on pin on disc apparatus under corrosion and non corrosion conditions. The main conclusions derived are:

1. All FSPed samples except 1500 and 1600 rpm without any reinforcements exhibited higher wear resistance than base sample.
2. FSPed with $B_4C$ has more effect on wear properties than base where as this can be reduced by increasing rpm.
3. From the results obtained, it is concluded that rpm is one of the main factors to decrease corrosion effect on wear resistance. By increasing rpm, corrosion impact was reduced due to proper interface bonding between reinforcements and parent material with low pores and cracks.

## References

1. Mohseni E, Zalnezhad E, Sarhan AAD, Bushroa AR (2014) A Study on surface modification of Al7075-T6 alloy against fretting fatigue phenomenon. Adv Mater Sci Eng, 1–17
2. Gordelier SC, Chivers TC (1979) A literature review of palliatives for fretting fatigue. Wear 56:177–190
3. Majzoobi GH, Jaleh M (2007) Duplex surface treatment on AL7075-T6 alloy against fretting fatigue behavior by application of titanium coating plus nitriding. Mater Sci Eng A 452–453:673–681
4. Harris SJ, Overs MP, Gould AJ (1985) The use of coatings to control fretting wear at ambient and elevated temperatures. Wear 106:35–52
5. McColl IR, Harris SJ, Hu Q, Spurr GJ, Wood PA (1997) Influence of surface and heat treatment on the fretting wear of an aluminium alloy reinforced with SiC particles. Wear 203–204:507–515
6. Gao H, Gu H, Zhou H (1991) Sliding wear and fretting fatigue resistance of amorphous Ni-P coatings. Wear 142:291–301

7. Hashemi R, Hussain G (2014) Wear performance of Al/TiN dispersion strengthened surface composite produced through friction stir process: a comparison of tool geometries and number of passes. Wear. https://doi.org/10.1016/j.wear.2014.11.024
8. Michael Rajan HB, Dinaharan I, Ramabalan S, Akinlabi ET (2016) Influence of friction stir processing on microstructure and properties of AA7075/TiB2 in situ composite. J Alloys Compounds 657:250–260
9. Ma ZY, Sharma SR, Mishra RS (2006) Effect of multiple-pass friction stir processing on microstructure and tensile properties of a cast aluminum–silicon alloy. Script Mater 54:1623–1626
10. Karthikeyan L, Senthilkumar VS, Balasubramanian V, Natarajan S (2009) Mechanical property and microstructural changes during friction stir processing of cast aluminum 2285 alloy. Mater Des 30:2237–2242
11. Bahrami M, Kazem M, Givi B, Dehghani K, Parvin N (2014) On the role of pin geometry in microstructure and mechanical properties of AA7075/SiC nano-composite fabricated by friction stir welding technique. Mater Des 53:519–527
12. Bauri R, Yadav D, Suhas G (2011) Effect of friction stir processing (FSP) on microstructure and properties of Al–TiC in situ composite. Mater Sci Eng A 528:4732–4739
13. Ni DR, Wang JJ, Zhou ZN, Ma ZY (2014) Fabrication and mechanical properties of bulk NiTip/Al composites prepared by friction stir processing. J Alloy Comp 586:368–374
14. Faraji G, Asadi P (2011) Characterization of AZ91/alumina nanocomposite produced by FSP. Mater Sci Eng A 528:2431–2440
15. Sharifitabar M, Sarani A, Khorshahian S, Afarani MS (2011) Fabrication of 5052Al/$Al_2O_3$ nanoceramic particle reinforced composite via friction stir processing route. Mater Sci Eng A 32:4164–4172
16. Zohoor M, Givi MKB, Salami P (2012) Effect of processing parameters on fabrication of Al–Mg/Cu composites via friction stir processing. Mater Des 39:358–365
17. Mishra RS, Mahoney M, McFadden S, Mara N, Mukherjee A (1999) High strain rate superplasticity in a friction stir processed 7075 Al alloy. Scripta Mater 42:163–168
18. Wang W, Shi Q-y, Liu P, Li H-k, Li T (2009) A novel way to produce bulk SiCp reinforced aluminum metal matrix composites by friction stir processing. J Mater Process Technol 209:2099–2103
19. Ramesh R, Murugan N (2013) Microstructure and metallurgical properties of aluminium 7075–T651 alloy/B4C 4 % Vol 1. Surface composite by friction stir processing. Adv Mater Manuf Charact 13:301–306
20. Rana HG, Badhek VJ, Kumar A (2016) Fabrication of Al7075/B4C surface composite by novel friction stir processing (FSP) and investigation on wear properties. Procedia Technol 23:519–528
21. Aruri D, Adepu K, Adepu K, Bazavada K (2013) Wear and mechanical properties of 6061-T6 aluminum alloy surface hybrid composites [(SiC + Gr) and (SiC + Al2O3)] fabricated by friction stir processing. J Mater Res Technol, 112–124
22. Navaser M, Atapour M (2017) Effect of friction stir processing on pitting corrosion and intergranular attack of 7075 aluminium alloy, pp 155–165

# A Survey on Flow Phenomena and Heat Transfer Through Expansion Geometry


**Sandip Saha**

## 1 Introduction

The fluid flow through expansion geometry seems to be very useful in fundamental fluid mechanics as well as in various industrial applications including heat exchanger models, diffusers, nuclear reactors, electronic cooling equipment, and mixing vessels also in medical sciences. In the last few years, it has become a major interest to investigate the flow of expansion geometry in reverse movement from symmetry to asymmetry [1–5]. Flow through sudden expansion has become recognized as a symbolic test bed, for the experimental and computational investigations of such flows, as a configuration considered having the simplest geometry [6–9]. But geometric simplicity does not inherently imply that flow phenomena are simple [1–9]. The important features attracted by many researchers [10–13] were also flow separation, reattachment, and various forms of flow bifurcation according to various values of Reynolds number and recirculated fluid flow areas. In recent times, flow through expansion geometry is well known for studying the flow instability at higher values of Reynolds number and the dynamic relationship between flow bifurcation and fluid rheology has of course begun to be highlighted. Paper can be formulized as follows: Sect. 2 described the model geometry, literature review drawn in Sect. 3 and lastly prescribed the conclusion and references.

S. Saha (✉)
Department of Mathematics, NIT Silchar, Silchar, Assam 788010, India
e-mail: sandip_rs@math.nits.ac.in



K. Jha et al. (eds.), *Recent Advances in Sustainable Technologies*,
Lecture Notes in Mechanical Engineering,
https://doi.org/10.1007/978-981-16-0976-3_25

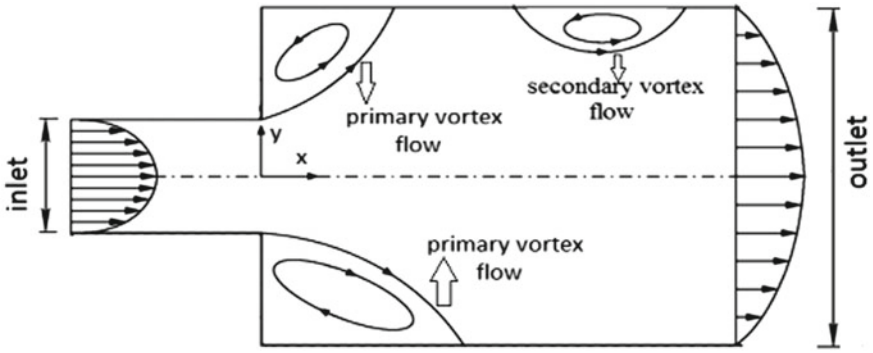


**Fig. 1** Sudden expansion geometry

## 2 Model Geometry

Figure 1 presents the computational domain of sudden expansion geometry, where the fluid flows through inlet section toward the outlet section.

## 3 Literature Survey

### *3.1 Experimental and Numerical Works on General Expansion Channel*

In this subsection, the experimental and numerical works of laminar, turbulent, and MHD flow phenomena on expansion channel have been discussed briefly. Previous research works on sudden expansion channel (Fig. 1) have been reviewed in Table 1 based on publication years and flow type.

### *3.2 On Modified Expansion Geometry*

Various works (Table 2) have been studied to understand the flow characteristics and the modification of expansion geometry namely incorporation of wall suction, diffuser zone in presence of fence incorporation, and expansion geometry in presence of swirling devices.

**Table 1** Review investigation on flow phenomena and heat transfer

| Authors | Publication year | Flow type and technique | Conclusion |
|---|---|---|---|
| [1] | 1962 | Turbulent flow by single- and double-step configuration | – Three different corner vortices appear when Ar (area ratio) > 1.5 |
| [2] | 1967 | Laminar flow by energy method | – Captive eddy exists on the lower and upper corner walls |
| [3] | 1972 | Turbulent flow by experimentally | – Wave instabilities are present in the shear layer |
| [4] | 1972 | Laminar isothermal flow using SIMPLE scheme | – Excess pressure drop increases as Re increases |
| [5] | 1978 | Laminar flow by LDA | – For low Re, flow patterns are steady and indistinguishable corner vortices appear |
| [6] | 1983 | Turbulent flow using LDA | – Secondary vortex forms at higher values of Re on both corner walls |
| [7] | 1988 | Turbulent flow using LDV | – One-dimensional LDV device play a major role to find mean velocity and turbulent kinetic energy |
| [8] | 1989 | Turbulent flow by convective-acoustic scheme | – Net effect of step height on flow is negligible if all the parameters of inlet geometry kept constant |
| [9] | 1990 | Laminar flow using energy based | – Steady and non-symmetrical solutions exist when $Re > Re_{cr}$, using |
| [10] | 1990 | Laminar flow by discretization | – Flow break the symmetry at Re = 40.5 |
| [11] | 1990 | Laminar flow using singular finite element | – Normal stress is more insensitive to construct a singular basis function |
| [12] | 1993 | Laminar flow using LDA | – Flow bifurcation break the symmetry for Re > 125 |
| [13] | 1993 | Turbulent flow by LDV | – At $X/H = 3.15$, flow reattachment is faster because of center body deflection |
| [14] | 1996 | Laminar flow using Cascade model | – When $Re > Re_{cr}$ flow becomes asymmetric |
| [15] | 1997 | Laminar flow by quadratic model | – Pressure drop increases with the increase of Re |
| [16] | 1997 | Laminar flow using continuation method | – For creeping flow weak corner vortices appear on the corner walls |

(continued)

**Table 1** (continued)

| Authors | Publication year | Flow type and technique | Conclusion |
|---|---|---|---|
| [17] | 1999 | Laminar flow using PAV | – An inverse relationship generate between eddy strength to Re |
| [18] | 1999 | Laminar flow using experimental technique | – Due to pressure coupling, isothermal flow asymmetry has been reduced |
| [19] | 2001 | Laminar flow using linear stability analysis | – Flow become linearly stable for $Re < Re_{cr}$ and unstable for $Re > Re_{cr}$ |
| [20] | 2001 | Turbulent flow by VLEC | – Strouhal number increases cause the increases of expansion ratio |
| [21] | 2002 | Laminar flow using VONOS convection scheme | – More than two corner vortices appear for |

### *3.3 $Re_{cr}$ and Flow Bifurcation*

Up to a certain value of Re, symmetry-breaking bifurcation (Coanda effect) exist. When, $Re > Re_{cr}$ flow bifurcation known as Hopf bifurcation, where the complex, unstable and periodic solution exists. Mazushima et al. [42] examined the flow instability by nonlinear stability analysis, where the flow bifurcation transition changes symmetric to asymmetric due to the increase of Re. They employed weak nonlinear stability analysis to analyze the structural instability of flow bifurcation. The results of experimental and the numerical results show a good agreement. The wide number of authors investigates the $Re_{cr}$ for symmetry-breaking bifurcation at different values of expansion ratios (ER), as shown in Tables 3 and 4.

## 4 Conclusion

The current work provides a brief survey of numerical and experimental studies of flow phenomena through sudden expansion microchannel. The following important features are concluded by various researchers.

- Vortex length and the values of Nu increases cause the increase of Reynolds number.
- Symmetry flow bifurcation exist, when $Re < Re_{cr}$, but for $Re > Re_{cr}$ flow becomes more critical and unstable.
- Due to the increase of recirculation region length causes the decrease of Nusselt number. Moreover, various authors studied the inverse relationship between Re and ER.

**Table 2** Review investigation with some modification

| Authors | Publication year | Flow type and technique | Conclusion |
|---|---|---|---|
| [33] | 1976 | Turbulent flow by PIV | – For area ratio 5.15, pressure recovery can be increased |
| [34] | 1989 | Turbulent flow using LDA | – Turbulence intensity is much higher for diffuser angles 140° and 180° as compared to $90^0$ |
| [35] | 1997 | Turbulent flow using finite difference scheme | – Injection rate increases near the corner wall |
| [36] | 2004 | Laminar flow by power law | – Critical Reynolds number for shear-thinning fluid becomes higher as compared to Newtonian fluids |
| [37] | 2006 | Laminar flow by HSMAC scheme | – Weak asymmetric flow patterns are exist for Re ∈ [100–1000], however in a vertical plane strong asymmetric flow patterns are noted |
| [38] | 2006 | Laminar flow by finite volume discretization scheme | – Flow becomes symmetric after a certain distance from the downstream zone of the geometry |
| [39] | 2008 | Laminar flow by finite difference discretization scheme | – As increase the blow speed recirculation length reduces significantly<br>– Increase of suction velocity causes the existence of asymmetry flow |
| [40] | 2013 | Turbulent flow using PIV | – In downstream of the tube, the rate of heat transfer increase 190–225% as in the presence of propeller |
| [41] | 2015 | Laminar flow by discretization | – Drag friction is slightly affected as an increase of obstacle thickness |

**Table 3** Drikakis et al. [16]

| ER | 2 | 3 | 4 | 5 | 6 | 8 | 10 |
|---|---|---|---|---|---|---|---|
| $Re_{cr}$ | 216 | 80 | 53 | 41 | 33 | 28 | 26 |

- Pressure loss reduces as the expansion ratio decreases, however excess pressure drop and pressure drop increases with the increase of Re.

**Table 4** Investigation of various authors

| Authors | $Re_{cr}$ | Authors | $Re_{cr}$ | Authors | $Re_{cr}$ |
|---|---|---|---|---|---|
| [16] ER = 2, 3 and 5 | 218, 80, and 42.5 | [45] ER = 3 | 80.9 | [45] ER = 1.43, 1.67, 1.82, 2, 3.2 and 4 | 1250–1290, 465–485, 330–350, 217–219, 75–85 and 50–60 |
| [43] ER = 1.5, 1.6, 2, 3 and 4 | 446, 340–345, 215, 81 and 54 | [22] ER = 2 | 200 | [46] ER = 3 | 92.4 |
| [44] ER = 2 | 125–200 | [36] ER = 3 | 90–100 | [9] ER = 2 and 3 | 215, 82.6 |
| [47] ER = 3 | 81 | [48] ER = 2 | 285 | [49] ER = 1.33, 2.6 and 4 | 4533, 100 and 75 |
| [20] ER = 3 | 80.7 | | | | |

## References


1. Abbot DE, Kline SJ (1962) Experimental investigation of subsonic turbulent flow over single and double backward facing steps. J Basic Eng 84:317–325
2. Macagno EO, Hung TK (1967) Computational and experimental study of a capative annular eddy. J Fluid Mech 28:43–64
3. Back LH, Roschke JE (1972) Shear-layer flow regimes and wave instabilities and reattachment lengths downstream of an abrupt circular channel expansion. J Appl Mech 39(3):677–681
4. Christiansen EB, Kelsey J, Carter RT (1972) Laminar tube flow through an abrupt contraction. AIChE J 18:372–380
5. Chedron W, Durst F, Whitelaw JH (1978) Asymmetric flows and instabilities in symmetric ducts with sudden expansions. J Fluid Mech 84:13–31 (1978)
6. Armaly BF, Durst F, Pereira JCF, Schonung B (1983) Experimental and theoretical investigation of Backward-facing step flow. J Fluid Mech 127:473–496
7. Durrett PR, Stevenson HW, Thompson DH (1988) Radial and axial turbulent flow measurements with an LDV in an axi-symmetric sudden expansion air flow. J Fluid Eng l(l0):367–372
8. So RMC, Ahmed SA (1989) Characteristics of dump combustor flows. Int J Heat Fluid Flow 10:66–74 (1989)
9. Sahpira M, Degani D, Weihs D (1990) Stability and existence of multiple solutions for viscous flow in suddenly enlarged channels. Comput Fluids 18:239–258
10. Fearn R, Mullin K, Cliffe K (1990) Non-linear flow phenomena in a symmetric sudden expansion. J Fluid Mech 211:595–608
11. Georgiou GC, William S, Lorraine GO (1990) Singular finite elements for the problems sudden-expansion and the die-swell. Int J Numer Methods Fluids 10(4):357–372
12. Durst F, Pereira JCF, Tropea C (1993) The plane symmetric sudden expansion flow at low Reynolds Number. J Fluid Mech 248:567–581 (1993)
13. Devenport JW, Sutton PE (1993) An experimental study of two flows through an axisymmetric sudden expansion. Experimental Fluids 14:423–432
14. Foumeny EA, Ingham DB, Walker AJ (1996) Bifurcations of incompressible flow through plane symmetric channel expansions. Comput Fluid 25:335–351
15. Drikakis D (1997) Bifurcation phenomenon in incompressible sudden expansion flow. Phys Fluids 9(1):77–87

16. Alleborn N, Nandakumar K, Rasziller H, Durst F (1997) Further contributions on the two dimensional flow in a sudden expansion. J Fluid Mech 330:169–188
17. Hammad KJ, Otugen MV, Arik EB (1999) A PIV study of the laminar axisymmetric sudden expansion flow. Experiments in Fluids 26:266–272
18. De Khezzar L, Zilwa SRN, Whitelaw JH (1999) Combustion of premixed fuel and air downstream of a plane sudden expansion. Experiments in Fluids 27:296–309
19. Hawa T, Ruzak Z (2001) The dynamics of a laminar flow in a symmetric channel with sudden expansion. J Fluid Mech 436:283–320
20. Guo B, Langrish ATG, Fletcher FD (2001) Numerical simulation of unsteady turbulent flow in axisymmetric sudden expansions. J Fluids Eng 123:574–587
21. Kadja M, Touzopoulos D, Bergeles G (2002) Numerical investigation of bifurcation phenomena occurring in flows through planar sudden expansions. Acta Mech 153:47–61
22. Paulo J (2003) Asymmetric flows of viscoelastic fluids in symmetric planar expansion geometries. J Non-Newtonian Fluid Mech 114:33–63
23. Tinney EC, Glauser NM, Eaton LE, Taylor AJ (2006) Low dimensional azimuthal characteristics of suddenly expanding axisymmetric flows. J Fluid Mech 567:141–155
24. Mistrangelomn C, Buhler L (2007) Numerical investigation of liquid metal flows in rechangular sudden expansions. Fusion Eng Des 82:2176–2182
25. Lima RC, Andrade CR, Zaparoli EL (2008) Numerical study of three recirculation zones in the unilateral sudden expansion flow. Int Commun Heat Mass Transf 35:1053–1060
26. Aloui F, Madani S (2008) Experimental investigation of wet foam flow through a horizontal expansion. Exp Thermal Fluid Sci 32:905–926
27. Zdanski PSB, Vaz JM (2009) Non-isothermal polymer melt flow in sudden expansions. J Non-Newtonian Fluid Mech 161:42–47
28. Zhang XR, Deng BL, Yamaguchi H (2010) Bifurcation phenomenon for forced convection of supercritical $CO_2$ sudden expansion flow and heat transfer in symmetric regime. Int J Heat Mass Transf 53:4467–4473
29. Sousa PC, Coelho PM, Oliveira MSN, Alves MA (2011) Laminar flow in three-dimensional square-square expansions. J Non-Newtonian Fluid Mech 166:1033–1048
30. Christopher D, Kanna R, Madhusudhan G, Mohammed H (2012) Numerical investigation of heat transfer from a two-dimensional sudden expansion flow using nanofluids. Numer Heat Transf Appl 61(7):527–546
31. Pakhomov AM, Terekhov IV (2016) Modeling of the flow patterns and heat transfer in a turbulent bubbly poly dispersed flow downstream of a sudden pipe expansion. Int J Heat Mass Transf 101:1251–1262
32. Ramanathan S, Thaneswar RM, Kanna RP, Gunnasegaren P (2019) A new method of enhancing heat transfer in sudden expansion channel using vortex generators with toe-out and toe-in configurations by acquiring perquisites of recirculation and secondary vortex flow. J Mech Sci Technol 33:3913–3925
33. Verigin IS (1976) Effect of porous injection and suction on the operation of a stalled conical diffuser. J Eng Phys Thermophys 30(4):646–652
34. Stieglmeier M, Tropea C, Weiser N, Nitsche W (1989) Experimental investigation of the flow through axisymetric expansions. J Fluid Eng 111(4):464–471
35. Yang YT, Kuo CL (1997) Numerical study of a backward-facing step with uniform normal mass bleed. Int J Heat Mass Transf 40:1677–1686
36. Manica R, Bortoli ALD (2004) Simulation of sudden expansion flows for power-law fluids. J Non-Newtonian Fluid Mech 121:35–40
37. Yamaguchi H, Ito A, Kuribayashi M, Zhang RX, Nishiyama H (2006) Basic flow characteristics in three-dimensional branching channel with sudden expansion. Eur J Mech B/Fluids 25(6):909–922
38. Wahba EM (2006) Iterative solvers and inflow boundary conditions for plane sudden expansion flows. Appl Math Model 31(11):2553–2563
39. Layek GC, Mukhopadhyay S, Midya C (2008) Effects of Suction and Blowing on Flow Separation and Asymmetry in a Symmetric Sudden Expanded Channel. J Nonlinear Anal Model Control 13:1–15 (2008)

40. Zohir AE, Gomaa AG (2013) Heat transfer enhancement through sudden expansion pipe airflow using swirl generator with different angles. Exp Thermal Fluid Sci 45:146–154
41. Khudheyer S, Mushatet A, Qais A, Fagr MH (2015) Numerical study of laminar flow in a sudden expansion obstacle channel. Thermal Sci 19(2):657–668
42. Mazushima J, Shiotani Y (2000) Structural instability of the bifurcation diagram for two dimensional flow in a channel with a sudden expansion. J Fluid Mech 420:131–145
43. Battaglia F, Tavener S, Kulkarni A, Merkle C (1997) Bifurcation of low Reynolds number flows in symmetric channels. AIAA J 35:99–105
44. Chedron W, Durst F, Whitelaw JH (1978) Asymmetric flows and instabilities in symmetric ducts with sudden expansions. J Fluid Mech 84:13–31
45. Moallemi N, Brinkerhoff RJ (2016) Numerical analysis of laminar and transitional flow in a planar sudden expansion. Comput Fluids 140:209–221
46. Luo S (1997) Symmetry breaking of flow in 2D symmetric channels, simulations by Lattice-Boltzmann method. Int J Mod Phys C 8:859–867
47. Schreck E, Schäfer M (2000) Numerical study of bifurcation in three-dimensional sudden channel expansions. Comput Fluids 29:583–593
48. Neofytou P (2006) Transition to asymmetry of generalized Newtonian fluid flows through a symmetric sudden expansion. J Non-Newton Fluid Mech 133:132–140
49. Saha S, Biswas P, Nath S (2020) Bifurcation phenomena for incompressible laminar flow in expansion channel to study Coanda effect. J Interdiscip Math 23(2):694–702

# Biolubricants Based on Non-edible Oil: A Review


**Sagar Galgat and Ankit Kotia**

## 1 Introduction

Lubrication is the process in which a layer or a film of oil is applied between two objects, which are in relative motion with each other, so as to reduce the friction between them. Lubricating oil or lubricant is a substance which is required to decrease the friction and wear between surfaces having relative motion with each other. The lubricant must have certain objectives such as reduce wear and power loss in overcoming friction reduce the oxidation and protect it from corrosion, act as a shock absorber in automotive engine parts, act as a cleansing agent in various application, and also reduce the heat from friction so can then act as a cooling agent. A good lubricant must have the characteristics of (1) high viscosity, (2) high viscosity index, (3) thermal stability, (4) high resistance to oxidation, and (5) prevention against corrosion [1]. The conventional source of lubricant is petroleum or crude oil. It is a by-product of the refining process of petroleum. Automotive sector utilizes the petroleum-based oil as lubricant from beginning. Though the uses of mineral oil are limited due to its less availability, the decay of oceanic as well as terrestrial environment is caused by the dispose of crude oil. The application of petroleum-based oil in automotive engine result in the emission having metal traces such as magnesium, zinc, and iron is harmful to the environment. These lubricants have discharge during application due to their non-degradability which can cause contamination of air, soil, or water. The petroleum-based lubricants harm environment because they are non-degradable and highly toxic. The shortage of mineral oil reserves also motivated the researchers to find an alternative for petroleum and its product. Lubricant obtained from mineral oil shows poor oxidation resistance and less resistance to the carbon formation and less resistance to the corrosion. Due to the depletion of fossil fuel

S. Galgat · A. Kotia (✉)
School of Mechanical, Lovely Professional University, Jalandhar–Delhi G.T. Road, Phagwara, Punjab, India



K. Jha et al. (eds.), *Recent Advances in Sustainable Technologies*,
Lecture Notes in Mechanical Engineering,
https://doi.org/10.1007/978-981-16-0976-3_26

resource, the cost of petroleum-based product increases. There is a need to develop a flexible environmental-friendly biolubricant from renewable sources. Finding an alternative to the petroleum-based product is a prominent area of research. This motivates researchers to work on biolubricants. These are plant-based oil or synthetic ester obtained by modifying the renewable oil.

Biolubricants are biodegradable and non-toxic to humans and have better physicochemical properties than petroleum-based lubricants. Biolubricants are more advantageous than mineral oil-based lubricants because it has a higher flash point, higher boiling point, high lubricity, high biodegradability, high viscosity index, low volatility, and less toxic. [2]. Biolubricants can be obtained from both edible and non-edible oils. The use of edible oil for the production of bio-oil is not practicable because they are in great urge for fulfilling the requirement of human food. As edible oil is used in the food chain, the use of edible oil as a lubricant can give rise to the ecological damage by using their land [3]. The employment of non-edible oil as lubricant has various advantages such as inedible plant can be cultivated in a harsh environment and does not cause ecological damage, easily obtainable, low price and biodegradable, and non-toxic. These biolubricants can be classified according to the chemical composition as natural and synthetic oil. Natural oils are obtained from plant or animal fat by various extraction or distillation process. Synthetic oil uses the natural oil as basic material and obtained by chemical modification of natural oils. The natural oil contains triglycerides which are obtained from glycerol and fatty acid chain. The percentage composition of fatty acid in oil affects the physicochemical properties of oils. Fatty acid is carboxyl acid with long carbon–carbon chain. Fatty acids are classified on the basis of presence of double bond in the carbon–carbon chain. Saturated fatty acid is those who do not have double bond, and unsaturated fatty acid has minimum one double bond. Synthetic oil is obtained from chemical modification of natural oil.

Thermo-physical properties of natural oil can be improved by chemical modification. Thermal and oxidation stability can be affected by the presence of the unsaturated part of natural oil. Chemical modification of natural oil is mainly focused on modification of unsaturated fatty acid because double bonds are more vulnerable with the oxidation reaction. The most common chemical modification includes transesterification process, epoxidation process, and hydrogenation process [2]. Epoxidation reaction is the chemical modification of unsaturated part of the natural oil and thereby increases the oxidation stability. Using a variety of reagents including air oxidation, hydrogen peroxide, peracetic acid, it converts the carbon–carbon double bond into oxiranes (epoxides). Epoxidation reaction results in an increase in thermal and oxidative stability, viscosity and lubricity of natural oil. Another method to advance the thermo-physical properties of lubricating oil is by the application of additives. These additives in lubricating oil are used for different purposes such as to improve the viscosity, viscosity index of the oil, to increase the oxidation stability of oil, and to improve the frictional and wear characteristic of oil. These additives are antiwear additives, high pressure additives, detergents and dispersants additives. High pressure and antiwear additives are mostly used. The function of this kind of additives is to improve the capacity of lubricating oil to withstand the extreme pressure and

thermal condition. Sulfur, phosphorous, and chlorines are this kind of additives but these are harmful to the environment. Metal containing nanoparticles can be used as additives for lubricant. Nanoparticles (NP) of metals, metal oxides, and sulfide can be used as additives for lubricating oil. The concentration, size, and morphology of nanoparticles affect the frictional characteristic. The size of nanoparticles is inversely proportional to its hardness. The smaller the size of nanoparticles there will be better dispersion stability and good tribological behavior. The shape of NP is related to its load handling capacity [4].

Nanoparticles are of considerable interest for increasing the properties of biodegradable lubricants. Nanoparticles are environmental-friendly, as they minimize the use of additives, which are harmful to the environment. Nanoparticles may additionally facilitate the minimization of energy consumption in production processes, thus leading the reduction in amount of carbon dioxide released into the atmosphere [4]. The application of nanoparticles is used for conquering the disadvantages of conventional additives. Various non-edible oils were considered for the creation of biolubricant by the chemical modification and addition of nanoparticles. The tribological applications of different non-edible plant were examined by various studies such as *Moringa oleifera* seed [5–7], *Calophyllum inophyllum* [8–10], Thumba (*Citrullus colocynthis* L.) seed [11], *Balanites aegyptiaca* [12], *Michelia champaca* [13], *Shorea robusta* [14], juliflora oil [15], and jojoba oil [16, 17]. Existing studies include the development of a biolubricant from non-edible plant by enhancing tribological properties through chemical modification and using nanoparticles. The chief objective of this current study is to provide the collective summary of the recent use of inedible plant for the production of biolubricant. This study involves the review of latest published research literatures on chemical modification of different inedible plant oil to obtain biolubricant.

## *1.1 Criteria for Selection of Article*

Google Scholar, Scopus, and Elsevier search engines were used for choosing the most significant articles for the subject of the current study. Biolubricant, non-edible oil, and nanoparticles keywords combination were used. The block diagrams for selection and identification of significant research article are as shown in Fig. 1. Selection of the relevant article is carried out in two stages.

- In first stage, articles are identified and selected on the basis of their title and abstract. The selection was according to three main criteria such as (a) the article must be from the past five years only, (b) the article must be on non-edible oil only, and (c) the articles must be on the non-edible oil whose were never considered for production of biolubricant. On the basis of above criteria, 13 articles were selected.
- The second stage consists of identifying and selecting the additional article published in current year for providing the basic knowledge about the study.

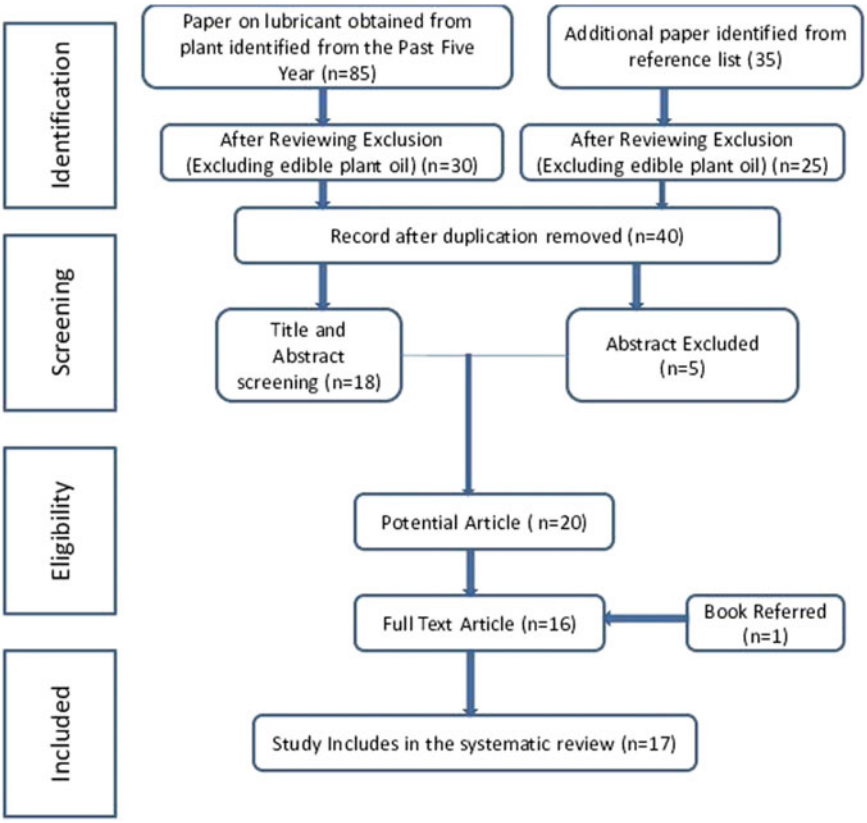


**Fig. 1** Block diagram for selection and identification of significant research article

Three articles were selected according to this stage. These articles were selected after studying the yearwise growth in the study of biolubricant for the past five years. The yearwise publication on biolubricant in "Fuel" Journal of Elsevier is as shown in Fig. 2. Most of the articles were selected from the "Fuel" Journal because it covers the topic of interest. After these two stages, 16 articles were finalized.

## 2 Biolubricant from Non-Edible Oil

**Moringa oleifera** generally known as "Moringa" is the most broadly developed types of the variety Moringa, which is the main class in the family Moringaceae. Moringa oil is obtained from the seeds of Moringa oleifera as shown in Fig. 3. Many researchers have considered this moringa oil for the production of biolubricant. Francis Uchennaet. Al. examined the tribological behavior of blends of Moringa

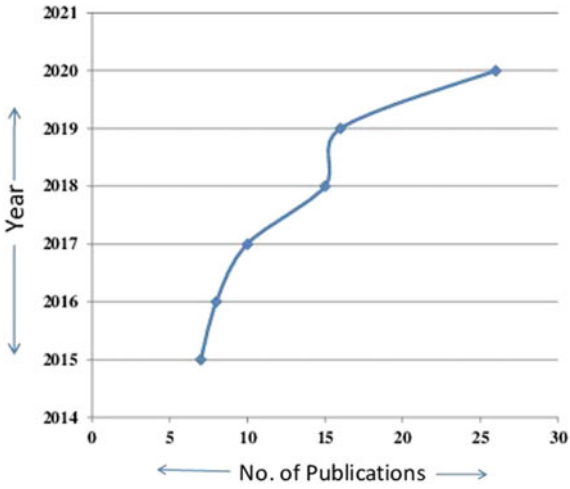


**Fig. 2** Yearwise publication on biolubricant in "Fuel" Journal of Elsevier


**Fig. 3** Extraction of *Moringa oleifera* oil

oleifera seed oil with conventional mineral oil. In this research, SAE 40 was considered as a base oil and blended it with moringa seed oil on percent basis of 10, 20, 30, and 40%. Pin-on-disc machine was used for analyzing the tribological behavior. The blend with 10% of moringa oil fulfills the condition for SAE 30 and SAE 40 grade [5]. Louis M. Nwokocha et al. investigate the tribological characteristics of moringa seed oil. This study includes the finding of the Moringa oleifera seed oil properties as a biolubricant. This oil contains more amount of oleic acid (72.73%) which has long carbon change (18:1) that leads to high viscosity. Rheological characteristic of moringa shows that it is solid at 10 °C, liquid at 30 to 70 °C, and thermally unstable at 90 °C [6]. Due to the high percentage of oleic acid, this oil can be considered in the tribological application as a biolubricant. But this oil is thermally unstable at high temperature and due to unsaturated fatty acid; there will be a risk of oxidation. The thermal and oxidation stability can be achieved by chemical modification of oil. Yashvir Singh et al. experimentally investigated the tribological characteristics of chemically modified moringa seed oil having 0.5% and 1% silicon carbide

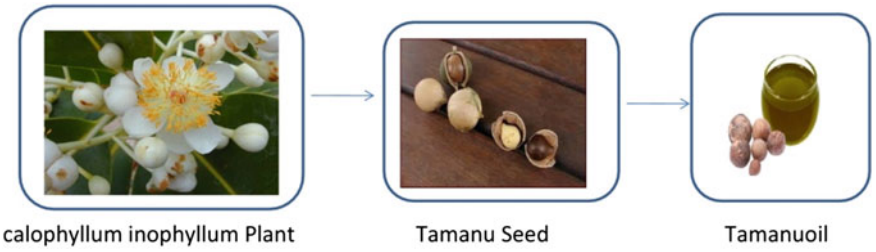


**Fig. 4** Extraction of tamanu oil

nanoparticle (SiC). Moringa oil was chemically modified by two-step transesterification reaction. Pin-on-disc machine and scanning electron microscope was used for conducting the experimentation, evaluating the wear characteristics. 0.5% of SiC nanoparticles show better result in terms of reducing coefficient of friction, wear rate, and less damage to the surface. The methodology used is complex and requires high accuracy [7].

**Calophyllum inophyllum oil (Tamanu oil)** is squeezed from seed as shown in Fig. 4 of either the *C. inophyllum* (typically) or the *Calophyllum tacamahaca* (ati), tropical trees having a place with Calophyllaceae family. This oil has a great potential for the production of biolubricant. M. Habibullah et al. perform the comparative experimental analysis of tribological property of Calophyllum inophyllum (CI)-based trimethylolpropane (TMP) ester and commercial mineral oil. TMP triesters are formed by the transesterification of trimethylpropane with Calophyllum inophyllum (CI) methyl ester. Four-ball triboester was used for the investigation of tribological properties of oil. In this study, the results show that CI TMP ester has promising future to supplant mineral oil-based oil as its presentation is vitality productive, hence decreasing energy subordinate [8]. Chandra Mouli et al. examined the tribological behavior of blends of Calophyllum inophyllum seed oil with commercial engine oil. First of all of Calophyllum inophyllum (CI)-based trimethylolpropane (TMP), ester pentaerythritol ester was synthesized from Calophyllum inophyllum seeds.

In this research, commercial engine oil was considered as a base oil and blended it with Calophyllum inophyllum seed oil on percent basis of 10, 15, 20, and 25%. 60-h endurance teston a motorbike was conducted for analyzing the tribological behavior. The blend with 15% of Calophyllum inophyllum seed oil shows better tribological property [9]. Mohammed Zaid et al. experimentally analyzed the tribological properties of Calophyllum inophyllum oil by chemical modification. In this experimentation, mineral oil is blended with the modified Calophyllum inophyllum oil with certain ratio 5 to 15%. A comparative analysis is carried out on these blends over their frictional characteristics. Coefficient of friction is less for 5 and 10% blend and increases with 15% blend. Similar results were seen for wear analysis [10]. Non-edible oil is discussed in this paper which is only used to modify the tribological characteristics but here more amount of conventional mineral oil is used so there will not be any chance for improving the degradability.


**Fig. 5** Extraction of thumba oil

**Thumba (Citrullus colocynthisL.) oil** is obtained from the seed of *C. colocynthis* as shown in Fig. 5. K. Kamalakar et al. experimentally investigate the tribological characteristics of chemical-modified thumba oil. In this experimentation different base stocks are prepared such as epoxy thumba oil, polyol esters, and 2-ethylhexyl ester from non-edible thumba oil. For lubricant properties, these base stocks were evaluated. Epoxy thumba oil shows higher viscosity, thermal stability, and oxidative stability from the other two base stocks. Polyol esters show low pour point compared to epoxy thumba oil [11]. Thumba oil contains more amount oflinoleic acid which leads to great lubricating properties. This oil can be chemically modified by epoxidation reaction. Nanoparticles can be used as additives to improve tribological properties.

**Desert date oil (Balanites aegyptiaca)** is obtained from the kernel of the tree as shown in Fig. 6. *Balanites aegyptiaca* is a member of family *Zygophyllaceae* or the *Balanitaceae*. Yashvir Singh et al. experimentally investigate the tribological properties of desert date oil (*B. aegyptiaca*) with copper nanoparticles addition. Desert date undergoes through transesterification process for chemical modification using two-step transesterification process and trimethylpropane was then added to the product. The modified desert date oil is tested for friction and wear behavior by using four-ball testers. The variation in the concentration of nanoparticles is from 0.3 to 1.6%. 0.9% of copper nanoparticles show better result in terms of reducing coefficient of friction, wear rate, and less damage to the surface [12]. The methodology used is complex and require high accuracy.

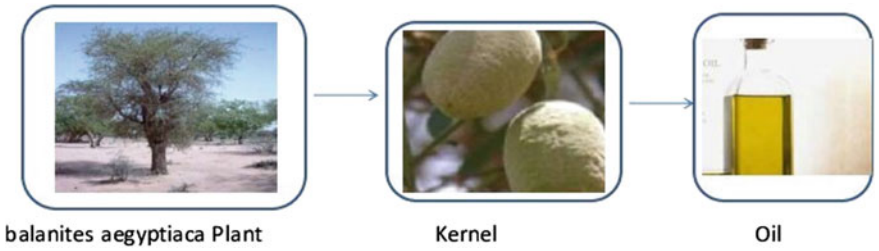


**Fig. 6** Extraction of desert date oil

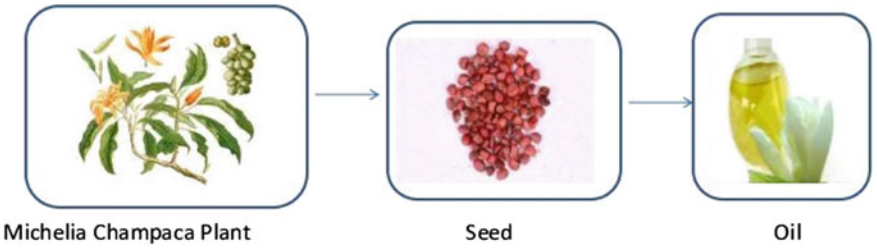


**Fig. 7** Extraction of *Michelia champaca* oil

**Michellia champaca oil** is obtained from seed of the Michelia champaca (shown in Fig. 7) member of the family Magnoliaceace. Yashvir Singh et al. perform comparative experimental analysis of tribological properties of raw Michellia champaca oil and chemically modified *M. champaca* oil and modified oil with a nanoparticle as additives. Michellia champaca oil undergoes through epoxidation reaction and $CuO_2$ nanoparticle was used as an additive. Pin-on-disc machine was used to conduct the experimentation. The nanoparticles are added to the epoxidized champaca oil on weight percentage basis (0.3, 0.6, and 1.2). Improvement in terms of reducing friction, less wear, and damage to the surface was seen by using 0.6% of copper nanoparticles [13]. There are other non-edible oils which consist of more amount of unsaturated fatty acid than *M. champaca* so can show greater tribological property after epoxidation reaction.

**Sal (Shorea robusta) oil** is obtained from seed of the *S. robusta* (shown in Fig. 8) member of the family Diptero carpaceae. Shailendra Kumar Chaurasia et al. perform the comparative experimental analysis of tribological properties of raw Sal (*S. robusta*) oil and chemically modified Sal (*S. robusta*) and modified oil with a nanoparticle as additives. Sal (*S. robusta*) undergoes through epoxidation reaction and $CuO_2$ nanoparticle was used as an additive. Pin-on-disc machine was used to conduct the experimentation. The nanoparticles are added to the epoxidized Sal oil on weight percentage basis (0.25, 0.5). Improvement in terms of reducing friction, less wear and damage to the surface was seen by using 0.5% of copper nanoparticles [14]. There are other non-edible oils which consist of more amount of unsaturated fatty

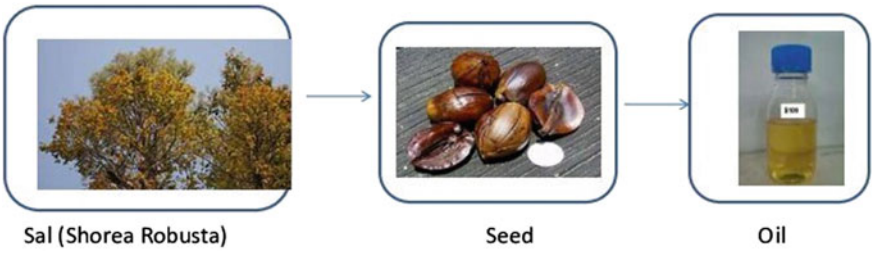


**Fig. 8** Extraction of Sal (*Shorea robusta*) oil

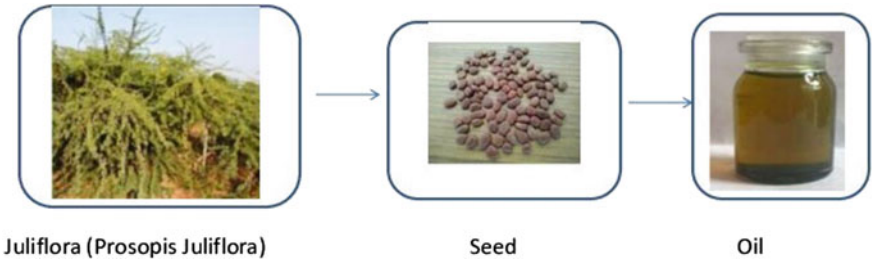


**Fig. 9** Extraction of juliflora (Prosopis juliflora) oil

acid than Sal (*S. robusta*) so can show greater tribological property after epoxidation reaction.

**Juliflora (Prosopis juliflora) oil** is obtained from seed of the *Prosopis juliflora* (shown in Fig. 9) member of the family Fabaceae. Yashvir Singh et al. experimentally investigate the tribological properties of juliflora (Prosopis juliflora) oil with $TiO_2$ nanoparticles addition. Juliflora oil undergoes through transesterification process for chemical modification using two-step transesterification process and trimethylpropane was then added to the product. The modified juliflora oil is tested for friction and wear behavior by using four-ball testers. The variation in the concentration of nanoparticles is from 0.6 to 1.2%. 0.6% of $TiO_2$ nanoparticles show better result in terms of reducing coefficient of friction, wear rate, and less damage to the surface [15]. The methodology used is complex and requires high accuracy.

**Jojoba oil** is obtained from seed of the *Simmondsia chinensis* (shown in Fig. 10.). Mohammed Sadriwala et al. examined the tribological behavior of blends of jojoba oil with conventional mineral oil. In this research, SAE20W40 was considered as base oil and blended it with jojoba oil on percent basis of 0, 5, and 10%. Pin-on-disc machine and Taguchi method were used for analyzing the tribological behavior. The blend with 10% of jojoba oil shows better tribological properties [16]. Sanchit Gupta et al. examined the tribological behavior of blends of jojoba oil with conventional mineral oil. In this research, SAE20W40 was considered as base oil and blended it with jojoba oil on percent basis of 5 to 20%. Pin-on-disc machine was used for


**Fig. 10** Extraction of jojoba oil

analyzing the tribological behavior. Al–7%Si alloy and steel materials were used for pin and disc, respectively. The blend with 10% of jojoba oil shows better tribological properties [17]. The summary of the literature review is shown in Table 1. The physicochemical properties of the oils discussed above are shown in Table 2.

**Table 1** Summary of the literature review

| Non-edible oil | Author | Year | Finding |
|---|---|---|---|
| *Moringa oleifera* | Francis Uchenna et al | 2014 | The blend with 10% of moringa oil fulfills the condition for SAE 30 and SAE 40 grade |
| | Louis M. Nwokocha et al | 2017 | Rheological characteristic of moringa shows that it is solid at 10 °C, liquid at 30–70 °C, and thermally unstable at $90^0$c |
| | Yashvir Singh et. al | 2020 | 0.5% of SiC nanoparticles with chemically modified moringa oil show better result in terms of reducing coefficient of friction, wear rate, and less damage to the surface |
| *Calophyllum inophyllum* | M. Habibullah et al | 2015 | In this study, the results show that CI TMP ester has promising future to supplant mineral oil-based oil as its presentation is vitality productive, hence decreasing energy subordinate |
| | Chandra Mouli et al | 2019 | The blend with 15% of Calophyllum inophyllum seed oil shows better tribological property |
| | Mohammed Zaid et al | 2020 | Coefficient of friction is less for 5 and 10% blend and increases with 15% blend. Similar results were seen for wear analysis |
| Thumba | K. Kamalakar et al | 2015 | Epoxy thumba oil shows higher viscosity, thermal stability and oxidative stability from the other two base stocks. polyol esters show low pour point compared to epoxy thumba oil |

(continued)

**Table 1** (continued)

| Non-edible oil | Author | Year | Finding |
|---|---|---|---|
| Desert date | Yashvir Singh et. al | 2020 | 0.9% of copper nanoparticles with chemically modified desert date oil show better result in terms of reducing coefficient of friction, wear rate, and less damage to the surface |
| *Michellia champaca* | Yashvir Singh et al | 2020 | Improvement in terms of reducing friction, less wear, and damage to the surface was seen by using 0.6% of copper nanoparticles with chemically modified champaca oil |
| *Shorea robusta* | Shailendra Kumar Chaurasia et al | 2020 | Improvement in terms of reducing friction, less wear, and damage to the surface was seen by using 0.5% of copper nanoparticles with chemically modified Sal oil |
| Juliflora | Yashvir Singh et al | 2020 | 0.6% of $TiO_2$ nanoparticles with chemically modified juliflora oil show better result in terms of reducing coefficient of friction, wear rate, and less damage to the surface |
| Jojoba | Mohammed Sadriwala et al | 2019 | The blend with 10% of Jojoba oil shows better tribological properties |
| | Sanchit Gupta et al | 2020 | The blend with 10% of jojoba oil shows better tribological properties when Al-7%Si alloy and steel materials were used for pin and disc, respectively |

## 3 Research Gap and Recommendation

From the literature review, it has been found that an attempt has been made to obtain an alternative to petroleum-based lubricating oil using non-edible oil. In addition, it demonstrates the analysis of tribological behavior of chemically modified biolubricant with nanoparticles as additives. Non-edible oils are biodegradable and have better physicochemical properties than petroleum-based lubricating oil but as a result of unsaturated fatty acid contents it shows less thermal and oxidative stability.

**Table 2** Physicochemical properties of the oils

| Non-edible oil | Kinematic viscosity ($mm^2/s$ at 40 °C) | Kinematic viscosity ($mm^2/s$ at 100 °C) | Viscosity index | Flash point ( °C) | Reference |
|---|---|---|---|---|---|
| *Moring oleifera* | 46.23 | 8.27 | 118 | 159.21 | Yashvir Singh et al. |
| *Calophyllum inophyllum* | 18.45 | 4.11 | 137 | 256.13 | Mohammed Zaid et al. |
| Epoxy thumba (*Citrullus colocynthis* L.) | 216 | 22.7 | 128 | 145 | K. Kamalakar et al. |
| Desert date (*Balanites aegyptiaca*) | 18.84 | 4.21 | 131 | 247 | Yashvir Singh et al. |
| *Michellia champaca* | 73.13 | 10.11 | 117 | 151 | Yashvir Singh et al. |
| Sal (*Shorea robusta*) | 38.3 | 10.29 | 118 | 123.8 | Shailendra Kumar Chaurasia et al. |
| Juliflora (*Prosopis juliflora*) | 45.23 | 8.23 | 112 | 181 | Yashvir Singh et al. |
| Jojoba oil | 174 | 15.7 | 210 | 221 | Sanchit Gupta et al. |

Non-edible oil can be chemically modified by different processes such as transesterification and epoxidation to enhance the thermal and oxidative stability. From the previous study, none of the research concentrated on developing a biolubricant which have greater thermal and oxidation stability along with the enhancing tribological properties by the application of nanoparticles. These studies did not conclude that biolubricant obtained with the application of nanoparticles has greater tribological properties together with thermal stability and oxidation stability. There is a need to develop a flexible environmental-friendly nanolubricant having excellent rheological, tribological properties and antioxidant properties which will be suitable in automotive.

## 4 Conclusion

Existing studies are lacking for dedicated study for developing a biolubricant which has greater thermal and oxidation stability along with the enhancing tribological properties by using of nanoparticles. These studies did not conclude that biolubricant obtained with the application of nanoparticles has greater tribological properties together with thermal stability and oxidation stability. There is a need to develop a

flexible environmental-friendly nanolubricant having excellent rheological, tribological properties and antioxidant properties which will be suitable in automotive application. Nanoparticle as additive is a recent fresh topic for research, there is need to develop a nanolubricant having good oxidation stability without reducing its friction and wear characteristics. For designing a nanolubricant, relationship of structure of nanoparticles and tribological characteristics of bio-oil must be considered and the examination of rheological and antioxidant properties should be in detail by using modern method for analysis.

## References


1. Crouse (2007) Automotive mechanics Tata McGraw-Hill Education, Motor vehicles
2. Cecilia JA, Plata DB, Saboya RMA (2020) An overview of the biolubricant production process: challenges and future perspectives. Processes 8(3):257
3. Singh Y, Sharma A, Singla A (2019) Non-edible vegetable oil–basedfeedstocks capable of bio-lubricant production for automotive sector application—a review. Environ Sci Pollut J: Res 26:14867–14882
4. Uflyand IE, Zhinzhilo VA, Burlakova VE (2018) Metal-containing nanomaterialsas lubricant additives: state-of-the-art and future development. Friction 7(2):93–116
5. Ozioko FU (2014) Synthesis and study of properties of biolubricant based on *Moringa oleifera* for industrial application. A U J T 17(3):137–142
6. Nwokocha LM, Aremu TB (2017) Studies on the biolubricant properties ofmoringaoleifera seed oil: correlating viscosity and fatty acid composition. Malaysian J Sci 36(2):116–131
7. Singh Y, Sharma A, Singh NK, Noor MM (2020) Effect of SiC nanoparticles concentration on novel feedstock Moringa Oleifera chemically treated with neopentylglycol and their trobological behavior. Fuel 280:118630
8. Habibullah M, Masjuki HH, Kalam MA (2015) Tribological characteristics of *Calophyllum inophyllum* based TMP (trimethylolpropane) ester as energy saving and biodegradable lubricant. Tribol Trans J 58(6), 1002–1011
9. Kotturu CMV, Srinivas V, Vandana V, Chebattina KRR, Seetha Rama Rao Y (2020) Investigation of tribological propertiesand engine performance of polyolester–based bio-lubricant: commercial motorbike engine oil blends. Sage 234(5):1304–1317
10. Zaid M, Singh Y, Kumar A, Gupta S (2020) Development of the *Calophyllum inophyllum* based biolubricant and their tribological analysis at differentconditions. Mater Today: Proc 26(Part 2):2582–2585
11. Kamalakar K, SaiManoj GNVT, Prasad RBN, Karuna MSL (2015) Thumba (*Citrullus colocynthis* L.) seed oil: a potential bio-lubricant base-stock. Int J Fats oil 66(1)
12. Singh Y, Sharma A, Singh NK, Chen W-H (2020) Development of biobased lubricant from modified desert date oil (*Balanites* aegyptiaca) with copper nanoparticles addition and their tribological analysis. Fuel 259:11625 (2020)
13. Singh Y, Abd Rahim E (2020) *Michelia champaca*: sustainable novel non-edible oil as nano based biolubricant with tribological investigation. Fuel 282:118830
14. Chaurasia SK, Singh NK, Singh LK (2020) Friction and wear behavior of chemically modified Sal (*Shorea robusta*) oil for bio based lubricant application with effect of CuO nanoparticles. Fuel 282:118762
15. Singh Y, Singh D, Singla A, Sharma A, Singh NK (2020) Chemical modification of juliflora oil with trimethylolpropane (TMP) and effect of $TiO_2$ nanoparticles concentration during tribological investigation. Fuel 280:118704
16. Sadriwala M, Singh Y, Sharma A, Singla A, Mishra S (2020) Friction and wear behavior of jojoba oil based biolubricant-Taguchi method approach. Mater Today Proc 25(Part 4):704–709

17. Gupta S, Zaid M, Kumar A, Singh Y (2020) Effect of Jojoba oil based biolubricant additive on the friction and wear characteristics of the Al-7Si alloy. Mater Today Proc 26(Part 2):2681–2684

# Effect of Nanoparticles on the Performance and Emission Characteristics of Diesel Engine Operated with Different Fuels


**Deresse Firew, Getachew Alemayehu, Ramesh Babu Nallamothu, and Sung Kyu Kang**

## 1 Introduction

Diesel engines are successfully used to power vehicles, aeroplanes, irrigation pumps, trains, ships, and electric generators used for production of electric power. Combustion of fossil fuels produces emissions which are negatively effecting human health and ecosystem. To overcome this problem, it has become an international target to develop clean alternate fuels those are available, internationally acceptable, and technically practicable. The realization of energy concerns and environmental problems related to the burning of fossil fuels has pushed researchers to study opportunity of using non-conventional energy sources, as alternative fuel source to fossil fuels and its derivatives [1, 2].

Availability and efficient utilization of energy determine the socioeconomic status of any country [3]. Diesel engines have outstanding characteristics out of the various energy conversion devices, such as higher thermal efficiency, utilization of leaner air–fuel mixtures, high compression ratios, low specific fuel consumption, reliability, and low maintenance and operating costs. Regardless of having incredible superiorities, diesel engines are emitting a large number of pollutants such as CO, $NO_x$, soot, and unburned hydrocarbons, which causes environmental degradation and serious health hazards [4–6]. Moreover, petroleum-derived fuels are depleting due to additional demand due to the growth of population and vast energy utilization [7].

Engine manufacturers are continuously improving their design to increase economy of fuel and to meet emission standards by reducing pollutants from exhaust

D. Firew · G. Alemayehu · R. B. Nallamothu (✉)
Mechanical Systems and Vehicle Engineering Department, SoMCME, Adama Science and Technology University, Adama, Ethiopia
e-mail: ramesh.babu@astu.edu.et

S. K. Kang
Mechanical Engineering Department, Jimma University, Jimma, Ethiopia



K. Jha et al. (eds.), *Recent Advances in Sustainable Technologies*,
Lecture Notes in Mechanical Engineering,
https://doi.org/10.1007/978-981-16-0976-3_27

emission [8, 9]. This condition has motivated many researchers to focus on alternative fuels to alleviate the problem in addition to engine design improvement. Fuel modification strategies consist of mainly improvising the fuel characteristics to improve combustion, which is responsible for better engine performance, low exhaust emissions, and high fuel economy [10].

The difficulties mentioned above can be overcome by finding out more environmentally friendly oxygenated fuels such as ethanol [2, 11]. Agricultural produce such as sugarcane, cassava, molasses, waste biomass materials, corn, sorghum, barley, and sugar beets can be used for ethanol production. Ethanol can be derived from ethane or ethylene through a chemical process. It is biobased renewable fuel with a simple molecular structure having hydrogen, carbon, and oxygen atoms [12]. Because of the water content, a wide range of temperature of the diesel fuel, hydrocarbon composition, and prevailing wax content, it is difficult to easily mix ethanol with diesel fuel. Especially more than 1% v/v ratio water content in ethanol makes phase separation to occur usually in the fuel blend [13–15]. To solve this problem emulsifier and co-solvent can be used. Important physicochemical properties such as heating value and cetane number are reduced in the diesel–alcohol blends. These properties can be improved by the use of additives.

The mixing of ethanol in diesel fuel causes physicochemical change. It can reduce the heat content, cetane number, flashpoint, and viscosity. For example, the blended fuel heat content is reducing by 2% for 5v/v% mixing of ethanol to diesel fuel. Table 1 shows the decrease in the heat content with the increase in ethanol content [16].

The cetane number of ethanol is very low, so this makes the diesel–ethanol blend fuel cetane number to significantly decrease, the cetane number [14, 16, 17]. The cetane number reduces four units in the diesel–ethanol blend for each 5% v/v ratio ethanol increase in the diesel fuel. Figure 1 shows the effect of ethanol content on cetane number.

Ethanol–diesel blends usually need additives to improve stability, miscibility lubricity, and cetane number to improve combustion efficiency due to of decreasing knock, and confirm the efficient operation of the engine [18]. Based on their functions, fuel additives are categorized into a variety of groups [19]. The additives category includes ignition promoters, combustion modifiers, antiknock compounds, antioxidants additives, anti-wear additives, stabilizers, etc., and based on their chemical nature are classified as oxygenized, metal-based, nonmetal-based additives, etc. Nanoparticles have amazing properties. Due to their size and can considerably change the combustion property of the fuel they are added. Moreover, for reducing exhaust

**Table 1** Heat of diesel–ethanol mixtures [16]

| Mixtures gross heat content | (MJ/kg) |
|---|---|
| Diesel | 42.35 |
| Diesel + 10% ethanol | 40.98 |
| Diesel + 15% ethanol | 40.75 |
| Diesel + 20% ethanol | 39.59 |

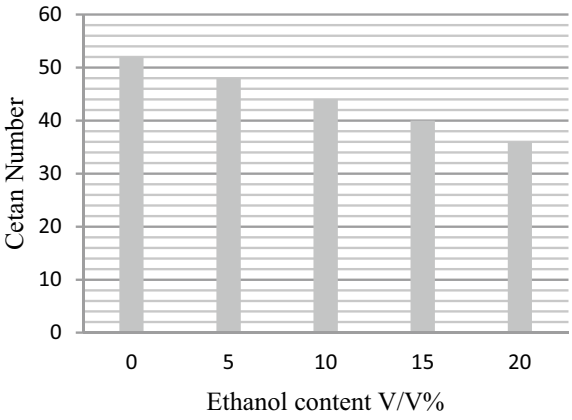


**Fig. 1** Effect of ethanol content on cetane number of diesel fuel [17]

emissions and for improving engine performance, nanoparticles are used as fuel additives [20].

The combustion performance of conventional fuel is improved by adding a few micrometer-sized metallic particles. But the problem with microsized metallic particles is the increase in ignition delay period which consequences engine knocks [21]. The reason for ignition delay is reported as due to smaller surface area to volume ratio compared to metallic nanoparticles fuel additives [22]. Fuels with nanoparticle additive called nanofluids are considered as a new variety of fuel that attracts the attention of many researchers because of their high heat transfer rate for heat exchangers and other strong thermophysical properties [23].

Many researchers have accepted that the mixing of nanoparticles improves fuel properties. The purpose of nanoparticles is to improve fuel properties as a result to achieve reduced pollutant exhaust emissions and to increase the performance of the engine as well as to use biofuel without engine modification. On commercially available fuel, nanoparticles are added to achieve certain properties and expected to reduce the exhaust pollution, increase the oxygen content in the engine, maintain fluid stability, reduction in ignition delay, enhance the lubricity index, and flashpoint, the chemical to chemical contact must be enhanced instead of metal to metal contact to reduce wear [24].

Blending alcohol with diesel fuel causes decrease in cetane number of blended fuel. The decrement in cetane number of alcohol–diesel fuel blends could increase noise and vibration [25]. On a research done on butanol–diesel fuel blend, the addition of $TiO_2$-based additive significantly reduced vibrations and noise. The additional oxygen content and catalytic effect of the $TiO_2$ nano-additive lead to reduced ignition delay, thus lowering of knocking tendency. It is also mentioned that at a lower percentage of alcohol nano-additives were more effective, but with a more percentage of ethanol, the observed difference is not significant [26].

The depletion of petroleum-based fuel and the hazards emission from engines is a motivational factor to research in the area of unconventional fuel specifically for diesel engines. For improving the performance properties such as BP, BSFC,

BTE, and to reduce the exhaust emission of diesel engine, nanoparticles addition is promising. The objective of this review article is to see the effect of nanoparticles addition in both diesel and blended fuels, on emission and performance characteristics of a diesel engine. The article is extracted from research journals published to the year 2020 which gives an idea about the recent trends in nano-additive researches.

## 2 Performance Characteristics

Biofuels having comparable properties of diesel are the most interesting alternative fuels and are expected to replace diesel fuels in the future. On the other hand, due to shortfalls like lower power and engine speed, higher BSFC and lower mixture stability, biofuel is not fully utilized in diesel engine. Numerous researchers are trying to find variety of methods and technologies to overcome the problems. One promising method of improving the properties of biofuel is the utilization of nanoadditives. The performance parameters of C.I engine such as BSFC, BP, BTE, of different biofuels with the mixing of different nanoparticles have been reviewed.

On many research papers, it is investigated that, the mixing of nanoparticles with diesel–biofuel (biodiesel and alcohol) emulsions progress fast and complete combustion process because of improved radiative and heat mass transport property, which improves combustion efficiency [27].

Compared to neat diesel, fuels with metallic-based additives showed a reducing trend in BSFC [28]. The consequence of $Al_2O_3$ nanoparticles on the emission characteristics and performance enhancement in a single-cylinder, four-stroke diesel engines is studied. Two different amounts 0.1 and 0.5% by weight of $Al_2O_3$ nanoparticles were utilized as a fuel additive. The performance test result is compared with net diesel fuel. The results designated that the fuel with a concentration of 0.5% nanoparticle gives better performance characteristics when compared with 0.1% and the addition of $Al_2O_3$ indicated a highest reduce of 31% in BSFC at maximum load as compared to that of diesel [29]. Nanoparticles addition increases the calorific value of fuels slightly hence causing a decrease in BSFC. High surface area of the metallic additives causes the decrease in BSFC and improved combustion quality [26].

Characteristics of a diesel engine by adding 60 ppm GQD nanoparticle to bioethanol with 10% biodiesel (B10) and 2, 4, and 6%, vol. of ethanol at different engine speeds of (1800, 2100, and 2400 rpm). It is concluded that the addition of GQD nanoparticle generally improves the performance of the engine and reduced exhaust emission. The specific fuel selected as B10 + E4 + GQD60 is the most favorable fuel at all speeds. In relation to pure diesel fuel, the optimal fuel (B10 + E4 + GQD60) improved the engine power and torque with 24.59% and 20.02%, respectively [30].

The experimental work focuses on the effect of $Al_2O_3$ nanoparticle on a combination of diesel 70%, biodiesel 20%, and ethanol 10% (called as BDE) by varying injection timing. The effects of 25 ppm $Al_2O_3$ in BDE blend at 19° bTDC IT in single-cylinder diesel engine. $Al_2O_3$ addition causes lower heat release and cylinder

pressure away from TDC, resulting in lesser BSFC better engine performance and combustion [31].

The collective effect of nanoparticle additives, injection timing, and combustion chamber geometry in single-cylinder diesel engine is with ethanol, diesel, and biodiesel mix was tested. The fuel is tested with different combustion chamber geometries and injection timings, namely 21°, 22°, 23°, and 24° bTDC. The result indicated the highest BTE of about 33.8%. Lowest BSFC profile was achieved at 22° bTDC with an increase of 11.51% BTE in comparison with neat diesel [32].

Effects of GQD nanoparticles on emission and performance of a diesel engine with ethanol–biodiesel blends in the blend of B10 are studied. The concentration of GQD nanoparticles used is 30 ppm for the fuel blend. The experiment is conducted at various engine speeds of 1800, 2100, and 2400 rpm. The performance parameters, such as power, torque, and SFC, were investigated and results are found. Mixing GQD nanoparticles to fuel improved power and torque by 28.18% and 14.35%, respectively, reduced SFC by 12.42% compared to D100 fuel [33].

Emission and performance characteristics study on the use of $TiO_2$ nanoparticles addition in neat diesel fuel. The study showed that characteristics of petroleum diesel such as viscosity, density, calorific value, and fire point improve with the mixing of the nanoparticles. Engine performance test results showed improvement in brake thermal efficiency and reduction in BSFC by 22% with the addition of the nanoparticles at the highest load [34].

Investigation on the result of CNT and molybdenum trioxide ($MoO_3$) nanoparticles on fuel consumption, performance, and emissions characteristics of diesel in a CRDI diesel engine is studied. The experiments are conducted in single-cylinder common rail diesel engine for investigating and comparing the engine emission and performance characteristics of the nanofuels with pure diesel. The test fuels include 100CNT (diesel + 100 mg/L CTAB + 100 mg/L CNT) and 100$MoO_3$ (diesel + 100 mg/L CTAB + 100 mg/L $MoO_3$). The BTE of the 100CNT is increased by 5.2% and 100$MoO_3$ by 2.3%, and BSFCs were decreased by 5.1% for 100CNT and 2.3% for 100$MoO_3$, respectively, compared to pure diesel [18].

Engine performance and emission characteristics of two fuels B20(80% diesel and 20% soybean biodiesel) and D80SBD15E4S1 þ alumina (80% diesel, 15% soybean biodiesel, 4% ethanol, and 1% surfactant, and alumina nanoparticles, 100 mg/L) fuel blends are compared with neat diesel. Brake thermal efficiency is higher for B20 and D80SBD15E4S1 þ alumina fuel mix compared to neat diesel at maximum load. An increase in brake thermal efficiency of 15.8% and 17.9% was observed in the case of B20 and D80SBD15E4S1 þ alumina fuel blend, respectively, contrasted with pure diesel at full load. It is due to the presence of higher oxygen in the fuel complete combustion occurred in the case of B20 and the case of D80SBD15E4S1 þ alumina fuel blend due to the presence of the alumina nanoparticle the further increase in efficiency is because of the higher evaporation rate and the microexplosion of the primary droplets. The BSFC is minimal compared to the neat diesel at higher loads of 75% and full load. The existence of the alumina nanoparticle improves the atomization rate that enhances complete combustion and increases the heat transfer from the combustion, thus lowering the sink temperature, resulting in

engine performance increment. The BSFC is 3.53 for D80SBD15E4S1 þ alumina, 3.7 for B20, and 4.33 for neat diesel. This shows the high viscosity within the case of B20 and D80SBD15E4S1 þ alumina fuel mix is overcome, by the diminishing in viscosity at higher temperatures within the case of the full-stack condition [35].

The effect of three different nanoparticles, $Al_2O_3$, CNT, and silicon oxide as a diesel fuel additive is investigated and compared on the performances and exhaust emissions in a four-stroke single-cylinder diesel engine. The nanoparticles were mixed in a dosage of 25, 50, and 100 ppm with pure diesel. The blended fuels were tested at engine loads of 0, 25, 50, 75, and 100% at a constant engine speed of 1800 rpm. The test results revealed that the BSFC of CNT blend is reduced by up to 19.8% and BTE improved by 18.8%. Silicon oxide blends show better results than $Al_2O_3$ blends in lower brake specific fuel consumption [36].

The investigation is made on the performance and emission characteristics of CIME nanoemulsions in a two-cylinder CI engine. The test is conducted with diesel, pure biodiesel, and biodiesel nanoemulsions dispersed with $TiO_2$ and ZnO nanoparticles. Calophyllum inophyllum biodiesel nanoemulsions at 50 and 100 ppm concentrations have been studied and the results were compared with pure biodiesel and neat diesel fuels. The engine performance result indicated that the highest brake thermal effectiveness is 33% for diesel fuel, 31% for biodiesel-T100, 30% for biodiesel-T50, 27% for biodiesel-Z100, 28% for biodiesel-Z50, and 26% for pure biodiesel at full engine load. The BSFC of pure Calophyllum inophyllum biodiesel and CIME nanoemulsions is higher compared to diesel fuel at all loadings. The BSFC of CIME-T100 is 0.24 kg/kWh and whereas 0.258 kg/kWh for CIME-Z100 at full engine load. The researchers concluded due to the lower calorific value of biodiesel increased the fuel consumption to achieve the same power output. It is evident that all nanoemulsions of CIME; CIME-Z50, CIMEZ100, CIME-T50, and CIME-T100 resulted in lower BSFC compared to CIME without nanoparticle addition [37].

The influence of different nanoparticles and hydrogen mix on engine characteristics of performance and emission on dual fuel systems is studied. The nanoparticles used for the study are CuO, CNT, $CeO_2$, $TiO_2$, and $Al_2O_3$. The nanoparticles are added at a dosage level of 100 ppm with 20% hydrogen fuel. The test is conducted at a speed of 1800 rpm in different engine loads of 0, 25, 50, 75, and 100%. The brake thermal efficiency by adding up of increases by 4.3% for $CeO_2$ and 2.5% for $Al_2O_3$. In the meantime, for $CeO_2$ the BSFC is observed to be insignificant. CNT and $TiO_2$ nanoparticles indicate a 23 and 22% decrease in BSFC than other blends [38].

The addition of nanoparticles improves fuel properties such as a rush in heating value, a fall in fuel viscosity improves cetane number due to the enhanced surface area/volume ratio of the nanoparticles which consequences improvement in BTE. Nanoparticles have a catalytic property that promotes combustion by generating microexplosion of primary droplets that could vaporize the fuel and enhances mixing with air to reduce ignition delay. The other helpful effect of nanoparticle additives is the increment in heat transfer so that it can facilitate combustion and increase the heat release rate. Therefore, adding nanoparticles to fuel increases the performance of engines by increasing the probability of complete combustion [37–39].

## 3 Emission Characteristics

Researchers have shown that in densely populated municipal areas, the usual revelation to diesel exhaust could pass damage to health. Despite the advantages, diesel engines are a severe cause of air pollution caused by exhaust dangerous gas emissions, including $CO_2$, CO, $NO_x$, and sulfur oxide [39]. The community concerning ecological and well-being has been blaming the topic of diesel engine exhaust emissions on the influence of human health. It is worrying to figure out that engine pollution affects human health on a huge level. Moreover, diesel engine emissions contain many toxic substances such as $NO_x$, $SO_x$, CO, $CO_2$ carcinogens, and mutagens. Additionally, animals and humans become major expose for lung cancer which has health risk in health research. Research on truck drivers and railroad workers exposed to diesel engine exhaust due to their occupation showed that tend to have to increase in getting lung cancer with escalating years of work in the exposed job and the workers have been found in risk [40].

To improve the emission characteristics of diesel engine, many researches have been done on fuel additives. The effect of metallic nanoparticles investigated in different researches is reviewed. The employment of aluminum oxide ($Al_2O_3$) nanoparticles as fuel additive reduces the emission of $NO_x$ ious waste like $CO_2$ and HC compared to petro-diesel fuel [29].

On the research work done to evaluate the performance parameters and emissions characteristics of a diesel engine by adding 60 ppm graphene quantum dot (GQD) nanoparticle to bioethanol fuel, a considerable emission reduction is achieved with 10% biodiesel (B10) and 2, 4, and 6%, volume of ethanol at different engine speeds of (1800, 2100, and 2400 rpm). The specific fuel selected as B10 + E4 + GQD60 reduced UHC and CO emissions by 42.05% and 35.60%, respectively, compared to the pure diesel fuel [34].

An experimental work which focuses on the effect of alumina ($Al_2O_3$) nanoparticle on a mix of 20% biodiesel, 70% diesel, and 10% ethanol (called as BDE) by varying injection timing is carried out. The effect of 25 ppm $Al_2O_3$ in BDE blend at 19° bTDC IT in a single-cylinder diesel engine effect in reductions of $NO_x$, HC, CO, and smoke opacity [31].

Harish Venu et al. experimented on the joint effect of nanoparticles additive, combustion chamber design, and injection timing in a diesel single-cylinder engine. Diesel, biodiesel, and ethanol blends which they called ternary fuel after alumina nanoparticles have been added to the fuel, they termed the resulting fuel as high-performance fuel. The high-performance fuel is tested with different combustion chamber shape and injection timings, namely 21°, 22°, 23°, and 24° bTDC. The test result indicated lesser HC and CO emissions of 9.18 and 16.83% in contrast to 22° bTDC and lowered $NO_x$ emissions by 22.53% in comparison with net diesel [32].

Graphene quantum dot nanoparticles are studied for performance and emissions on a diesel engine with ethanol–biodiesel mix in diesel engine. The concentration of GQD nanoparticles used is 30 ppm. An experiment is conducted at various engine speeds of 800, 2100, and 2400 rpm. Emission parameters such as CO, $CO_2$, UHC, and

$NO_x$ were investigated. CO and UHC decreased by 29.54% and 31.12%, respectively, and $NO_x$ emission resulted in 1.29% increment, compared to net diesel fuel [33].

The study on the influence of TiO2 nanoparticles additive in neat diesel fuel on the emission characteristics of CI engine is performed with and without $TiO_2$ nanoparticles additive. It is watched that with the expansion of nanoparticles there is a diminish on the emission of unburnt hydrocarbons by 18% and carbon monoxide by 25% [34].

Deqing Mei et al. have investigated the effect of carbon nanotube (CNT) and nano molybdenum trioxide ($MoO_3$) on emissions characteristics of diesel in a common rail diesel engine. Single-cylinder common rail diesel engine is used to conduct the experiments for investigating and comparing the engine emissions characteristics of nanofuels with neat diesel. The test fuels include 100CNT (dsiesel + 100 mg/L CTAB + 100 mg/L CNT) and 100$MoO_3$ (diesel + 100 mg/L CTAB + 100 mg/L $MoO_3$). The test result showed that emissions of HC, CO, $NO_x$, and soot with the adding of CNT and $MoO_3$ to pure diesel were declined to different levels. CNT shows better capability in lowering all the emissions HC 11.4%, CO 9.6%, $NO_x$ 8.9%, and smoke 15.2%, than neat diesel and $MoO_3$ resulted in an emission reduction of HC 7.5%, CO, 6.8%, $NO_x$ 5.2%, and smoke 8.3%, than neat diesel [18].

T. Shaafi and R. Velraj have investigated the emission characteristics and engine performance of two modified fuels B20(80% diesel and 20% soybean biodiesel) and D80SBD15E4S1, alumina (80% diesel, 15% soybean biodiesel, 4% ethanol, and 1% isopropanol as an emulsifier, and alumina nanoparticles of 100 mg/L) fuel blends, in comparison with pure diesel. They also reported very encouraging results on the emission characteristics. The emission reduction is due to the inbuilt oxygen present in the soybean biodiesel and its improved utilization by the occurrence of the alumina nanoparticle. However, at full load condition alumina nanoparticle increased $NO_x$ emission, by 9.9% in case of D80SBD15E4S1, alumina fuel blend correspondingly, when compared to pure diesel [35].

Ang F. Chena et al. investigated exhaust emissions characteristics of carbon nanotubes, aluminum oxide, and silicon oxide nanoparticles in a four-stroke single-cylinder engine. From the experiment, it is revealed that CNT nanoparticles product in elevated CO, $CO_2$, HC and lower $NO_x$ emissions of 4.48%. CNT blends with diesel show a better performance result to improve the emission characteristics carbon nanotubes have the possible to be more research as an additive for diesel fuel due to important combustion decrease in $NO_x$ emissions [36, 41].

The research done by K. Nanthagopal et al. investigated the emission characteristics and performance of Calophyllum inophyllum biodiesel (CIME) nanoemulsions on two cylinders CI engine. The unburned HC and CO emissions are lower for all CIME nanoemulsions relative to pure CIME and conventional diesel fuel because of the oxidation effect of $TiO_2$ and ZnO nanoparticles. The fuel CIME-T100 provided a maximum decrease in HC emission measure up to all other fuel. The CO emission is 24.5% lesser for CIME fuel process than that of pure diesel at full load. CO emission is relatively lesser for CIME-T100 nanoemulsion measure up to CIME-Z100 nanoemulsion fuel. $NO_x$ emission reduction of 7–29% is observed for all CIME

nanoemulsions fuels compared to neat Calophyllum inophyllum biodiesel at full engine load. This is because of the catalytic effect of the nanoparticles [37, 42].

On the study conducted by S. Manigandan et al. on $Al_2O_3$, CNT, $TiO_2$, $CeO_2$, and CuO nanoparticles and hydrogen mix on emission characteristics, the test is done at different engine load conditions. The exhaust emission results showed hydrogen and nanoparticles addition decreases carbon dioxide, monoxide, and hydrocarbon emissions considerably. However, for $NO_x$ emission, CNT is the only blend which showed a decrease in $NO_x$ than other blends. From the results, they concluded that the addition of hydrogen and nanoparticles pure diesel reduced exhaust gas emission [38, 43–45].

The expansion of nanoparticles in fuel advances total combustion due to its catalytic property and increase in cetane number. Complete combustion comes about in diminish of CO and concentration of HC emanation [39, 40, 46]. In diesel motors, $NO_x$ is shaped due to the oxidation of the air nitrogen $N_2$ in crest combustion temperature. The blending of nanoparticles with diesel rises the top combustion temperature, causing more $N_2$ within the combustion chamber to be oxidized to $NO_x$ amid combustion [2, 44]. Be that as it may, diesel blended with the nanoparticle, biodiesel emulsified fuel it has been found that $NO_x$ outflow levels were diminished in comparison with diesel fuel. This was ascribed due to heat sink impact of emulsified fuel which smothers the in-cylinder gas temperatures amid combustion. Summary of the nanoparticles influence on diesel and different biofuels is given in Table 2.

## 4 Conclusion

This review intends to see the effect of different nanoparticles on CI engine when added into neat diesel and variety of biofuels. The exhaust emission and performance characteristics of different nanoparticles such as CNT, $MoO_3$, $Al_2O_3$, $TiO_2$ ZnO, $CeO_2$, and GQD are reviewed. In this review, the fuels covered are neat diesel, diesel biodiesel and ethanol emulsion, ethanol–biodiesel blends, biodiesel, diesel + 20% hydrogen. From the researches done by combining the mentioned nanoparticles and fuels, the following conclusion is drawn.

CNT and $Al_2O_3$ nanoparticles additives dispersed in diesel and diesel, biodiesel and ethanol emulsion, respectively, have shown relatively the highest BTE. The increment in BTE is due to the increase in calorific value and short ignition delay time because of improvement in fuel combustion property.

The addition of all the nanoparticles indicated a significant reduction in BSFC as a hall. The highest BSFC reduction is reported for the $Al_2O_3$ in neat diesel addition by 31% and the minimum is for the combination of $MoO_3$ in neat diesel which is 2.3%.

Regarding brake power and brake torque even though there is a shortage of data on the reviewed papers the available data for GQD in bioethanol with 10% (B10) and ethanol-biodiesel blends fuels indicates significant increment.

**Table 2** Summary of nanoparticles influence on neat diesel and different biofuels

| References | Fuel | Nanoparticle | BTE | BSFC | BP | Tb | $CO_2$ | CO | UHC | $NO_x$ |
|---|---|---|---|---|---|---|---|---|---|---|
| [31] | Neat diesel | $Al_2O_3$ | _ | 31%↓ | _ | _ | ↓ | _ | ↓ | _ |
| [32] | Bioethanol with 10% (B10) | GQD | _ | ↓ | 24.59%↑ | 20.02%↑ | _ | 35.60%↓ | 42.05%↓ | _ |
| [33] | Diesel, biodiesel, and ethanol emulsion | $Al_2O_3$ | _ | ↓ | _ | _ | _ | ↓ | ↓ | ↓ |
| [34] | Biodiesel and ethanol blend | Alumina nanoparticles | 11.51% ↑ | _ | _ | _ | _ | 16.83%↓ | 9.18% ↓ | 22.53%↓ |
| [35] | Ethanol–biodiesel blends | GQD | _ | 12.42% ↓ | 28.18%↑ | 14.35% ↑ | _ | 29.54%↓ | 31.12%↓ | 1.29%↑ |
| [36] | Neat diesel | $TiO_2$ | ↑ | 22%↓ | _ | _ | _ | 25%↓ | 18%↓ | _ |
| [19] | Neat diesel | CNT and $MoO_3$ | 5.2% and 2.3%, ↑ | 5.1% and 2.3%↓ | _ | _ | _ | 9.6% And 6.8%↓ | 11.4%, and 7.5%↓ | 8.9% And 5.2%↓ |
| [37] | Diesel, biodiesel, and ethanol emulsion | $Al_2O_3$ | 17.9%↑ | 18.5%↓ | _ | _ | 3.3% ↓ | 66% ↓ | _ | 9.9%↑ |
| [38] | Neat diesel | CNT | 18.8%↑ | 19.8% ↓ | _ | _ | ↑ | ↑ | ↑ | 4.48%↑ |
| [39] | Calophyllum inophyllum biodiesel | $TiO_2$ and ZnO | 4% and 2%, ↑ | 0.24 and 0.258 kg/kWh↓ | _ | _ | _ | ↓ | ↓ | 7–29%↓ |
| [40] | Diesel + 20% hydrogen | $CeO_2$ and $Al_2O_3$ | 4.3% and 2.5%↑ | 23% and 22%↓ | _ | _ | ↓ | ↓ | ↓ | ↓ |

*Note* ↑—Increase, ↓—decrease

When we see the CO and HC emission 90% of the research investigations show a reduction in varying level. $Al_2O_3$, GQD, and $TiO_2$ nanoparticles resulted in a very significant reduction of HC and CO emission.

For $NO_x$ emission, inconsistent results are seen from the reports. The majority of the research indicated there is a reduction of $NO_x$ emission. Some of the reports which are done as CNT in neat diesel, $Al_2O_3$ in diesel, biodiesel and ethanol emulsion and GQD in ethanol–biodiesel blends showed an increment in $NO_x$ emission relative to the base fuel.

## References


1. Carraretto C, Macor A, Mirandola A, Stoppato A, Tonon S (2004) Biodiesel as alternative fuel: experimental analysis and energetic evaluations. Energy 29(12–15)
2. Ahmad A, Yasin NM, Derek C, Lim J (2011) Microalgae as a sustainable energy source for biodiesel production: a review. Renew Sustain Energy Rev 15(1):584–593
3. Kumar N, Varun, Chauhan SR (2013) Performance and emission characteristics of biodiesel from different origins: a review. Renew Sustain Energy Rev 21:633–658
4. Bhandarkar S (2013) Vehicular pollution, their effect on human health and mitigation measures. Veh Eng 1(2):33–40
5. Kumar, Tyagi SK (2006) Benzene and toluene profiles in ambient air of Delhi as determined by active sampling and GC analysis. J Sci Ind Res 65:252–257
6. U.S. Environmental Protection Agency (2009) Summary and analysis of comments: control of emissions from new marine Compression Ignition engines at or above 30 liters per cylinder, Assessment and Standards Division Office of Transportation and Air Quality. EPA-420-R-09-015.
7. "A Report of International Energy Agency". www.eia.gov.cfm for executive summary: short-term energy outlook, analysis and projections. Report Number DOE/EIA-0484(2016), OECD/IEA (2016).
8. Banapurmath NR, Budzianowski WM, Basavarajappa YH, Hosmath RS, Yaliwal VS, Tewari PG (2014) Effects of compression ratio, swirl augmentation techniques and ethanol addition on the combustion of CNG-biodiesel in a dual-fuel engine. Int J Sustain Eng 7:55–70
9. Kumar N, Varun, Chauhan SR (2016) Evaluation of the effects of engine parameters on performance and emissions of diesel engine operating with biodiesel blend. Int J Ambient Energy 37:121–135.
10. Saxena VK, Tiwari HP, Banerjee PK (2013) A noble technique for accessing the cooking potential of coals/coal beds for non-recovery coke making process. Fuel 107:615622
11. Chockalingam SR, Sambandam A, Subramanian S, Ganapathy S (2010) Performance analysis of 1,4 dioxane-ethanol-diesel blends on diesel engines with and without thermal barrier coating. Thermal Sci 14:979–988
12. Cahyono B, Bakar RA (2011) Effect of ethanol addition in the combustion process during warm-ups and half-open throttle on port injection gasoline engine. Am J Eng Appl Sci 4:66–69
13. Lincy R, Wang KH (2003) The fuel properties of three phases emulsion as an alternative fuel for diesel engine. Fuel 82:1367–1375
14. Gerdes KR, Suppes GJ (2001) Miscibility of ethanol in diesel fuels. Ind Eng Chem Res 40:949–956
15. Mccormick RL, Parish R (2001) Advanced petroleum based fuels program and renewable diesel program, milestone report: technical barriers to the use of ethanol in diesel fuel. National Renewable Energy Laboratory
16. Satgé De Caro P, Mouloungui Z, Vaitilingomb G Berge JCh (2001) Interest of combining an additive with diesel–ethanol blends for use in diesel engines. Fuel 80:565–574

17. Chao HR, Lin TC, Chao MR, Chang FH, Huang CI, Chen CB (2000) J Hazard Mater B73:39–54
18. Shaafi T, Velraj R (2015) Influence of alumina nanoparticles, ethanol and isopropanol blend as additive with diesel soybean biodiesel blend fuel: Combustion, engine performance and emissions. Renew Energy 80:655
19. Shaafi T, Sairam K, Gopinath A, Kumaresan G, Velraj R (2015) Effect of dispersion of various nano additives on the performance and emission characteristics of a CI engine fuelled with diesel, biodiesel and blends a review. Renew Sust Energ Rev 49:563
20. Hunt EM, Pantoya ML (2005) Ignition dynamics and activation energies of metallic thermites: from nano- to micron-scale particulate composities. J Appl Phys 98:034909, 8
21. Dreizin EL, Schoentitz M (2015) Correlating ignition mechanisms of aluminum-based reactive materials with thermoanalytical measurements. Prog Energy Combust Sci 50:81–105
22. Wong KV, de Leon O (2010) Applications of nanofluids: current and future. Adv Mech Eng. Article ID 519659
23. Ribeiro NM et al (2007) The role of additives for diesel and diesel blended (ethanol or biodiesel) fuels: a review. Energy Fuels 21(4):2433–2445
24. Tutak W, Lukács K, Szwaja S, Bereczky Á (2015) Fuel 154:196. https://doi.org/10.1016/j.fuel.2015.03.071
25. Yaşar A, Keskin Ş, Yıldızhan E, Uludamar, Ocakoğlu K (2018) Int J Glob Warm 15:38. https://doi.org/10.1504/IJGW.2018.091950
26. Soudagara MEM, Nik-Ghazalia N-N, Abul Kalam M, Badruddin IA, Banapurmath NR, Akrama N (2018) The effect of nano-additives in diesel-biodiesel fuel blends: a comprehensive review on stability, engine performance and emission characteristics. Energy Convers Manag 178:146–177
27. Qi D, Chen H, Geng L, Bian YZ (2010) Experimental studies on the combustion characteristics and performance of a direct injection engine fueled with biodiesel/ diesel blends. Energy Convers Manag 51(12)2985–2992
28. D'Silva R, Binu KG, Bhat T (2015) Performance and emission characteristics of a CI engine fuelled with diesel and $TiO_2$ nanoparticles as fuel additive. Mater Today Proc 2:3728–3735
29. Heidari-Maleni A, Gundoshmian TM, Karimi B, Jahanbakhshi A, Ghobadian B (2020) A novel fuel based on biocompatible nanoparticles and ethanol-biodiesel blends to improve diesel engines performance and reduce exhaust emissions. Fuel 276:118079
30. Venu H, Madhavan V (2016) Effect of $Al_2O_3$ nanoparticles in biodiesel-diesel-ethanol blends at various injection strategies: performance, combustion and emission characteristics. Fuel 186:176–189
31. Venu H, Dhana Raju V, Subramani L (2019) Combined effect of influence of nano additives, combustion chamber geometry and injection timing in a DI diesel engine fuelled with ternary (diesel-biodiesel-ethanol) blends. Energy 174:386e406.
32. Heidari-Maleni A, Gundoshmian TM, Jahanbakhshi A, Ghobadian B (2020) Performance improvement and exhaust emissions reduction in diesel engine through the use of graphene quantum dot (GQD) nanoparticles and ethanol biodiesel blends. Fuel 267:117116
33. D'Silva R, Binu KG, Bhat T (2015) Performance and Emission Characteristics of a C.I. Engine fuelled with diesel and $TiO_2$ nanoparticles as fuel additive. Mater Today: Proc 2:3728–3735.
34. Mei D, Zuo L, Adu-Mensah D, Li X, Yuan Y (2019) Combustion characteristics and emissions of a common rail diesel engine using nanoparticle-diesel blends with carbon nanotube and molybdenum trioxide. Appl Therm Eng 162:114238
35. Chena AF, Akmal Adzmia M, Adamb A, Fahmi Othmana M, Kamal Kamaruzzamana M, Mrwana AG (2018) Combustion characteristics, engine performances and emissions of a diesel engine using nanoparticle-diesel fuel blends with aluminium oxide, carbon nanotubes and silicon oxide. Energy Convers Manag 171:461–477
36. Nanthagopal K, Ashok B, Tamilarasu A, Johny A, Mohan A (2017) Influence on the effect of zinc oxide and titanium dioxide nanoparticles as an additive with Calophyllum inophyllum methyl ester in a CI engine. Energy Convers Manag 146:8–19
37. Manigandan S, Sarweswaran R, Booma Devi P, Sohret Y, Kondratiev A, Venkatesh S, Rakesh Vimal M, Jensin Joshua J, Comparative study of nanoadditives $TiO_2$, CNT, $Al_2O_3$, CuO and $CeO_2$ on reduction of diesel engine emission operating on hydrogen fuel blends. Fuel

38. Prabu, Anand RB (2016) Emission control strategy by adding alumina and cerium oxide nano particle in biodiesel. J Energy Inst 89:366e372.
39. Aalam CS, Saravanan CG, Samath CM (2015) Influence of iron (Ii, Iii) oxide nanoparticles fuel additive on exhaust emissions and combustion characteristics of CRDI system assisted diesel engine. Int J Adv Eng Res Sci 2(3):23–28
40. Nallamothu RB, Nallamothu AK, Nallamothu SK, Niranjan Kumar IN, Appa Rao BV (2018) Experimental investigation on effect of injection timing in multiple injection on $NO_x$ and smoke from CRDI diesel engine fueled with biodiesel blend. The Ethiop J Sci Sustain Dev (EJSSD) 5(2)
41. Nallamothu RB, Nallamothu AK, Nallamothu SK, Niranjan Kumar IN, Appa Rao BV (2018) Experimental investigation on $NO_x$ and smoke emission from CRDI diesel engine operated with biodiesel blend varying dwell between main and pre-injection. The Ethiop J Sci Sustain Dev (EJSSD), 5(2)
42. Nallamothu RB, Niranjan Kumar IN, Appa Rao BV, Anantha Kamal N, Seshu Kishan N (2018) Emission analysis of CRDI diesel engine fueled with cotton seed oil biodiesel with multiple injection strategy. Int J Emer Technol Innov Res 5(9):707–712
43. Nallamothu RB, Birbirsa G, Niranjan Kumar IN, Appa Rao BV, Seshu Kishan N (2019) A review on performance of biodiesel in engines with and without addition of nanoparticles. Int J Manag Technol Eng IJMTE/1592, IX(II)
44. Nallamothu RB, Nallamothu AK, Nallamothu SK Emission characteristics of CSOME in CRDI diesel engine with multiple injection strategy. In: Narasimham GSVL, Babu AV, Reddy SS, Dhanasekaran R (eds) Recent trends in mechanical engineering. Lecture Notes in Mechanical Engineering. Springer, Singapore. https://doi.org/10.1007/978-981-15-7557-0_9. (2021).
45. Nallamothu RB, Anantha Kamal N, Seshu Kishan N, Niranjan Kumar IN, Appa Rao BV (2020) Effect of multiple injection strategy on combustion of cotton seed oil biodiesel in CRDI diesel engine. In: Narasimham G, Babu A, Reddy S, Dhanasekaran R (eds) Recent trends in mechanical engineering. Lecture Notes in Mechanical Engineering. Springer, Singapore. https://doi.org/10.1007/978-981-15-1124-0_9
46. Nallamothu RB, Lemma M, Niranjan Kumar IN, Appa Rao BV, Anantha Kamal N, Seshu Kishan N (2019) Performance of cotton seed biodiesel with nano additives in diesel engines: a review. J Appl Sci Comput VI(II):142–147. ISSN: 1076-5131

# Analysis of Hypersonic Flow Over Pin Protrusions on a Blunt Body


**N. Akshay and S. R. Nagaraja**

## 1 Introduction

Hypersonic flow analysis is very complex phenomena so the vehicle which is flying at hypersonic speeds should have great aerodynamics. Even a small disturbance will affect the body very badly. But protrusions will exist on the surface of most of the aerodynamic bodies. These protrusions over the body are due to fuel lines, electrical cables, control surfaces, rivet joints, etc. In the vicinity of these protrusions, severe heating and aerodynamics loads are present. These loads can cause damage to the entire hypersonic vehicle. Many researchers have analyzed hypersonic flow over flat plate, different types of cones in the presence of protrusions. They have studied variation of boundary layer thickness, flow separation, heating and aerodynamic loads. Kumar et al. [1–3] have investigated separation region, heat flux in the vicinity of a three-dimensional protuberance on flat plates and cones. They have found separation length and location of hot spot, i.e., location at which heat flux is maximum, for different protrusion heights on flat plates and cones. They have analyzed the heat loads for different enthalpies and deflection angles. They have reported that separation length depends on the height of protrusion. They have reported that the hotspot is at foot of the protrusion. Another important conclusion from their work is that for smaller protrusion heights the hotspot is on the sides of the protrusion, rather than in front of it. Zahir [4] has done a computational study of blunt cones with circular protrusion which are exposed to hypersonic flow. The analysis mainly concentrates on the aerodynamic moment created by the protrusion and how effectively this mechanism is providing maneuverability. Lu [5] explains how the flow happens over the micro-vortex generators. These are mainly to control the shock

N. Akshay · S. R. Nagaraja (✉)
Department of Mechanical Engineering, Amrita School of Engineering, Bengaluru, Amrita Vishwa Vidyapeetham, Bengaluru, India
e-mail: sr_nagaraja@blr.amrita.edu



K. Jha et al. (eds.), *Recent Advances in Sustainable Technologies*,
Lecture Notes in Mechanical Engineering,
https://doi.org/10.1007/978-981-16-0976-3_28

wave boundary layer interaction. This vortex generator seems like a protrusion on the body and it creates vortex systems. The flow field over rectangular protrusions over flat plate is analyzed by Nair et al. [6]. The analysis is done for different heights of protrusion, distance from leading edge, Mach numbers, and distance from leading edge. Li et al. [7] have reported experimental results of hypersonic flow at Mach 5 over rectangular cylinders mounted over flat plates. They have reported that peak pressure occurs just above triple point on the protrusion. Akshay and Nagaraja [8] have done transient analysis of hypersonic flow over blunt body having cylindrical protrusions. They have analyzed the flow field at different heights of the protrusion. Hemateja et al. [9] have reported the effect of nose radius of blunt cones on drag and heat transfer at different Mach numbers. The effect of Mach number on the flow separation region in a blunt cone fitted with a spike with aero-disk was studied by Sai Krishna Mohan et al. [10]. In this paper, computational analysis is done to study the pressure distribution, separation length, and the heat flux data for a blunt body with pin protrusions in Mach 8 flow.

## 2 Computational Methodology

The steady-state hypersonic flow over a blunt body with protrusions is done using the computational fluid dynamics software ANSYS Fluent. The Navier Stokes equations are solved using the density-based solver with k-omega turbulent model. The working fluid is air with ideal gas condition and the Sutherland viscosity model is used.

### *2.1 Geometry of Model*

A blunt cone model used in this study has a base diameter of 80 mm, blunt cone radius of 35 mm, and apex angle of 58°. The leading edge of the blunt body is at a distance of 5 mm from the origin. This model is same as used by Sriram and Jagadeesh [11] and is validated with their experimental results. The enclosure used to surround the blunt body is similar to the one used by authors [11]. Figure 1 shows the computational domain with the blunt body. A cylindrical protrusion of diameter (D) 2.5 mm is used. Four different protrusion heights (H) are used with H = 0.1, 0.5, 1, and 1.5 times the diameter. Figure 2 shows the upper part of body with location of the protrusion.

### *2.2 Mesh and Boundary Conditions*

Grid independence study is done for three element sizes. Drag coefficient of model without protrusion is used for comparison. The results are shown in Table 1. It can

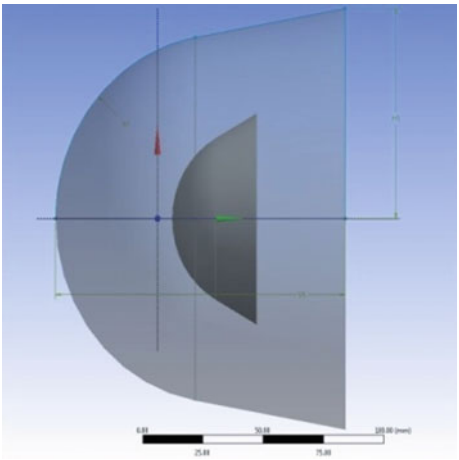

**Fig. 1** Computational domain

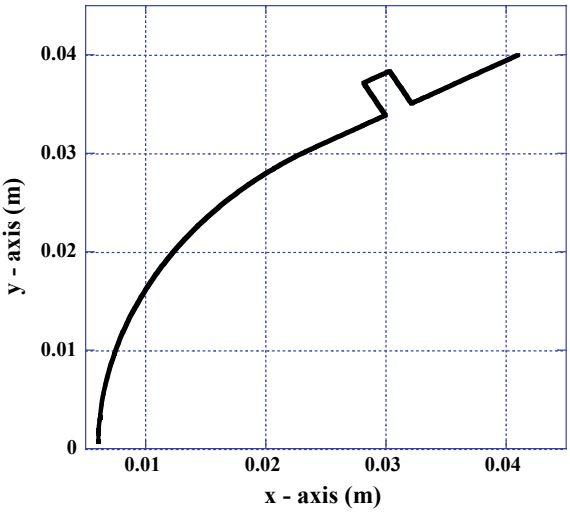


**Fig. 2** Upper surface of the body with protrusion

**Table 1** Grid independence study

| Element size of the mesh (mm) | 1 mm | 0.95 mm | 1.5 mm |
|---|---|---|---|
| Total number of elements | 3,536,255 | 3,939,544 | 221,397 |
| Coefficient of drag ($C_D$) | 0.8264 | 0.826 | 0.837 |

be observed that the drag coefficient is same for 1 and 0.95 mm element size. Hence, an element size of 1 mm is used. In order to get better results near the surface of the body and protrusion, an inflation around the body with a first layer thickness of 0.1 mm for a total 40 layers is used. The large numbers of elements affect the

convergence criteria and time required of the simulation but the result will be more accurate.

The analysis is done by solving Reynolds-Averaged Navier–Stokes equations. To predict the turbulence, two equation k-omega (k–ω) turbulence model is used in these simulations. This model uses variables turbulence kinetic energy (k) and specific rate of dissipation (ω) to predict turbulence. The density-based solver in ANSYS Fluent is used. Since the geometry is small, double precision is used. The inlet conditions are pressure = 1 kPa, Mach number = 8, and temperature = 100 K. These values are chosen to compare the simulated results with experimental results available in the literature.

## 3 Results and Discussions

Steady-state analysis is done with and without protrusion. The validation of the current methodology is done by comparing experimental results of Sriram and Jagadeesh [11]. The experiment consists comparison of heat flux values between small microjet flow in the body and without jet. The heat flux varies from nearly 66 W/cm$^2$ at a distance of 15 mm to 32 W/cm$^2$ at a distance of 35 mm from the stagnation point. The variations of the wall heat flux on the blunt body in the present simulations are also similar to these experimental results (Fig. 4). The free stream conditions for all the cases considered are constant. The flow conditions ahead of the protrusion are different from that of free stream conditions. The pressure and heat flux data on the blunt body are analyzed. The distance at which flow separation takes place is noted. Also, variation of heat flux in the dead air region is analyzed. The dead air region is region between the protrusion and separation point.

### *3.1 Comparison Pressure on the Blunt Body with and Without Protrusion*

Figure 3a, b shows variation of pressure and Fig. 4a, b shows variation of heat flux on the blunt body with and without protrusion. The protrusion location on the blunt body is decided based on the pressure variation on it without protrusion. It is positioned on the surface of the blunt body such that it is subjected to constant values of pressure and heat flux. These values become constant at a distance of 20 mm from the leading edge of the blunt body as seen in Figs. 3a and 4a, respectively. Hence, the protrusion is placed at a distance of 25 mm on the blunt body and the conditions ahead of the protrusion are constant. The maximum values of pressure and heat flux are at the stagnation point of blunt body without protrusion. For the case with protrusion, the peak values vary with the height of the protrusion. The introduction of the protrusion has increased the heating loads on the blunt body. Hence, it is important to study

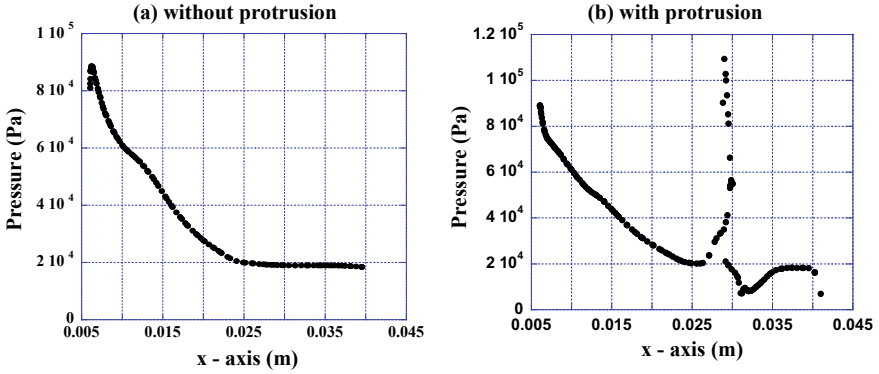


**Fig. 3** Pressure variation on blunt body **a** without protrusion and **b** with protrusion

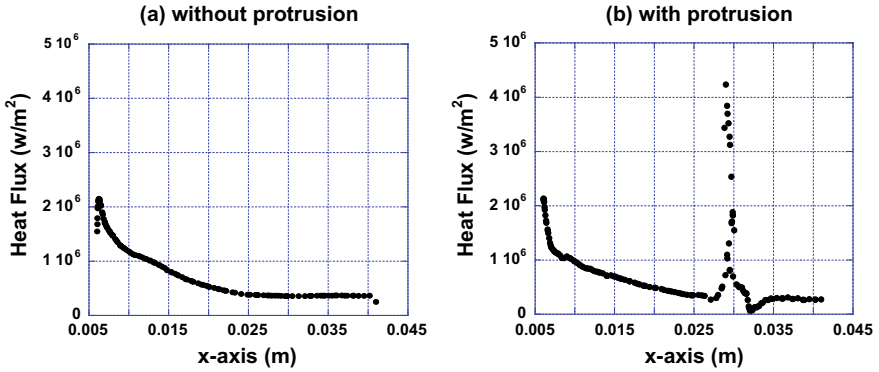


**Fig. 4** Heat flux variation on blunt body **a** without protrusion and **b** with protrusion

the variation of heat flux and pressure for different types of protrusions. Sharief and Nagaraja [12] have studied the variation of pressure and heat flux for different shapes of protrusions. In this paper, the effect of height is presented. The results shown in Figs. 3 and 4 are for height (H) of the protrusion equal to the diameter (D) of it, i.e., H = D.

## *3.2 Separation Length and Dead Air Region*

The location at which flow separates can be found by studying the variation of heat flux or pressure or extending the shock wave formed using flow visualization techniques. More accurate values are obtained using the variation of pressure in front of the protrusion. The separation is the point at which the slope of pressure graph changes. Figure 5 shows variation of pressure for case with H = 1.5D, it can be seen

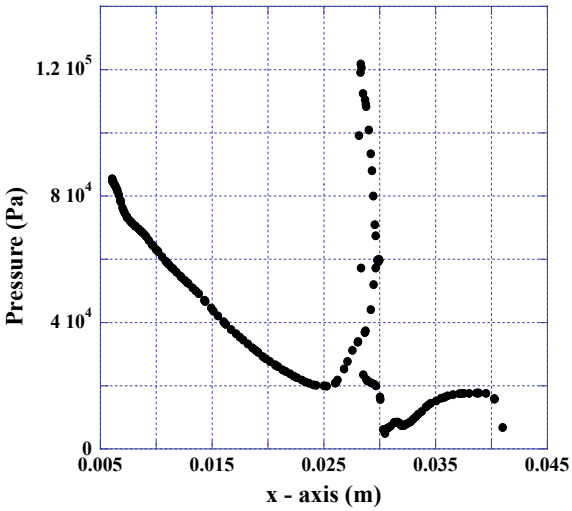


**Fig. 5** Pressure variation for H = 1.5D

that there is sudden change in pressure gradient at a distance of 5.5 mm from the protrusion. The point at which the pressure rapidly starts increasing after reaching a plateau is the separation point. In this case, it is at a distance of around 0.025 m from the origin. The pressure variation on the blunt body in front of the protrusion is shown in Fig. 6. The flow separates at a distance of 5.5 mm from the foot of the protrusion for H = 1.5D. The separation length for different protrusion heights is shown in Fig. 7. The separation length increases as protrusion height increases.

The pressure value is the main parameter which decides the flow separation and also it induces force on the protrusion. The maximum value of the pressure in the

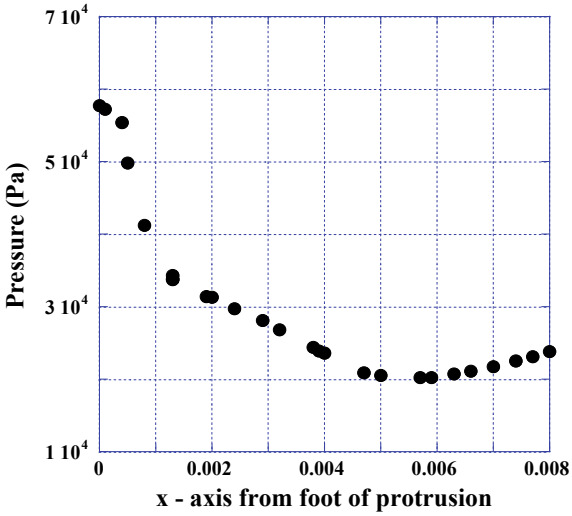


**Fig. 6** Pressure variation in dead air region

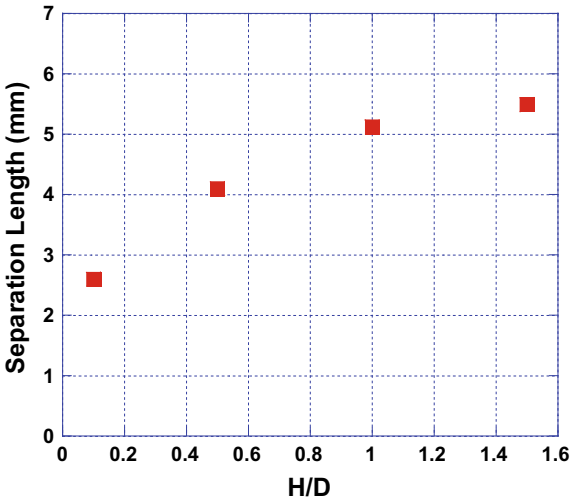


**Fig. 7** Separation length for different protrusion heights

entire flow field lies on the protrusion except for protrusion for which H = 0.1D (Fig. 8). The peak pressure occurs on the protrusion surface below top of the protrusion. As the protrusion height becomes smaller, the peak pressure on the surface of the protrusion also reduces. For protrusion with H = 0.1D, the peak pressure is at the stagnation point on the blunt body.

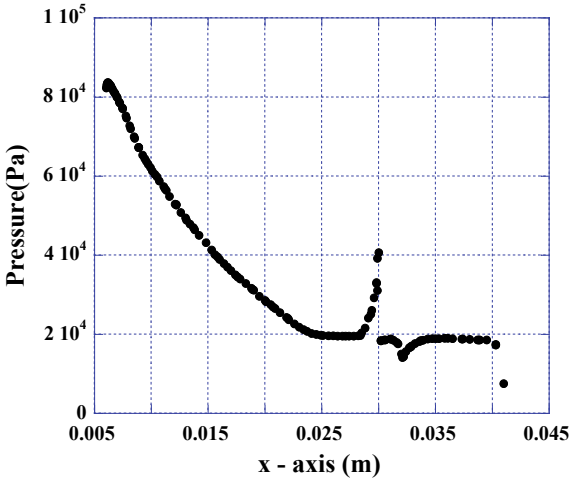


**Fig. 8** Variation of pressure for H = 0.1D

### 3.3 Heat Flux

Heat flux is another important parameter in the hypersonic flow field which causes the aerodynamic heating. The magnitude of heat flux value continuously decreases from the stagnation point and reaches a minimum value, then it increases suddenly due to the presence of protrusion. The maximum heat flux occurs at point between center and top of the protrusion for all cases considered except for protrusion with H = 0.1D, for which it is at the top of the protrusion. The heat flux in the vicinity of the protrusion is higher especially in the separation region near the protrusion foot. Figure 4b shows the variation of heat flux for protrusion with H = D. The variation of heat flux in the dead air region for protrusion with H = 1.5D is shown in Fig. 9. For protrusions with H = D and H = 1.5D the maximum value of the heat flux in separation region is not exactly at the foot of the protrusion, but it lies at some distance before the foot. Similar to pressure variation the maximum heat flux in the flow field occurs on the protrusion except for H = 0.1D, for which it is at the stagnation point. The maximum heat flux on the blunt body in the separation region increases with increased protrusion height (Fig. 10). Due to the presence of protrusion, the peak heat flux in the flow is about 2.2, 1.97, 1.71, and 0.72 times that at the stagnation point for protrusion with H = 1.5D, D, 0.5D, and 0.1D, respectively. The heat flux on the blunt body at location where protrusion is placed is about 2.7, 4.0, 4.7, and 5 times the heat flux at that location without the protrusion for H = 0.1D, 0.5D, D, and 1.5D, respectively. Overall the presence of protrusion increases the heat flux on the blunt body.

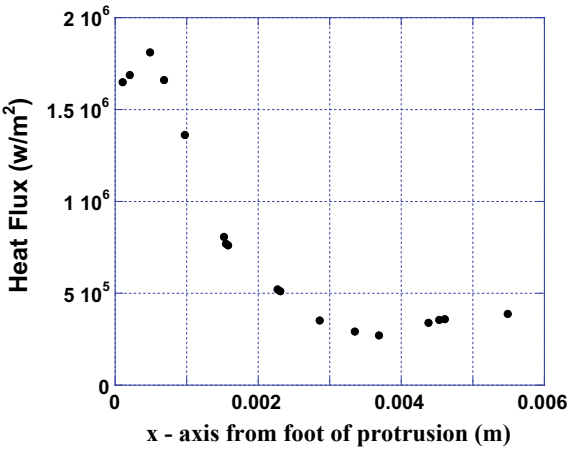


**Fig. 9** Variation of heat flux in dead air region

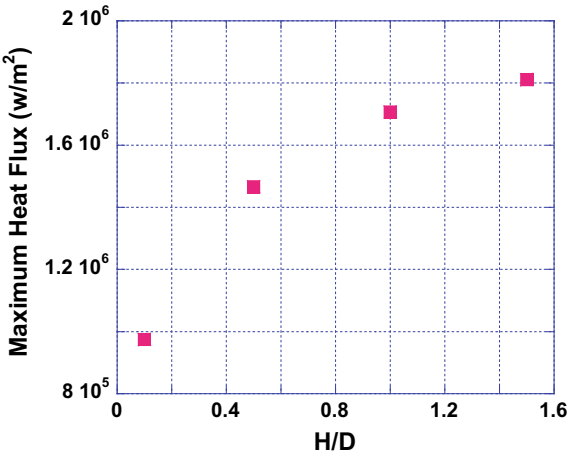


**Fig. 10** Variation of maximum heat flux with protrusion height in the separation region

## 4 Conclusions

Computational analysis of the blunt body with protrusion of different heights in a hypersonic flow is done. The distance at which flow separation happens in front of the protrusion is measured. The distance at which flow separation occurs increases with height of protrusion. The variation of pressure and heat flux on the blunt body with protrusion is compared with those without protrusion. It is found that for all protrusions studied the peak pressure and heat flux values are on the surface of the protrusion except for the case with H = 0.1D for which it is at the stagnation point of the blunt body. The peak heat flux in the flow varies from 0.72 to 2.2 times that at the stagnation point for protrusion with H = 0.1D to 1.5D. There is large pressure and heat flux occurs the dead air region which may cause damage for the entire body. The increase in heat flux on the blunt body at the location of protrusion is 2.7, 4.0, 4.7, and 5 times the value without protrusion for H = 0.1D, 0.5D, D, and 1.5D, respectively.

## References

1. Kumar CS, Reddy KPJ (2014) Hypersonic interference heating on cones with short three-dimensional protuberances. J Exp Therm Fluid Sci 55:29–41
2. Kumar CS, Singh T, Reddy KPJ (2014) Investigation of the separated region ahead of three dimensional protuberances on plates and cones in hypersonic flaws with laminar boundary layers. Phys Fluids 26:126101
3. Kumar CS, Reddy KPJ (2013) Experimental investigation of heat fluxes in the vicinity of protuberances on a flat plate at hypersonic speeds. J Heat Transfer 135:121701–121707
4. Zahir S (2014) Computational aerodynamic interaction of hypersonic flow with pin-protuberance on blunted cones. Arab J Sci Eng 39:7275–7288

5. Lu FK (2015) Visualization of supersonic flow around a sharp-edged, sub-boundary-layer protuberance. J Vis 18:619–629
6. Nair A, Nagaraja SR (2016) Simulation and analysis of protrusions on flat plate at hypersonic speeds. Indian J Sci Technol 9(45):1–6
7. Li S-X, Chen Y-K, Ni Z-Y (2001) Flow field features on hypersonic flow over rectangular obstacles. J Vis 4:73–79
8. Akshay N, Nagaraja SR (2019) Transient analysis of a blunt body with cylindrical protrusion in hypersonic flow. IOP Conf Ser: Mater Sci Eng. 577:012178. https://doi.org/10.1088/1757-899X/577/1/012178
9. Hemateja A, Ravi Teja B, Dileep Kumar A, Rakesh SG (2017) Influence of nose radius of blunt cones on drag in supersonic and hypersonic flows. IOP Conf Ser: Mater Sci Eng 225:012045
10. Sai Krishna Mohan KVNB, Bandaru K, Prabhudev BM (2018) Numerical studies on effect of changing Mach number on aero disk model on flow contours and drag force. IOP Conf Ser: Mater Sci Eng 377:012096. https://doi.org/10.1088/1757-899X/377/1/012096
11. Sriram R, Jagadeesh G (2009) Film cooling at hypersonic Mach numbers using forward facing array of micro-jets. Int J Heat Mass Transf 52:3654–3664
12. Sharief SN, Nagaraja SR (2019) Analysis on a blunt cone with protrusion in hypersonic flow. AIP Conf Proc 2200:020067

# Design and Analysis of Zero Turning Radius Steering System for Light Vehicles (Bajaj QUTE)


**Getachew Fentaw, Ramesh Babu Nallamothu, Anantha Kamal Nallamothu, Seshu Kishan Nallamothu, and Daniel Hambissa Datti**

## 1 Introduction

Many existing cities in the world were not built by considering an increase in the number of cars. Therefore, drivers find it difficult to park their car on crowded city streets and to turn in a small radius. However, it is possible to create cars to suit the traffic conditions of the cities [1, 2].

The difficulty of parking in narrow space and at multiplexes, the problem of easy removal of a vehicle from the traffic jams, the difficulty of turning back at narrow roads, wastage of time and fuels during turning and parking and a high degree of tyre wears are the main problem in current automobiles [3–5]. The vehicle will have a zero turning radius when the role centre axis passes through the centre of gravity of that vehicle, and it is achieved by rotating all the four wheels opposite to each other [6–8]. It helps to turn the vehicle with a minimum space possible, i.e. a circle with a diameter of the length of the vehicle itself is required to rotate the vehicle fully [9–11].

The main consideration in the design of the steering system is to produce pure rolling motion of the wheels while manoeuvring the tightest turns on the dirt road tracks [12, 13]. The steering system must also offer adequate feel to the driver while turning [14, 15]. For maximum life of the tyres, the steering system is designed such

G. Fentaw (✉)
Mechanical Engineering Department, School of Mechanical and Chemical Engineering, Woldia Institute of Technology, Woldia University, Woldia, Ethiopia

R. B. Nallamothu · D. H. Datti
Mechanical Systems and Vehicle Engineering Department, Adama Science and Technology University, Adama, Ethiopia
e-mail: ramesh.babu@astu.edu.et

A. K. Nallamothu · S. K. Nallamothu
School of Industrial and Information Engineering, Politecnico Di Milano, Milano, Italy



K. Jha et al. (eds.), *Recent Advances in Sustainable Technologies*,
Lecture Notes in Mechanical Engineering,
https://doi.org/10.1007/978-981-16-0976-3_29

that it maintains proper angles between the tyres while turning and while braking in the corner along with straight-ahead position [16, 17]. The driver should be able to turn vehicle with minimum effort but it should not be directionally unstable. The steering system is thus designed in a very unique way by compelling many factors and formulating mathematical model [18, 19].

## 2 Methodology

### *2.1 Materials*

CATIA V5 and ANSYS 18.1 were used for geometrically modelling and analysing the stresses induced on individual components, respectively.

During the study, ANSYS static structural and eigenvalue buckling analysis have been done for checking the strength of each individual designed part. Different mesh element type as per the shape of the component, i.e. mapped mesh with hexagonal element, was used for the two shafts and selector, whereas the tetrahedral element was used for modelling all gears and tie rod. Mesh refinement process was done to get the optimum value and reduce the error. In addition to this, analytical methods were used for verifying the final result obtained from ANSYS 18.1.

Besides, the kinematic analysis of the assembled system was carried out using CATIA DMU kinematics to see how the motion of the mechanism look like and to check whether it can move as required or not.

### *2.2 Methods*

The methodology followed while doing this work has four major parts, namely literature review, data collection, design and analysis, and manufacturing and assembly of prototype.

ANSYS 18.1 Software Result Verification.

The analysing software used here (ANSYS 18.1) has been verified in the following way. First, the analysis was done using the software and the actual analytical solutions were calculated using formulas and then the outcome of the software result is compared with the analytical solutions. Here it is considered a cantilever beam which has a cross section of 20 × 20 mm and a length of 100 mm in which 1 kN force is applied at its free end as shown in Fig. 1. The curb weight of the vehicle is 400 kg, which results in 4000 N weight (W) and assuming 50:50 weight distribution

$$\text{weight on each tire } (F_z) = \frac{W}{4} \tag{1}$$

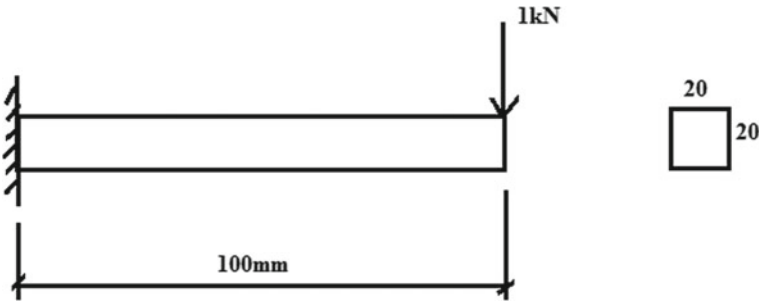


**Fig. 1** Cantilever beam for software validation

$$F_Z = 1000N$$

The lateral force acting on the steering knuckle is a function of normal force and coefficient of friction ($\mu_y$)

$$F_y = \mu_y F_z \tag{2}$$

the maximum lateral force is equal to the normal force, i.e. obtained when the coefficient of friction is 1.

$$F_y = F_z = 1000\,\text{N} = 1\,\text{kN}$$

From beam theory, the bending stress is

$$\sigma_b = 75\,\text{MPa}$$

And the ANSYS result for the same problem in different mesh size is shown in Fig. 2a–c.

Similarly, further analyses were done for a mesh size of 2, 1.5, 1, 0.8 and 0.7 mm and obtained values are listed in Table 1.

By using the results obtained, a convergence graph is plotted in Fig. 3 for both mesh size versus von Mises stress and mesh size versus total deformation.

From Table 1, it is clear that the maximum stress is increased from 39.692 MPa at a mesh size of 5 mm to 74.712 MPa which is almost equal with the analytical solution of 75 MPa. This shows that as the mesh size becomes finer the software result converges to the exact value of the problem. In von Mises stress software analysis of Fig. 3, it can be seen that the maximum stress occurs at the fixed end and the stress at the free end is zero which is the same with beam bending theory. In addition to this, Fig. 3 shows both the total deformation and von Mises stress value increase as the mesh size decreases. After a mesh size of 0.9 mm, the results become constant which indicates the convergence of the case. Therefore, the software result matches with the analytical result with negligible errors so that ANSYS 18.1 has

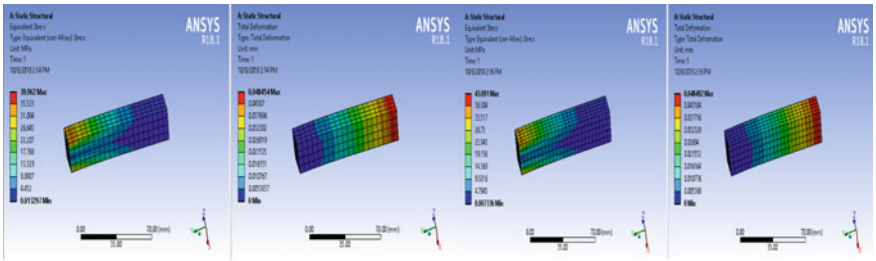

a) Mesh size 5mm b) Mesh size 4mm

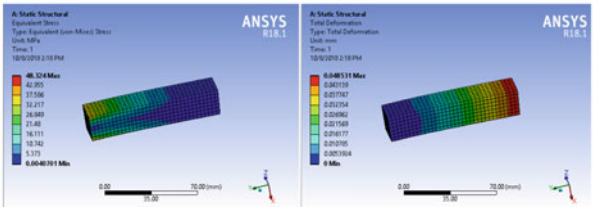

c) Mesh size 3mm

**Fig. 2** ANSYS von Mises and normal stress results at a different mesh size

**Table 1** Convergence analysis and software result validation

| Mesh size (mm) | Maximum von Mises stress (MPa) | Maximum total deformation (mm) | Nodes | Elements |
|---|---|---|---|---|
| 5 | 39.962 | 0.04845 | 1865 | 320 |
| 4 | 43.091 | 0.04849 | 3396 | 625 |
| 3 | 48.324 | 0.04853 | 8336 | 1666 |
| 2 | 55.051 | 0.04856 | 23,441 | 5000 |
| 1.5 | 58.736 | 0.048569 | 173,481 | 40,000 |
| 1 | 74.712 | 0.048572 | 254,352 | 59,248 |
| 0.8 | 74.712 | 0.048572 | 333,476 | 78,125 |
| 0.7 | 74.712 | 0.048572 | 508,860 | 120,203 |

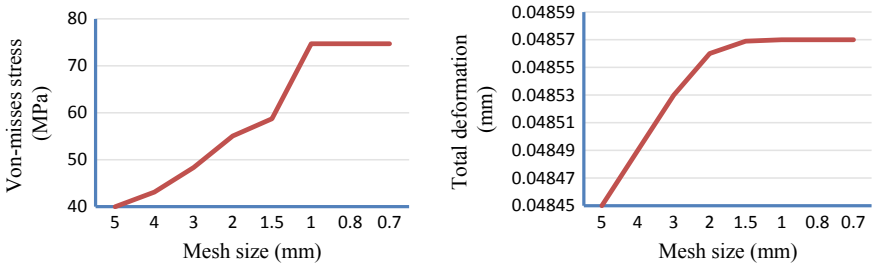


**Fig. 3** Convergence analysis and ANSYS result validation graph

**Fig. 4** Manufactured prototype

been validated and used for the other component stress and deformation analysis of the current mechanism.

**Manufacturing and Assembly**
Once the design and simulation part ends up, the next part is the method of manufacturing each parts and assembling. So the part and assembly drawings are done using CATIA V5. Besides, the manufactured prototype has been shown in Fig. 4.

**Concept Generation**
The first step is obtaining and identifying the product design specifications which meet the objective of the research work. A black box approach conceptual design process was carried out, and the red thick arrows on Table 2 indicate the efficient design path. After the concept is developed, the 3D model of the designed mechanism is prepared as shown in Fig. 5.
**Concept Selection for Steering Mechanism**

## 3 Result and Discussion

**Component Strength analysis results in ANSYS**
The component strength analysis has been done using ANSYS 18.1 and compared with the analytically calculated values, and the results of each component are shown in Fig. 6.

**Performance Comparison of the New System with the existing**
Here the main results of the analysis, namely reduction in the turning radius, critical speed for each mode and reduction in required area for 3600 rotation of the vehicle, are discussed one by one as follows. The comparison of the new system with the existing mechanism based on some common criteria's is shown in Table 3.

**Table 2.** Efficient design path

| Energy source | Steering mechanism | Transferring mechanism to rear steering system | Torque multiplication |
|---|---|---|---|
| Human | Rack and Pinion | Chain drive | Power assist |
| | Worm gear type | Belt drive | |
| | Linkage type | Bevel gear and shaft | Manual |

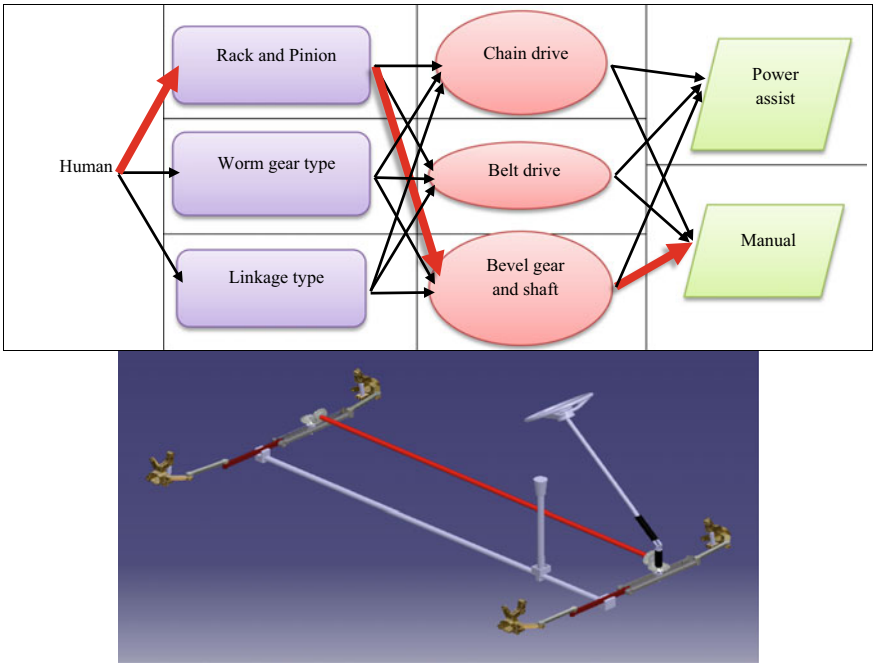


**Fig. 5** Geometric model in CATIA V5

The result shows that using minimum turning configuration will save 62.4% extra radius for manoeuvring a vehicle 3600 in a required direction and during zero turning radius mode it will save almost 100% extra radius spaces which will enable the driver to turn tightly with the minimum space available. The only problem using this configuration is the speed limit.

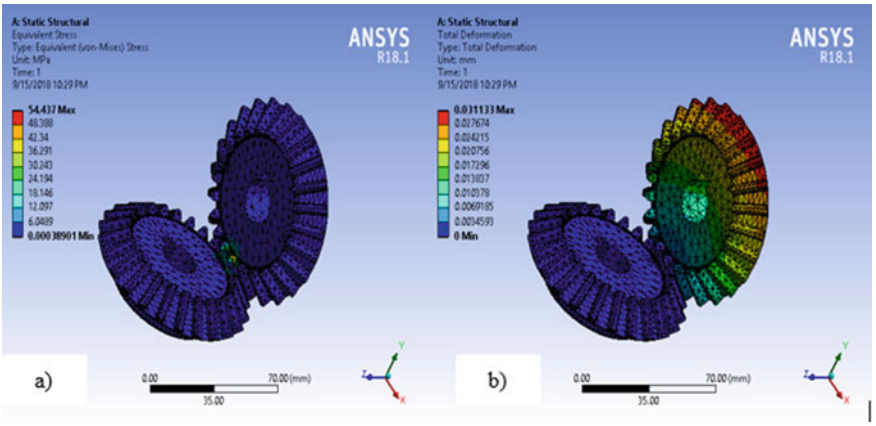


Bevel gear; a) Von-misses stress b) Total deformation

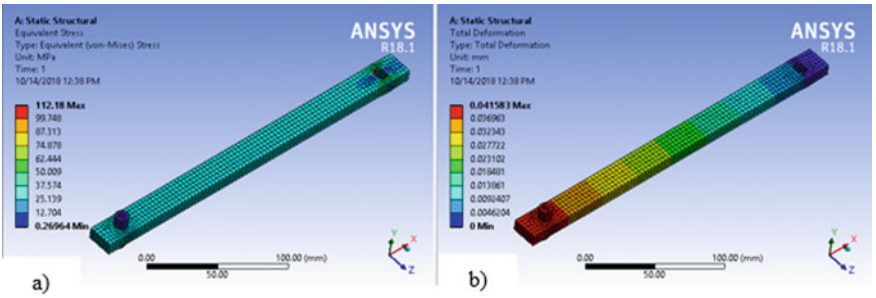


Selector; a) Von-misses stress b) Total deformation

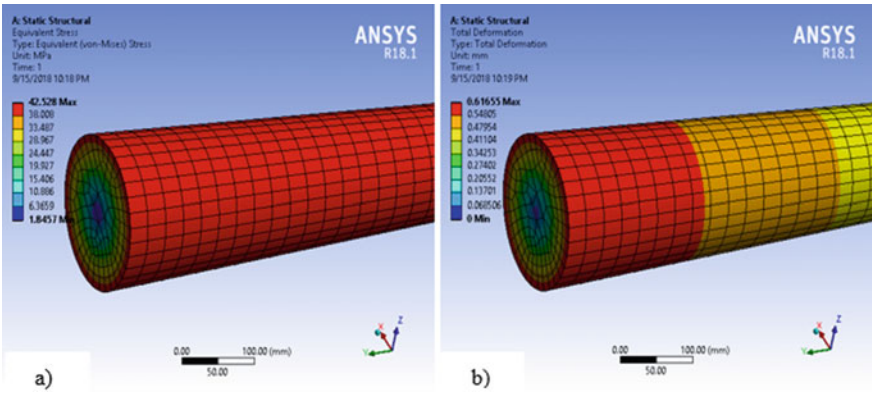


Long Shaft; a) Equivalent stress,b) Total deformation

**Fig. 6** ANSYS component strength analysis results

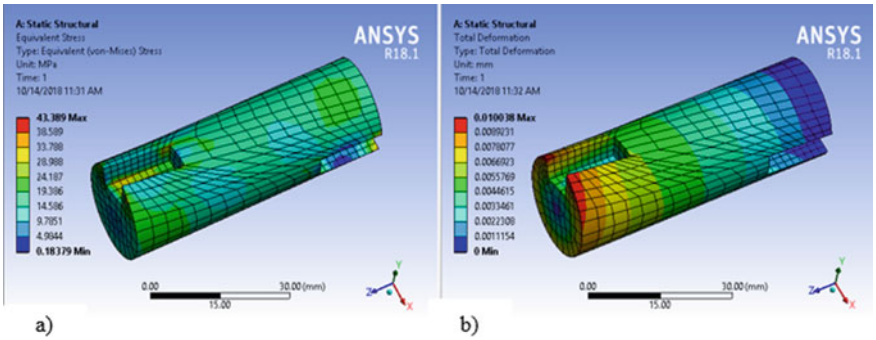


Short shaft; a) Von-misses stress, b) Total deformation

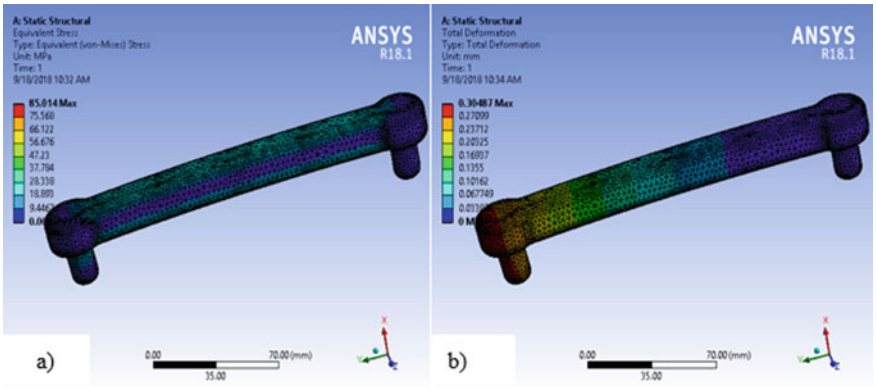


Tie rod; a) Von-misses stress, b) Total deformation

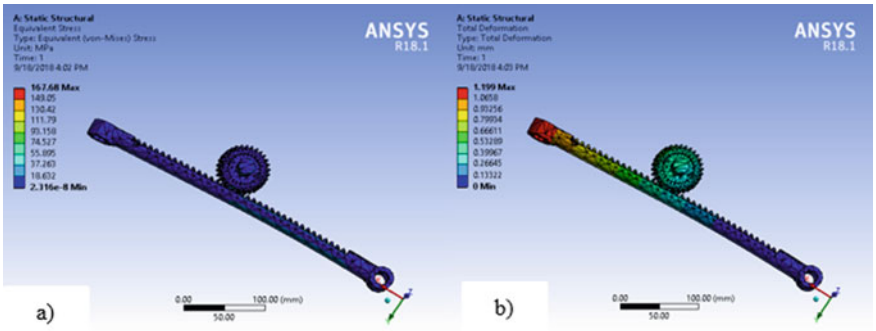


Rack and pinion; a) Von-misses stress, b)Total deformation

**Fig. 6** (continued)

**Table 3** Comparison of the new system with the existing one

| Criteria | Conventional | Minimum turning radius mode | Zero turning radius mode |
|---|---|---|---|
| Turning radius (m) | 3.5 | 1.13 | 0 |
| Critical speed (km/h) | 70 | 43 | 31 |
| Area required for 360° rotation ($m^2$) | 54.26 | 19.1 | 7.3 |
| Turning radius reduction (%) | – | 67.8 | 100 |
| Reduction in the area required to rotate the vehicle 360° (%) | – | 64.8 | 86.55 |

The critical speed of the vehicle is reduced to 43 km/h during the minimum turn configuration at maximum steer angle and 31 km/h during zero turn configuration mode. That means in driving at speed of more than or equal to 31 km/h, the driver should not use zero turning radius mode and when the speed of the vehicle is more than 43 km/h the steering angle should not be maximum; otherwise, it will lead to vehicle instability. The comparison of the obtained results in turning radius and area requirement is shown in Fig. 7a–e in the form of a bar graph for more clarification.

## 4 Conclusion

- The designed steering system has a maximum steer angle of 600 in both cases, i.e. for the minimum turning as well as zero turning configuration mode, and it has a steering ratio of 12:1. The system has a selecting mechanism which is used to shift and select either of the two modes based on the requirement of the driver, road conditions and speed of the vehicle.
- For minimum turning configuration mode, it is found that the turning radius is reduced from 3.5 to 1.13 m which has a total reduction of 67.8% that enables the vehicle to turn in a tight space of approximately 19.1 $m^2$. Although the benchmark vehicle (Bajaj QUTE) can move up to a maximum speed of 70 km/h in normal conditions, while using this mode at its highest value of steer angle, i.e. 600, the speed of the vehicle should be kept below 43 km/h; otherwise, it will cause vehicle instability because of lateral load transfer during cornering.
- For minimum turning configuration, there is a reduction in a turning radius from 3.5 to 0 m that means during this mode the instantaneous centre of rotation lies at the centre of gravity. Due to this, the reduction in a turning radius is about 100% at its maximum steer angle of 600. It is obvious that if the turning radius is very small, its speed should be low for keeping the car stable during cornering. So in this mode, the critical speed is found to be 31 km/h which is less than that of the

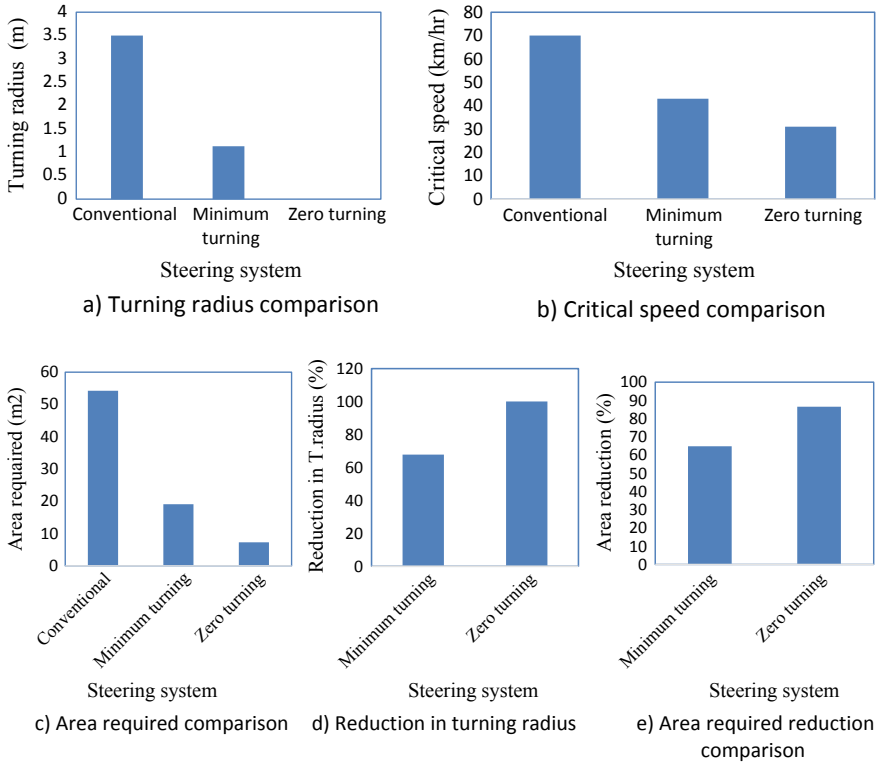


**Fig. 7** Performance comparison of the new system with the existing

critical speed of minimum turning configuration which has a critical speed value of 43 km/h due to the reduction in a turning radius from 1.13 to 0 m.

## References

1. Lohith K, Shankapal S, Gowda M (2013) Development of four wheel steering system for a car. SASTECH J 12(1)
2. Arvind V (2013) Optimizing the turning radius a vehicle using symmetric four wheel steering system. Int J Sci Eng Res 4(12):2177–2184
3. Doraya A, Panesir MS, Bhardwaj B, Bochare A (2015) 4-Wheel steering system mechanism using DPDT switch. Int J Mech Eng Technol 6(11):176–182
4. Akhtar D (2013) Wheel steering system. Int J Eng Res Technol 6(13):393–398
5. Bari D, Wahane A, Hakke P, Tripathi P, Suryawanshi S (2014) Design and manufacturing of a system to measure the turning radius of vehicle. Int J Eng Sci Adv Technol 4(6):536–540
6. Bhishikar S, Gudhka V, Dalal N, Mehta P, Bhil S, Mehta A (2014) Design and simulation of 4 wheel steering system. Int J Eng Innov Technol 3(12):351–367

7. Choudhari D (2014) Four-wheel steering system for future. Int J Mech Eng Robot Res 3(4):383–387
8. Gao Z, Wang J, Wang D (2011) Dynamic modeling and steering performance analysis of active front steering system. Adv Control Eng Inf Sci 1030–1035
9. Kumar A, Kamble D (2014) Zero turn four wheel steering system. Int J Sci Eng Res 5(12):1635–1640
10. Kumar P, Krishna R, Venkatesh J (2017) Analysis of Davis steering gear mechanism for four wheels and six wheels. Int J Innov Res Sci Technol 3(8):112–116
11. Laad N, Agrawal P, Verma N (2016) Design of four wheel active steering. Int J Res Aeronaut Mech Eng 4(6):27–37
12. Malu D, Katare N, Runwal S, Ladhe S (2016) Design methodology for steering system of an Atv. Int J Mech Eng Technol 7(5):272–277
13. Nalecz GA, Bindemannt A (1988) Investigation into the stability of four-wheel steering vehicles. Int J Veh Des 9(2)
14. Raut C, Chettiar R, Shah N, Prasad C, Bhandarkar D (2017) Design, analysis and fabrication of steering system used in student formula car. Int J Res Appl Sci Eng Technol 5(5):1529–1540
15. Singh A, Kumar A, Chaudhary R, Singh C (2014) Study of 4 wheel steering systems to reduce turning radius and increase stability. Paper presented at the International Conference of Advance Research and Innovation, India
16. Varghese C, Babu D, Kuriyakose D, Harikrishnan AS (2016) Different modes in four wheel steered multi-utility vehicles. Int J Eng Sci 6(4):95–101
17. Zhao S, Liu X, Feng J, Dai J (2013) Design of an Ackermann-type steering mechanism. Paper presented at the ARCHIVE Proceedings of the Institution of Mechanical Engineers Part C, Journal of Mechanical Engineering Science
18. Alemayehu Z, Nallamothu RB, Liben M, Nallamothu SK, Nallamothu AK (2020) Experimental investigation on characteristics of sisal fibre as a composite material for light vehicle body applications. Mater Today: Proc. Elsevier. https://doi.org/10.1016/j.matpr.2020.07.386
19. Siraj A, Ramesh Babu N, Srinivasa Reddy K (2019) Static analysis of dump truck chassis frame made of composite materials. Int J Eng, Sci Technol 11(2):21–32

# Nanostructures as High Absorption Energy Materials—A Review

**Shaik Afzal Mohiuddin, Ajay Kumar Kaviti, and T. Srinivasa Rao**

## 1 Introduction

As water insufficiency is among the most significant global problems of our time, there is a momentous need to find the technological solution to water scarcity [1]. Solar desalination, which produces distilled water from brine by sunlight, has been heavily investigated [2, 3]. However, solar stills for desalination purposes are finite because of its low efficiency and cost [3]. In order to overcome this drawback, noble metal-based plasmonics [3–6] were largely experimented in the area of solar energy [7, 8] because of their strong infrared and visible plasmonic responses coinciding significantly with the solar spectrum. After working on NPs' plasmonic responses, researchers are now developing nanostructures with NPs' help to have a very high absorption of solar radiation (≈96%) for a wide range of wavelengths and omnidirectional incidence angle. Some works done in nanostructure are very recently developed nanostructures to study its effect on different absorber plates [9], hybridization model for the plasmon response of complicated nanostructures [10], hierarchical microstructured copper phosphate (HCuPO) [11], polypyrrole (PPY)-coated stainless steel mesh [12], black titania nanocage structure [13], hierarchical graphene foam [14] flexible networked structure [15], reduced graphene oxide-polyurethane (rGO-PU) nanocomposite foam [16], plasmonic biofoam [17], biodegradable polydopamine-filled bacterial nanocellulose (PDA-BNC) [18], versatile salt-resistant Janus absorber [19], plasmonic bamboo nanostructure [20], nickel (Ni) and gold (Au)-flexible hierarchical nanostructures [21]. The novelty of this review paper is described in Fig. 1. In this current review paper, different types of nanostructures have been explained.

S. A. Mohiuddin · A. K. Kaviti (✉)
Department of Mechanical Engineering, VNRVJIET, Hyderabad 500090, India

T. Srinivasa Rao
Department of Automobile Engineering, VNRVJIET, Hyderabad 500090, India



K. Jha et al. (eds.), *Recent Advances in Sustainable Technologies*,
Lecture Notes in Mechanical Engineering,
https://doi.org/10.1007/978-981-16-0976-3_30

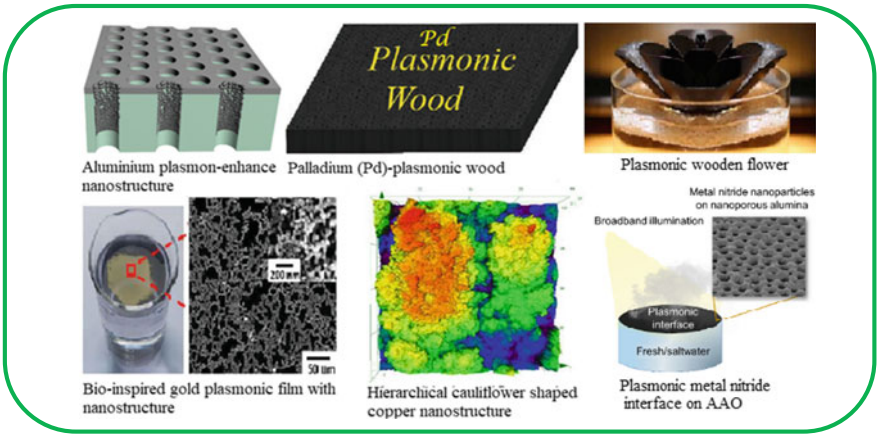


**Fig. 1** Nanostructures for efficient solar desalination [22, 24, 25, 27–29]

## 2 Nanostructures

### *2.1 Aluminium and Gold Plasmon-Enhanced Nanostructures*

Zhou et al. [22] developed a plasmon-enhanced solar desalination device through self-assembly of Al NPs into a 3-D porous membrane, referred to as aluminium nanoparticles-anodic aluminium oxide membrane (Al NP/AAM). In their preparation of Al NP/AAM, they took the aluminium foil (Fig. 2a) and performed anodic oxidation to generate a transparent (Fig. 2b) porous AAM. The porous AAM with nanopores was then moved into the physical vapour deposition (PVD) machine for Al evaporation. In the evaporation stage, Al ions move to the topmost surface of the membrane and form a slim layer (Fig. 2c). In contrast, some of the Al ions deeply penetrate the nanopores, impact the sidewall, collide with one another, move diffusively and then condense, developing self-assembly of Al NPs in the pores of the AAM. The transparent AAM was transformed to black after the Al NPs deposition (Fig. 2f), a clear indication of better light absorption of the fabricated Al-based plasmonic structure. The developed porous plasmonic absorber was capable of floating effortlessly on the water surface, able to absorb broad solar spectrum efficiently (>96%) and concentrate the absorbed energy at the water surface to facilitate effective (~90%) desalination. They remarked that the Al NP/AAM structure's significant desalination effect could give a portable desalination solution.

Similarly again, Zhou et al. [23] fabricated Au-NPs/AAM that can absorb ~99% of radiations in the wavelength range of 400 nm–10 μm. The preparation of the Au-NPs/AAM nanostructure was the same as that of Al NPs/AAM except Au-NPs was used for deposition instead of Al NPs in the PVD chamber. The structure achieved over 90% solar steam generation efficiency under 4 $kWm^{-2}$ solar intensity. Traver

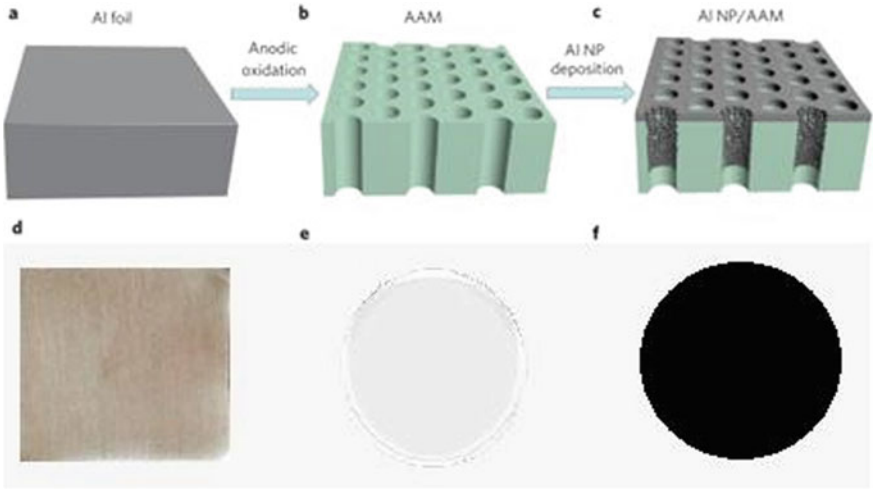


**Fig. 2** Fabrication of Al NP/AAM. **a** Al foil. **b** Anodic oxidation of Al foil resulting in AAM. **c** The Al NP/AAM structure. **d–f** Optical photographs of the Al foil [22]

et al. [24] developed plasmonic interfaces of titanium nitride (TiN), zirconium nitride (ZrN) and hafnium nitride (HfN) NPs by drop-casting on anodic aluminium oxide (AAO) membranes having nanopores. They found that HfN-plasmonic interface gave the maximum evaporation rate of $1.36 \pm 0.03$ kgm$^{-2}$ h$^{-1}$ with solar to vapour efficiency of 95%.

## *2.2 Plasmonic Woods*

Zhu et al. [25] developed a plasmonic wood for high-efficiency solar steam production. They have taken a basswood slice that was built up with numerous nanochannels and microchannels to transport water from the base to the wood's top surface. In order to assemble fine metal NP's into the 3-D mesoporous matrix of typical wood, an aqueous solution of $PdCl_2$ (0.01 M) was prepared by mixing 88.5 mg of $PdCl_2$ with 50 ml HCl solution ($20 \times 10^{-3}$ M) followed by heating for 1 h at 60 °C to dissolve $PdCl_2$ powder completely. The basswood slice was then made to immerse in the prepared $PdCl_2$ solution and heated at 80 °C to get the Pd-based plasmonic wood.

The plasmonic wood was able to absorb 99% of light for a broad spectrum of wavelengths from 200 to 2500 nm because of microchannels, wave-guide effect (Fig. 3a) and plasma resonance of metal nanoparticles (Fig. 3b) in the wood. Due to the capillary action, water could transport up along the wood's microchannels, as shown in Fig. 3c. The device has achieved a record 85% solar conversion efficiency

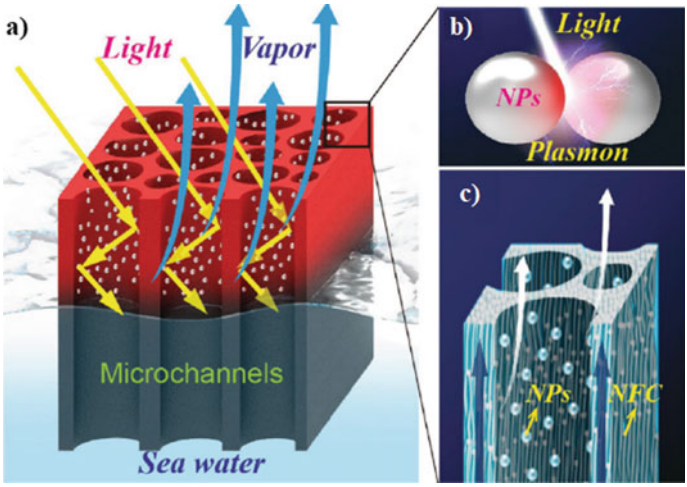


**Fig. 3** **a** Wave-guide effect of microchannels for max absorption of solar radiation. **b** Plasmonic effect of NPs. **c** Magnified illustration of the water movement along microchannels in wood. Plasmonic wood made of nanofibrous cellulose (NFC) [25]

under 10-sun illumination (10 $kWm^{-2}$) and was stable for 144 h, without having any degradation.

The other wood structure was designed and fabricated by Liu et al. [26] a novel composite comprised of wood and graphene oxide (GO) for effective solar desalination and solar steam generation. They have deposited graphene oxide layer on top of the wood surface by drop-casting and set aside to dry naturally to get the wood-GO composite. The wood-GO combined structure achieved ~83% solar thermal efficiency under virtual solar illumination of power density 12 $kW/m^2$.

Chen and his co-researchers [27] developed a plasmonic wood flower by depositing silver-polydopamine (Ag-PDA) core–shell structured NPs on the flower petals. The plasmonic flower could able to absorb 98.65% of light. The Ag-PDA NPs facilitated the formation of thin water films on either side of the flower petal. The plasmonic wooden device has achieved an evaporation rate of 2.08 $kgm^{-2}\ h^{-1}$ with a high solar to vapour conversion efficiency of 97.6% under one sun illumination.

## *2.3 Bio-Inspired Gold Plasmonic Film*

Wang et al. [28] developed a bio-inspired plasmonic film of gold (Au) NPs that can be used for steam generation and distillation process. Vapours of formic acid were made to diffuse into the gold NP's solution to obtain the assembled film. Figure 4a shows the photograph of an Au-plasmonic film of diameter >3 cm at the air–water interface. Figure 4b displays the SEM picture of the film having a disordered network structure due to the random arrangement of NPs in the self-assembly process.

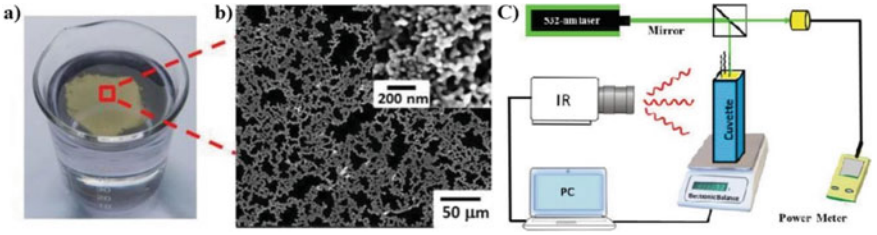


**Fig. 4** **a** Photograph an Au-plasmonic film. **b** SEM image of the film. **c** Schematic of experimental setup [28]

A hot zone at the air and water interface was created by the plasmonic light to heat transformation process, which resulted in localized heating of the water surface. Such localized heating reduces the loss of heat energy to the bulk liquid and enhances evaporation efficiency. A comparative study of the evaporation process of plasmonic film and water mixed with Au-NP's was made. An illustrative diagram of the experimental setup is displayed in Fig. 4c. The beaker containing the plasmonic film was placed on the electronic balance to assess the evaporation's weight loss. Heating of the plasmonic film was performed by using a 532-nm laser having a 5 mm diameter impinging at the right angle to the surface of the film. The cuvette's temperature distribution containing the plasmonic film was analysed by an infrared (IR) camera. The above procedure was repeated for Au-NP's solution.

Figure 5a, b, displays the optical and infrared photographs of the plasmonic film, and Fig. 5c, d displays the optical and infrared photographs of Au nanoparticles ($\approx 4.39 \times 10^{13}$ particles/mL) solution at 10.18 W/cm $^2$ of laser illumination. It can be seen that the hot zone is very much confined for the self-assembled film compared to that of Au-NP's solution. Figure 5e displays the change in evaporation rate concerning the time of laser illumination (10.18 W/Cm$^2$) for the plasmonic film and Au-NP's solution. For the film, the evaporation rate rapidly reached an elevated value ($\approx$0.4 mg/s) and the total time took was 150 s for the film to reach a steady

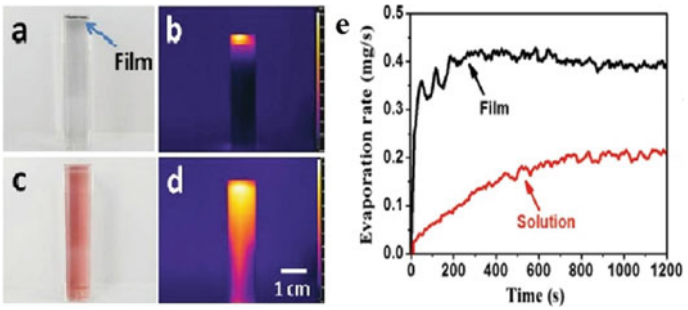


**Fig. 5** **a**, **c** Optical and **b**, **d** infrared photographs of the plasmonic film and Au-NP's solution. **e** Evaporation rate versus time of laser illumination [28]

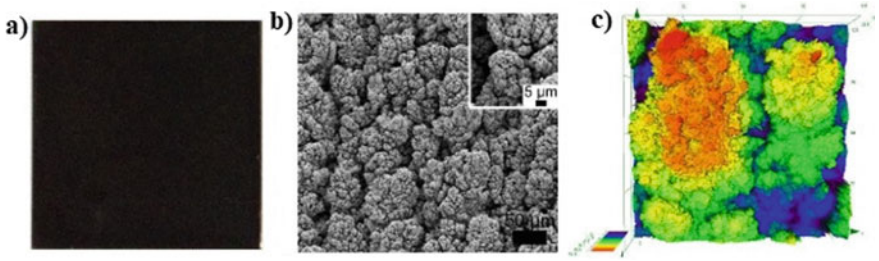


**Fig. 6** Hierarchical Cu nanostructure: **a** photograph, **b** SEM image, **c** 3-D laser confocal microscope image [29]

rate. However, for the Au-NP's solution, the evaporation rate improved gradually and reached a steady rate after the 800 s. The reason for the delay in reaching the steady rate for the solution was because of travel of vapour bubbles to the solution surface and heat loss to the bulk liquid. Thus, it can be inferred that free-floating plasmonic film of Au-NP's can provide localized surface heating and higher absorption of solar radiation, which leads to fast and effective evaporation needed for water desalination.

## *2.4 Hierarchical Cauliflower-Shaped Copper Nanostructure*

Fan et al. [29] fabricated a flexible femtosecond (fs) laser-induced hierarchical cauliflower-shaped nanostructure on the copper (Cu) surface, as shown in Fig. 6. The surface was fabricated using TrumpfTruMicro 5000 laser system. The hierarchical Cu nanostructure so developed was able to absorb 98% of solar radiation for a wavelength range of 200–800 nm, and the angular dependence was below 0.1% for the 0–60° incident angle. Such high omnidirectional absorption property can cause heating up effect under solar illumination. They found that for approximately 1 $kWm^{-2}$ solar power density, the overall photothermal conversion efficiency was over 60% in evaporating water experiment of hierarchical cauliflower-shaped nanostructure on a Cu surface. Authors claimed that such a technology could provide a reliable, cost-effective, and simple way of realizing effective solar energy utilization.

## *2.5 Carbon Nanostructures*

Liu and his co-researchers [30] developed carbon-black-based superhydrophobic gauze to enhance solar evaporation at the water surface. It was developed by dip-coating in a solution that contains 1.5 g of CB nano-particles, 1 g of PDMS and 30 ml of hexane. The developed superhydrophobic gauze was able to float naturally

on water, absorb light efficiently and localize the heat at air–water interface leading to high evaporation rate needed for effective desalination.

Liu et al. [31] fabricated a geopolymer-based mesoporous carbon composite (GBMCC) device to generate water vapour by harvesting energy from the sun. The device could able to achieve an evaporation rate of 1.58 $kgm^{-2}\ h^{-1}$ under one sun illumination, with light to the heat conversion efficiency of up to 84.95%.

Mu et al. [32] developed a monolithic carbon aerogels having randomly concentrated hollow-carbon-nanotubes (HCNTs) by carbonization of microporous nanotubes. In order to increase the hydrophilic nature, they treated the developed aerogels with sulphuric acid/ammonium peroxydisulfate, which results in quick transportation of water molecules. The device could able to absorb 99% of light and gave a high photothermal conversion efficiency of 86.8% under one sun illumination.

Liu et al. [33] fabricated versatile photothermal steam generation device by deposition of hierarchical porous carbon (HPC) on hydrophilic thin paper. The HPC was prepared by carbonization of dehalogenated polyvinyl chloride. The small pores sizes of HPC facilitated quick water and vapour transportation. The device achieved a record evaporation rate of 7.87 $kgm^{-2}\ h^{-1}$ with a high energy conversion efficiency of 95.8% under five solar sun intensity of 5 $kWm^{-2}$. Table 1 displays the different nanostructures, wavelength range in which the nanostructure is most effective, light absorption percentage and light to heat conversion efficiencies.

**Table 1** Nanostructures types, wavelength range, light absorption and steam generation efficiency

| S. No. | Type of nanostructure | Wavelength range | Light absorption | Steam generation efficiency (%) |
|---|---|---|---|---|
| 1. | Al NP/AAM [22] | 500–2500 nm | >96% | 88.4% under 4 sun |
| 2. | Au-NP/AAM [23] | 400 nm–10 μm | ~99% | 90% under 4 sun |
| 3. | HfN NP/AAM[24] | 300–1300 nm | Not given | 95% under 1 sun |
| 4. | Pd-Plasmonic wood [25] | 200–2500 nm | ~99% | 85% under 10 sun |
| 5. | Wood-GO composite [26] | 500–1100 nm | >80% | ~ 83% under 12 sun |
| 6. | Plasmonic wooden flower [27] | 420–2500 nm | 98.65% | 97.6% under 1 sun |
| 7. | Cu nanostructure [29] | 200–800 nm | ~98% | >60% under 1 sun |
| 8. | GBMCC [31] | 250–2500 nm | 90–95% | 84.9% under 1 sun |
| 9. | Carbon aerogels [32] | 200–2500 nm | ~99% | 86.8% under 1 sun |
| 10. | Hierarchical porous carbons [33] | 250–2500 nm | ~91% | 95.8% under 5 sun |

## 3 Conclusions

- The paper explains types of nanostructures that exhibit plasma-enhanced resonance, wave-guide effect, interfacial heat localization and capillary action, making them efficient solar desalination devices.
- The light absorption characteristics of all these nanostructures are above 96% for a wide range of wavelengths.
- The combination of the substantial desalination effect, superior stability, low material price, abundance and scalable manufacturing processes suggests that this type of nanostructure device can give a portable desalination solution.

## References

1. Elimelech M, Phillip WA (2011) The future of seawater desalination: energy, technology, and the environment. Science 333:712–717
2. Xiao G et al (2015) A review on solar stills for brine desalination. Appl Energy 103:642–652
3. Kuzyk A et al (2014) Reconfigurable 3D plasmonic metamolecules. Nat Mater 13:862–866
4. Yang S et al (2014) Feedback-driven self-assembly of symmetry breaking optical metamaterials in solution. Nature Nanotech 9:1002–1006
5. Klinkova A, Choueiri RM, Kumacheva E (2014) Self-assembled plasmonic nanostructures. Chem Soc Rev 43:3976–3991
6. Liu N, Mesch M, Weiss T, Hentschel M, Giessen H (2010) Infrared perfect absorber and its application as plasmonic sensor. Nano Lett 10:2342–2348
7. Neumann O et al (2013) Solar vapor generation enabled by nanoparticles. ACS Nano 7:42–49
8. Liu Y et al (2015) A bioinspired, reusable, paper-based system for high-performance large-scale evaporation. Adv Mater 27:2768–2774
9. Arunkumar T, Murugesan D, Raj K, Denkenberger D, Viswanathan C, Rufuss DDW et al (2019) Effect of nano-coated CuO absorbers with PVA sponges in solar water desalting system. Appl Therm Eng 148:1416–1424
10. Prodan E, Radloff C, Halas NJ, Nordlander P (2003) A hybridization model for the plasmon response of complex nanostructures. Science 302:419–422
11. Hua Z, Li B, Li L, Yin X, Chen K, Wang W (2017) Designing a novel photothermal material of hierarchical microstructured copper phosphate for solar evaporation enhancement. J Phys Chem C 121:60–69. https://doi.org/10.1021/acs.jpcc.6b08975
12. Zhang L, Tang B, Wu J, Li R, Wang P (2015) Hydrophobic light-to-heat conversion membranes with self-healing ability for interfacial solar heating. Adv Mater, 4889–4894
13. Zhu G, Xu J, Zhao W, Huang F (2016) Constructing black titania with unique nanocage structure for solar desalination. ACS Appl Mater Interfaces, 6–11. https://doi.org/10.1021/acsami.6b11466
14. Ren H, Tang M, Guan B, Wang K, Yang J, Wang F et al (2017) Hierarchical graphene foam for efficient omnidirectional solar-thermal energy conversion. Adv Mater 29:1–7
15. Sajadi SM, Farokhnia N, Irajizad P, Hasnain M, Ghasemi H (2016) Flexible artificially-networked structure for ambient/high pressure solar steam generation. J Mater Chem A 4:4700–4705
16. Wang G, Fu Y, Guo A, Mei T, Wang J, Li J et al (2017) Reduced graphene oxide-polyurethane nanocomposite foam as a reusable photoreceiver for efficient solar steam generation. Chem Mater 29:5629–5635

17. Tian L, Luan J, Liu KK, Jiang Q, Tadepalli S, Gupta MK et al (2016) Plasmonic biofoam: a versatile optically active material. Nano Lett 16:609–616
18. Jiang Q, Gholami H, Ghim D, Cao S, Jun YS, Singamaneni S (2017) Polydopamine-filled bacterial nanocellulose as a biodegradable interfacial photothermal evaporator for highly efficient solar steam generation. J Mater Chem A 5:18397–18402
19. Xu W, Hu X, Zhuang S, Wang Y, Li X, Zhou L et al (2018) Flexible and salt resistant janus absorbers by electrospinning for stable and efficient solar desalination. Adv Energy Mater 8:1–7. https://doi.org/10.1002/aenm.201702884
20. Sheng C, Yang N, Yan Y, Shen X, Jin C, Wang Z et al (2020) Bamboo decorated with plasmonic nanoparticles for efficient solar steam generation. Appl Therm Eng 167:114712
21. Kim C, Ryu Y, Shin D, Urbas AM, Kim K (2020) Efficient solar steam generation by using metal-versatile hierarchical nanostructures for nickel and gold with aerogel insulator. Appl Surf Sci 517:146177. https://doi.org/10.1016/j.apsusc.2020.146177
22. Zhou L, Tan Y, Wang J, Xu W, Yuan Y, Cai W et al (2016) 3D self-assembly of aluminium nanoparticles for plasmon-enhanced solar desalination. Nat Photonics 10:393–398
23. Zhou L, Tan Y, Ji D, Zhu B, Zhang P, Xu J et al (2016) Self-assembly of highly efficient , broadband plasmonic absorbers for solar steam generation. Appl Opt
24. Traver E, Karaballi RA, Monfared YE, Daurie H, Gagnon GA, Dasog M (2020) TiN, ZrN, and HfN nanoparticles on nanoporous aluminum oxide membranes for solar-driven water evaporation and desalination. ACS Appl Nano Mater
25. Zhu M, Li Y, Chen F, Zhu X, Dai J, Li Y et al (2018) Plasmonic wood for high-efficiency solar steam generation. Adv Energy Mater 8:1–7
26. Liu KK, Jiang Q, Tadepalli S, Raliya R, Biswas P, Naik RR et al (2017) Wood-graphene oxide composite for highly efficient solar steam generation and desalination. ACS Appl Mater Interfaces 9:7675–7681. https://doi.org/10.1021/acsami.7b01307
27. Chen S, Sun Z, Xiang W, Shen C, Wang Z, Jia X et al (2020) Plasmonic wooden flower for highly efficient solar vapor generation. Nano Energy 76:104998
28. Wang Z, Liu Y, Tao P, Shen Q, Yi N, Zhang F et al (2014) Bio-inspired evaporation through plasmonic film of nanoparticles at the air-water interface. Small 10:3234–3239
29. Fan P, Wu H, Zhong M, Zhang H, Bai B, Jin G (2016) Large-scale cauliflower-shaped hierarchical copper nanostructures for efficient photothermal conversion. Nanoscale 8:14617–14624
30. Liu Y, Chen J, Guo D, Cao M, Jiang L (2015) Floatable, self-cleaning, and carbon-black-based superhydrophobic gauze for the solar evaporation enhancement at the air-water interface. ACS Appl Mater Interfaces 7:13645–13652
31. Liu F, Zhao B, Wu W, Yang H, Ning Y, Lai Y et al (2018) Low cost, robust, environmentally friendly geopolymer—mesoporous carbon composites for efficient solar powered steam generation. Adv Funct Mater 1803266:1–11
32. Mu P, Zhang Z, Bai W, He J, Sun H, Zhu Z (2019) Superwetting monolithic hollow-carbon-nanotubes aerogels with hierarchically nanoporous structure for efficient solar steam generation. Adv Energy Mater 1802158:1–9
33. Bradley R, Zhao B (2019) Highly efficient solar seawater desalination with carbons derived from halogen-containing polymers. R Soc Chem, 29414–19423

# Improving Frontal Body Shape of Locally Built FSR Isuzu Bus for Reduction of Aerodynamic Resistance


**Bahiru Belachew, Ramesh Babu Nallamothu, Seshu Kishan Nallamothu, and Anantha Kamal Nallamothu**

## 1 Introduction

Buses are a basic piece of a man's transportation framework. Buses are made to satisfy the consistently developing requests of clients [1]. In contemporary, transportation by bus is less expensive and simpler; however, it has disadvantages due to the air contamination that originates from motor fumes gases [2, 3]. Decreasing the mileage of business buses is fundamental for colossal armadas of buses that are utilized each day to convey enormous quantities of travellers to delayed separations [4]. They are incapable as far as fuel utilization; hence, to diminish the fuel utilization of vehicles, the streamlined features of bus shapes increment to the worth. The efficiently effective structure of the bus diminishes the drag force expanding eco-friendliness [5].

Fuel consumption spent on aerodynamic drag is more than ½ of the energy consumption of the vehicle. Out of the total drag, 80% is pressure drag and the boundary layer separation from the surface of the rear window due to the vehicle geometry, very much influences the pressure drag. It is found that around 40% of the drag force is generated at the rear after the body of the vehicle [6, 7]. The study on [8] showed that heavy vehicles due to their large frontal area and bluff shapes are ineffective aerodynamically and consumption of fuel to overcome drag mounts to 65%. Streamlined obstruction represents more than ¾ of largely motor power while

B. Belachew
Department of Mechanical Engineering, Bule Hora University, Bule Hora, Ethiopia

Mechanical Systems and Vehicle Engineering Department, SoMCME, Adama Science and Technology University, Adama, Ethiopia

R. B. Nallamothu (✉)
Department of Mechanical Systems and Vehicle Engineering, Adama Science and Technology University, SoMCME, Adama, Ethiopia

S. K. Nallamothu · A. K. Nallamothu
School of Industrial and Information Engineering, Politecnico di Milano, Bovisa, Italy



K. Jha et al. (eds.), *Recent Advances in Sustainable Technologies*,
Lecture Notes in Mechanical Engineering,
https://doi.org/10.1007/978-981-16-0976-3_31

working at higher speeds since the drag is proportional to the square of the speed. As the motor burden rises essentially, which furtherly raises the fuel utilization rate [9–11].

This study emphasis on the vehicle's optimal design mostly drags imports for the bus that impacts legitimately fuel utilization. FSR Isuzu buses, the design has inefficient on the overall performance due to aerodynamics. So, it focuses to diminish the streamlined obstruction of the FSR Isuzu bus by improving aerodynamic body shape.

## 2 Methodology

Numerical simulations of different FSR Isuzu bus configurations were been performed. Started with an evaluation of the baseline simulation, Compared to baseline model, in modified models drag force observe to be reducing. For each shape, the CFD analysis was done, following the process described (Fig. 1). According to the investigation on [12], the acceptable level of drag reduction was considered from the design point of view.

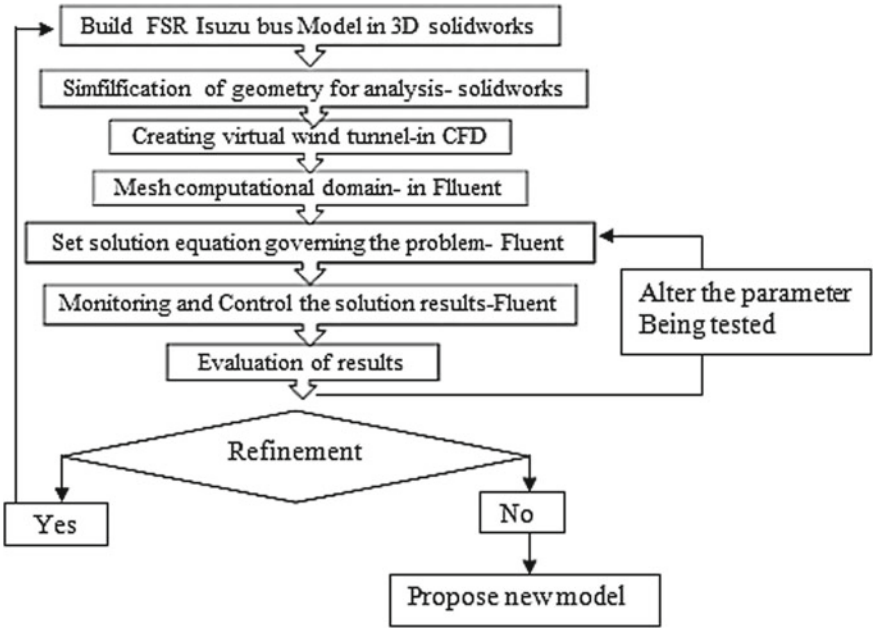


**Fig. 1** CFD flowchart

**Fig. 2** Existing FSR Isuzu bus

## *2.1 Benchmarking the Baseline Model*

This baseline model is one of the FSR Isuzu countrywide bus shapes (Fig. 2). The dimensions of the body are almost considered for aerodynamic analysis; FSR Isuzu bus was benchmarked for the study. It is the most recent model well known in Ethiopia these days.

The current situation prompts the study of the bus since this bus is used by many government and private organizations as a service and public transports. However, the design has inefficient in the overall performance due to aerodynamics. The dimensions of the body that are almost considered for aerodynamic analysis were benchmarked for the study and the geometry creation was no more than 7% of the actual dimension [13–15].

## *2.2 Design Scaled-Down Model Specifications*

FSR Isuzu bus was chosen for this study; it ought to be noticed that the CAD model utilized was not an accurate imitation of the FSR Isuzu transport, yet it is a rough model (Tables 1 and 2).

The first bus, for providing better-streamlined flow, has front tapering [1]. The second and third buses have an aerodynamically shaped and front tapering with drag reduction-curved device. Other parameters are similar to the first bus. The fourth bus has an aerodynamically shaped front with complete tapering. It also has a front side and roof smoothness toward the rear end as shown in Fig. 3. As investigated on [16–19] that a reduction of 14% of streamline drag is achieved, which compares to an 8.4% decrease in fuel utilization with a curved device.

**Table 1** Bus specifications

| Make | Isuzu FSR, Japan |
|---|---|
| Model | FSR 33L |
| Seating capacity | 44 |
| GVW (kg) | 11,000 |
| Cargo dimension ($L \times W \times H$) (mm) | 9200 × 2350 × 3000 |
| Wheelbase (mm) | 4770 |
| Front overhang | 1700 |
| Rear overhang | 2730 |
| Engine type | Diesel, 6cyl, Inline OVH, Direct injection, Water cooled 6HH1-N |
| Capacity (cc) | 8226 |
| Max output (hp/rpm) | 175/2850 |
| Transmission | Manual, 5 forward speed with overdrive |
| Brakes front/rear | The air over hydraulic dual circuits and drums |
| Fuel tank capacity (L) | 200 |
| Tyre size front/rear | 8.25-R20 radials |

**Table 2** Aerodynamic specification

| S. No. | Aerodynamic specifications |
|---|---|
| 1 | Front tapering with an angle of 15° to 25° |
| 2 | Maximum trailing edge radius of 100 mm |
| 3 | Minimum front Fairing radius of 100 mm |
| 4 | Curved device for drag reduction is added at the front of the bus |
| 5 | Curved front end |
| 9 | Front-top, middle, and bottom fairing of 100 mm, 80 mm, and 40 mm radius, respectively |
| 7 | Complete front top fairing with smoothing surface |
| 8 | Bottom fairing and smoothing surface |

## *2.3 Driving Speed Selection*

The setting of speed limits has proven an effective measure to manage driver's speed and thereby the risk of road accidents. The experienced importance of the other factors are.

- Driver background (age, gender, driving, experience, and other characteristics)
- Trip characteristics (travel purpose and trip length)
- Motives (time, pressure, safety, pleasure, and fear of apprehension)
- Car characteristics (make, model year, equipment, and power output)

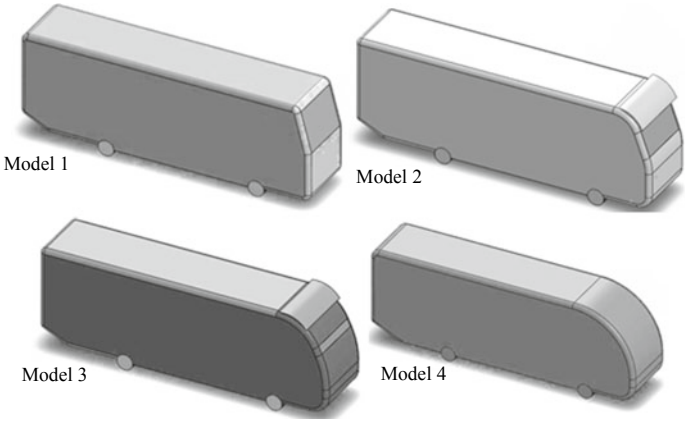


**Fig.3** Geometrical modeling of all bus models

- Driving speed limit enforcement of the Ethiopian government.

## *2.4 Turbulence Modeling*

In this study, the realizable k-ε turbulence model (RKE) described in the turbulence modeling section was used. The solver used for the analysis is ANSYS 18.1 and it solves the governing equations numerically by using a control volume method. Pressure-based implicit solver was selected [3, 5, 20]. It solves the momentum and continuity equations sequentially. It solves the equations using the second-order upwind method by considering the flow is incompressible and steady. The well-known robust turbulence k-ε model is selected [21–23]. Due to its quick convergence with moderate accuracy, this model was selected. The realizable k-ε model predicts more precisely the spreading rate of both round and planar. Non-physical turbulent viscosities are produced by the realizable k-ε model in situations when both stationary and rotating zones are existing in the computational domain [10, 24, 25]. Pressure field was calculated using pressure and velocity coupling. No independent equation is available to calculate pressure because the fluid is considered incompressible. The second-order upwind method is applied for the solution of the kinetic energy, momentum, kinetic energy, and the dissipation rate.

## *2.5 Geometry Generation*

The initial step on the familiar arrangement was to characterize the geometry that would be displayed by Solid Works CAD software to represent the air surrounding the bus. After the vehicle model has uploaded, an enclosure was generated surrounding

**Table 3** One-fourteenth of the existing dimension for wind tunnel enclosure in fluent

| Upstream | Downstream | Width | Height |
|---|---|---|---|
| 1.1403 m | 3.0702 m | 1.694 m | 0.903 m |

it. The enclosure was designed based on the recommendation from fluent for accurate results. The dimensions of the control volume that was generated approximately $10L \times 2L \times 1.5L$ where $L = 0.644$ m. The enclosure command was used to generate control volume [26, 27]. To make sure that all necessary turbulent length-scales in the flow was captured, the developed model was placed in the control volume with a spacing of $6.6L$ downstream and $2.4L$ upstream [13]. As recommended by Rodi, the appropriate dimensions of computational wind tunnel were as follows: for the upstream length 3.5 times, the overall height of the bus model, for the downstream length 9 times the height, for the width 10 times the height, and 6 times the height for the height of the wind tunnel [11]. Therefore, for better accuracy, the average values were taken. In general commercial buses, like all other vehicles, are geometrically symmetric about their longitudinal axis; to achieve this symmetry, plane is inserted along the XY-plane of the bus. With this, the bus model was cut in half longitudinally [3, 12] (Table 3).

For avoiding the meshing of the removed volume, the volume was subtracted from the control volume by using a Boolean operator. It does not affect the solution because the software fluent takes no-slip condition on surfaces where the volume is removed. It reduces the size of the mesh, thereby considerably reduces the computational time.

## *2.6 Meshing Generation*

A polyhedral mesh type was developed in this study. Polyhedral or hexahedral or a hybrid of both is generally recommended to be used in the ANSYS fluent software [3, 12]. It is utilized for decently complex geometry like the bus model in this investigation. Converted polyhedral meshes rather than constructed in the mesh component of the setup in fluent, which is used to reduce the cell count When meshing type changed from tetrahedral mesh to polyhedral mesh, the cell count reduced and the computational time also reduced. For having minimum size elements around the curvature of the bus and gradually increased the size of elements as moving away from the surface of the bus, advanced size function was used. Finally, unstructured tetrahedral hybrid elements of 620,866 for model 1,737,366 for model 2, 750,991 for model 3, and 1,532,367 for model 4 were generated at symmetry plane (Fig. 4).

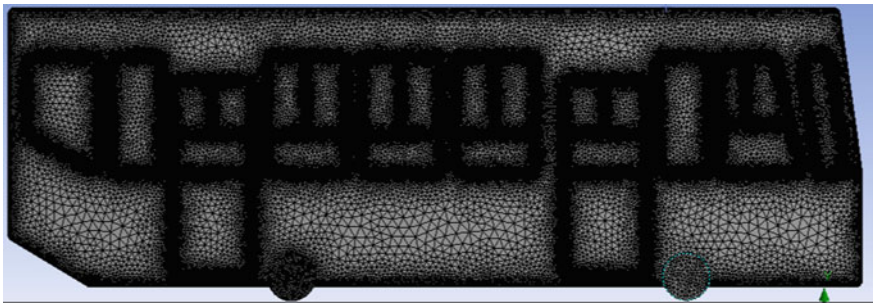

**Fig. 4** Baseline model with unstructured polyhedral mesh at the symmetry plane

**Table 4** Boundary conditions

| Boundary | Boundary conditions | Values |
|---|---|---|
| Inlet | Constant velocity | $v = 60$ kmph, 80 kmph and 100 kmph |
| | Turbulent intensity | 1% |
| | Intensity and viscosity ratio | 10 |
| Outlet | Pressure outlet | Constant pressure = 101,325 N/m$^2$ |
| Road | Wall is moving, specified shear | $v = 60$ kmph, 80 kmph and 100 kmph |
| Vehicle surface | No-slip-stationary wall | – |
| Domain top and side (Enclosure) | Wall is stationary with no-slip | – |

## *2.7 Boundary Conditions*

Rotating wheel on moving road condition was used for carrying out the analysis. Only head on wind was considered in this analysis. Three different vehicle speeds of 60 kmph, 80 kmph, and 100 kmph were selected for the analysis (Table 4).

## *2.8 Fluent Setup and Simulation Procedures*

All models of the busses with and without front fairings are simulated by fluent software using the realizable k-ε model. The polyhedral mesh is used to run the realizable k-ε turbulence model. The simulations were run with a velocity of 60 kmph, 80 kmph, and 100 kmph impeding the motion of the bus, which is a boundary condition. The velocity's origin was set at the named section "Velocity inlet" in the direction of the named section "Pressure outlet" about the "Air". The turbulence

intensity was reduced to 1% for the velocity inlet. For the pressure–velocity coupling, coupled scheme was chosen. For study flows, like the flow assumed in this work, this coupled scheme is more efficient and robust. Coupled scheme was employed. The flow courant number was set to 30 for the first time and second 50 while both the explicit relaxation factors for momentum and pressure to 0.25 were tested. The reduced explicit relaxation factors allowed for a quicker convergence of a skewed mesh, about 0.85. A factor of 0.95 is taken as the turbulent viscosity relaxation factor. Convergence was defined as the drag coefficient residual remaining constant at the $1 \times 10^{-5}$ value for ten consecutive iterations [12]. When convergence was reached, the solution was analyzed to determine the effectiveness of new designs being studied.

## *2.9 Grid Independence Test*

As the complexity of the geometries increases, the structured meshes become skewed extremely, and may lead to inaccurate solutions and unphysical solutions and can cause increased computational time [14]. CFD should give the solutions independent of the grid/mesh used in the numerical calculations.

For ensuring the obtaining of independence from the grid type, an analysis is to be conducted using various grids of increasing node density. When the values of the variables of interest like pressure, velocity, wall stress, etc., are not varying with a number of nodes in the grid, then one can say grid independence is obtained (Fig. 5).

The results showed that consistency at mesh element after 543,740 at the symmetry plane has similar output.

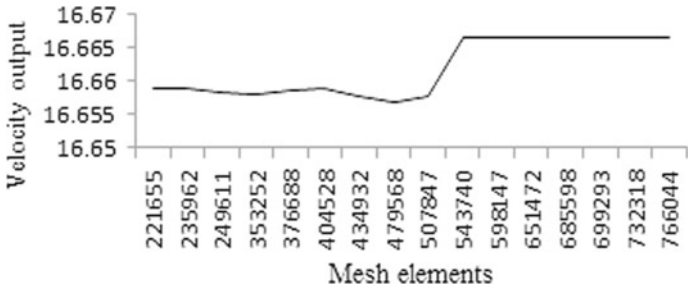


**Fig. 5** Grid independence test at the symmetry plane for the baseline model

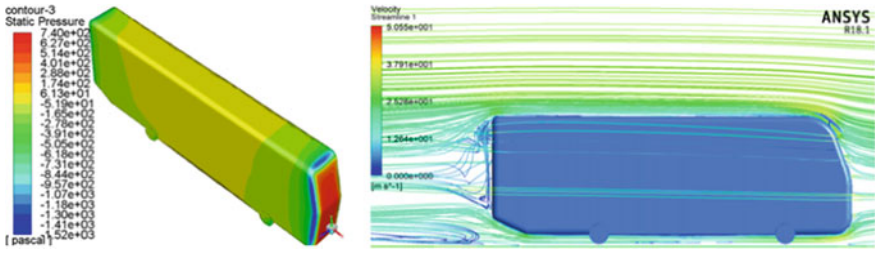


(a) (b)

**Fig. 6** Pressure contour of model 1 (**a**) and velocity streamline of model 2 (**b**) at 100 kmph, symmetry

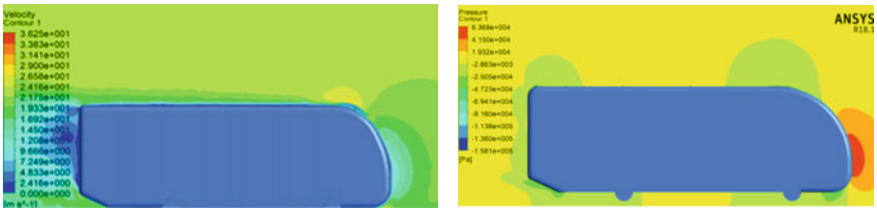


(a) (b)

**Fig. 7** Velocity contour of model 3 at 80 kmph (**a**) and pressure contour of model 4 at speed of 80 kmph (**b**)

## 3 Results and Discussions

### *3.1 Pressure and Velocity Distribution of Different Models at Varying Speeds*

See Figs. 6 and 7.

### *3.2 Comparing Drag Coefficient and Lift Coefficient*

Based on established data, on the results of the previous section, overall views of all cases have been demonstrated (Table 5). It is clear that the lowest value $C_d = 0.4141$, which corresponds to a total drag reduction of 24.03%, is obtained for case model 4. This is the case with modification of the frontal by slight curvature. This is the best case. However, the worst case is model 1 with $C_d = 0.5748$ and total drag increased to 4.25%.

**Table 5** $C_d$ and $C_l$ results at various speeds for all models

| Model | $V$ (kmph) | $C_d$ | $C_l$ | $F_d$ (N) | $F_L$ (N) | $F_t$ (N) | % $P_{sav}$ | Fuel saved (gal/h) | Fuel con. (gal) | g $CO_2$ /km produced | %$Co_2$ saved |
|---|---|---|---|---|---|---|---|---|---|---|---|
| Baseline | 60 | 0.5378 | −0.195 | 322.67 | −117.17 | 513.32 | – | – | 0.706825 | 117.72 | – |
| | 80 | 0.5462 | −0.202 | 582.24 | −215.86 | 782.47 | – | – | 1.43615 | 179.40 | – |
| | 100 | 0.5514 | −0.265 | 918.75 | −441.88 | 1128.58 | – | – | 2.589719 | 258.80 | – |
| Average | **80** | 0.5451 | −0.221 | 581.07 | −235.58 | 781.3 | – | – | 1.434003 | 179.134 | – |
| Model 1 | 60 | 0.5474 | −0.015 | 328.43 | −9.24 | 519.08 | −1.12202 | −0.00793 | 0.714756 | 119.048 | −1.122 |
| | 80 | 0.5507 | −0.035 | 587.04 | −36.88 | 787.27 | −0.61341 | −0.00881 | 1.44496 | 180.50 | −0.61 |
| | 100 | 0.5748 | −0.291 | 957.73 | −484.20 | 1167.56 | −3.45392 | −0.08945 | 2.679166 | 267.74 | −3.45 |
| Average | **80** | 0.5576 | −0.113 | 594.39 | −120.99 | 794.62 | −1.70487 | −0.02445 | 1.458451 | 182.19 | −1.71 |
| Model 2 | 60 | 0.5354 | −0.076 | 321.23 | −45.36 | 511.88 | 0.280506 | 0.001983 | 0.704842 | 117.40 | 0.28 |
| | 80 | 0.5371 | −0.109 | 572.54 | −116.08 | 772.77 | 1.239652 | 0.017803 | 1.418347 | 177.18 | 1.24 |
| | 100 | 0.5419 | −0.332 | 902.92 | −552.52 | 1112.75 | 1.40265 | 0.036325 | 2.553394 | 255.17 | 1.41 |
| Average | **80** | **0.5372** | −0.172 | 572.65 | −183.35 | 772.88 | 1.077689 | 0.015454 | 1.418549 | 177.20 | 1.08 |
| Model 3 | 60 | 0.5229 | −0.109 | 313.73 | −65.64 | 504.38 | 1.741617 | 0.01231 | 0.694515 | 115.68 | 1.74 |
| | 80 | 0.5261 | −0.111 | 560.82 | −118.22 | 761.05 | 2.737505 | 0.039315 | 1.396836 | 174.49 | 2.74 |
| | 100 | 0.5593 | −0.329 | 931.91 | −548.52 | 1141.74 | −1.16608 | -0.0302 | 2.619917 | 261.82 | −1.17 |
| Average | **80** | 0.5361 | −0.183 | 571.48 | −195.28 | 771.71 | 1.22746 | 0.017602 | 1.416401 | 176.94 | 1.23 |
| Model 4 | 60 | 0.4033 | −0.095 | 241.97 | −57.058 | 432.62 | 15.72121 | 0.111121 | 0.595704 | 99.22 | 15.72 |
| | 80 | 0.4078 | −0.229 | 434.71 | −244.00 | 634.94 | 18.85443 | 0.270778 | 1.165372 | 145.58 | 18.85 |
| | 100 | 0.4313 | −0.238 | 718.64 | −396.39 | 928.47 | 17.73114 | 0.459187 | 2.130532 | 212.92 | 17.73 |
| Average | 80 | 0.4141 | −0.187 | 441.43 | −199.66 | 641.66 | 17.87279 | 0.256296 | 1.177706 | 147.12 | 17.87 |

Bold values indicates the changes in the lift force, drag force, fuel consumption and CO2 emissions

### 3.3 Comparing Drag Force and Lift Force

The drag force is derived from the drag coefficient whereas the lift force is derived from the lift coefficient.

$$F_D = \frac{1}{2}\rho A C_d v^2 \text{ and } F_L = \frac{1}{2}\rho A C_l v^2 \tag{1}$$

The deviance of the drag force of the second- and third-bus models regarding the baseline model bus will give a clear idea about how much the drag force increases as the speed of the vehicle increases. From Table 5, it is observed that the values of lift forces are negative, which is very much necessary to increase the road-holding capacity of the vehicle and improve the steerability of the bus. Model 4 has a better drag force and lift force than the baseline model that can be important in stability and road-holding capability. This is due to the front streamlined shape modification in model 4.

### 3.4 Power and Fuel Savings

According to Kim [15] power saved on the streamlined bus model comparing the original bus model, given by

$$P_{\text{sav}} = (F_{d(\text{Model}-0)} - F_{d(\text{Model}-X)}) * v_{\text{bus}} \tag{2}$$

The power required to pull the bus against the resistance in a level road surface is calculated and their corresponding values for various speeds are given in Table 5.

$$P = \frac{F_t V}{\eta_t} \tag{3}$$

where $P$ = Power, $F_t$ = Total resistance, $v$ = Vehicle speed, and $\eta_t$ = transmission efficiency with input parameters of symmetry body [Air density in kg/m$^3$ = 1.225, frontal area in m$^2$ = 3.525, mass in kg (m) = 1100, transmission efficiency ($\eta_t$) = 0.9].

Fuel saved by the reduction in drag force Kim [15]:

$$\dot{m}_{\text{fuel}} = \frac{P_{\text{sav}}}{Q_{\text{LHV}} * \rho_{\text{fuel}} * \eta_{\text{engine}}} \tag{4}$$

where $Q_{\text{LHV}}$ = 42.5 MJ/kg is the lower heating value of diesel fuel, $\rho_{\text{fuel}}$ = 860 kg/m$^3$is the fuel density at ambient temperature, and ɳ engine = 35% is the thermal efficiency of the diesel engine.

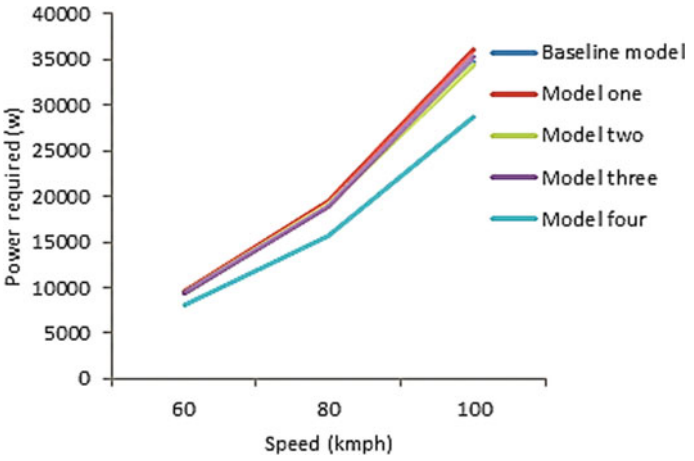


**Fig. 8** Power required graph at various speeds for all models

$$F_r = (0.015 + 0.00016V)W \tag{5}$$

where v = bus speed in m/s, $W$ = weight of bus in N

$$F_t = F_d + F_r + F_g \tag{6}$$

where $F_d$—Drag force, $F_r$—Rolling resistance, $F_g$—Gravitational force but $F_g = 0$ (leveled surface) = $W \sin \theta$.

As presented in Fig. 8, total resistance to come up with model 1 is more than the others are, and model 4 has less resistance force. Therefore, about 3.45% of total power was lost in model 1 and 17.73% of power was saved by model 4, which is maximum for the baseline model at 80 kmph.

The power required by model 1 is greater than model 2, model 3, and model 4. The power required in model 4 is much lower than the remaining models, which indicates model 4 consumes less fuel than the three models and similarly, model 1 consumes more than model 3 and model 4. Therefore, model 1 needs major improvements. Model 4 has suitable power and fuel utilization as shown in Table 5.

## *3.5 Reduction of Fuel Exhaust Emission*

The investigation on vehicles [13] shows the consumption of the fuel by ground vehicles is high and emissions account for over 30% of $CO_2$ and other greenhouse gas (GHG) emissions. One liter of diesel weighs 835 g. Diesel consists of 86.2% of carbon or 720 g of carbon per liter diesel. To combust this carbon to $CO_2$, 1920 g of oxygen are needed. The sum is then 720 + 1920 = 2640 grams of $CO_2$/liter diesel.

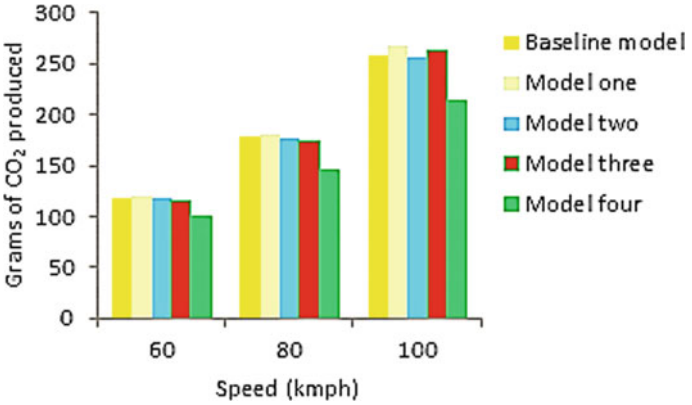


**Fig. 9** Grams of emission produced at various speeds for all models

Thus,

$$CO_{2\ \text{produced}} = x\ l_{\text{Fuel-consumed}} \times \frac{2640\ \text{g}}{Y\ \text{km}} \tag{7}$$

where $x$ is liters of fuel consumed and $y$ is km traveled.

From this investigation, the percentage reduction of the modified model relative to the baseline model was calculated to be 15.72115%, 18.85444%, and 17.73115% emissions reduced in model 4 at 60kmph, 80kmph, and 100kmph, respectively. Thus, the average emission reduction was 17.87284%, as shown in Table 5. As shown in Fig. 9 that average emission on modified models indicates, there is a maximum reduction in model 4.

## *3.6 Comparison with Similar Works of ASTU*

Yesfalgn and Ramesh [18] modeled a new bus body design compared with the Yutong cross-country bus by using a turbulence model with quadrilateral mesh. The new bus concept was based on the frontal area. They found that the drag force reduction was about 34.4%. Lelalem [19] modified only the frontal part and add-on the device used as a drag reduction device. He simulated the model using the RKE turbulence model with converted polyhedral mesh. The results showed that the drag coefficient was reduced by 22.754%. In this work, the total amount of drag force reduction was about 24.03% by frontal body modification. This investigation shows that qualified design without any addition of a drag reduction device. This shows the high cost and drags reduction with a small modification.

# 4 Conclusion and Future Work

## *4.1 Conclusion*

The objective of the current investigation was to develop a framework for a simplified FSR Isuzu bus model frontal body geometry and aerodynamic shape optimization with the dimensions obtained on actual bus and findings of the similar previous works using available CFD software. After this problem, initialization process, the CFD model is generated. In the process of redesigning, four study cases, to improve the aerodynamics of existing FSR Isuzu bus plying on Ethiopian roads, were investigated and the reduction in total drag, emissions, and fuel was observed.

The drag coefficient was reduced from 0.5471 for the baseline model to 0.4141for model 4; thus, the reduction in $C_d$ is 24.03% at an average velocity of 80kmph. Subsequently, the drag force has reduced from 581.07 N to 441.43 N, thus reducing the power required to 15,841.87kw and about 3447.56 kW power can be saved (17.87% reduction). The study indicated that model 4 has lesser $CO_2$ emissions, 147.11738 g/km by17.87 percentage reduction on average due to due to reduced fuel consumption (0.256296 gal/h).

The study indicated that modifications made on the front reduced drag by approximately streamlining the frontal body shape and only slanting of the front have increased the drag as shown in model 1. Thus, reduced the drag force, results in increased performance of the bus, reduced emission release to the atmosphere, and reduced fuel requirement. Therefore, the objectives are been achieved.

## *4.2 Future Work*

It is recommended that the proposed framework should be implemented on the overall exterior geometries in the future and besides, the curved device modification should be applied to the rear bus geometry. In the current investigation, only numerical analysis is performed, so in the future, wind tunnel, experimental test results should be compared with the same models. The effects of aerodynamic drag on the inclined roads are should be studied.

**Acknowledgements** The authors would like to acknowledge the support extended by Adama Science and technology university in accomplishing this research work.

## References


1. Pawar YP, Chaware SD (2017) Improvement in fuel efficiency of bus using a roof fairing. J Emerg Technol Innov Res 4(11):624–628
2. Akash Bath Kumar M, Rana P (2018) Int J Adv Eng Res Dev 5(3):434–439. 2348-4470
3. Rasu NG, Renil AM, Sachin SJ (2016) CFD analysis of commercial bus models for improvement of aerodynamic performance. J Chem Pharm Sci 3:106–110
4. Takroni EAM (2015) Aerodynamic characteristics and drag reduction of buses. MSc thesis
5. Raveendran A, Sridhara SN, Rakesh D, Shankapal SR (2009) Exterior styling of an intercity transport bus for improved aerodynamic performance. SAE Tech. Pap., vol. 2009-Decem, no. December, pp. 9–16, 2009. https://doi.org/10.4271/2009-28-0060.
6. Sudin MN, Abdullah MA, Shamsuddin SA, Ramli FR, Mohd M, Tahir MM (2014) Review of research on vehicles aerodynamic drag reduction methods. Int J Mech Mechatronics Eng 14(02):35–47
7. Kanekar S, Udawant K, Patwardhan M (2019) Methodology development for external aerodynamic evaluation of a bus and its impact on fuel economy along with experimental validation. SAE Tech. Pap., vol. 2019-Janua, no. January, pp. 1–6. https://doi.org/10.4271/2019-26-0294
8. Altaf A, Omar AA, Asrar W (2014) Review of passive drag reduction techniques for bluff road vehicles. IIUM Eng J 15(1):61–69. https://doi.org/10.31436/iiumej.v15i1.477
9. Gophane M, Salvi G, Pratik GP, Ravi K (2014) Effect of aerodynamic forces over the bus body and design of conceptual bus for enhanced performance. Int J Eng Trends Technol 11(4), 159–162. https://doi.org/10.14445/22315381/ijett-v11p231
10. Lorenzon A. Antonello, Berto F (2018) Critical review of turbulence models for CFD for fatigue analysis in large steel structures
11. Rodi W (1997) Comparison of LES and RANS calculations of the flow around bluff bodies. J Wind Eng Ind Aerodyn 69–71:55–75. https://doi.org/10.1016/S0167-6105(97)00147-5
12. Littlewood R (2013) Novel methods of drag reduction for squareback road vehicles. Available: https://dspace.lboro.ac.uk/dspace-jspui/handle/2134/12534
13. Dias G, Tiwari NR, Varghese JJ, Koyeerath G (2016) Aerodynamic analysis of a car for reducing drag force. IOSR J Mech Civ Eng (IOSR-JMCE) 13(3):114–118. https://doi.org/10.9790/1684-130301114118
14. Heck ML (2015) Investigation of flow through complicated microfluidic devices and over micro patterned surfaces using computational fluid dynamics. University of Oklahoma
15. Bae Geun H, Lee S, Eui Jae L, Jeong Jae K, Kim M, You D, Sang Joon L (2016) Reduction of drag in heavy vehicles with two different types of advanced side skirts. J Wind Eng Ind Aerodyn J 155:36–46. https://doi.org/10.1016/j.jweia.2016.04.009
16. Mohamed EA (2015) computational investigation of aerodynamic characteristics and drag reduction of a bus model. Am J Aerosp Eng. 2(1):64. https://doi.org/10.11648/j.ajae.s.2015020101.16
17. Shinde SS, Shende PMD (2017) Enhancement of aerodynamic drag reduction of passenger vehicle using CFD analysis. Int J Innov Res Sci Eng Technol 6(1), 437–448
18. Yesfalgn Damissie H, Ramesh Babu N (2017) Aerodynamic drag reduction on locally built bus body using computational fluid dynamics ( CFD ): a case study at Bishoftu automotive industry. Int J Eng Res Technol 6(11)
19. Lealem Tilahun T (2018) Study of aerodynamic drag reduction of locally built bus body using CFD analysis: a case study on Bishoftu automotive industry. Adama Science and Technology University
20. Siraj A, Ramesh Babu N, Srinivasa Reddy K (2019) Static analysis of dump truck chassis frame made of composite materials. Int J Eng Sci Technol 11(2):21–32. www.ajol.info/index.php/ijest
21. Alemayehu G, Nallamothu RB (2017) Programmable logic controller (Plc) application for hybrid electric vehicle (Hev) simulator. Int J Mech Eng Technol (IJMET) 8(9):281–292
22. Negera DW, Bhaskaran J, Ilmi I, Nallamothu RB (2019) Characterisation of hybrid composite made of false banana fiber and sisal fiber. Int J Eng Adv Technol (IJEAT) 9(2). ISSN: 2249-8958

23. Getu D, Nallamothu RB, Masresha M, Nallamothu SK, Nallamothu AK (2020) Production and characterization of bamboo and sisal fiber reinforced composite for interior automotive body application. Mater Today: Proc. https://doi.org/10.1016/j.matpr.2020.08.780
24. Alemayehu Z, Nallamothu RB, Liben M, Nallamothu SK, Nallamothu AK (2020) Experimental investigation on characteristics of sisal fiber as composite material for light vehicle body applications. Mater Today: Proc. https://doi.org/10.1016/j.matpr.2020.07.386
25. Feliche E, Nallamothu RB et al (2017) A study on cause of rollover of sugar cane haulage semitrailer truck in Ethiopia Sugar Estate: case of Wonji Sugar Factory. Int J Eng Trends Technol (IJETT) V43(4):205–211. https://doi.org/10.14445/22315381/IJETT-V43P235. ISSN: 2231-5381. www.ijettjournal.org published by seventh sense research group
26. Ashagrie G, Nallamothu RB, Nallamothu AK, Nallamothu SK (2017) A study on driving stability of bus using computational fluid dynamics (CFD). Int J Res Appl Sci Eng Technol 5(XI)
27. Molla KY, Chul-Ho K, Ramesh Babu N (2017) Aerodynamic design of the Ethiopian train for energy economy under crosswind conditions. In: 2017년도 한국철도학회 추계계학술대회 논문집, KSR 2017, South Korea
28. Abebe L, Nallamothu RB, Subrahmanyam KHS, Nallamothu SK, Nallamothu AK (2016) Thermal analysis of disc brake made of different materials. SSRG Int J Mech Eng (SSRG-IJME), V3(6):5–9. ISSN: 2348-8360. https://doi.org/10.14445/23488360/IJME-V316P102. www.internationaljournalssrg.org/IJME/index.html